

August 2022

Nonreciprocal Electromagnetics of Layered Media

Samaneh Pakniyat
University of Wisconsin-Milwaukee

Follow this and additional works at: <https://dc.uwm.edu/etd>



Part of the [Electrical and Electronics Commons](#)

Recommended Citation

Pakniyat, Samaneh, "Nonreciprocal Electromagnetics of Layered Media" (2022). *Theses and Dissertations*. 3055.
<https://dc.uwm.edu/etd/3055>

This Dissertation is brought to you for free and open access by UWM Digital Commons. It has been accepted for inclusion in Theses and Dissertations by an authorized administrator of UWM Digital Commons. For more information, please contact scholarlycommunicationteam-group@uwm.edu.

NONRECIPROCAL ELECTROMAGNETICS OF LAYERED MEDIA

by

Samaneh Pakniyat

A Dissertation Submitted in
Partial Fulfillment of the
Requirements for the Degree of

Doctor of Philosophy
in Electrical Engineering

at

The University of Wisconsin-Milwaukee

August 2022

ABSTRACT

NONRECIPROCAL ELECTROMAGNETICS OF LAYERED MEDIA

by

Samaneh Pakniyat

The University of Wisconsin-Milwaukee, 2022
Under the Supervision of Professor George W Hanson

In plasmonic systems, interaction of light and surface plasmons leads to excitation of surface plasmon polaritons (SPPs) carrying energy on the surface. In an isotropic plasmonic system, the SPPs optical response is reciprocal, which means that the forward and backward surface waves have identical propagation behaviors and SPPs refract when they encounter a discontinuity on the surface. In order to excite SPPs resilient to the surface disorders, the system reciprocity needs to be broken by different techniques such as applying an external magnetic bias. In this case, the plasmonic system becomes a gyrotropic medium. Recently, it has been shown that magnetized continuous plasmonic systems such as semiconductors and graphene support unidirectional SPPs, the surface waves that are propagating only in one direction and are robust to the surface impurities. This topic has attracted the attention of many researchers, including our group. In this work, we study the properties of unidirectional SPPs in different plasmonic configurations. Our findings set a solid foundation for future active nonreciprocal plasmonic devices based on unidirectional SPPs.

First, we study SPPs in the well-known topological Voigt configuration. Since indium antimonide (InSb) crystal is often cited as a suitable magneto-optics platform that supports unidirectional SPPs, we evaluate the functionality of this crystal as a topological platform by considering realistic conditions. So, using the far-field time-domain THz spectroscopy measurement, our group, along with colleagues at the University of West Virginia, examine the magneto-optical effects of the undoped InSb crystal at different temperatures varied from 5K to 300K. We apply a multi-carrier material model to consider the effect of both electrons and holes charge carriers. Then, using the measured data we examine the unidirectional SPPs and discuss the constraints that limit applications. We design a grating metallic coupler on the surface of the magnetized InSb to launch unidirectional SPPs. The measured reflection data reveals strongly nonreciprocal SPPs that are tunable by temperature and magnetic field intensity. The patterned InSb sample is tilted to examine topological behavior. The measured data are consistent with the theoretical predictions.

Next, via simulation we study unidirectional SPPs on the surfaces of a magnetized plasma slab coated by a dielectric material below the plasma frequency. The equi-frequency contours are extracted from dispersion surface which follows by obtaining the group velocity vectors to estimate the SPP propagation behaviors at different operation frequencies. We mainly focus on a frequency window wherein there exists narrow-beam

unidirectional SPPs. We present a Green's function model for a gyrotropic slab to examine the effect of thickness on the narrow SPP beams. We observe that when the slab is thin, in addition of two excited narrow beams at the top interface, two other narrow beams form at the bottom interface due to energy coupling. We characterize them by an asymptotic dispersion relation derived from a quasi-static approach.

Then, we study the nonlocality effects and Chern numbers in a continuous plasma medium. Topological SPPs are characterized by integer Chern invariants. When a continuous plasma system is model by the (overly simplistic, but often used) local Drude model, there is a dispersion band that is ill-behaved at large wavenumbers and assigned by a non-integer Chern number. In this case, the number of unidirectional edge modes cannot be determined using the bulk-edge correspondence principle. This problem has been previously solved by introducing an ad hoc material model which includes a spatial cutoff wavenumber in the model. However, the proposed nonlocal model leads to some difficulties such as non-realistic material response at large wavenumbers and the need to interpolate the interfaced materials so that the Chern numbers sum to zero as they must. To overcome this issue, we instead suggest applying the hydrodynamic material model which is a more realistic, physical, nonlocal model. In this case, we evaluate the Chern numbers and dispersion bands. We show that this model form a complete, self consistent model that clarifies the topological physics of plasma continua.

In the next work, we propose a new plasmonic configuration to excite nonreciprocal curved SPPs. We demonstrate that by applying radial bias in a plasma system, one-way SPPs travel on a circular path, unlike in an axially-biased system which supports SPPs with linear trajectory. We derive a Green's function model for a radially-biased plasma system to examine curved SPPs. A nonreciprocal circular junction is proposed to effectively guide SPPs on the curvature.

Finally, we examine the unidirectional SPPs in two-dimensional plasmonic platform. It has been previously shown that graphene monolayer biased by external magnets supports unidirectional edge modes. Here, we evaluate the magneto-optical effects of graphene/chromium triiodide (CrI₃) heterostructure. The exchange field between layers provides an effective out of magnetic field. The optical conductivity is a tensor with non-zero off-diagonal elements which manifest the nonreciprocal response. We obtain one-way edge modes and Faraday rotation in this multi-layer structure. However, we argue that the nonreciprocal response of this heterostructure is weaker than the isolated graphene biased by external magnets. Therefore, CrI₃ magnetic monolayer does not work as an alternative magnetic source that causes strong non-reciprocity.

© Copyright by Samaneh Pakniyat, 2022
All Rights Reserved

To Mojtaba, and my daughter, Sophia

TABLE OF CONTENTS

| | |
|---|-----------|
| LIST OF FIGURES | xx |
| LIST OF TABLES | xx |
| LIST OF ABBREVIATIONS | xx |
| ACKNOWLEDGEMENTS | xxii |
| 1 Introduction | 1 |
| 1.1 Reciprocal Surface Plasmon Polaritons | 2 |
| 1.2 Nonreciprocal Plasma Media | 4 |
| 1.3 Topological Insulators | 4 |
| 1.4 Topological Surface Plasmon Polaritons | 5 |
| 1.5 Berry Phase, Berry Curvature, and Chern number | 7 |
| 1.6 Application of Topological SPP | 9 |
| 1.7 Purpose and Originality of this Work, and Chapters Contents | 9 |
| 2 Magnetized Semiconductors | 17 |
| 2.1 Material Model | 18 |
| 2.1.1 Local Drude Model | 18 |
| 2.1.2 Non-local Hydrodynamic Model | 21 |
| 2.1.3 Non-local Spatial Cutoff Model | 23 |
| 2.2 Bulk Modes in a Gyrotropic Plasma Medium | 24 |
| 2.2.1 Bulk Modes in the Voigt Configuration | 25 |
| 2.2.2 Bulk Modes with Propagation Angle α_b ; The Existence of Common Bandgaps | 26 |
| 2.3 Bulk Modes in a Gyrotropic Medium Described by the HD Model | 28 |
| 2.4 Field Vectors in a Gyrotropic Region | 29 |
| 2.5 Field Vectors in an Isotropic Region | 31 |
| 2.6 SPP Dispersion of a Single-Interface Structure | 31 |
| 2.6.1 SPP Dispersion in Voigt Configuration | 33 |

| | | |
|----------|--|-----------|
| 2.6.2 | SPP Dispersion in a Multi-Layer Structure | 34 |
| 2.7 | Reflection from a Single-Interface Structure | 34 |
| 2.7.1 | Reflectance in the Voigt Configuration | 36 |
| 3 | Experimental Detection of Unidirectional SPP in the Voigt Configuration | 38 |
| 3.1 | Bulk and SPP Modes in the Voigt Configuration | 39 |
| 3.2 | Magneto-Optics Properties of Indium Antimonide | 42 |
| 3.2.1 | Reflection from InSb Sample Interface | 42 |
| 3.2.2 | Temperature-Dependent InSb Carrier Parameters | 46 |
| 3.3 | SPP Properties for Realistic InSb Model | 47 |
| 3.4 | Experimentally Detection of Tunable Unidirectional SPP | 50 |
| 3.4.1 | Verification of SPP Unidirectional Behavior by a Tilted Sample | 54 |
| 3.5 | Summary | 60 |
| 4 | Narrow-Beam Unidirectional SPP in Magnetized Semiconductor | 61 |
| 4.1 | Green Function for a Finite-thickness Plasma | 63 |
| 4.2 | SPP Propagation Properties Below the Plasma Frequency | 64 |
| 4.3 | SPP Field Profile at the Interface of a Half-space Gyrotropic Medium | 67 |
| 4.3.1 | SPP Field Profile on the Surfaces of a Magnetized Plasma Slab | 70 |
| 4.4 | Quasi-Static Approximation | 73 |
| 4.5 | Summary | 75 |
| 5 | Chern Numbers in Magnetized Semiconductors | 76 |
| 5.1 | Chern Number Relations for a Nonlocal System | 77 |
| 5.2 | Chern Numbers of a Local Drude Model | 80 |
| 5.3 | Chern Numbers of the Nonlocal Hydrodynamic Model | 82 |
| 5.4 | Chern Numbers of the Nonlocal Spatial Cutoff Model | 83 |
| 5.5 | Summary | 84 |
| 6 | Unidirectional Curved SPP in a Radially Magnetized System | 86 |
| 6.1 | Bulk and SPP Modes in a Radially Magnetized Plasma System | 87 |
| 6.2 | Dyadic Green's Function for a Radially Magnetized Plasma | 91 |
| 6.2.1 | Reflection Tensor in a Radially Biased System | 93 |
| 6.3 | Electric Field Profile of Curved SPPs and Their Propagation Properties | 94 |
| 6.4 | An Application for Curved SPPs | 97 |
| 6.5 | Summary | 98 |

| | |
|---|------------|
| 7 Nonreciprocal Effects in CrI3/graphene Heterostructure vs. Magnetized graphene Monolayer | 99 |
| 7.1 Optical Conductivity of Graphene and CrI3/Graphene | 100 |
| 7.2 Surface Bulk Modes in the Infinite Sheets of Graphene and CrI3/Graphene | 107 |
| 7.3 Unidirectional Edge Modes in the Semi-Infinite Sheets of Graphene and CrI3/Graphene . . . | 108 |
| 7.4 Faraday Rotation in Graphene Monolayer vs. in Graphene/CrI3 | 110 |
| 7.5 Summary | 114 |
| Conclusion | 115 |
| References | 118 |
| Curriculum Vitae | 131 |

LIST OF FIGURES

| | | |
|-----|---|----|
| 1.1 | (a) Surface charge distribution and electric field at the interface of a metal and dielectric (b) exponential decay of the electric field intensity normal to the interface, reprinted with permission from [1] (c) schematic of reciprocal SPPs excited by a metal grating under normally incident plane wave at the interface of an isotropic plasma medium and a dielectric (d) bulk and SPP dispersion diagrams in an isotropic plasma medium. | 3 |
| 1.2 | Basic topological continua configurations (a) a plasma magnetized by out-of-plane magnetic field (b) Voigt configuration (c) Faraday configuration. $\mathbf{k}_t = k_x \hat{\mathbf{x}} + k_y \hat{\mathbf{y}}$ is the wave vector of the SPPs on the plasma surface. | 6 |
| 1.3 | Parallel transport about a closed contour (a) on a flat surface, (b) on a sphere surface. . . . | 8 |
| 2.1 | Dispersion diagram of biased plasma bulk modes for different angles of propagation, where $k_p = \omega_p/c$. Gray shaded regions highlight bandgaps in the dispersion. The dashed red line corresponds to a wave which is independent of bias, while the solid black lines correspond to the waves which are dependent on bias. | 27 |
| 2.2 | Dispersion bands and associated Chern numbers of (a) nontrivial bulk modes and (b) trivial modes using the local Drude and nonlocal hydrodynamic Drude models; $k_p = \omega_p/c_0$, where c_0 is the speed of light in free space. | 28 |

- 3.1 Bulk modes and surface plasmons for a metal-InSb (idealized) interface. (a) Bulk and SPP dispersion for dissipation-less InSb characterized by parameters $n_e = 3 \times 10^{21} \text{m}^{-3}$, $m^* = 0.015m_0$, $\varepsilon_\infty = 15.68$, and mobility $\mu = \infty$ ($\omega_p^* = \omega_p/\sqrt{\varepsilon_\infty} = 2\pi(1.014\text{THz})$). The in-plane magnetic field is $B = 0.7\text{T}$ ($\omega_c = 1.28\omega_p^* = 2\pi(1.3\text{THz})$), and the metal permittivity is $\varepsilon_m = -10^4$. The gray regions are the magnetic-field dependent bandgaps (b) The geometrical schematic of the structure under study. SPPs are excited by a dipole source located at the metal-InSb interface. (c) The electric field distribution (E_z) of SPPs at different frequencies P1-P4, 0.5, 0.7, 1.76 and 4 THz, respectively, marked in (a). Points P1 and P3 are points on the SPP dispersion where the SPPs are topologically protected. Reprinted with permission from [2]. 40
- 3.2 Excitation of unidirectional SPP by a metal grating under normally incident plane wave. (a) Dispersion diagram; topologically protected unidirectional SPPs (red) emerging from the bulk gaps (gray regions). Parameters used are $\omega_p/2\pi = 6 \text{ THz}$, $\omega_c/2\pi = 1.4 \text{ THz}$. (c) and (d) Simulated electric field intensities for the sample structure illustrated in (b). The size of the simulation area is $2\text{mm} \times 0.7\text{mm}$. The grating period used for SPP launching is $d = 2\pi/k_0 = 84\mu\text{m}$. Reprinted with permission from [3]. 41
- 3.3 Magnetic field induced bulk plasmon band gap (a, d, g) The calculated dispersion diagrams of TM bulk modes in isotropic ($B = 0$) and gyrotropic ($B \neq 0$) plasma media. Room temperature carrier properties of an undoped InSb single crystal sample are used in this calculation: $n_e = 1.5 \times 10^{22} \text{m}^{-3}$, $m_e^* = 0.019m_0$, $n_{hh} = 1.49 \times 10^{22} \text{m}^{-3}$, $m_{hh}^* = 0.43m_0$, $n_{lh} = 1.38 \times 10^{20} \text{m}^{-3}$, $m_{lh}^* = 0.019m_0$, $\varepsilon_\infty = 15.7$. Blue solid curves correspond to the ideal dissipation-less cases with infinite mobility and the dashed curves correspond to practical cases with finite carrier mobilities of $\mu_e = \mu_{lh} = 5 \text{m}^2/\text{Vs}$ and $\mu_{hh} = 0.01 \text{m}^2/\text{Vs}$. (b, e, h) The calculated Voigt-configuration reflectance at an air/plasma interface. Inset in (b) shows the modeling and experiment geometry. (c) The polarization of TM mode at $B = 0.7T$ and $B = 0T$ (inset). (f, i) The field-induced reflectance change calculated by dividing the nonzero-field reflectance by the zero-field value. In all plots, the two field-induced bandgaps are highlighted in grey. Reprinted with permission from [4]. 43
- 3.4 Measured field-dependent THz reflectances of undoped InSb (a, b) Reflectance spectra of InSb at 300K and 50K measured under different in-plane magnetic fields. (c, d) Corresponding field-induced reflectance changes comparing data obtained with and without a magnetic field. Dashed curves in (a-d) show the fitting results based on reflectance equation, r_{TM} . Reprinted with permission from [4], and produced by Cen's group. 44

| | | |
|-----|---|----|
| 3.5 | Temperature-frequency (a, b) and magnetic field-frequency (d, e) diagrams of the THz reflectance from an InSb sample. Dashed lines trace the changes in the critical frequencies. (a, d) show the experimental data, and (b, e) show the simulated results. (c, f) The carrier densities(c), mobility(f) of electron, heavy hole, light hole at various temperatures. Reprinted with permission from [4], and produced by Cen's group. | 45 |
| 3.6 | Anisotropy of carrier properties in InSb. (a, b) Temperature-dependent electron density (a) and mobility (b) measured at different in-plane sample rotations. As shown by the inset of (a), marks the angle between the external magnetic field and the [110] lattice axis. Reprinted with permission from [4], and produced by Cen's group. | 47 |
| 3.7 | (a,b,c) The SPP dispersion diagrams and SPP propagation length (indicated by the size of the circles) at different temperatures by considering realistic InSb model. The carrier density and mobility at each temperature are extracted from the measurement as $n_e = 3.5 \times 10^{20} \text{ m}^{-3}$, $\mu = 18 \text{ m}^2/\text{Vs}$ at 50°K , $n_e = 8.5 \times 10^{20} \text{ m}^{-3}$, $\mu = 11.5 \text{ m}^2/\text{Vs}$ at 200°K , and $n_e = 1 \times 10^{22} \text{ m}^{-3}$, $\mu = 5.2 \text{ m}^2/\text{Vs}$ at 300°K . Shaded gray regions indicate the bandgaps. Reproduced with permission from [2], and produced by Cen's group. | 48 |
| 3.8 | Bulk modes and nonreciprocal InSb-metal interface SPPs for a realistic InSb model with finite dissipation, (a-b) bulk and SPP dispersion diagrams using InSb material parameters at $T = 230^\circ\text{K}$. Solid lines correspond to finite dissipation and dotted lines correspond to the infinite mobility cases. (b) The electric field distribution of the unidirectional SPP, at two resonance frequencies P1 and P3, excited by a point source located at the interface for the finite-mobility case. (c) SPP propagation length (L_{SPP}) in a dissipative system at three different temperature, where $\Lambda_{\text{SPP}} = L_{\text{SPP}}/\lambda_{\text{SPP}}$. (d) Density plot of normalized SPP propagation length, Λ_{SPP} , versus frequency and temperature. Shaded regions indicate the bandgaps. Reprinted with permission from [2]. | 48 |

- 3.9 Surface magnetoplasmons generated at InSb/Au interface by normal incident light (A) Schematic of the measurement configuration. Inset shows the optical image of the Au grating (scale bar represents $50 \mu\text{m}$). (B) Side view of the measurement geometry. (C, D) Field-dependent reflectance spectra obtained on the unpatterned half of the sample (C) and the patterned half (D) at 50 K. The cyclotron frequencies are marked by small circles, and the SPP peaks are highlighted in grey. (E) Calculated SPP resonance frequencies for different fields. Left-traveling SPPs are plotted using red bubbles and right-traveling SPPs are plotted with blue bubbles. The bubble size represents the SPP propagation lengths normalized by the wavelengths (L_{SPP}/λ_{SPP}). (F-H) SPP dispersions for three different magnetic fields. The red and blue lines show the grating resonance conditions for the left-traveling (red) and right-traveling (blue) SPPs under normal incidence. In G and H, the two field-induced bulk gaps are marked by grey shaded areas. Reprinted with permission from [3], and produced based on collected data by Cen's group following our designs and simulations. 51
- 3.10 The far-field measurement of the unidirectional SPP at various temperatures. (a) The schematic geometry of the structure under test. (b) The reflection spectrum of the pattern InSb sample, measured at various temperatures. $R(B)$ and $R(0)$ are the reflectance of the biased/unbiased pattern sample, respectively. The red peaks are observed unidirectional SPP resonances. (c) The analytically estimated SPP resonance frequencies at different temperatures, obtained using the SPP dispersion diagram and the effective momentum $\beta_0 = 2\pi/d$ due to the symmetric grating as illustrated in the insert plot. (d) The reflection spectrum of the pattern InSb, results from a COMSOL simulation. Reprinted with permission from [2]. 52
- 3.11 (a) a half-space plasma medium characterized by $n_e = 0.25 \times 10^{21} \text{ m}^{-3}$, $\mu = 22 \text{ m}^2/\text{Vs}$, $m^* = 0.015m_0$ and $\varepsilon_\infty = 15.68$, under a normally incident plane wave. Reflectance spectrum of (b) an unbiased plasma and (c) a biased plasma ($B = 0.6\text{T}$) of bare sample. (d) A plasma medium covered by a metal sheet with a grating ($d = 84\mu\text{m}$ is the period of grating), where (e) and (f) show the reflectance spectrums for $B = 0$ and $B = 0.6T$, respectively. (g) A patterned plasma medium under an oblique plane wave with incident angle $\alpha = 60^\circ$. (h) Reflectance spectrum of g when (h) $B = 0$ and (i) $B = 0.6T$ 54

| | | |
|------|---|----|
| 3.12 | Unidirectional SPPs generated by light with a nonzero incidence angle. (A) Schematic of the measurement configuration. (B) Side view of the measurement geometry. (C) Field-dependent reflectance spectra measured on unpatterned and patterned sample halves at 50 K. Curves corresponding to unidirectional SPP excitations are highlighted in green. (D) SPP resonance frequencies calculated for the two incidence angles of $\pm 45^\circ$. The field ranges corresponding to unidirectional SPPs are marked in green. (E)–(G) SPP dispersions for three field values. Reprinted with permission from [3], and produced based on collected data by Cen’s group following our designs and simulations. | 56 |
| 3.13 | Calculated InSb/Au interfacial SPP properties at 50 K when using the Drude model-based Au permittivity value $\varepsilon_m^{Drude} = -2.3 \times 10^5 + i8.6 \times 10^5$. (A) Field dependent SPP resonances for a 45 degree light incidence. (B, C) SPP dispersions for $B = 0.2$ T and $B = 0.7$ T, respectively. Reprinted with permission from supplement of [3], and produced by Cen’s group. | 58 |
| 3.14 | Nonreciprocal SPP responses and temperature dependence. (A) Field-induced reflectance changes on bare (top) and patterned (bottom) sample regions at 50 K. (B) Field-induced reflectance changes at 0.7 T with normal (solid curve) and $\pm 45^\circ$ (dashed curve) incidences. The inset shows the difference between the data obtained at $B = 0.7T$. (C) Dispersion relations of bulk modes (brown) and SPPs (black) at $B = 0.7T$. (D) SPP resonance frequencies calculated for $\theta = 0^\circ$ and 45° . (E)–(L) are similar to (A)–(D) but for higher temperatures of 180 K and 250 K. In (D), (H), and (L), bulk gaps are marked by grey and unidirectional field windows are marked by green. The unidirectionality of the modes residing in the overlapping regions is topologically protected. The modes residing inside the green region but outside the grey region are also unidirectional but are not topologically protected. Reprinted with permission from supplement of [3], and produced based on collected data by Cen’s group. . . | 59 |
| 4.1 | Slab of gyrotropic material with finite thickness h . The slab is biased with a static magnetic field along the y-axis. A vertical dipole is suspended a distance d above the slab and is responsible for exciting the displayed field pattern near the top surface of the slab. Reprinted with permission from [5]. | 63 |
| 4.2 | SPP dispersion surface for a biased-plasma-vacuum interface, obtained by solving for the roots of (2.86). (a) Perspective view of the upper and lower bands. (b) Close-up of the lower band, where the solid black lines are the equi-frequency contours for a few representative frequencies and ω^\pm outline the region of SPP resonance. The designations I-IV refer to Fig. 4.4. The common bulk-bandgap is in Regions II and III. Reprinted with permission from [5]. | 64 |

- 4.3 Density plot of the scattered field integrand in Eq. (4.5), and equi-frequency contours (solid red), which correspond to the intersection of the surface dispersion shown in Fig. 4.2b and an ω -constant plane, for a half-space biased-plasma medium at different frequencies. The notation I-IV refers to the regions shown in Fig. 4.4. Red arrows indicate the group velocity vectors. Reprinted with permission from [5]. 65
- 4.4 (a) Two dimensional dispersion of the SPP for different propagation angles, ϕ_s , with respect to the positive (negative) x-axis for right (left) branches of the dispersion. The bulk dispersion (solid black lines) for $\alpha_b = 0^\circ$ indicate the lower bulk bandgap common to all propagation angles. The solid orange lines show the dispersion of light in vacuum, e.g., $\omega/\omega_p = \pm k_s/k_p$. (b) Density plot of the scattered field integrand in Eq. (4.5) in the $\omega - k_s$ plane. The bright parts correspond to the flat parts of the 2D dispersion curves in part (a), representing the dominant contribution to the narrow beams. Reprinted with permission from [5]. 66
- 4.5 Top panels: polar patterns of the scattered electric field, $|E_z^r|$, obtained from the Green function for a magnetized plasma-vacuum interface, $(\rho, z, \varphi) = (0.7\lambda, 0.016\lambda_p, 0 < \varphi < 2\pi)$, and $\Gamma = 0.015\omega_p$. The panel dimensions are $2\lambda \times 2\lambda$. Bottom panels: the electric field distribution in the x-y plane generated using COMSOL. The dashed circle of radius $\rho = 0.7\lambda$ indicates the spatial contour over which the Green function results in the bottom panels are shown. Panel (f) shows results for several values of frequency, whereas the corresponding panel (e) is for one of the frequencies in Panel (f). λ is free space wavelength and $\lambda_p = 2\pi c/\omega_p$. Reprinted with permission from [5]. 68
- 4.6 Poynting vector: (a) absolute value of tangential Poynting vector for observation points on circles with different radii, $(\rho, z, \varphi) = (\rho', 0.016\lambda_p, -\pi < \varphi < \pi)$ (b) direction of maximum Poynting vector for observation points along the two main narrow beams, $(\rho, z, \varphi) = (\rho, 0.016\lambda_p, \varphi_{beam1,2} = \pm 32^\circ)$. $\hat{\mathbf{n}}$ is the unit normal vector to the interface. The dashed lines show the beam angles, and it is seen that the Poynting vector becomes aligned with the beam angle, as expected, for observation points not too close to the source. The operating and collision frequency are $\omega = 0.65\omega_p$ and $\Gamma = 0.015\omega_p$, respectively. Reprinted with permission from [5]. 69
- 4.7 a. Electric field distribution (E_z) computed using COMSOL at the interface of a half-space gyrotropic plasma in the presence of a hole discontinuity. b. The same as (a), but at the interface of a finite thickness slab ($h = 0.12\lambda_p$) in the presence of a discontinuity; the SPP, excited on the top interface by a point dipole, propagates around the open surface to the bottom side of the plasma. $\Gamma = 0.04\omega_p$. Reprinted with permission from [5]. 69

- 4.8 SPP beam pattern excited by a vertical dipole source at the first interface of a finite thickness biased-plasma slab, obtained by evaluating integral (4.5) for set observation point $(\rho, z, \varphi) = (0.5\lambda, 0.03\lambda, 0 < \varphi < 2\pi)$ where λ denotes the free space wavelength. The frequency of operation is set within the bulk bandgap of the plasma $\omega = 0.65\omega_p$ and the collision frequency is set to $\Gamma = 0.015\omega_p$. Four values of thickness are considered such that (a) $h = 0.3\lambda_p$, (b) $h = 0.1\lambda_p$, (c) $h = 0.07\lambda_p$, and (d) $h = 0.045\lambda_p$. Panel (e) shows how the beam grows logarithmically as thickness increases. Reprinted with permission from [5], generated by coauthor A. Holmes. 71
- 4.9 Squared amplitude of the scattered electric field profile (z component) excited by a vertical dipole source located at the first interface ($d = 0$) of a thin finite thickness biased-plasma slab of thickness $h = 0.04\lambda_p$. The squared amplitudes of the scattered electric field below and above the slab are obtained in (a)-(b) using the FEM in COMSOL ($\Gamma = 0.05\omega_p$) and in (c)-(d) by evaluating the Sommerfeld integrals in (4.5)-(4.6). In (c) the observation point is chosen to be $z = -h - 0.1\lambda$, $\rho = 0.9\lambda$ and $0 < \varphi < 2\pi$, and in (d) the observation point is chosen to be $z = 0.03\lambda$, $\rho = 0.5\lambda$, and $0 < \varphi < 2\pi$, and $\Gamma = 0.015\omega_p$. The operating frequency is $\omega = 0.65\omega_p$. Reprinted with permission from [5], (c-d) plots generated by coauthor A. Holmes. 72
- 4.10 Solutions to the quasi-static SPP dispersion relation (4.9) for a finite thickness slab of thickness $h = 0.25\lambda_p$ and wavenumber $k_s = 10k_p \gg 1/h$. The cyclotron frequency ranges from 0 to $0.4\omega_p$. Reprinted with permission from [5]. 74
- 5.1 Dispersion bands and associated Chern numbers of (a) spatial cutoff (SC) model with nonlocal factor of $\kappa = 1/(1 + k^2/k_{\max}^2)$, (b) modified spatial cutoff (MSC) model with nonlocal factor $\kappa = 1/(1 - k^2/k_{\max}^2)$, where $k_{\max} = 200k_p$. (c) a dispersion plot including dispersion diagram of four material models; SC, MSC, hydrodynamic (HD) and local Drude (LD) models. The magnetized plasma region is characterized by $n_e = 3.6 \times 10^{21}(\text{m}^{-3})$, $\varepsilon_\infty = 15.68$, $m^* = 0.0175m_0$, $B_0 = 0.6\text{T}$, $\mu = \infty$, given $\omega_p^* = 2\pi(1.03\text{THz})$, $\omega_c/\omega_p = 0.23$ and $\gamma = 0$. Reprinted with permission from [6]. 85

- 6.1 Unidirectional curved SPP vs. linear propagating SPP. (a) Geometry sketch (b) Bulk and SPP dispersion diagrams. The gray regions denote the band gaps. The electric field profile (E_z) of the SPP propagating at the interface of an isotropic medium and a plasma region magnetized by (c) a static radial bias $\mathbf{B} = B_0\hat{\rho}$ that is centered on the origin, (d) an axial bias $\mathbf{B} = -B_0\hat{\mathbf{x}}$, and (e) an axial bias $\mathbf{B} = B_0\hat{\mathbf{y}}$. The SPPs are excited by a point source with the input power of 1W, located at $(\rho_0, \phi_0, z) = (R_a/2, \pi, 0)$, where $R_a = 500\mu\text{m}$ is the radius of the plasma region. (f,g,h) The electric field oscillation, respectively along the circular, vertical and horizontal trajectories shown by white dashed lines in (c,d,e). λ_{SPP} is the SPP wavelength. In (f), s is the arc length defined as $s = \rho_0 \cos(\phi - \phi_0)$ where ϕ is the angle of the observation point with respect to the x-axis and ρ_0 is the radius of the dashed circle. The magnetized plasma is characterized by Eq. (2.11) where $n_e = 3.6 \times 10^{21}\text{m}^{-3}$, $m^* = 0.0175m_0$, $\varepsilon_\infty = 15.68$, $B_0 = 0.6\text{T}$, given $\omega_p^* = \omega_p/\sqrt{\varepsilon_\infty} = 2\pi(1.03\text{THz})$, $\omega_c/\omega_p^* = 0.93$ and $\Gamma = 0.00015\omega_p$. The top region is metal with dielectric constant of $\varepsilon_r = -10^4$. The resonance frequency $f = 1.567\text{THz}$ is within the upper band gap. Reprinted with permission from [7]. 89
- 6.2 Saddle point approximation vs. exact solution (the integrand of (6.12) and (6.11), respectively, over q variation) for $f = 1.567\text{THz}$ at $(\rho = 250\mu\text{m}, \phi = 5\pi/4, z = 0.003\lambda_p)$. $n_e = 3.6 \times 10^{21}\text{m}^{-3}$, $m^* = 0.0175m_0$, $\varepsilon_\infty = 15.68$, $B_0 = 0.6\text{T}$, and $\varepsilon_r = 8$. Reprinted with permission from [7]. 92
- 6.3 Electric field distribution (E_z) of the curved SPPs excited at the interface of dielectric/ radially magnetized plasma ($\mathbf{B} = B_0\hat{\rho}$) media using (a) Green's function model (6.12) and (b) a full-wave COMSOL simulation. The radial bias is centered on the origin and the dipole with input power 1W is located at $(250\mu\text{m}, \pi, 0)$. The observation points are on a plane with distance $z = 0.003\lambda_p$ above the interface ($\lambda_p = 2\pi/\omega_p$). (c) The electric field oscillation along the circular trajectories (white dashed semicircles). The electric field profile of the linear propagating SPPs excited at the interface of the dielectric/axially biased plasma ($\mathbf{B} = -B_0\hat{\mathbf{x}}$) using (d) GF model (e) COMSOL simulation. (f) The extracted data from dashed line trajectories. The resonance frequency is $f = 1.567\text{THz}$. Reprinted with permission from [7]. 95
- 6.4 (a,b) Unidirectional curved SPPs by considering different amounts of dissipation (metal or dielectric on top) (c) A vertical cross-section view of the two-layer magnetized system ($h_i = h_g = 200\mu\text{m}$). Energy leakage occurs in the dielectric region after several wavelengths of curved SPP propagation (d) Electric field density of the curved SPPs on the surfaces parallel to the interface located at different distances (z) from the interface $z = 0$ ($\varepsilon_r = 8$). $n_e = 3.6 \times 10^{21}\text{m}^{-3}$, $m^* = 0.0175m_0$, $\varepsilon_\infty = 15.68$, $B_0 = 0.6\text{T}$, $f = 1.567\text{THz}$. Reprinted with permission from [7]. 96

| | | |
|-----|--|-----|
| 6.5 | Electric field profile of the SPP propagating at the interface of metal/magnetized plasma, passing through (a) a 90° circular bend junction under radial bias vs. (b) an oblique junction under $5\pi/4$ axial bias. (c) Output power vs. frequency. $n_e = 3.6 \times 10^{21} \text{m}^{-3}$, $m^* = 0.0175m_0$, $\varepsilon_\infty = 15.68$, $B_0 = 0.6 \text{T}$, $\Gamma = 0.00015\omega_p$, $\varepsilon_r = -10^4$, $f = 1.567 \text{THz}$, $w = 4h = 360 \mu\text{m}$, $d = 300 \mu\text{m}$. Reprinted with permission from [7]. | 97 |
| 7.1 | (a) Top and (b) side views of the $(\sqrt{3} \times \sqrt{3})$ CrI_3 -(5×5) graphene structure (C: yellow; Cr: blue; I: green), with the commensurate supercell given in black. (c) Calculated 2D contributions to the optical properties: Drude intraband contribution, Ω_{Drude} (blue); anomalous Hall, σ_{xy}^{2D} (red); and interband, σ_{xx}^{2D} (green). The empty diamonds at 3.25 and 3.75 Å correspond to the twisted (2×2) CrI_3 -($\sqrt{31} \times \sqrt{31}$) graphene calculations. Reprinted with permission from [8], and generated by Prof. Weinert. | 102 |
| 7.2 | (a, b): Two-dimensional conductivity of graphene in the presence of the CrI_3 exchange field for separations $d \in \{2.5 \text{\AA}, 3.25 \text{\AA}, 3.75 \text{\AA}\}$, and the conductivity of isolated graphene (Iso-GR) computed by considering an external field of 100T, the chemical potential $\mu = -0.3 \text{ eV}$, $\Gamma = 2 \times 10^{12} \text{ s}^{-1}$ and $T = 40 \text{ K}$. (c) Off-diagonal element vs. CrI_3 -graphene separation compared with the isolated-graphene external bias case. (d) The off-diagonal element normalized by the frequency average of the diagonal element. $G_0 = 2e^2/h$. Reprinted with permission from [8], and generated by coauthor A. Holmes using the optical conductivity data computed by Prof. Weinert. | 103 |
| 7.3 | Dispersion bands of bulk quasi TM (dashed red) and bulk quasi TE modes (solid red) for graphene in an external bias. The blue dots show the TM edge modes for external bias $B = 100T$ and black dots are the edge modes when the bias is reversed ($B = -100T$). The shaded region indicates the bulk band gap. $\omega_B = 526.2 \times 10^{12}$ is the frequency of the first Landau level, $\mu = -0.3 \text{ eV}$, $T = 40 \text{ K}$, $\Gamma = 2 \times 10^{12} \text{ s}^{-1}$, $B = 100 \text{ T}$, and $l_B = \sqrt{\hbar/eB} = 2.6 \text{ nm}$ is the magnetic length. VAC indicates vacuum dispersion. Panel b is a better illustration of the optical response at low frequency range by applying denormalized scales in the axes. Reprinted with permission from [8], and generated by coauthor A. Holmes. | 105 |
| 7.4 | Bulk (solid red) and edge (dots) TM-like dispersion of graphene modes in an exchange field for two CrI_3 -graphene separations. VAC indicates vacuum dispersion. Reprinted with permission from [8], and generated by coauthor A. Holmes. | 106 |
| 7.5 | Edge SPP launched by a dipole source near the graphene edge for several values of external magnetic bias. $f = 13.87 \text{ THz}$, $\mu = 0.05 \text{ eV}$, $T = 40 \text{ K}$, $\Gamma = 2 \times 10^{12} \text{ s}^{-1}$. Reprinted with permission from [8]. | 109 |

| | | |
|-----|--|-----|
| 7.6 | Edge SPP launched by a dipole source near the graphene-vacuum edge for the exchange field magnetic bias corresponding to two CrI ₃ -graphene separations. Reprinted with permission from [8]. | 110 |
| 7.7 | (a) Edge SPP propagation length (left branch of Fig. 7.4) and (b) SPP wavelength on graphene in an exchange field as CrI ₃ -graphene separation varies. (c) Edge SPP propagation length and (d) SPP wavelength on graphene in an external bias for different frequencies. $\mu=0.05$ eV, $T=40$ K, $\Gamma = 2 \times 10^{12}$ s ⁻¹ . For (c)-(d), the first LL occurs at $8.8\sqrt{ B }$, well beyond the considered frequencies. For comparison for the separations 2.5 Å, 3 Å, 3.5 Å, 4 Å, the effective bias fields are 750 T, 600 T, 450 T, and 90 T, respectively. Reprinted with permission from [8], and generated by coauthor A. Holmes. | 111 |
| 7.8 | (a,b) Faraday rotation and (c,d) ellipticity of graphene as a function of frequency for different external bias values, and (e, f) density plots of Faraday rotation. ω_B is the frequency of the first Landau level for each bias. $\mu=0.2$ eV, $T=40$ K, and $\Gamma=2$ THz. Reprinted with permission from [8]. | 112 |
| 7.9 | (a) Faraday rotation and (b) ellipticity of the CrI ₃ -graphene heterostructure as a function of frequency for different separations. The dotted curve shows FR for externally-biased graphene using the effective field strengths corresponding to different layer separations. Reprinted with permission from [8]. | 113 |

LIST OF TABLES

| | | |
|-----|---|----|
| 3.1 | SPP propagation length and bandgap width in frequency at various temperatures. BG_1 (which starts at 0 THz; the provided value is for the top of the bandgap) and BG_2 are the lower and upper bandgaps, respectively. BTWN-BGs indicates at the midpoint between the two bandgaps (in the bulk passband), $\epsilon_m = -800 + i550$ [9], $B = 0.7T$, and $\Lambda_{SPP} = L_{SPP}/\lambda_{SPP}$. | 49 |
| 3.2 | Comparison of plasmon propagation properties in the undoped, N-doped and P-doped crystals at $T = 77^\circ K$, considering $m^* = 0.015m_0$, $\epsilon_\infty = 15.7$ and $\epsilon_m = -800 + i550$. $\Lambda = L_{SPP}/\lambda_{SPP}$. Dashes indicate no SPP exists. BG_1 starts at 0 THz; the provide value is for the top of the bandgap. | 50 |
| 5.1 | Comparison of material dielectric tensor and Chern numbers of the LD, SC, MSC and HD models | 85 |

LIST OF ABBREVIATIONS

| | |
|------------------------|------------------------------------|
| ϵ_0 | Vacuum Permittivity |
| μ_0 | Vacuum Permeability |
| E | Electric Field Intensity |
| H | Magnetic Field Intensity |
| D | Electric Elux Density |
| c | Vacuum Speed of Light |
| SPP | Surface Plasmon Polariton |
| THz | Terahertz |
| InSb | Indium Antimonide |
| CrI₃ | Chromium triiodide |
| LD | Local Drude |
| HD | hydrodynamic |
| SC | Spatial Cutoff |
| MSC | Modified Spatial Cutoff |
| MO | Magneto-Optics |
| GF | Green's Function |
| FR | Faraday Rotation |
| KR | Kerr Rotation |
| SP | Surface Plasmon |
| LL | Lambda Level |
| THz-TDS | Terahertz Time-Domain Spectroscopy |
| EFC | Equi-Frequency Contour |
| DFT | Density Functional Theory |

| | | |
|-----------------|-------|------------------------|
| BG | | Bandgap |
| vdW | | van der Waals |
| T | | Temperature |
| ω | | Angular Frequency |
| ω_p | | Plasma Frequency |
| ω_c | | Cyclotron Frequency |
| Γ | | Collision Frequency |
| L_{SPP} | | SPP Propagation Length |
| λ_{SPP} | | SPP Wavelength |
| k_{SPP} | | SPP Momentum |

ACKNOWLEDGEMENTS

I would like to express my sincere gratitude to my Ph.D. adviser, Professor George W Hanson, for his support and guidance throughout this project. Many thanks to other committee members, Prof. Armstrong, Prof. Law, Prof. Weinert, and Prof. Guptasarma. I am also grateful for unconditional support of my family, especially my husband, who is always by my side.

Chapter 1

Introduction

1.1 Reciprocal Surface Plasmon Polaritons

The field of plasmonics has seen rapid growth in both research and application over the last decades. Plasmonic and nanophotonic devices are extremely light, miniature in size, and less expensive compared to the conventional systems. Studying the light-matter interaction in plasmonic systems is important, because it leads to invention of novel plasmonic devices and development of plasmonic and nanophotonic technologies for medical and industrial applications.

Plasmonic media such as metals, semiconductors, and electron gases consist of free charge particles. By turning on and off a static electric source, the particles start oscillating back and forth at the plasma frequency until their initial energy is lost due to damping. The particle oscillation can be quantized by plasmons. That is, a plasmon is a quantum of plasma oscillation, like a photon that is a quantum of optical oscillation. Surface plasmons are those plasmons that are confined to the surface of the plasmonic material. Surface plasmons can couple with photons and create plasmon polaritons. Thus, surface plasmon polaritons (SPPs) are the surface waves excited at the interface due to the interaction of the surface plasmons and light photons. Surface charge oscillation and electric field distribution associated to the SPPs with wavelength λ_{SPP} are shown in Fig. 1.1a. As shown in Fig. 1.1b, the electric field exponentially decays into the plasma and dielectric regions with skin depth δ , and SPPs are very confined to the surface. While SPPs are propagating on the surface, their energy is being absorbed by the plasma medium or scatters outside. The SPP propagation length (L_{SPP}) is another important length scale, which represents a distance where the SPP energy is diminished on the surface by $1/e$ of the initial value.

To excite SPPs, the momentum of the incident light must be matched to the SPPs momentum (k_{SPP}). The SPP momentum is relatively large, due to the mass of the charged particles, whereas light momentum is, although finite, quite small. The momentum matching can be provided using different configurations such as prism couplers, a grating structure, a vertical dipole probe, and a single, or an array, of resonators. Figure 1.1c is a sketch of SPPs excited at the interface of an isotropic plasma medium and a dielectric by a grating structure under a normally incident plane wave. Fig. 1.1d shows dispersion (momentum vs. frequency) diagram of the bulk plasmons and SPP modes. Below the plasma frequency, the plasma medium behaves like an opaque material, such that the light does not transmit inside the plasma region and a bandgap forms. However, the light energy flows on the surface by coupling to SPPs. The SPPs dispersion bands are outside the light cone, which means that the SPP propagation velocity is smaller than the speed of light in the dielectric region, such that the SPPs are relatively slow waves with respect to the light speed. Their dispersion diagram is symmetric, meaning that the forward and backward waves, with positive and negative momentum, respectively, have the same dispersion properties. In fact, the SPPs do not have any preferential direction for propagation at the interface of two isotropic materials with opposite-

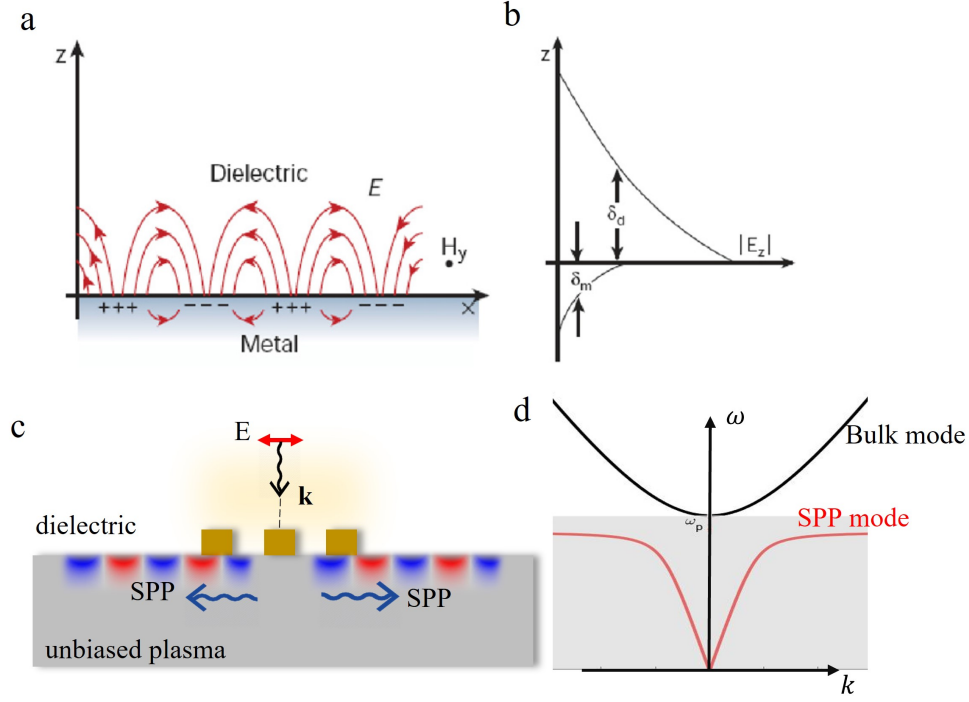


Figure 1.1: (a) Surface charge distribution and electric field at the interface of a metal and dielectric (b) exponential decay of the electric field intensity normal to the interface, reprinted with permission from [1] (c) schematic of reciprocal SPPs excited by a metal grating under normally incident plane wave at the interface of an isotropic plasma medium and a dielectric (d) bulk and SPP dispersion diagrams in an isotropic plasma medium.

sign permittivity. Therefore, the media such as unbiased semiconductors are reciprocal (reciprocity and non-reciprocity concepts are defined in the next subsection).

Different techniques can be applied to dynamically manipulate the propagation direction of the SPPs on the surface and guide them only in one direction. Unidirectional SPPs, can be excited by engineering the design of the SPP launchers, for example designing metasurfaces [10, 11], asymmetric gratings, simple metallic gratings coated by nonlinear optical materials [12], grooves with different depth and width [13], slits and resonators [14, 15], and changing the incident wave polarization [16]; see Ref. [17] for a comprehensive review. In these cases, even though the directionality is tunable, the excited SPPs still are reciprocal. As a result, when they encounter a discontinuity or defect on the surface, they reflect or refract. So, they are not inherently protected waves from back-scattering or diffraction. In this work, we study the SPPs that are inherently unidirectional and robust waves. They exist in nonreciprocal plasmonic structures.

1.2 Nonreciprocal Plasma Media

A system whose input and output can be interchanged without altering the system response is said to be reciprocal. For example, a reciprocal antenna can be used as a transmitter or a receiver with the same radiation or receiving pattern. In a two-port reciprocal system, the voltage at port 2 induced by a current source at port 1 is equal to the voltage at port 1 when the same current source is used in port 2. A reciprocal system consists of linear passive devices. From the wave propagating aspect, when a wave travels through a reciprocal medium in some direction, the wave-material interaction is the same, no matter what the wave propagation direction is.

Unlike reciprocity, nonreciprocity (NR) phenomena implies that the field created by a source, and observed at an observation point, is not the same as the case when the source and observation points are interchanged. In an NR system, the interaction of the wave and the system is dependent on the propagation direction. As a circuit example, a resistor is reciprocal whereas a diode is nonreciprocal.

Different techniques can be used to break reciprocity in a plasmonic medium. One common way is to apply an external magnetic field. In this case, the Lorentz force affects the motion of the charged particles and breaks time-reversal symmetry (refer to Ref. [18] which provides a comprehensive study on the concept of electromagnetic reciprocity and time reversal). As a result of applying the magnetic field, the dispersion properties of the bulk and surface modes change. A new band-gap opens above the plasma frequency in the bulk dispersion diagram. The SPP dispersion band becomes asymmetric, meaning that the forward and backward SPPs have different propagation properties. In addition, a frequency window forms wherein the backward SPPs are not allowed to propagate. SPPs within a frequency range which overlaps between this nonreciprocal window and the bulk material bandgap are protected waves from reflection and diffraction, because they cannot propagate backward or radiate within the plasma region. These resilient surface waves are known as unidirectional topological SPPs. The host materials supporting topological SPPs are called topological insulators. Among different types of topological insulators, we focus on Chern-type continuous plasma media that are magnetized by an external magnetic bias. In the next section, we review the origin of topological insulators.

1.3 Topological Insulators

Topology is a branch of mathematics that examines the properties of geometrical objects that are invariant under continuous deformation, such as bending, stretching, and without opening or closing a hole. For example, a square is topologically equivalent to a circle, because one can be reshaped into another under continuous transformation. However, a torus and a sphere are not topologically equivalent geometries, because a hole would have to be opened in a sphere to transform it into a torus. Geometrical surfaces can be

topologically classified by their genus, g , which corresponds to the number of holes. For instance, a sphere has $g = 0$, while a torus (donut) has $g = 1$. This number is unaffected by continuous deformation of the system. Topological geometries characterized by the same integer number g are classified as being in the same category. [19, 20].

The topology concept was first applied to condensed matter systems by Thouless and Simon, et al. [21, 22]. They proved that the Hall conductivity of a periodic potential is quantized by an integer number known as the Chern number (which plays the role of genus, and which is immutable unless a change in the topology of the momentum space occurs), which led to the introduction of electronic topological insulators. Like ordinary insulators, topological insulators have an electronic band structure with a bandgap separating the conduction and valence bands. Each band is assigned by an integer Chern number and the gap Chern number is defined as the sum of Chern numbers of bands below the bandgap. When a topological insulator with nonzero gap Chern number slowly interpolates with a gap-less trivial insulator with zero Chern number, somewhere along the way the energy gap has to vanish. This energy flows at the interface between topological insulator and trivial insulator by an edge state. Therefore, in this topological system, there exists an edge state that connects different bands. The gap Chern number gives the number of edge states at the interface of these two materials. This number cannot change unless the general band structure of the bulk material changes. So, the propagation properties of the edge states are unaffected by deformation of the material surface, and they are resilient to surface impurities [23–25]. Then, Haldane and Raghu brought the concept of topological Chern insulators from condensed matter physics to photonics and electromagnetics [26, 27]. They proposed a periodic photonic crystal that consists of magnetically biased Ferrite rods in which they observed a topological edge state and derived the associated Chern invariant. Topological behaviors in artificial topological periodic configurations have been studied in Refs. [28, 29]. Next, Silveirinha classified the continuous plasma media as Chern-type topological insulators by deriving the integer Chern numbers associated to the frequency bands of the bulk material [30]. Ref. [31] provides a review on other classes of topological insulators including \mathbb{Z}_2 wave insulators, valley Hall wave insulators with broken inversion symmetry, Floquet topological insulators, and topological semimetals with Weyl and 3D Dirac points. Our work is related to the continuous plasma topological insulators.

1.4 Topological Surface Plasmon Polaritons

Nonreciprocal topological SPPs in plasma continua have several important features. They are unidirectional (i.e., they can only propagate in one direction). Due to their strongly nonreciprocal behavior, they do not reflect upon encountering a discontinuity. They also can not radiate into the plasma material, because they operate in the bulk bandgap of a topologically nontrivial material. Thus, they are immune from back-

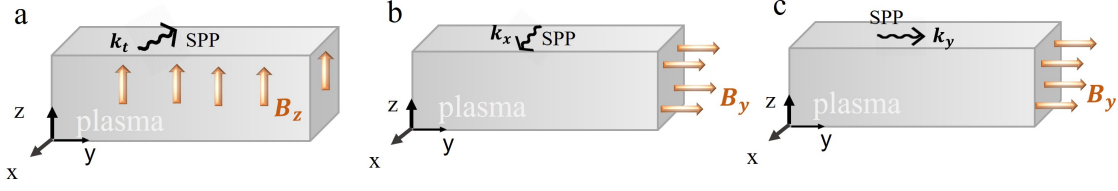


Figure 1.2: Basic topological continua configurations (a) a plasma magnetized by out-of-plane magnetic field (b) Voigt configuration (c) Faraday configuration. $\mathbf{k}_t = k_x \hat{\mathbf{x}} + k_y \hat{\mathbf{y}}$ is the wave vector of the SPPs on the plasma surface.

scattering and diffraction and pass over any type of defect and discontinuity on the surface. From a wave-propagation aspect, it is an interesting feature which can be used for efficient energy routing or in the design of nonreciprocal devices.

Topological SPPs can be characterized by an integer invariant (e.g., Chern number), which cannot change except when the underlying momentum-space changes (the momentum-space analog of opening or closing a hole in the object). Thus, another view of the reflection- and diffraction-free aspect of topological SPPs is that they are governed by bulk material properties, and they are not sensitive to surface features. So they can only change qualitatively when the bulk topology changes. A change in topology arises when a bandgap is closed or opened.

In addition to the nonreciprocal effects of SPPs in magnetized continua, dynamic manipulation of their propagation direction or properties is possible. They can be tuned by changing the magnetic bias direction or intensity, which is important in some plasmonic applications. Unlike other types of unidirectional SPPs excited by for example asymmetric launchers, topological SPPs are inherently unidirectional and reflection-free.

In addition of general features discussed above for topological SPPs in magnetized plasma media, SPPs may gain unique properties depending on the magnetized plasma configuration. The properties of SPPs in different biased plasma configurations have been widely studied [32–34]; see the comprehensive review in Ref. [35]. Some of these basic configurations are i. the external magnetic bias is perpendicular to the interface, and, correspondingly, the SPP propagation vector (Fig. 1.2a), ii. the magnetic bias is parallel to the interface, but perpendicular to the propagation vector, called the Voigt configuration (Fig. 1.2b), and iii. the magnetic bias is parallel to the interface and also parallel to the propagation vector, known as the Faraday configuration (Fig. 1.2c).

Topological SPPs in the Voigt configuration cross the bulk bandgap and exist above the plasma frequency. This configuration was re-examined in [36] and their topological behavior has been demonstrated. In Refs. [30, 37], the associated Chern invariants were calculated. Following that, in [38] the insensitivity of SPPs to three-dimensional defects was investigated and argued that even though there is no back-scattering,

there exists side-scattering which affects the SPPs properties. In [39], a master equation was derived for a nonreciprocal plasma to examine qubit entanglement dynamics in several waveguides. Dual to a plasma Voigt system, in [40] topological modes in a magnetized ferrite were detected.

In the Faraday configuration, SPPs travel along the in-plane external magnetic bias. In this case, there are longitudinal modes which are unaffected by the magnetic field intensity, unlike two circularly polarized transverse modes [41]. When the magnetic field intensity is large, the cyclotron frequency becomes larger than the plasma frequency. In this case, the frequency bands of the longitudinal and transverse modes intersect, forming two degeneracy points at the intersections known as Weyl points, which are the source of Berry curvature and Berry phase in momentum space [42–44].

In addition to magnetized semiconductors, graphene also supports topological SPPs. Graphene is a two-dimensional plasmonic platform (a single plane of graphite). Graphite consists of parallel atomic layers of carbon atoms, the layers being weakly bound together by van der Waals (vdW) forces. As such, graphite is easily cleaved to form few layer materials, or even monolayers (graphene). Since its experimental isolation in 2004 [45], graphene has been an object of considerable study for both scientific and industrial investigators. Graphene’s most notable feature is its atomic hexagonal lattice, which results in linear electronic dispersion and the presence of Dirac points at the Fermi level. As a result, electrons behave as massless particles in the vicinity of the Dirac point, leading to extraordinary electrical and mechanical properties [46].

When graphene is biased by an out-of-plane magnetic field, it is characterized by a conductivity tensor with non-zero off-diagonal elements due to the Hall effect. In [47], it was shown that a normal magnetic bias not only breaks reciprocity in a graphene monolayer, but also opens a non-trivial bulk bandgap around zero frequency, with a gap Chern number equal to ± 1 . So, graphene supports unidirectional surface plasmon polaritons propagating at the edge of a graphene sheet.

1.5 Berry Phase, Berry Curvature, and Chern number

Unidirectional, back-scattering immune properties of topological SPPs arise from the momentum-space topology of the nonreciprocal system with broken time-symmetry. To explain this phenomenon, it is necessary to introduce several concepts such as Berry phase, Berry curvature, and the relation between these concepts and Chern number.

The momentum space of a periodic structure is the Brillouin zone, which is equivalent to a torus, while the momentum space of a continuous material is the Riemann sphere. Consider a vector undergoing parallel transport (e.g. the vector pointed to the local east) on a closed path in momentum space. If the path is on a flat surface (Fig. 1.3a), the vector direction at the end point is the same as the initial points, but this does not occur on a curve surface. According to the adiabatic theorem, after a full-round cycling about

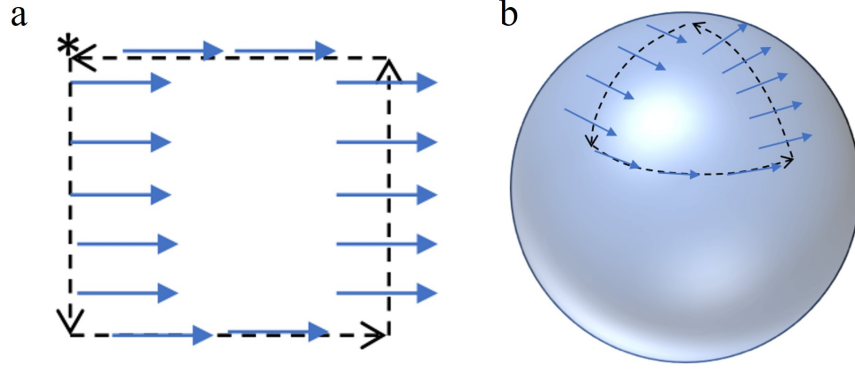


Figure 1.3: Parallel transport about a closed contour (a) on a flat surface, (b) on a sphere surface.

a close contour on a sphere surface (Fig. 1.3b), the vector returns to the initial state subject to acquiring some phase, known as the Berry phase. This geometrical phase is physical and observable, like the dynamic phase. Now consider $\omega_n(\mathbf{k})$ as an eigenmode of a typical Hermitian eigenvalue problem. In the momentum space, starting from the initial point \mathbf{k}_i , along a close path ends up to the momentum \mathbf{k}_f such that $\mathbf{k}_i = \mathbf{k}_f$, the eigenmode evolves. The relation between eigenmode at the start and end point is $\omega_n(\mathbf{k}_i) = e^{i\gamma_n} \omega_n(\mathbf{k}_f)$, where γ_n is the Berry phase and defined as [48, 49]

$$\gamma_n = \oint d\mathbf{k} \cdot \mathbf{A}_n(\mathbf{k}), \quad (1.1)$$

where $\mathbf{A}_n = i\omega_n^\dagger(\mathbf{k}) \cdot \nabla_{\mathbf{k}} \omega_n(\mathbf{k})$ is Berry connection, also known as Berry vector potential, that connects the eigenmode at point \mathbf{k} and $\mathbf{k} + d\mathbf{k}$. The curl of Berry connection is the Berry curvature $\mathbf{F}(\mathbf{k}) = \nabla_{\mathbf{k}} \times \mathbf{A}$. The integral of Berry curvature over the Riemann surface gives an integer quantity C_n known as the Chern number [48, 49]

$$\oint_S \mathbf{F} \cdot \mathbf{n} dS = 2\pi C_n. \quad (1.2)$$

C_n is analogous to the genus g of the geometrical surface (the number of holes), wherein the integral of the Gaussian curvature over the geometry surface is related to the genus ($2\pi(2 - 2g)$). So, Chern number changes only if the momentum space topology changes. In addition, this number indicates the number of Berry monopoles, which are sources of Berry curvature, within the closed surface.

Now consider the interface of two materials with common bandgaps. According to the bulk-edge correspondence principle, the difference of the gap Chern numbers gives the number of topological edge modes. The property of the edge modes is related to the topology of momentum space of the energy bands, and it is insensitive to the surface impurities, which leads to back-scattering immune property.

1.6 Application of Topological SPP

Topological surface waves have been studied for two decades. Due to their unique propagation properties, they can be used in wave propagating applications and energy routing. Unidirectional SPPs have applications in nonreciprocal systems where one-way propagation is required. For example, in the plasmonic isolator, in which the wave propagates from port one to port two, but there is no power transmission in the opposite way, from port two to port one. The same scenario is in the plasmonic circulators with three or four ports. They can also be used in the design of nonreciprocal switches. These are important components in plasmonic and photonic integrated circuits for imaging, energy routing, and data processing. These novel plasmonic components operate in the optical and infrared frequency range. Their invention leads to development of high frequency technologies, which are important in high frequency communication and data processing. These technologies are important because they provide more bandwidth, increase the data rate transmission and capacity of the communication systems, and lead to high-resolution data processing. In addition, in medicine, infrared frequencies have less harmful effects than X-ray frequencies for the human body.

Like other plasmonic components, these nonreciprocal components are extremely light, miniature in size, and less expensive than their traditional counterparts.

Unidirectional SPPs can also be used for generating hotspots. When the surface wave reaches the waveguide terminal, it cannot propagate backward and its energy is blocked there. Then, the energy intensity enhances at the terminal point and generates a hotspot, which is useful for enhancing nonlinearities [50].

1.7 Purpose and Originality of this Work, and Chapters Contents

In the second chapter, we discuss different material models for magnetized semiconductors. We compare dielectric tensor and permittivity elements of the local Drude, nonlocal spatial cutoff, and nonlocal hydrodynamic models. Then, we obtain the bulk dispersion equation for these material models and compare their dispersion diagrams. We identify a bulk bandgap common to all propagation directions of the plasma bulk modes, within which the SPPs exist. Next, we derive the SPP dispersion equations as well as reflectance from single interface of a plasmonic system. We use these relations frequently through the thesis. Chapter 3 to Chapter 7 are related to each project done in this research. The contents are discussed in the following.

The propagation properties of SPPs in the Voigt configuration have been widely studied theoretically, but there is still a lack of experimental evaluation. We set up an experiment to measure unidirectional SPPs for the first time in this well-studied geometry, and study the SPPs properties by considering realistic conditions. We believe that the outcomes of this work pave the path toward the real-world applications of topological SPPs. It should be mentioned that this project has been done in collaboration of our team at University of Wisconsin-Milwaukee and an experimental group at West Virginia University. Our collaborators have

performed the measurements and processed data, and we have contributed to the theoretical/numerical calculations and evaluation as well as measured data processing. From the outcomes of this work we have published three papers [2–4], which we explain their contents in the next several paragraphs.

Theoretical/simulation studies of nonreciprocal SPPs, including topological SPPs, often cite Indium Antimonide (InSb) crystal as an example of a material providing the gyrotropic permittivity tensor necessary for nonreciprocal phenomena [50–56]. InSb is a narrow-gap semiconductor with high electron mobility and low effective masses. In this crystal, the carrier dynamics can effectively mediate the coupling between light and static fields [57–73]. InSb hosts strong magneto-optical (MO) couplings that are tunable by temperature and doping [73–78]. Tailored MO effects in InSb have enabled a variety of intriguing functionalities, such as field induced transparency [68, 77], nonreciprocal polarization rotation or optical isolation [52, 73, 74], and nontrivial photonic topologies [67].

Besides these successful demonstrations, the interplay between the plasmonic charge oscillations and cyclotron resonances in InSb can also produce field-controlled reflectivity modulations with superior performances. Such effects produced at THz frequencies by intrinsic samples are less explored in the existing literature, and thus needs to be systematically mapped out, particularly at low temperatures.

In this regard, we measure reflectance from the bare InSb samples using far-field THz time-domain spectroscopy (THz-TDS). Using the measured data we extract the magneto-optical properties of InSb at a wide range of temperature and magnetic field intensity variations. This provides important information for future active THz device developments. Then, we evaluate the functionality of InSb as a platform to support unidirectional SPPs by considering realistic conditions. We show that, while SPPs with reasonable propagation characteristics can be obtained, there exists severe constraints that limit performance. In particular, we find that for InSb to serve as a viable SPP platform under modest bias field strengths, one needs to use undoped materials and low, but not too-low, temperatures to obtain sufficiently-high mobility and a reasonably-sized bulk bandgap.

Next, we detect unidirectional SPPs at the interface of an isotropic metal and a gyrotropic metal in the Voigt configuration. Previously, it has been derived that at isotropic metal-gyrotropic metal interfaces [79–81], the SPPs are strictly unidirectional at a frequency window without any thermodynamic paradox [82]. The unidirectionality of SPPs in this frequency window is further protected by topology of the bulk optical band structure [30, 37, 83–85]. They arise from a bias-induced asymmetry, and thus it is preserved when nonlocal effects are present. To experimentally demonstrate this effect, in this work we excite and characterize terahertz (THz) surface magneto-plasmons at a grating-coupled gyrotropic-metal/isotropic-metal interface at low temperatures. The theoretically predicted nonreciprocal SPP dispersions are clearly observed. This system also allows active control over both the SPP directionality and frequency with weak magnetic fields. To bridge our work with future applications, we also discuss how the nonreciprocal SPP propagation is

affected by practical material characteristics.

The results of this project are reported in the third chapter. The measured THz reflectances of undoped InSb single crystals in a Voigt geometry with transverse magnetic fields up to 0.7 T and at varied temperatures from 5 K to 300 K are available. The carrier parameters of InSb sample are extracted from the measure data. Then, the properties of topological SPPs are examined by considering realistic conditions in a plasma system. It is shown that temperature plays an important role in optimizing the SPP propagation properties. Then, with the help of a symmetric grating launcher, the SPPs are observed at the interface of gold/InSb at various temperatures using a far-field measurement. Lastly, using a tilted patterned sample, the unidirectional behavior of SPPs is verified.

The next project is a study on propagation behavior of unidirectional SPPs on the surface of a semi-conductor slab coated by a dielectric material. In a frequency window below the plasma frequency, SPPs form two narrow beams with nonreciprocal response. Their propagation behavior is rather different than the SPPs in Voigt configuration above the plasma frequency.

These narrow beams were first discovered in [86,87] with focus on the quantum force on a decaying atom. Then, in [82] the excitation of narrow beam modes was considered using circular-polarized dipole sources. In the present work, we investigate these below-the-gap SPPs in more detail. They are, similar to topological SPPs, unidirectional, operate in a bulk bandgap (and so are diffraction-free), and only change their properties qualitatively when the topology of momentum space is changed. Moreover, and unlike the previously-studied topological SPPs, they form narrow beam-like patterns. This narrow beam directional propagation is originated from their quasi-hyperbolic dispersion, similar to the case of hyperbolic media [88,89]. We obtain an asymmetric hyperbolic funnel-like surface for their dispersion surface, which represents the nonreciprocal propagation behavior. According to the equi-frequency contours (EFCs) and group velocity vector, three general types of propagation are predicted below the plasma frequency, omnidirectional, asymmetric bi-directional and narrow-beam directional. Then, we derive a Green's function model for a magnetized plasma slab with finite thickness and obtain the radiation patterns of the surface waves to demonstrate the narrow beam propagation. The effect of slab thickness and defect on propagation behavior is investigated. Although we indicate their reflection-free behavior, we call these modes quasi topological SPPs. We use this term since it seems difficult or perhaps impossible to assign a topological integer-invariant to describe these SPPs as they propagate in different directions at different frequencies within the gap, and so, strictly-speaking, these SPPs are not purely topological.

Chapter four is organized as follows based on the outcomes of this project. We derive a Green's function model for a finite-thickness plasma slab. Then, we examine the propagation properties of SPPs at the slab interfaces below the plasma frequency. We observe three type of propagation; omni-directional, bi-directional, and narrow beam directional. We mainly focus on studying narrow beams. It follows by computing the

Poynting vector, group velocity, power flow and back-scattering immune properties in the presence of defects on the surface. We show that the angle of narrow beams is tunable by frequency and magnetic field intensity. The SPP's field profile is obtained in a two layer and multi-layer system. Finally, a quasi-static approximation approach is presented. Paper [5] has been published from this project.

In the next project, we study the effect of nonlocality on topological SPPs. In Ref. [90] it has been argued that by modeling a gyrotropic plasma using the hydrodynamic Drude model, a truly unidirectional SPP will not exist at the interface of dielectric and magnetized plasma media below the plasma frequency due to the effect of nonlocality. It has been demonstrated that the surface waves have nonreciprocal bi-directional propagation behavior, which is in contradiction with purely unidirectional propagation behavior predicted by applying a simple Drude model. However, in Refs. [82,91], it has been clarified that the nonlocality does not affect a class of unidirectional SPPs that exists at the interface of opaque and magnetized plasma media above the plasma frequency. In addition, for the case that the top layer is a dielectric material, the backward modes with short wavelength oscillation vanish by considering a realistic level of dissipation. The backward mode only exists at large wavenumber, which may be relatively unimportant from a practical standpoint.

Following these studies, we obtain integer Chern invariants to formally validate the existence of topological unidirectional SPPs by considering realistic conditions using the nonlocal hydrodynamic model. In Refs. [26, 27] a method for Chern number calculation in periodic photonic crystals has been introduced by Raghu and Haldane. Then, Silveirinha has developed this method for anisotropic continua [30]. He found that the Chern numbers in continuous materials are integer invariants subject to considering spatially dispersive material models. He has introduced an ad hoc nonlocal material model having a large spatial cutoff wavenumber. This model is called the spatial cutoff model. By this assumption, the Hamiltonian becomes well-behaved at large momentum, unlike in the local material model. As a result, integer Chern invariants of $\{+1, -2\}$ are obtained, respectively for high and low frequency bands of the TM bulk modes, which does not add up to zero as required. To solve this problem, it was suggested to apply an interpolate material model which represents a continuous transition from an isotropic plasma to a gyrotropic plasma medium. Hereupon, a new frequency band appears at very low frequencies, whose Chern number is $+1$. Therefore, the appearance of this new low frequency band resolved the issue of nonzero summation of Chern numbers, but at the expense of a complicated permittivity interpolation of interfaced materials. Although this is a clever way to fix the deficiencies of the model, this ad hoc spatial cutoff model does not provide a self-contained description of plasmonic materials. In this regard, we propose to solve the non-integer Chern invariants of the plasma continua via solving the hydrodynamic equation in the magnetized plasma for continuous photonic topological platforms. We evaluate the effect of nonlocality due to the pressure (a manifestation of non-locality) on topology of the bulk modes and the associated Chern numbers in magnetized plasma systems. For the hydrodynamic model, we calculate the band Chern numbers and obtain integer invariants

of ± 1 , which guarantees topological behavior by considering a realistic nonlocal material model.

The bulk-edge correspondence principle links the Chern invariants of two topological insulators having a common bandgap with the number of unidirectional SPP modes that exist at the interface of the two materials [83, 92, 93]. While this principle works well for topological photonic insulators based on periodic structures, subtle issues arise in the case of topological photonic continua due the absence of intrinsic periodicity. Reference [94], studied two general classes of the bulk-edge correspondence principle violations for continuous topological photonic materials: (i) inconsistency between the gap chern number and the number of edge states and (ii) incomplete gap coverage by the edge state line. As further discussed in [94], these violations are associated with the asymptotic behavior of the surface modes for large wave numbers. In addition, it has been shown that although the above-mentioned violations can be restored by adding hydrodynamic nonlocality, the correspondence principle is physically violated for practical purposes, even with zero intrinsic bulk losses, due to Landau damping or nonlocality-induced radiation leakage. The present work focuses on the bulk modes in continuous photonic media and the issues of noninteger Chern numbers and their nonzero sum. In [30] it has been shown that the former can be resolved by adding a spatial cut-off wavenumber and the latter can be addressed by interpolating the interfaced material models. However, in this work by comparing all different nonlocal models, their effects on Chern number, bulk bands and their pros and cons, we show that the hydrodynamic nonlocal model can resolve the two issues associated with Chern numbers all at once.

In the fifth chapter, we present the Chern number calculation for a local, nonlocal hydrodynamic model, and nonlocal spatial cutoff model in a plasmonic system. We compare the results and discuss the effect of nonlocality. We have reported this research in article [6].

So far, we consider that the plasma medium is biased by an in-plane axial magnetic bias. We realize that by applying a radial magnetic field, SPPs tend to propagate perpendicular to the radial bias at the interface between gyrotropic and isotropic media. In fact, this new configuration suggests the excitation of SPPs with circular trajectory due to applying the radial bias. Analogue to the well-known Voigt configuration in which the SPPs travel along a straight line perpendicular to the in-plane axial magnetic bias vector, in a radially biased system, SPPs propagate perpendicular to the radial bias along a circular path.

To analytically investigate the properties of the unidirectional curved SPPs, we derive a dyadic Green's function (GF) for a radially magnetized plasma. We show that the SPP direction is steerable by changing the direction of the magnetic bias. By applying the radial bias we are able to guide topological SPPs at right-angle bends, then we propose a nonreciprocal reflection-free bend junction.

We believe that applying radial bias is a new technique for excitation of reflection-free curved SPPs. In this regard, Airy SPP beams and hook SPPs are also known as self-bending and diffraction-free surface waves in plasmonic systems. They propagate along a parabolic trajectory. Airy beams are generated by applying

a spatial light modulator (SLM) or a composite optical element with cubic phase. Illuminating Airy beams into a simple grating or applying a metasurface providing the required cubic phase, leads to excitation of Airy SPPs [95, 96]. Due to poor operation of SLM in the terahertz frequency range, a more complex mechanism is required to excite THz Airy SPPs. SPP Bessel beams are another type of diffraction-free surface waves that are generated by a similar mechanism as Airy SPP beams, but they have a linear trajectory [97, 98]. Plasmonic hook beams are newly-discovered curved SPPs, which are generated using a simple asymmetric prism [99, 100]. However, their curved trajectory exists only in the near-field. Another possibility is an SPP vortex, which is an electromagnetic wave carrying orbital angular momentum. It is excited using spiral slits [101] or nanoslits that provide the required phase difference [102]. Here, we use the concept of topological insulators to excite curved SPPs which are unidirectional and reflection-free. Comparing to other techniques, excitation of curved SPPs at THz frequencies by applying radial bias seems less complicated. In addition, larger curvature is achievable and their propagation properties are simply tunable by the magnetic field intensity as well as frequency. These curved SPPs also have topological behavior. They are resistant to disorder because of their one-way propagation properties, which results in longer propagation even along, say, rough surfaces or surfaces with discontinuities. The unidirectional curved SPP propagates on the surface of a homogeneous medium, and there is no need to apply a grating or other structural pattern with narrow bandwidth to steer SPPs in a circular path. As a result, better performance, higher power transmission and wider bandwidth are achievable.

Like other types of curved SPPs, unidirectional curved SPPs can be used in applications such as plasmonic tweezers, particle manipulation, bio-plasmonic systems, switches and energy routing in plasmonic circuitry. Moreover, they can be used in design of nonreciprocal devices, such as plasmonic circulators or in generating hotspots [50, 103, 104].

Chapter sixth is about the curved SPPs in a radially magnetized plasma system. It is organized as follows. We derive a Green's function model to obtain the field profile of SPPs and characterize their propagation properties. Also numerical results based on finite element method using COMSOL are presented to validate the analytical model. We discuss the effect of different parameters on properties of the curved propagating SPPs. Finally, we propose an application for the curved SPPs.

In the next project, we evaluate the unidirectional edge surface plasmon polaritons in two-dimensional plasmonic layers. This work has been done in collaboration with Prof. Weinert's group in the UWM Physics department, and Monticone's group in Cornell University. Magnetized graphene monolayer is a 2D platform that supports unidirectional edge modes. This is a well-studied problem. We only examine topological behavior of graphene by considering super strong magnetic biases. We show that at strong magnetic biases, longer propagation length and better properties is achievable for unidirectional edge modes. Also, giant Faraday rotation, an optical analogue of the Hall effect, can be obtained near the λ -level frequency.

Since the fundamental requirement of external magnets restricts on-chip integration and device miniaturization, scientists look for alternative magnetic field sources to generate nonreciprocal effects. Here, our idea is to use a ferromagnetic Chromium triiodide (CrI_3) monolayer underneath the graphene sheet, such that the exchange field of this van der Waals heterostructure provides an out of plane magnetic field and serves as an alternative to external magnets. It leads to design of magnet-less devices for optical and plasmonic on-chip applications.

Bulk CrI_3 is a layered vdW material that can be easily cleaved, and is relatively stable in ambient conditions [105]. Bulk CrI_3 is a ferromagnetic insulator with a relatively high Curie temperature of $T_c=61$ K [105]. The 2D monolayer form of CrI_3 consists of Cr^{3+} ions and I^- ions that form edge-sharing octahedra arranged in a hexagonal honeycomb lattice with an approximate thickness of 0.6 nm. Like its bulk form, monolayer CrI_3 is also a ferromagnetic insulator, with an out-of-plane easy axis and somewhat reduced T_c of 45 K [106]. In its monolayer form, CrI_3 exhibits massive local Cr magnetic moments of $3\mu_B$, where μ_B is the Bohr magneton, which potentially can induce large exchange splittings in adjacent layers of a heterostructure. Since 2D CrI_3 has a hexagonal structure, it is well lattice-matched with graphene. Magnetic order in CrI_3 has been studied experimentally in [106–110], and in other 2D magnets, such as MnSe_2 [111, 112] and CrGeTe_3 [113, 114]. In all cases, these 2D magnets have out of the plane magnetization. In some cases, magnetic effects can be controlled via electrostatic gating [109, 110], or strain [115, 116]. A Chern insulating state can be realized in graphene in proximity to CrI_3 , via the magnetic exchange field and Rashba spin-orbit coupling (SOC) [116, 117]. However, to achieve this, the heterostructure needs to be compressed from its equilibrium state which increases the effective field [117].

In Ref. [8], using the first-principles density functional theory (DFT) calculations it was shown that the proximity exchange in graphene due to monolayer CrI_3 can result in an enormous exchange field, and then the conductivity of graphene due to the CrI_3 exchange field has been calculated. It was derived that CrI_3 exhibits massive local Cr magnetic moments of $3\mu_B$, which can induce exchange splitting in adjacent layers of a heterostructure. The equilibrium (minimum energy) separation between CrI_3 and graphene is approximately 3.75 angstrom, at which point the exchange splitting is 21 meV, corresponding to an effective exchange field of 100T and a chemical potential of -0.3 eV, which self-biases graphene.

In this work, we evaluate the nonreciprocal effects of a CrI_3 /graphene heterostructure. By solving Poisson's equation in the quasi-static (near-field) limit, we derive an approximation dispersion relation for the edge modes in a 2D heterostructure. We then analyze the electric field profile in the vicinity of the edge, as well as source-driven fields for both the bulk and edge cases. We observe one-way edge modes, but in the non-equilibrium separation distance. We also calculate Faraday rotation due to the exchange field. Comparing to a graphene monolayer biased by an external magnetic field, the resulting nonreciprocity from the CrI_3 /graphene layer is found to be drastically weaker. Landau levels, which are the most prominent

feature of the graphene conductivity in a strong external field, are absent in the case of the exchange field. In the far-infrared considered here, the intraband conductivity is dominant, with diagonal element values that are approximately the same as isolated graphene with no applied magnetic bias and $\mu = -0.3\text{eV}$, whereas the off-diagonal elements are similar in magnitude to those in the external bias case. Because of the large diagonal conductivity response compared to having an external bias (in which case most of the Drude weight is transferred to the Landau levels), the resulting non-reciprocity due to the exchange field is, unfortunately, considerably less than for an external magnetic field of the same strength. For smaller separation (achievable through, e.g., strain), nonreciprocal effects in Faraday rotation are still rather modest, but a unidirectional edge SPP can be found. Eventually, we conclude that the physics of this heterostructure is quite different from a monolayer biased by an external field and the effective magnetic field does not work as an alternative source for the external magnets.

This research has been reported in chapter seven, which is organized as follows. The nonreciprocal effects of CrI₃/graphene heterostructure are compared with a monolayer graphene biased by external magnets. First, their optical conductivity is compared. Then, we look for the unidirectional edge modes propagating at the edge of both structures. We indicate that the edge SPPs for the exchange field are slightly non-reciprocal for the equilibrium separation, whereas for the external bias case they are highly nonreciprocal (unidirectional), tightly-confined, long-lasting, and robust to material discontinuities. Next, Faraday rotation is calculated for both the exchange field and external bias fields cases, where, again, the exchange field is shown to produce modest Faraday rotation. We published these results in Physical Review B journal, article [8].

Chapter 2

Magnetized Semiconductors

In this chapter, first we discuss common material models used to characterize a magnetized plasma medium. Then, we derive the dispersion equation of the bulk modes propagating inside a gyrotropic medium, and compare the dispersion bands for the local and nonlocal models. Next, we determine electric and magnetic field vectors in an isotropic and a gyrotropic region to derive the SPP dispersion relation in two and multi-layer structures. Finally, we compute the reflection coefficients from a gyrotropic interface.

2.1 Material Model

In the next several subsections, we present various material models. The conductivity and dielectric tensors of the magnetized plasma material are obtained using the equation of motion of the mobile particles in a plasma medium, by considering local and nonlocal conditions. Then, we compare and contrast these material models.

2.1.1 Local Drude Model

Consider a plasma medium consisting of n_e free electrons with the effective mass of m^* per volume. Since the ions are much heavier than the electrons, we can ignore them in the interaction of electromagnetic wave and material. A static magnetic field bias $\mathbf{B}_c = B_0 \hat{\mathbf{b}}_c$ is applied in the plasma region, where B_0 is the magnetic field intensity and $\hat{\mathbf{b}}_c$ is a unit vector along the magnetic field vector. There are two forces acting on the free electrons, $e\mathbf{E}(\mathbf{r})$ arising from the electric field of the wave and $e(\mathbf{v} \times \mathbf{B}_c)$ arising from the motion of the electrons with the average velocity of \mathbf{v} through the static magnetic field \mathbf{B}_c , where e is the electron charge. Here, we ignore the small self-consistent time-varying magnetic field. Then, the equation of motion of the electrons in time-domain is

$$\frac{d\mathbf{v}}{dt} + \Gamma\mathbf{v} = \frac{e}{m^*} [\mathbf{E}(\mathbf{r}, t) + \mathbf{v} \times \mathbf{B}_c]. \quad (2.1)$$

Γ is collision frequency, a damping term arising from the collision between particles. It is defined as $\Gamma = -q_e/\mu m^*$, where μ is the electron mobility and $q_e = -e$. Considering the time harmonic of $e^{-i\omega t}$, the equation of motion is written in the frequency domain as

$$-i(\omega + i\Gamma)\nu = \frac{e}{m^*} [\mathbf{E}(\mathbf{r}, \omega) + \nu \times \mathbf{B}_c]. \quad (2.2)$$

Substitution of the electronic convection current density $\mathbf{J}_c = n_e e \nu$ and $\mathbf{B}_c = B_0 \hat{\mathbf{b}}_c$ gives the induced current equation as

$$-i(\omega + i\Gamma) \frac{\mathbf{J}_c}{n_e e} = \frac{e}{m^*} \mathbf{E}(\mathbf{r}, \omega) + \frac{e B_0}{m^* n_e} \mathbf{J}_c \times \hat{\mathbf{b}}_c \quad (2.3)$$

$$\omega(\omega + i\Gamma) \mathbf{J}_c = i\omega \left(\omega_p^{*2} \varepsilon_0 \varepsilon_\infty \mathbf{E}(\mathbf{r}, \omega) - \omega_c \mathbf{J}_c \times \hat{\mathbf{b}}_c \right) \quad (2.4)$$

$$\mathbf{J}_c = i\omega \omega_p^{*2} \varepsilon_0 \varepsilon_\infty \left(\omega(\omega + i\Gamma) \bar{\mathbf{I}} - i\omega \omega_c \hat{\mathbf{b}}_c \times \bar{\mathbf{I}} \right)^{-1} \cdot \mathbf{E}(\mathbf{r}, \omega), \quad (2.5)$$

where $\omega_c = -eB_0/m^*$ and $\omega_p^* = \omega_p/\sqrt{\varepsilon_\infty}$ ($\omega_p = \sqrt{n_e e^2/m^* \varepsilon_0}$) are the cyclotron and reduced plasma frequencies, respectively, ε_∞ is the background permittivity (high-frequency dielectric constant), and ε_0 is the free-space permittivity. From $\mathbf{J}_c = \bar{\sigma} \cdot \mathbf{E}$, the conductivity tensor is obtained as

$$\bar{\sigma} = i\omega \varepsilon_0 \varepsilon_\infty X_0 \left(\bar{\mathbf{I}} - iY_0 \hat{\mathbf{b}}_c \times \bar{\mathbf{I}} \right)^{-1}, \quad (2.6)$$

where $X_0 = \omega_p^{*2}/[\omega(\omega + i\Gamma)]$ and $Y_0 = \omega_c/(\omega + i\Gamma)$. The dielectric tensor of the material is

$$\bar{\varepsilon}_r = \varepsilon_\infty \left(\bar{\mathbf{I}} + i \frac{1}{\omega \varepsilon_0} \bar{\sigma} \right) \quad (2.7)$$

$$= \varepsilon_\infty \bar{\mathbf{I}} - \varepsilon_\infty X_0 \left(\bar{\mathbf{I}} - iY_0 \hat{\mathbf{b}}_c \times \bar{\mathbf{I}} \right)^{-1}. \quad (2.8)$$

Considering $\bar{\mathbf{C}} = \lambda \bar{\mathbf{I}} + \mathbf{c} \times \bar{\mathbf{I}}$, the inverse of the matrix is $\bar{\mathbf{C}}^{-1} = \text{adj}(\bar{\mathbf{C}})/|\bar{\mathbf{C}}|$ where $|\bar{\mathbf{C}}| = \lambda(\lambda^2 + c^2)$ and $\text{adj}(\bar{\mathbf{C}}) = \lambda(\lambda \bar{\mathbf{I}} - \mathbf{c} \times \bar{\mathbf{I}}) + cc$, where cc stands for complex conjugate of the first bracket and adj stands for the adjoint of a matrix. Then, we have

$$\frac{\bar{\varepsilon}_r}{\varepsilon_\infty} = \bar{\mathbf{I}} - X_0 \frac{(\bar{\mathbf{I}} + iY_0 \hat{\mathbf{b}}_c \times \bar{\mathbf{I}}) - Y_0^2 \hat{\mathbf{b}}_c \hat{\mathbf{b}}_c}{1 - Y_0^2} \quad (2.9)$$

$$= \left(1 - \frac{X_0}{1 - Y_0^2} \right) (\bar{\mathbf{I}} - \hat{\mathbf{b}}_c \hat{\mathbf{b}}_c) - i \frac{Y_0 X_0}{1 - Y_0^2} \hat{\mathbf{b}}_c \times \bar{\mathbf{I}} + (1 - X_0) \hat{\mathbf{b}}_c \hat{\mathbf{b}}_c. \quad (2.10)$$

Eventually, the dielectric tensor of a gyrotropic plasma medium is

$$\bar{\varepsilon}_r(\omega) = \varepsilon_t (\bar{\mathbf{I}} - \hat{\mathbf{b}}_c \hat{\mathbf{b}}_c) + i\varepsilon_g (\hat{\mathbf{b}}_c \times \bar{\mathbf{I}}) + \varepsilon_a \hat{\mathbf{b}}_c \hat{\mathbf{b}}_c, \quad (2.11)$$

where the permittivity elements are defined as

$$\varepsilon_a(\omega) = \varepsilon_\infty (1 - X_0) = \varepsilon_\infty - \frac{\omega_p^2}{\omega(\omega + i\Gamma)} \quad (2.12)$$

$$\varepsilon_t(\omega) = \varepsilon_\infty \left(1 - \frac{X_0}{1 - Y_0^2} \right) = \varepsilon_\infty - \frac{\omega_p^2(1 + i\Gamma/\omega)}{(\omega + i\Gamma)^2 - \omega_c^2} \quad (2.13)$$

$$\varepsilon_g(\omega) = \varepsilon_\infty \frac{-Y_0 X_0}{1 - Y_0^2} = \frac{1}{\omega} \frac{\omega_p^2 \omega_c}{\omega_c^2 - (\omega + i\Gamma)^2}. \quad (2.14)$$

Relation (2.11) represents a gyrotropic medium, where ε_a is the anomalous permittivity, the axial permittivity element along the magnetic bias, ε_t is transverse component and ε_g is gyrotropic component, the off-diagonal element arising from the magneto-optical interaction. In the absence of the external magnetic field ($B_0 = 0$), the gyrotropic plasma medium turns to an isotropic material with dielectric constant of $\varepsilon_r = \varepsilon_a$.

Multi-carrier Drude model

For a semiconductor with one electron and two hole bands near the Fermi level, the permittivity elements are defined as

$$\varepsilon_a(\omega) = \varepsilon_\infty - \sum_j \frac{(\omega_p^j)^2}{\omega(\omega + i\Gamma_j)} \quad (2.15)$$

$$\varepsilon_t(\omega) = \varepsilon_\infty - \sum_j \frac{(\omega_p^j)^2 (1 + i\Gamma_j/\omega)}{(\omega + i\Gamma_j)^2 - (\omega_c^j)^2} \quad (2.16)$$

$$\varepsilon_g(\omega) = \sum_j \frac{1}{\omega} \frac{(\omega_p^j)^2 \omega_c^j}{(\omega_c^j)^2 - (\omega + i\Gamma_j)^2} \quad (2.17)$$

where j indicates electron (e), light hole (lh) and heavy hole (hh) contributions, with the effective mass m_j^* , the carrier density n_j , and mobility μ_j , given the cyclotron frequency $\omega_c^j = q_e B_0 / m_j^*$, the plasma frequency $\omega_p^j = \sqrt{n_j e^2 / m_j^* \varepsilon_0}$, and the collision frequency $\Gamma = -q_e / \mu_j m_j^*$. In a semiconductor, electron and light hole are much more lighter than heavy hole $m_e^* \simeq m_{lh}^* \ll m_{hh}^*$, and for an undoped crystal, $n_e \simeq n_{lh} + n_{hh}$. Under these conditions, we have $\omega_p^e \gg \omega_p^{hh} > \omega_p^{lh}$ and $\omega_c^e \approx \omega_c^{lh} \gg \omega_c^{hh}$. As a result, the electron has the main contribution at terahertz resonances and it is good approximation to ignore the effect of the hole particles. However, at frequencies near ω_c^{hh} , the effect of the heavy hole is considerable.

For p-type semiconductors, the effect of holes is significant, because the hole density is larger than the electron density ($n_h \gg n_e$). At high frequencies ($\omega_p^e, \omega_p^h \ll \omega$), the cyclotron resonance absorption of each carrier is independent of the other. When $\omega_p^e \ll \omega \ll \omega_p^h$, there is a magneto-plasma resonance due to the majority carriers (holes), given by $\omega = \frac{n_h e h}{\varepsilon_0 (k_i + 2) B_0}$ and the cyclotron resonance absorption of minority carriers (electrons) is $\omega = \frac{e B_0}{m_e}$. Lastly, if both carrier concentrations are high ($\omega \ll (\omega_{pe}, \omega_{ph})$), there is an ordinary

magnet-plasma resonance $\left(\frac{n_h e_h + n_e e}{\epsilon_0 (k_i + 2) B_0} \right)$, and a hybrid resonance arising from the interaction of two carriers $\left(\omega^2 = \frac{e B_0}{m_e} \left[\frac{n_h / n_e + e_h / e}{n_h / n_e + m_h / m_e} \right] \right)$.

In Chapter 3, we first apply this multi-carrier Drude model to evaluate the effect of all charge carriers. Since the effect of heavy and light holes is negligible at the operating frequency range we are working in, we switch to the simple Drude model.

Lorentz-Drude Model

By taking into consideration the phonon contributions, the semiconductor is described by Lorentz-Drude model. In this case, the material permittivity elements are defined as

$$\epsilon_t = \epsilon_\infty - \frac{\omega_p^2 (\omega + i\Gamma)}{\omega [(\omega + i\Gamma)^2 - \omega_c^2]} + \frac{A_L \omega_L^2}{\omega_L^2 - \omega^2 - i\gamma_L \omega} \quad (2.18)$$

$$\epsilon_a = \epsilon_\infty - \frac{\omega_p^2}{\omega (\omega + i\Gamma)} + \frac{A_L \omega_L^2}{\omega_L^2 - \omega^2 - i\gamma_L \omega} \quad (2.19)$$

$$\epsilon_g = \frac{\omega_c \omega_p^2}{\omega [\omega_c^2 - (\omega + i\Gamma)^2]}, \quad (2.20)$$

where the last term in transverse and anomalous elements is associate to the Lorentz term with longitudinal optic-phonon frequency (ω_L), scattering time $\tau_L = 1/\gamma_L$, and amplitude A_L . This term arises from the lattice variations and phonon contribution, which can not be ignored at very high frequencies. In theory, the Lorentz term can be affected by the magnetic field, but since the lattice are much heavier than the electrons, the corresponding cyclotron frequency is negligible and the Lorentz term remain isotropic in the presence of the magnetic bias.

In this research, we ignore the phonon contribution in the material model, which is an accurate assumption at frequencies below the optical phonon resonances (and at low temperatures). So, we do not use the Lorentz-Drude model.

2.1.2 Non-local Hydrodynamic Model

In the hydrodynamic model, the equation of motion of the particles is [118]

$$\frac{d\mathbf{v}}{dt} + \gamma \mathbf{v} + (\mathbf{v} \cdot \nabla) \mathbf{v} = \frac{e}{m^*} (\mathbf{E}(\mathbf{r}, t) + (\mathbf{v} \times \mathbf{B}_c)) - \beta^2 \frac{\nabla n(\mathbf{r}, t)}{n}. \quad (2.21)$$

The last term represents the pressure, where β is a nonlocal parameter proportional to the Fermi velocity (v_F) in the semiconductors; $\beta^2 = v_F^2 (3/5\omega + 1/3i\Gamma)/(\omega + i\Gamma)$ [119]. In the local model, the induced charge distribution is assumed to be confined to the boundary of the plasma region by a Dirac delta function.

However, in the hydrodynamic model, the induced charge density spreads into the bulk plasma region with charge distribution depth of $\delta = \beta/\omega_p$ which is a function of the nonlocal parameter β [120].

By linearizing the equation of motion, and considering the continuity equation $\partial_t n = -\nabla \cdot (n\mathbf{v})$ and the convection current density $\mathbf{J}_c = n_e e \mathbf{v}$, the induced current equation is given as [118]

$$\beta^2 \nabla (\nabla \cdot \mathbf{J}_c) + \omega(\omega + i\Gamma) \mathbf{J}_c = i\omega \left(\omega_p^{*2} \varepsilon_0 \varepsilon_\infty \mathbf{E}(\mathbf{r}, \omega) - \omega_c \mathbf{J}_c \times \hat{\mathbf{b}}_c \right), \quad (2.22)$$

where ω_c , ω_p^* and Γ are the cyclotron, reduced plasma, and collision frequencies, respectively. By doing the spatial Fourier transform and considering $\mathbf{J}_c(k, \omega) = \bar{\sigma}(k, \omega) \cdot \mathbf{E}(k, \omega)$, the conductivity tensor is governed as

$$\bar{\sigma}(k, \omega) = i\omega \varepsilon_0 \varepsilon_\infty X \left(\bar{\mathbf{I}} - iY \hat{\mathbf{b}}_c \times \bar{\mathbf{I}} \right)^{-1}, \quad (2.23)$$

where $X = \omega_p^{*2} / (\omega(\omega + i\Gamma) - \beta^2 k^2)$ and $Y = \omega \omega_c / (\omega(\omega + i\Gamma) - \beta^2 k^2)$. By taking the inverse of this term, we obtain the dielectric tensor as

$$\begin{aligned} \bar{\varepsilon}(k, \omega) &= \varepsilon_\infty \left(\bar{\mathbf{I}} + i \frac{1}{\omega \varepsilon_0} \bar{\sigma}(k, \omega) \right) \\ &= \varepsilon_{t, \text{nl}} (\bar{\mathbf{I}} - \hat{\mathbf{b}}_c \hat{\mathbf{b}}_c) + i \varepsilon_{g, \text{nl}} (\hat{\mathbf{b}}_c \times \bar{\mathbf{I}}) + \varepsilon_{a, \text{nl}} \hat{\mathbf{b}}_c \hat{\mathbf{b}}_c, \end{aligned} \quad (2.24)$$

where the permittivity elements are defined as

$$\varepsilon_{a, \text{nl}}(k, \omega) = \varepsilon_\infty (1 - X) = \varepsilon_\infty - \frac{\omega_p^2}{\Omega_k} \quad (2.25)$$

$$\varepsilon_{t, \text{nl}}(k, \omega) = \varepsilon_\infty \left(1 - \frac{X}{1 - Y^2} \right) = \varepsilon_\infty - \frac{\omega_p^2 \Omega_k}{\Omega_k^2 - (\omega \omega_c)^2} \quad (2.26)$$

$$\varepsilon_{g, \text{nl}}(k, \omega) = \varepsilon_\infty \frac{-YX}{1 - Y^2} = \frac{-\omega \omega_c \omega_p^2}{\Omega_k^2 - (\omega \omega_c)^2}, \quad (2.27)$$

with $\Omega_k = \omega(\omega + i\Gamma) - \beta^2 k^2$. Relation (2.25) with the corresponding permittivity elements represents a nonlocal HD dielectric model. By assuming $\varepsilon_\infty = 1$ and $\Gamma = 0$ and defining a nonlocal factor as $\chi = 1/(1 - k^2/k_m^2)$, where $k_m = \omega/\beta$, the nonlocal permittivity elements are simplified as

$$\begin{aligned} \varepsilon_{a, \text{nl}}(k, \omega) &= 1 - \chi \frac{\omega_p^2}{\omega^2}, \quad \varepsilon_{t, \text{nl}}(k, \omega) = 1 - \chi \frac{\omega_p^2}{\omega^2 - \chi^2 \omega_c^2}, \\ \varepsilon_{g, \text{nl}}(k, \omega) &= \frac{-1}{\omega} \frac{\chi^2 \omega_c \omega_p^2}{\omega^2 - \chi^2 \omega_c^2}. \end{aligned} \quad (2.28)$$

In the limit of $\beta \rightarrow 0$, then $\chi \rightarrow 1$ and the local Drude dielectric model is recovered.

We apply the hydrodynamic Drude model in Chapter 5 to evaluate the effect of nonlocality due to the

pressure.

2.1.3 Non-local Spatial Cutoff Model

In Ref. [30], to define a nonlocal material model a momentum cutoff k_{\max} is manually added to the local Drude model as

$$\bar{\varepsilon}_r(\omega, k) = \bar{\varepsilon}_R(\omega) + \frac{1}{1 + k^2/k_{\max}^2} \bar{\chi}_{\text{NR}}(\omega), \quad (2.29)$$

where $\bar{\varepsilon}_R(\omega)$ is a symmetric matrix that determines the time-reversal invariant response and $\bar{\chi}_{\text{NR}}$ is the susceptibility. We call this ad-hoc nonlocal model, the non-local spatial cutoff model. In general, $\bar{\chi}_{\text{NR}}$ gives the nonreciprocal component of the material response that breaks time-reversal symmetry. It was suggested that this component is required to be associated to a spatial cutoff k_{\max} to obtain integer Chern numbers as explained further later. So from (2.29) the permittivity elements of a lossless plasma system ($\Gamma = 0$) are derived as

$$\varepsilon_a(\omega, k) = \varepsilon_\infty - \kappa \frac{\omega_p^2}{\omega^2}, \quad (2.30)$$

$$\varepsilon_t(\omega, k) = \varepsilon_\infty - \kappa \frac{\omega_p^2}{\omega^2 - \omega_c^2}, \quad (2.31)$$

$$\varepsilon_g(\omega, k) = \kappa \frac{\omega_c \omega_p^2}{\omega(\omega_c^2 - \omega^2)}, \quad (2.32)$$

where the nonlocal factor is defined as $\kappa = 1/(1 + k^2/k_{\max}^2)$. In the local case $k_{\max} \rightarrow \infty$ and $\kappa \rightarrow 1$. In addition, an interpolate material model representing a continuous transition between an isotropic plasma ($\tau \rightarrow 0^+$) with the plasma frequency of ω_m and a gyrotropic plasma ($\tau \rightarrow 1^-$) with the plasma frequency of ω_p is given by

$$\bar{\varepsilon}_{r,\tau}(\omega) = \varepsilon_\infty + \tau [\bar{\varepsilon}_r(\omega, k) - \varepsilon_\infty] + (1 - \tau) [\bar{\varepsilon}_{\text{Drude}} - \varepsilon_\infty], \quad (2.33)$$

where the tensor elements are governed as

$$\varepsilon_a = \varepsilon_\infty - \tau \kappa \frac{\omega_p^2}{\omega^2} - (1 - \tau) \frac{\omega_m^2}{\omega^2}, \quad (2.34)$$

$$\varepsilon_t = \varepsilon_\infty - \tau \kappa \frac{\omega_p^2}{\omega^2 - \omega_c^2} - (1 - \tau) \frac{\omega_m^2}{\omega^2}, \quad (2.35)$$

$$\varepsilon_g = \tau \kappa \frac{\omega_c \omega_p^2}{\omega(\omega_c^2 - \omega^2)}. \quad (2.36)$$

In Chapter 5, we use this interpolated spatial cutoff model to rederive Chern numbers and compare the results with the hydrodynamic model.

2.2 Bulk Modes in a Gyrotropic Plasma Medium

Bulk polaritons are propagating wave modes inside a plasma medium which does not have boundaries (the plasma is an infinite medium). In the following we derive the bulk mode dispersion equation to study the optical bulk band structure of the gyrotropic medium and examine the frequency range that bulk modes are allowed or forbidden to propagate.

A plane wave in a gyrotropic medium satisfies the Maxwell's equations

$$\mathbf{k} \times \mathbf{E} = \omega \mu_0 \mathbf{H}, \quad \mathbf{k} \times \mathbf{H} = -\omega \varepsilon_0 \bar{\varepsilon}_r(\omega, \mathbf{k}) \cdot \mathbf{E}. \quad (2.37)$$

The combination of two curl Maxwell's equations gives the wave equation as

$$\mathbf{k} \times (\mathbf{k} \times \mathbf{E}) + k_0^2 \bar{\varepsilon}_r(\omega, \mathbf{k}) \cdot \mathbf{E} = \mathbf{0} \quad (2.38)$$

where $k_0 = \omega \sqrt{\mu_0 \varepsilon_0}$ is the free space wavenumber. Using the vector identity $\mathbf{k} \times (\mathbf{k} \times \mathbf{A}) = \mathbf{k}(\mathbf{k} \cdot \mathbf{A}) - (\mathbf{k} \cdot \mathbf{k}) \mathbf{A} = \mathbf{k}\mathbf{k} \cdot \mathbf{A} - k^2 \bar{\mathbf{I}} \cdot \mathbf{A}$, the wave equation can be written as

$$(\mathbf{k}\mathbf{k} - k^2 \bar{\mathbf{I}}) \cdot \mathbf{E} + k_0^2 \bar{\varepsilon}_r(\omega, \mathbf{k}) \cdot \mathbf{E} \quad (2.39)$$

$$= (k_0^2 \bar{\varepsilon}_r(\omega, \mathbf{k}) - k^2 \bar{\mathbf{I}} + \mathbf{k}\mathbf{k}) \cdot \mathbf{E} = \mathbf{0}. \quad (2.40)$$

A non-zero solution of \mathbf{E} exists only if

$$|k_0^2 \bar{\varepsilon}_r(\omega, \mathbf{k}) - k^2 \bar{\mathbf{I}} + \mathbf{k}\mathbf{k}| = 0. \quad (2.41)$$

The dispersion equation of bulk modes in a gyrotropic medium can be obtained by setting this determinant to zero. For a plasma medium magnetized by an in-plane magnetic field of $\mathbf{B} = B_0 \hat{\mathbf{y}}$, the dielectric tensor (2.11) is simplified as

$$\bar{\varepsilon}_r(\omega) = \begin{pmatrix} \varepsilon_t & 0 & i\varepsilon_g \\ 0 & \varepsilon_a & 0 \\ -i\varepsilon_g & 0 & \varepsilon_t \end{pmatrix}. \quad (2.42)$$

By substituting the dielectric tensor and wave vector $\mathbf{k} = k_x \hat{x} + k_y \hat{y} + k_z \hat{z}$ into (2.41), we have

$$\begin{vmatrix} k_0^2 \varepsilon_t - k^2 + k_x^2 & k_x k_y & i k_0^2 \varepsilon_g + k_x k_z \\ k_x k_y & k_0^2 \varepsilon_a - k^2 + k_y^2 & k_y k_z \\ -i k_0^2 \varepsilon_g + k_x k_z & k_y k_z & k_0^2 \varepsilon_t - k^2 + k_z^2 \end{vmatrix} = 0. \quad (2.43)$$

Using $k^2 = k_t^2 + k_y^2$, where $k_t^2 = k_x^2 + k_z^2$, the determinant is expanded as

$$\varepsilon_t k_t^4 - [(\varepsilon_t (\varepsilon_t + \varepsilon_a) - \varepsilon_g^2) k_0^2 - (\varepsilon_a + \varepsilon_t) k_y^2] k_t^2 + [(\varepsilon_t^2 - \varepsilon_g^2) \varepsilon_a k_0^4 - 2\varepsilon_t \varepsilon_a k_y^2 k_0^2 + \varepsilon_a k_y^4] = 0. \quad (2.44)$$

Solving the above polynomial expression for variable k_t^2 gives

$$k_t^2 = \frac{1}{2\varepsilon_t} [(\varepsilon_t (\varepsilon_t + \varepsilon_a) - \varepsilon_g^2) k_0^2 - (\varepsilon_a + \varepsilon_t) k_y^2] \quad (2.45)$$

$$\pm \frac{1}{2\varepsilon_t} \sqrt{[(\varepsilon_t (\varepsilon_t + \varepsilon_a) - \varepsilon_g^2) k_0^2 - (\varepsilon_a + \varepsilon_t) k_y^2]^2 - 4\varepsilon_t \varepsilon_a [(\varepsilon_g + \varepsilon_t) k_0^2 - k_y^2] [(\varepsilon_t - \varepsilon_g) k_0^2 - k_y^2]}. \quad (2.46)$$

Then, from $k_t^2 = k_x^2 + k_z^2$, four following solutions are obtained for k_z as

$$k_z = \pm k_{z,j} : j \in \{1, 2\}, \quad (2.47)$$

where

$$k_{z,1} = \sqrt{-k_x^2 + \frac{1}{2} \left(\kappa - \sqrt{\kappa^2 - v} \right)} \quad (2.48)$$

$$k_{z,2} = \sqrt{-k_x^2 + \frac{1}{2} \left(\kappa + \sqrt{\kappa^2 - v} \right)}, \quad (2.49)$$

with

$$\kappa = \{(\varepsilon_t + \varepsilon_a) k_y^2 - [\varepsilon_t (\varepsilon_t + \varepsilon_a) - \varepsilon_g^2] k_0^2\} / \varepsilon_t, \quad (2.50)$$

$$v = \{4\varepsilon_a [(\varepsilon_t + \varepsilon_g) k_0^2 - k_y^2] [(\varepsilon_t - \varepsilon_g) k_0^2 - k_y^2]\} / \varepsilon_t. \quad (2.51)$$

2.2.1 Bulk Modes in the Voigt Configuration

For bulk modes propagating perpendicular to the magnetic bias, we set $k_y = 0$. For this particular case, the determinant (2.41) is simplified to

$$\begin{vmatrix} k_0^2 \varepsilon_t - k^2 + k_x^2 & 0 & i k_0^2 \varepsilon_g + k_x k_z \\ 0 & k_0^2 \varepsilon_a - k^2 & 0 \\ -i k_0^2 \varepsilon_g + k_x k_z & 0 & k_0^2 \varepsilon_t - k^2 + k_z^2 \end{vmatrix} = 0 \quad (2.52)$$

A polynomial expression is derived after determinant expansion. Solving it for k^2 , the following relations

are obtained [36]

$$k_{\text{TM}}^2 = k_0^2 \frac{\varepsilon_t^2 - \varepsilon_g^2}{\varepsilon_t} \quad (2.53)$$

$$k_{\text{TE}}^2 = k_0^2 \varepsilon_a. \quad (2.54)$$

These are dispersion equation of TE and TM bulk modes known as ordinary and the extraordinary waves, respectively. In fact, for this particular case the plane wave can be decomposed into a TE (with electric field along the magnetic bias) and a TM (with electric field in a plane perpendicular to the bias direction) wave.

2.2.2 Bulk Modes with Propagation Angle α_b ; The Existence of Common Bandgaps

The characteristics of the bulk modes in a gyrotropic medium depend on the direction of propagation with respect to the magnetic bias. In a structure exhibiting bulk band-gaps, these gaps will also be direction-dependent. In this subsection, we study the bulk dispersion behavior of a gyrotropic medium in order to identify a bulk bandgap, common to all propagation directions. We utilize this information later on.

We begin with a plane wave having wavevector \mathbf{k}_b , propagating in a gyrotropic medium at angle α_b , with respect to the bias field (the y -direction). Assuming a plane wave solution to Maxwell's equations leads to a homogeneous system of equations for which non-trivial solutions are obtained when $|k_0^2 \bar{\varepsilon}_r - k_b^2 \bar{\mathbf{I}} + \mathbf{k}_b \mathbf{k}_b| = 0$. Considering $\mathbf{k}_b = \mathbf{k}_t + \hat{\mathbf{y}} k_y$ such that $|\mathbf{k}_t| = k_b \sin \alpha_b$ and $k_y = k_b \cos \alpha_b$, the evaluation of the determinant leads to the dispersion equation for the bulk modes,

$$[(\varepsilon_t^2 - \varepsilon_g^2 + \varepsilon_a \varepsilon_t) \sin^2 \alpha_b + 2\varepsilon_a \varepsilon_t \cos^2 \alpha_b] k_0^2 k_b^2 - (\varepsilon_t \sin^2 \alpha_b + \varepsilon_a \cos^2 \alpha_b) k_b^4 - \varepsilon_a (\varepsilon_t^2 - \varepsilon_g^2) k_0^4 = 0. \quad (2.55)$$

The dispersion diagrams associated with the bulk modes of the biased plasma with different propagation angles are shown in Fig. 2.1. Figures 2.1a and 2.1b show the dispersion of bulk modes which propagate parallel ($\alpha_b = 0^\circ$) and perpendicular ($\alpha_b = 90^\circ$) to the magnetic bias, respectively. In the perpendicular case, the plane wave can be decoupled into a TE and a TM wave as discussed earlier. In the parallel case, the plane wave can be decoupled into left- and right-handed circularly polarized waves [121]. Otherwise, the waves have a hybrid nature. The two intersection points in the parallel case correspond to Weyl points that arise from crossings between longitudinal plasma modes and transverse helical modes [42]. Figures 2.1c and 2.1d show the dispersion for two arbitrary angles in the range, $0^\circ < \alpha_b < 90^\circ$.

As seen in Fig. 2.1, there are four dispersion branches. The second branch from the top (dashed red) corresponds to a wave which is independent of the magnetic bias and does not lead to a topological SPP (it is the TE wave in the perpendicular case, $\alpha_b = 90^\circ$). Although the flat dashed red section in Fig. 2.1a may appear to naturally belong to the flat solid black dispersion line, the situation admits two viewpoints.

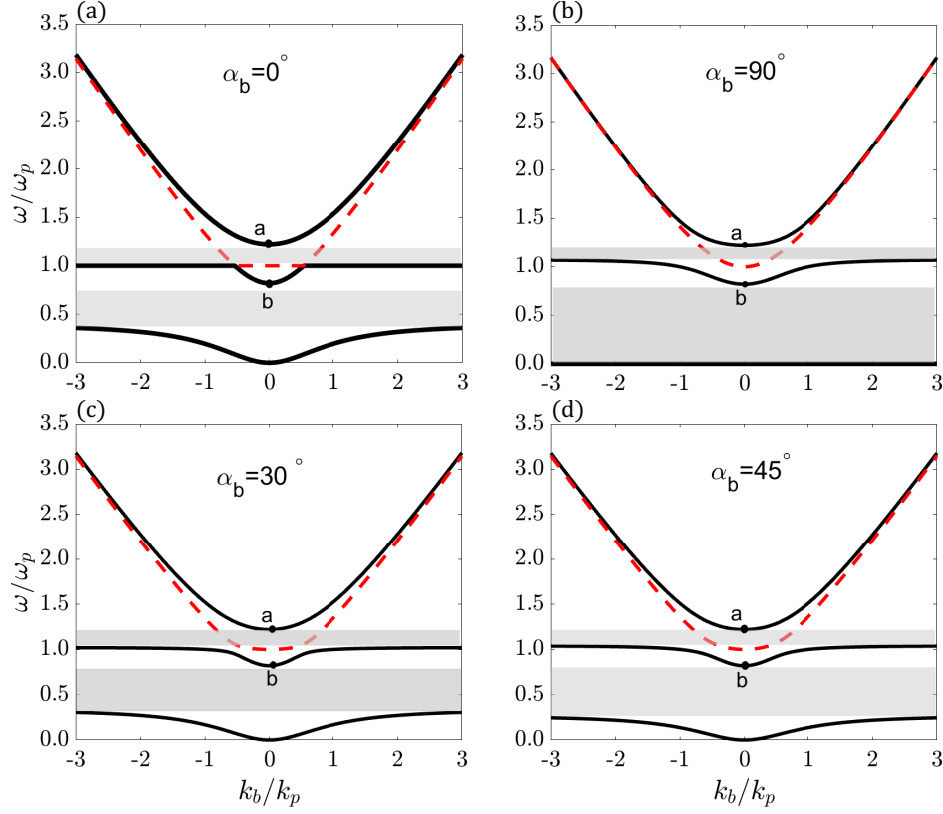


Figure 2.1: Dispersion diagram of biased plasma bulk modes for different angles of propagation, where $k_p = \omega_p/c$. Gray shaded regions highlight bandgaps in the dispersion. The dashed red line corresponds to a wave which is independent of bias, while the solid black lines correspond to the waves which are dependent on bias.

For $\alpha_b = 0$ in the lossless case, one could view the horizontal black line as continuing through the red dashed section, since this represents one polarization, whereas the parabolic sections represent a different polarization. That is, there is an eigenvalue degeneracy, but not an eigenfunction degeneracy. However, analytic continuation for small non-zero angles indicates that the parabolic red dashed section continues to the nearly-flat red dashed section (this is evident in Panel c, but is more predominant for smaller angles). The eigenfunctions (and in this case also the eigenvalues) cannot be globally defined as smooth analytical functions in k -space.

Two bandgaps form between the other three branches as shown in the shaded regions of Fig. 2.1. The size of the bandgaps depend on the propagation direction as well as the magnetic bias field strength. The upper bandgap is smallest when $\alpha_b = 90^\circ$. Conversely, the lower band-gap is smallest when $\alpha_b = 0^\circ$. As such, we take the smallest upper (lower) band-gap to represent the upper (lower) bandgap common for all propagation angles, $0^\circ < \alpha_b < 90^\circ$. Points a and b do not change with the propagation angle. The common bandgap and its impact on surface waves is considered further in the following.

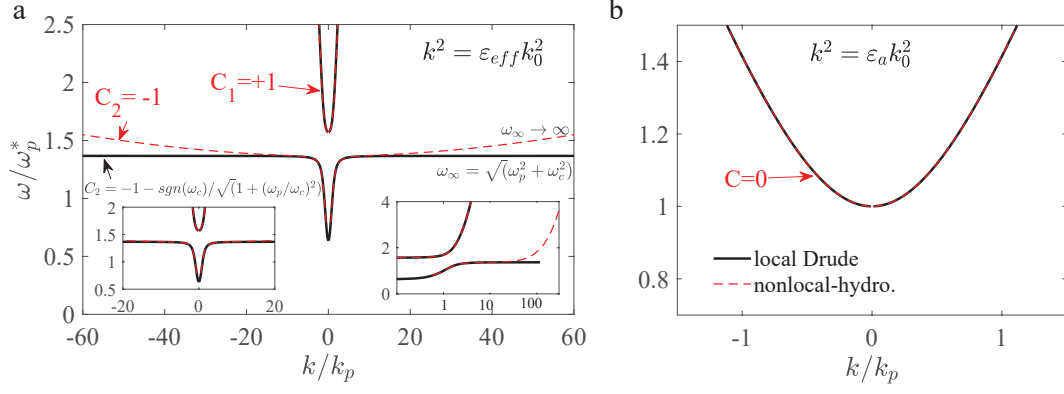


Figure 2.2: Dispersion bands and associated Chern numbers of (a) nontrivial bulk modes and (b) trivial modes using the local Drude and nonlocal hydrodynamic Drude models; $k_p = \omega_p/c_0$, where c_0 is the speed of light in free space.

2.3 Bulk Modes in a Gyrotropic Medium Described by the HD Model

For spatially dispersive materials, the response of a particle at position \mathbf{r} depends on what happened to the particle at position \mathbf{r}' . In this condition, the displacement vector is given as $\mathbf{D}(\mathbf{r}, \omega) = \varepsilon_0 \int \bar{\varepsilon}_r(\mathbf{r}, \mathbf{r}', \omega) \cdot \mathbf{E}(\mathbf{r}', \omega) d^3\mathbf{r}'$. In a nonlocal homogeneous medium, $\bar{\varepsilon}_r(\mathbf{r}, \mathbf{r}', \omega) = \bar{\varepsilon}_r(\mathbf{r} - \mathbf{r}', \omega)$. Then, using the convolution theorem in space domain and spatial Fourier transform we have $\mathbf{D}(\mathbf{k}, \omega) = \varepsilon_0 \bar{\varepsilon}_r(\mathbf{k}, \omega) \cdot \mathbf{E}(\mathbf{k}, \omega)$. The wave equation $(k_0^2 \bar{\varepsilon}_r(\mathbf{k}, \omega) - k^2 \bar{\mathbf{I}} + \mathbf{k}\mathbf{k}) \cdot \mathbf{E}(\mathbf{k}, \omega) = \mathbf{0}$ is obtained by combining the Ampere and Faraday equations and using the vector identity $\mathbf{k} \times (\mathbf{k} \times \mathbf{A}) = \mathbf{k}\mathbf{k} \cdot \mathbf{A} - k^2 \bar{\mathbf{I}} \cdot \mathbf{A}$. Then, the non-zero solutions of \mathbf{E} exists only if $|k_0^2 \bar{\varepsilon}_r(\mathbf{k}, \omega) - k^2 \bar{\mathbf{I}} + \mathbf{k}\mathbf{k}| = 0$. Since we are looking for the bulk modes propagating in a plane perpendicular to the static magnetic vector, we set $k_y = 0$ in the above determinant, assuming that the in-plane magnetic bias is along the y -direction, $\mathbf{B} = B_0 \hat{\mathbf{y}}$. For this particular case, the determinant is simplified to two equations, $k_{\text{TM}}^2 = k_0^2 \varepsilon_{\text{eff}}$ and $k_{\text{TE}}^2 = k_0^2 \varepsilon_{\text{a,nl}}$, where $\varepsilon_{\text{eff}} = (\varepsilon_{\text{t,nl}}^2 - \varepsilon_{\text{g,nl}}^2) / \varepsilon_{\text{t,nl}}$ and the permittivity elements are defined in (2.28). In the local Drude model, these modes are corresponding to the nontrivial TM and trivial TE modes.

Figure 2.2 shows the dispersion diagram of the trivial and nontrivial bulk modes for nonlocal hydrodynamic v.s. local Drude models. The magnetized plasma region is modeled by (2.25), using the parameters $n_e = 3.6 \times 10^{21} \text{ (m}^{-3}\text{)}$, $\varepsilon_\infty = 15.68$, $m^* = 0.0175 m_0$, $B_0 = 0.6 \text{ T}$, $\mu = \infty$, corresponding to $\omega_p^* = 2\pi(1.03 \text{ THz})$, $\omega_c/\omega_p = 0.23$ and $\gamma = 0$, related to the InSb crystal at low temperature, and the nonlocality parameter of $\beta = 0.77 \times 10^6 \text{ m/s}$. The plot displays where the nonlocality has significant effect on the dispersion properties. As shown in Fig. 2.2a, the high frequency bands of both models are completely matched. The left inset plot shows that the low frequency bands are also matched for relatively small wavenumbers. The difference appears at very large wavenumbers according to the log scale inset plot on the right side. Fig. 2.2b

demonstrates that the trivial modes of both models are identical for the entire momentum domain. Each dispersion band is characterized by a Chern number that we explain in Chapter 5.

In the local case, the low frequency band is asymptotic to a constant value of $\omega_n = \sqrt{\omega_c^2 + \omega_p^2}$. This behavior proposes a thermodynamic paradox, because it suggests infinite energy in a limited frequency range, meaning that at $k \rightarrow \infty$ the plasmonic material is still polarized which is not a physically correct behavior. This problem can be solved by including nonlocality in the material model. As seen, the flat parts of the low frequency band wing up when nonlocality is included in the material model via the hydrodynamic model. It also can be understood by looking at (2.28), where for $k \rightarrow \infty$, all permittivity elements converge to the high frequency dielectric constant.

2.4 Field Vectors in a Gyrotropic Region

In this section we obtain the electric and magnetic field vectors in a gyrotropic medium. We use these relations later to impose boundary conditions and derive SPP dispersion equation and reflectance.

Consider an orthogonal coordinate system with unit vectors $\{\hat{\mathbf{k}}_t, \hat{\mathbf{y}}, \hat{\mathbf{k}}_t \times \hat{\mathbf{y}}\}$ where $\hat{\mathbf{k}}_t = \mathbf{k}_t/k_t$, $\mathbf{k}_t = \hat{\mathbf{x}}k_x + \hat{\mathbf{z}}k_z$ and $k_t = \sqrt{k_x^2 + k_z^2}$. Here, the half-space plasma medium ($z < 0$) is biased by an in-plane magnetic field $\mathbf{B} = B_0\hat{\mathbf{y}}$. The electric field vectors can be decomposed into its components as

$$\mathbf{E} = \alpha_1\hat{\mathbf{k}}_t + \alpha_2\hat{\mathbf{y}} + \alpha_3(\hat{\mathbf{k}}_t \times \hat{\mathbf{y}}), \quad (2.56)$$

Putting (2.56) into the wave equation $\mathbf{k} \times (\mathbf{k} \times \mathbf{E}) + k_0^2\bar{\varepsilon}_r(\omega, \mathbf{k}) \cdot \mathbf{E} = \mathbf{0}$ and using the dyadic identities $\mathbf{k} \cdot (\hat{\mathbf{k}}_t \times \hat{\mathbf{y}}) = \hat{\mathbf{k}}_t \cdot (\hat{\mathbf{y}} \times \mathbf{k})$ and $(\hat{\mathbf{y}} \times \bar{\mathbf{I}}) \cdot \mathbf{E} = \hat{\mathbf{y}} \times \mathbf{E}$, we obtain $(\mathbf{k}\mathbf{k} - k^2\bar{\mathbf{I}}) \cdot \mathbf{E} + k_0^2\bar{\varepsilon}_r \cdot \mathbf{E} = \mathbf{0}$. Then,

$$\begin{aligned} & [(k_0^2\varepsilon_t - k_y^2)\alpha_1 + \alpha_2k_yk_t + ik_0^2\varepsilon_g\alpha_3]\hat{\mathbf{k}}_t \\ & + [\alpha_1k_tk_y + (k_0^2\varepsilon_a - k_t^2)\alpha_2]\hat{\mathbf{y}} \\ & - [ik_0^2\varepsilon_g\alpha_1 + (k^2 - k_0^2\varepsilon_t)\alpha_3](\hat{\mathbf{k}}_t \times \hat{\mathbf{y}}) = 0. \end{aligned} \quad (2.57)$$

By setting each component to zero, we derive a system of equations with the matrix form

$$\begin{pmatrix} k_0^2\varepsilon_t - k_y^2 & k_yk_t & ik_0^2\varepsilon_g \\ k_yk_t & k_0^2\varepsilon_a - k_t^2 & 0 \\ -ik_0^2\varepsilon_g & 0 & k_0^2\varepsilon_t - k^2 \end{pmatrix} \begin{pmatrix} \alpha_1 \\ \alpha_2 \\ \alpha_3 \end{pmatrix} = \begin{pmatrix} 0 \\ 0 \\ 0 \end{pmatrix}. \quad (2.58)$$

Solving the equations gives

$$\alpha_2 = \frac{-k_yk_t}{(k_0^2\varepsilon_a - k_t^2)}\alpha_1, \quad \alpha_3 = \frac{ik_0^2\varepsilon_g}{(k_0^2\varepsilon_t - k^2)}\alpha_1 \quad (2.59)$$

Plugging them into (2.56), the electric field is proportional to

$$\mathbf{E} \propto \hat{\mathbf{k}}_t + \frac{-k_y k_t}{(k_0^2 \varepsilon_a - k_t^2)} \hat{\mathbf{y}} + \frac{ik_0^2 \varepsilon_g}{(k_0^2 \varepsilon_t - k^2)} (\hat{\mathbf{k}}_t \times \hat{\mathbf{y}}) \quad (2.60)$$

or equivalently,

$$\mathbf{E} \propto \mathbf{k}_t + k_y \theta \hat{\mathbf{y}} + \Delta (\mathbf{k} \times \hat{\mathbf{y}}) \quad (2.61)$$

Therefore, in the plasma region, the field can be written as superposition of two plane waves with the wave vectors $\mathbf{k}_j = k_x \hat{\mathbf{x}} + k_y \hat{\mathbf{y}} - k_{z,j} \hat{\mathbf{z}} : j \in \{1, 2\}$, propagating in the $-z$ direction. Then,

$$\mathbf{E} = [A_1(\mathbf{k}_{t,1} + k_y \theta_1 \hat{\mathbf{y}} + \Delta_1 (\mathbf{k}_1 \times \hat{\mathbf{y}})) e^{ik_{z,1}z} + A_2(\mathbf{k}_{t,2} + k_y \theta_2 \hat{\mathbf{y}} + \Delta_2 (\mathbf{k}_2 \times \hat{\mathbf{y}})) e^{ik_{z,2}z}] e^{i\mathbf{k}_{||} \cdot \mathbf{r}}, \quad (2.62)$$

where

$$\Delta_j = \frac{ik_0^2 \varepsilon_g}{\xi_j} : \xi_j \equiv k_0^2 \varepsilon_t - k_j^2 \quad (2.63)$$

$$\theta_j = \frac{-k_{t,j}^2}{\varpi_j} : \varpi_j \equiv k_0^2 \varepsilon_a - k_{t,j}^2. \quad (2.64)$$

and $\mathbf{k}_{||} = k_x \hat{\mathbf{x}} + k_y \hat{\mathbf{y}}$. The magnetic field is

$$\begin{aligned} \omega \mu_0 \mathbf{H} &= \mathbf{k} \times \mathbf{E} \\ &= [A_1 [\Delta_1 k_y \mathbf{k}_{t,1} - \Delta_1 k_{t,1}^2 \hat{\mathbf{y}} + k_y (\theta_1 - 1) (\mathbf{k}_{t,1} \times \hat{\mathbf{y}})] e^{ik_{z,1}z} \\ &\quad + A_2 [\Delta_2 k_y \mathbf{k}_{t,2} - \Delta_2 k_{t,2}^2 \hat{\mathbf{y}} + k_y (\theta_2 - 1) (\mathbf{k}_{t,2} \times \hat{\mathbf{y}})] e^{ik_{z,2}z}] e^{i\mathbf{k}_{||} \cdot \mathbf{r}} \end{aligned} \quad (2.65)$$

By substituting $\mathbf{k}_{t,j} = \hat{\mathbf{x}} k_x - \hat{\mathbf{z}} k_{z,j}$ into (2.62) and (2.65), we derive the field components as

$$E_x = A_1 (k_x + \Delta_1 k_{z,1}) e^{ik_{z,1}z} + A_2 (k_x + \Delta_2 k_{z,2}) e^{ik_{z,2}z} \quad (2.66)$$

$$E_y = A_1 k_y \theta_1 e^{ik_{z,1}z} + A_2 k_y \theta_2 e^{ik_{z,2}z} \quad (2.67)$$

$$E_z = A_1 (\Delta_1 k_x - k_{z,1}) e^{ik_{z,1}z} + A_2 (\Delta_2 k_x - k_{z,2}) e^{ik_{z,2}z} \quad (2.68)$$

and

$$\omega \mu_0 H_x = A_1 [\Delta_1 k_x k_y + k_y k_{z,1} (\theta_1 - 1)] e^{ik_{z,1}z} + A_2 [\Delta_2 k_x k_y + k_y k_{z,2} (\theta_2 - 1)] e^{ik_{z,2}z} \quad (2.69)$$

$$\omega \mu_0 H_y = -A_1 \Delta_1 k_{t,1}^2 e^{ik_{z,1}z} - A_2 \Delta_2 k_{t,2}^2 e^{ik_{z,2}z} \quad (2.70)$$

$$\omega \mu_0 H_z = A_1 [(k_x k_y (\theta_1 - 1) - \Delta_1 k_{z,1} k_y)] e^{ik_{z,1}z} + A_2 [(k_x k_y (\theta_2 - 1) - \Delta_2 k_{z,2} k_y)] e^{ik_{z,2}z} \quad (2.71)$$

2.5 Field Vectors in an Isotropic Region

We assume that the gyrotropic medium is covered by an isotropic material. In this section, we obtain the electric and magnetic field vectors in an isotropic medium. In a half-space isotropic region ($z > 0$) with the permittivity ε_r , the electric and magnetic fields can be expanded, respectively, as

$$\mathbf{E} = [B_1 (\mathbf{k}_d \times \hat{\mathbf{z}}) + B_2 \mathbf{k}_d \times (\mathbf{k}_d \times \hat{\mathbf{z}})] e^{ik_{zd}z}, \quad (2.72)$$

and

$$\omega\mu_0\mathbf{H} = \mathbf{k}_d \times \mathbf{E} = [B_1 \mathbf{k}_d \times (\mathbf{k}_d \times \hat{\mathbf{z}}) - B_2 k_d^2 (\mathbf{k}_d \times \hat{\mathbf{z}})] e^{ik_{zd}z}, \quad (2.73)$$

with the wave vector $\mathbf{k}_d = \hat{\mathbf{x}}k_x + \hat{\mathbf{y}}k_y + \hat{\mathbf{z}}k_{zd}$ and $k_{zd} = \sqrt{k_d^2 - k_x^2 - k_y^2}$ where $k_d = k_0\sqrt{\varepsilon_r}$. The field components are

$$E_{x,d} = [B_1 k_y + B_2 k_{zd} k_x] e^{ik_{zd}z} \quad (2.74)$$

$$E_{y,d} = [-B_1 k_x + B_2 k_{zd} k_y] e^{ik_{zd}z} \quad (2.75)$$

$$E_{z,d} = B_2 (-k_x^2 - k_y^2) e^{ik_{zd}z} \quad (2.76)$$

and

$$\omega\mu_0 H_{x,d} = [B_1 k_{zd} k_x - B_2 k_d^2 k_y] e^{ik_{zd}z} \quad (2.77)$$

$$\omega\mu_0 H_{y,d} = [B_1 k_{zd} k_y + B_2 k_d^2 k_x] e^{ik_{zd}z} \quad (2.78)$$

$$\omega\mu_0 H_{z,d} = [B_1 (-k_x^2 - k_y^2)] e^{ik_{zd}z}. \quad (2.79)$$

2.6 SPP Dispersion of a Single-Interface Structure

Considering the plasma region is bounded, the SPP can be excited on the surface boundary due to coupling of the surface plasmons and EM wave. In this section, from continuity of the tangential electric and magnetic fields at the interface of the gyrotropic and isotropic region, we derive the SPP dispersion equation to examine the propagation properties of the SPPs.

A surface wave that propagates along the interface between a gyrotropic medium and an isotropic medium, with propagation angle ϕ_s with respect to the x -axis, has wavevector $\mathbf{k}_s = \hat{\mathbf{x}}k_x + \hat{\mathbf{y}}k_y$ in the x - y plane. From the bulk dispersion equation describing the biased plasma (2.55), we obtain the solutions $\hat{\mathbf{k}}_{b,j}^\pm = \mathbf{k}_s \pm \hat{\mathbf{z}}i\gamma_j$

for $j \in \{1, 2\}$, where

$$\gamma_1 = \sqrt{k_x^2 + \frac{1}{2} \left(\kappa - \sqrt{\kappa^2 - v} \right)}, \quad (2.80)$$

$$\gamma_2 = \sqrt{k_x^2 + \frac{1}{2} \left(\kappa + \sqrt{\kappa^2 - v} \right)}, \quad (2.81)$$

such that

$$\kappa = \left\{ (\varepsilon_t + \varepsilon_a) k_y^2 - [\varepsilon_t (\varepsilon_t + \varepsilon_a) - \varepsilon_g^2] k_0^2 \right\} / \varepsilon_t, \quad (2.82)$$

$$v = \left\{ 4\varepsilon_a [(\varepsilon_t + \varepsilon_g) k_0^2 - k_y^2] [(\varepsilon_t - \varepsilon_g) k_0^2 - k_y^2] \right\} / \varepsilon_t, \quad (2.83)$$

and in the isotropic dielectric regions, the solutions are simply $\hat{\mathbf{k}}^\pm = \mathbf{k}_s \pm \hat{\mathbf{z}} i \gamma_0$ where $\gamma_0 = \sqrt{k_s^2 - k_0^2 \varepsilon_r}$. The dispersion relation for the SPP can be obtained by matching the tangential components of the electric and magnetic fields, using (2.66)-(2.71 and (2.74)-(2.79)), at the interface ($z = 0$), leading to the 4×4 system of homogeneous equations,

$$\begin{pmatrix} \beta_1^- & \beta_2^- & k_y & i\gamma_0 k_x \\ k_y \theta_1 & k_y \theta_2 & -k_x & i\gamma_0 k_y \\ k_y \phi_1^- & k_y \phi_2^- & i\gamma_0 k_x & -k_0^2 \varepsilon_r k_y \\ -\delta_1 k_{t,1}^2 & -\delta_2 k_{t,2}^2 & i\gamma_0 k_y & k_0^2 \varepsilon_r k_x \end{pmatrix} \begin{pmatrix} A_1 \\ A_2 \\ B_1 \\ B_2 \end{pmatrix} = \mathbf{0}, \quad (2.84)$$

where β_j^\pm , ϕ_j^\pm , δ_j , and θ_j ($j \in \{1, 2\}$) are defined as

$$\begin{aligned} \beta_j^\pm &= k_x \mp i\gamma_j \delta_j, \quad \phi_j^\pm = \delta_j k_x \mp i\gamma_j (\theta_j - 1), \\ \delta_j &= i k_0^2 \varepsilon_g / \xi_j, \quad \theta_j = -k_{t,j}^2 / \varpi_j, \quad \gamma_0 = \sqrt{k_x^2 + k_y^2 - k_0^2 \varepsilon_r}, \\ \xi_j &= k_0^2 \varepsilon_t - k_{b,j}^2, \quad \varpi_j = k_0^2 \varepsilon_a - k_{t,j}^2, \\ k_{t,j}^2 &= k_x^2 - \gamma_j^2, \quad k_{b,j}^2 = k_{t,j}^2 + k_y^2. \end{aligned} \quad (2.85)$$

Non-trivial solutions are obtained when the determinant of the coefficient matrix on the left hand side of (2.84) is set equal to zero. Evaluation of the determinant and dividing through by a factor of $-i k_s^2 k_y / \varpi_1 \varpi_2 \xi_1 \xi_2 \neq 0$, ($j \in \{1, 2\}$), leads to the SPP dispersion equation

$$(k_y^2 - \gamma_0^2) Q_A - k_x Q_B^- + k_x k_y^2 Q_C^- - (k_x^2 - \gamma_0^2) Q_D^- + \gamma_0 (Q_E^- - \varepsilon_r \chi^-) = 0, \quad (2.86)$$

where the quantities Q_A , Q_B^- , Q_C^- , Q_D^- , Q_E^- and χ^- are defined as

$$Q_A = \varepsilon_g k_{t,1}^2 k_{t,2}^2 (\varpi_1 \xi_2 - \varpi_2 \xi_1), \quad (2.87)$$

$$Q_B^\pm = \varepsilon_g \varpi_1 \varpi_2 (k_{t,1}^2 \alpha_2^\pm - k_{t,2}^2 \alpha_1^\pm), \quad (2.88)$$

$$Q_C^\pm = k_{t,1}^2 \zeta_2^\pm \xi_1 - k_{t,2}^2 \zeta_1^\pm \xi_2, \quad (2.89)$$

$$Q_D^\pm = \zeta_2^\pm \alpha_1^\pm \varpi_1 - \zeta_1^\pm \alpha_2^\pm \varpi_2, \quad (2.90)$$

$$Q_E^\pm = \varepsilon_g k_0^2 (k_{t,1}^2 \zeta_2^\pm \varpi_1 - k_{t,2}^2 \zeta_1^\pm \varpi_2), \quad (2.91)$$

and

$$\zeta_j^\pm = \varepsilon_g k_x \varpi_j \pm \varepsilon_a \xi_i \gamma_{z,j}, \quad (2.92)$$

$$\alpha_j^\pm = k_x \xi_j \pm \varepsilon_g k_0^2 \gamma_{z,j}, \quad (2.93)$$

$$\chi^\pm = k_{t,1}^2 \xi_1 \varpi_2 \alpha_2^\pm - k_{t,2}^2 \xi_2 \varpi_1 \alpha_1^\pm. \quad (2.94)$$

2.6.1 SPP Dispersion in Voigt Configuration

Here, we derive the SPP dispersion equation for the well-studied case of propagation perpendicular to the bias ($k_y = 0$) [32, 36]. By enforcing the continuity of tangential electric and magnetic field components at the interface $z = 0$ and setting $k_y = 0$, we have $B_1 = 0$ and from

$$\omega \mu_0 H_y(z = 0) = \omega \mu_0 H_{y,d}(z = 0), \quad (2.95)$$

we have

$$B_2 = -A_1 \frac{\Delta k_t^2}{k_d^2 k_x}, \quad (2.96)$$

where $\Delta = i\varepsilon_t/\varepsilon_g$. Substituting $k_t^2 = k_0^2 \varepsilon_{\text{eff}}$ and $k_d = k_0 \sqrt{\varepsilon_r}$ gives

$$B_2 = -A_1 \frac{\Delta \varepsilon_{\text{eff}}}{\varepsilon_r k_x}. \quad (2.97)$$

Then, from $E_x(z = 0) = E_{x,d}(z = 0)$ we have

$$A_1 (k_x + \Delta k_z) = B_2 k_{zd} k_x \quad (2.98)$$

By plugging B_2 , Δ , and $k_{zd} = -i\gamma_d = \sqrt{k_0^2 \varepsilon_r - k_x^2}$ and $k_z = -i\gamma_{\text{eff}} = \sqrt{k_t^2 - k_x^2} = \sqrt{k_0^2 \varepsilon_{\text{eff}} - k_x^2}$, we derive the SPP dispersion equation as

$$\frac{\gamma_{\text{eff}}}{\varepsilon_{\text{eff}}} + \frac{\gamma_d}{\varepsilon_r} = \frac{k_x \varepsilon_g}{\varepsilon_t \varepsilon_{\text{eff}}}, \quad (2.99)$$

where $\varepsilon_{\text{eff}} = (\varepsilon_t^2 - \varepsilon_g^2) / \varepsilon_t$. This relation is only valid for the $k_y = 0$ case. However, for $k_y \neq 0$, the general dispersion equation (2.86) must be used.

2.6.2 SPP Dispersion in a Multi-Layer Structure

Consider a multi-layer structure consisting of a magnetized plasma medium ($-\infty < z < 0$), a gold slab with finite thickness h ($0 < z < h$), and an isotropic layer with dielectric constant ε_r ($h < z < \infty$). The gold layer is characterized by dispersive dielectric constant of

$$\varepsilon_m = \varepsilon_\infty - \frac{\omega_{\text{p,Au}}^2}{\omega(\omega + i\gamma_{\text{Au}})}. \quad (2.100)$$

The field vectors in the gold region are

$$\mathbf{E} = [C_1 (\mathbf{k}_m^+ \times \hat{\mathbf{z}}) + C_2 \mathbf{k}_m^+ \times (\mathbf{k}_m^+ \times \hat{\mathbf{z}})] e^{ik_{zm}z} + [C_3 (\mathbf{k}_m^- \times \hat{\mathbf{z}}) + C_4 \mathbf{k}_m^- \times (\mathbf{k}_m^- \times \hat{\mathbf{z}})] e^{-ik_{zm}z}, \quad (2.101)$$

and $\omega\mu_0\mathbf{H} = \mathbf{k}_m^\pm \times \mathbf{E}$, where $\mathbf{k}_m^\pm = \hat{\mathbf{x}}k_x + \hat{\mathbf{y}}k_y \pm \hat{\mathbf{z}}k_{zm}$ and $k_{zm} = \sqrt{k_0^2\varepsilon_m - k_x^2 - k_y^2}$ ($k_m = k_0\sqrt{\varepsilon_m}$). We determined the field vectors in the plasma and dielectric regions before. For particular case $k_y = 0$, by enforcing the boundary conditions at the interfaces ($z = 0, h$), the SPP dispersion equation is obtained as

$$\frac{k_{zd}}{\varepsilon_r} \left(\frac{-i\varepsilon_g k_x}{\varepsilon_t \varepsilon_{\text{eff}}} + \frac{k_z}{\varepsilon_{\text{eff}}} + \frac{k_{zm}^2 / \varepsilon_m^2}{k_{zd} / \varepsilon_r} \right) \tan k_{zm}h = \frac{k_{zm}}{\varepsilon_m} \left(\frac{-i\varepsilon_g k_x}{\varepsilon_t \varepsilon_{\text{eff}}} + \frac{k_z}{\varepsilon_{\text{eff}}} + \frac{k_{zd}}{\varepsilon_r} \right), \quad (2.102)$$

where $k_z = \sqrt{k_0^2\varepsilon_{\text{eff}} - k_x^2}$, $k_{zm} = \sqrt{k_0^2\varepsilon_m - k_x^2}$, and $k_{zd} = \sqrt{k_0^2\varepsilon_r - k_x^2}$. When $h \rightarrow 0$, the dispersion equation is equal to the single-interface case.

2.7 Reflection from a Single-Interface Structure

In this section, the reflection coefficient from the interface of two half-space gyrotropic/dielectric media is calculated. This coefficient will be used in calculation of the Green's function, and also describes how electromagnetic waves reflect from the interface. The tangential electric and magnetic field components in the gyrotropic region at $z = 0$ are related as

$$\begin{pmatrix} H_{x,g} \\ -H_{y,g} \end{pmatrix} = \mathbf{Y}_g \cdot \begin{pmatrix} E_{y,g} \\ E_{x,g} \end{pmatrix}, \quad (2.103)$$

so that

$$\mathbf{Y}_g = \frac{1}{\omega\mu_0} \begin{pmatrix} \Phi_1 & \Phi_2 \\ \Delta_1 k_{t,1}^2 & \Delta_2 k_{t,2}^2 \end{pmatrix} \cdot \begin{pmatrix} k_y \theta_1 & k_y \theta_2 \\ k_x + \Delta_1 k_{z,1} & k_x + \Delta_2 k_{z,2} \end{pmatrix}^{-1}, \quad (2.104)$$

In the isotropic region, they are related as

$$\begin{pmatrix} H_{x,d} \\ -H_{y,d} \end{pmatrix} = \pm \mathbf{Y}_0 \cdot \begin{pmatrix} E_{y,d} \\ E_{x,d} \end{pmatrix}, \quad (2.105)$$

such that

$$\mathbf{Y}_0 = \frac{1}{\omega\mu_0 k_{zd}} \begin{pmatrix} k_{zd}^2 + k_x^2 & k_y k_x \\ k_y k_x & k_{zd}^2 + k_x^2 \end{pmatrix}, \quad (2.106)$$

Assuming a point source in the dielectric region, the total field in $z > 0$ is superposition of the incident and reflected waves

$$\mathbf{E}_d = \mathbf{E}_i + \mathbf{E}_r = (\mathbf{I} - \mathbf{R}) \cdot \mathbf{E}_i \quad (2.107)$$

$$\mathbf{H}_d = \mathbf{H}_i + \mathbf{H}_r \quad (2.108)$$

and in the gyrotropic plasma, there is only transmitted wave

$$\mathbf{E}_g = \mathbf{E}_t = \mathbf{T} \cdot \mathbf{E}_i \quad (2.109)$$

$$\mathbf{H}_g = \mathbf{H}_t. \quad (2.110)$$

Enforcing continuity of tangential components of the electric and magnetic field at $z = 0$ and using $\mathbf{H}_g = \mathbf{Y}_g \cdot \mathbf{E}_g$ and $\mathbf{H}_d = \pm \mathbf{Y}_d \cdot \mathbf{E}_d$, we have

$$(\mathbf{I} - \mathbf{R}) \cdot \mathbf{E}_i = \mathbf{T} \cdot \mathbf{E}_i \quad (2.111)$$

$$\mathbf{Y}_d \cdot (\mathbf{I} + \mathbf{R}) \cdot \mathbf{E}_i = \mathbf{Y}_g \cdot \mathbf{T} \cdot \mathbf{E}_i. \quad (2.112)$$

After combination of two equations, the reflection matrix is derived as

$$\mathbf{R} = (\mathbf{Y}_g + \mathbf{Y}_d)^{-1} \cdot (\mathbf{Y}_g - \mathbf{Y}_d). \quad (2.113)$$

This relation is valid only if $k_y \neq 0$, otherwise the first term is not invertible. The total reflection coefficient can be obtained by dividing the total reflected power and the incident power, then

$$R = \frac{\langle \mathbf{S}_r \rangle \cdot \hat{\mathbf{z}}}{\langle \mathbf{S}_i \rangle \cdot (-\hat{\mathbf{z}})} = \frac{Re(E_x H_y^* - E_y H_x^*)_r}{-Re(E_x H_y^* - E_y H_x^*)_i}, \quad (2.114)$$

where \mathbf{S}_r and \mathbf{S}_i denote the Poynting vectors of the reflected and incident wave, and the field components are related as

$$\begin{pmatrix} E_y^r \\ E_x^r \end{pmatrix} = \mathbf{R} \cdot \begin{pmatrix} E_y^i \\ E_x^i \end{pmatrix}, \quad \begin{pmatrix} H_x^r \\ -H_y^r \end{pmatrix} = \mathbf{Y}_d \cdot \mathbf{R} \cdot \begin{pmatrix} E_y^i \\ E_x^i \end{pmatrix}. \quad (2.115)$$

2.7.1 Reflectance in the Voigt Configuration

For particular case of $k_y = 0$, the plane wave in the gyrotropic region can be decomposed into TM and TE modes. The field components of a TM mode are

$$E_{x,g} = A_1 (k_x + \Delta k_z) e^{ik_z z}, \quad E_{y,g} = 0 \quad (2.116)$$

$$H_{x,g} = 0, \quad \omega \mu_0 H_{y,g} = -A_1 \Delta k_t^2 e^{ik_z z}, \quad (2.117)$$

with $k_t^2 = k_z^2 = k_0^2 \varepsilon_{\text{eff}}$, $\varepsilon_{\text{eff}} = (\varepsilon_t^2 - \varepsilon_g^2)/\varepsilon_t$ and $\Delta = i\varepsilon_g/(\varepsilon_t - \varepsilon_{\text{eff}})$. The impedance of TM wave is defined by

$$Y_{2,\text{TM}} = -\frac{H_y}{E_x} = \frac{1}{\omega \mu_0} \frac{\Delta k_0^2 \varepsilon_{\text{eff}}}{k_x + \Delta k_z}. \quad (2.118)$$

For normal incident plane wave, $k_x = k_y = 0$, then

$$Y_{2,\text{TM}} = \frac{1}{\omega \mu_0} \frac{k_0^2 \varepsilon_{\text{eff}}}{k_z} = \frac{\sqrt{\varepsilon_{\text{eff}}}}{\eta_0}, \quad (2.119)$$

where η_0 is the intrinsic wave impedance of vacuum. The wave impedance in the isotropic region is

$$Y_1 = \sqrt{\frac{\varepsilon_r \varepsilon_0}{\mu_0}} = \frac{\sqrt{\varepsilon_r}}{\eta_0}. \quad (2.120)$$

Applying the boundary conditions at $z = 0$ leads to

$$R = \frac{Y_2 - Y_1}{Y_2 + Y_1}. \quad (2.121)$$

Then, the total reflection for a TM mode is

$$R_{\text{TM}} = \frac{Y_{2,\text{TM}} - Y_1}{Y_{2,\text{TM}} + Y_1} = \frac{\sqrt{\varepsilon_{\text{eff}}} - \sqrt{\varepsilon_r}}{\sqrt{\varepsilon_{\text{eff}}} + \sqrt{\varepsilon_r}}. \quad (2.122)$$

Similarly, for TE mode we have

$$Y_{2,\text{TE}} = -\frac{H_y}{E_x} = \frac{1}{\omega\mu_0} \frac{k_t^2}{k_z} = \frac{\sqrt{\varepsilon_a}}{\eta_0}, \quad (2.123)$$

where we used $k_t^2 = k_0^2 \varepsilon_a$. The TE reflectance is

$$R_{\text{TE}} = \frac{Y_{2,\text{TE}} - Y_1}{Y_{2,\text{TE}} + Y_1} = \frac{\sqrt{\varepsilon_a} - \sqrt{\varepsilon_r}}{\sqrt{\varepsilon_a} + \sqrt{\varepsilon_r}}. \quad (2.124)$$

Chapter 3

Experimental Detection of Unidirectional SPP in the Voigt Configuration

This chapter includes the outcomes of our first project, which is about experimental detection of unidirectional SPP at the interface of magnetized plasma and metal in the Voigt configuration. The measurement is based on a far-field measurement using THz Time-Domain Spectroscopy. This work bridges the theoretical studies on topological SPPs and real-world applications. It leads to invention and manufacture of nonreciprocal components for plasmonic circuitry.

In this chapter, we present a brief review of topological SPP properties in a dissipation-less system in the Voigt configuration, in which the propagation vector is perpendicular to the in-plane magnetic bias, and there are topological SPPs crossing the bulk bandgaps of the gyrotropic plasma medium. Then, we examine the magneto-optical properties of InSb by measuring the reflectance spectrum from the samples. We extract the carrier parameters of InSb samples at various temperatures. The goal is to determine the best condition for measuring the unidirectional SPPs. Next, we excite and detect unidirectional SPPs at the interface of an isotropic and a gyrotropic metal. Finally, we apply a far-field measurement technique to verify the SPPs unidirectional nature. Also, we show that their dispersion properties are tunable by different parameters such as temperature and magnetic field intensity. The contents of this chapter are extracted from [2–4] papers. As mentioned before, our colleague in WVU did the measurement and we contributed to design and theoretical/numerical evaluation before running each test.

3.1 Bulk and SPP Modes in the Voigt Configuration

Consider a half-space plasma medium with unit normal vector \hat{z} , biased by an in-plane external magnetic field $\mathbf{B}_0 = \hat{\mathbf{y}}B_0$. The plasma medium is InSb crystal. The gyrotropic InSb is characterized by a simplified Drude model with a dielectric tensor in the form $\bar{\epsilon}_r = \epsilon_t \bar{\mathbf{I}}_t + i\epsilon_g(\hat{\mathbf{y}} \times \bar{\mathbf{I}}) + \epsilon_a \hat{\mathbf{y}}\hat{\mathbf{y}}$, where the permittivity elements are defined in (2.12-2.14). Here, we ignore the phonon contribution in the material model, which is an accurate assumption at frequencies below the optical phonon resonances (and at low temperatures). There are also contributions from heavy and light hole bands [122] but both were found to be negligible; the former because of the large mass and the latter due to small carrier density, even at room temperature. The plasma frequency ω_p sets the frequency scale for the occurrence of bandgaps, and we need a sufficient magnetic bias so that the cyclotron frequency ω_c is not too small compared to ω_p in order to achieve a usual amount of nonreciprocity.

In the well-known Voigt configuration, the bulk modes are propagating perpendicular to the magnetic bias. In this case, the bulk waves can be decoupled into a TE (with electric field along the magnetic bias) and a TM (with electric field in a plane perpendicular to the bias) wave described by $k_{\text{TE}}^2 = \epsilon_a k_0^2$ and $k_{\text{TM}}^2 = \epsilon_{\text{eff}} k_0^2$, respectively, where $\epsilon_{\text{eff}} = (\epsilon_t^2 - \epsilon_g^2)/\epsilon_t$ and k_0 is the free space wave number. Figure 3.1a (black lines) shows the dispersion diagram of TM bulk modes propagating in dissipation-less InSb. There

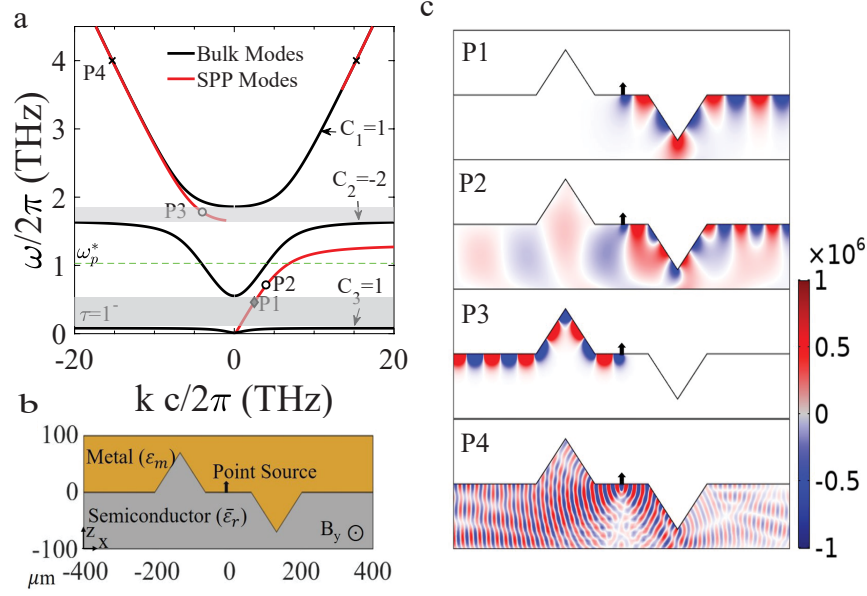


Figure 3.1: Bulk modes and surface plasmons for a metal-InSb (idealized) interface. (a) Bulk and SPP dispersion for dissipation-less InSb characterized by parameters $n_e = 3 \times 10^{21} \text{m}^{-3}$, $m^* = 0.015m_0$, $\epsilon_\infty = 15.68$, and mobility $\mu = \infty$ ($\omega_p^* = \omega_p / \sqrt{\epsilon_\infty} = 2\pi(1.014 \text{THz})$). The in-plane magnetic field is $B = 0.7 \text{T}$ ($\omega_c = 1.28\omega_p^* = 2\pi(1.3 \text{THz})$), and the metal permittivity is $\epsilon_m = -10^4$. The gray regions are the magnetic-field dependent bandgaps (b) The geometrical schematic of the structure under study. SPPs are excited by a dipole source located at the metal-InSb interface. (c) The electric field distribution (E_z) of SPPs at different frequencies P1-P4, 0.5, 0.7, 1.76 and 4 THz, respectively, marked in (a). Points P1 and P3 are points on the SPP dispersion where the SPPs are topologically protected. Reprinted with permission from [2].

are two magnetic-field dependent bandgaps. Each TM band is characterized by a non-zero integer Chern number C_n , an intrinsic property of the bulk band structure, so that Chern numbers sum to zero. The gap Chern number, that is, the sum of the Chern numbers below the gap, is non-zero, indicating the number of topologically protected surface modes crossing the band gaps. The TE mode, with $C_n = 0$, is topologically-trivial and won't be discussed further. Despite the non-reciprocal nature of the medium itself, in the Voigt configuration the bulk dispersion behavior is reciprocal, although an interface will break this reciprocity. The TM-SPP dispersion equation is

$$\frac{\gamma_{zm}}{\epsilon_m} + \frac{\gamma_z}{\epsilon_{\text{eff}}} = \frac{\epsilon_g k_x}{\epsilon_t \epsilon_{\text{eff}}}, \quad (3.1)$$

where $\gamma_z = \sqrt{k_x^2 - k_0^2 \epsilon_{\text{eff}}}$, $\gamma_{zm} = \sqrt{k_x^2 - k_0^2 \epsilon_m}$, and ϵ_m is the effective permittivity of the top (metal) layer. The SPP is propagating on the $x - y$ plane (interface of two media) with the propagation constant k_x . If isotropic materials form the interface, for an SPP to propagate the two permittivities must have opposite signs. In the gyrotropic plasma-isotropic metal case, it can be shown analytically that in the bandgaps, where $\epsilon_{\text{eff}} < 0$, for an SPP to exist we need $\epsilon_t > 0$. The dispersion of the SPP modes at the interface of a dissipation-less gyrotropic semiconductor and an opaque medium (geometry shown in Fig. 3.1b) is

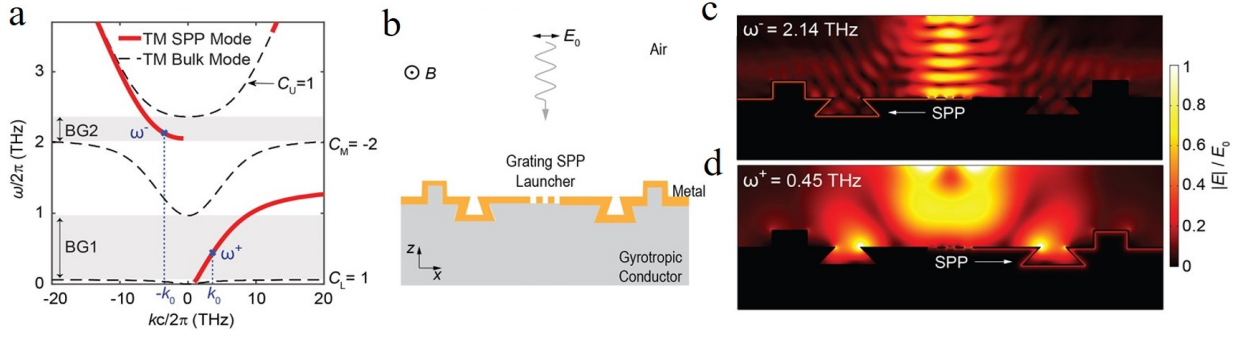


Figure 3.2: Excitation of unidirectional SPP by a metal grating under normally incident plane wave. (a) Dispersion diagram; topologically protected unidirectional SPPs (red) emerging from the bulk gaps (gray regions). Parameters used are $\omega_p/2\pi = 6$ THz, $\omega_c/2\pi = 1.4$ THz. (c) and (d) Simulated electric field intensities for the sample structure illustrated in (b). The size of the simulation area is $2\text{mm} \times 0.7\text{mm}$. The grating period used for SPP launching is $d = 2\pi/k_0 = 84\mu\text{m}$. Reprinted with permission from [3].

shown by red lines. Figure 3.1c shows the electric field profile of SPP propagation at different points on the dispersion curve, P1-P4, shown in Fig. 3.1a, obtained from a full wave simulation using COMSOL assuming a dipole source. As discussed above, SPPs crossing the bandgaps, for example at frequency points P1 and P3, are topologically protected surface waves, meaning they are unidirectional and propagate along the surface without reflection when they encounter sharp discontinuities. In the frequency range between the two bandgaps, although the dispersion is strongly nonreciprocal, upon reflection, surface wave can couple into the bulk modes, see, e.g., point P2. At higher frequencies, for example at point P4, SPPs are bi-directional; the right- and left-going SPPs have approximately the same momentum, $\omega(k) = \omega(-k)$. Partial reflection of the wave occurs, since at this frequency the material itself allows propagation in both directions.

In another design shown in Fig. 3.2b, a metal launcher under normally incident plane wave is used to excite unidirectional SPPs. The grating at the center is designed to be in resonance with two in-gap SPP modes traveling in opposite directions: (k_0, ω_+) and $(-k_0, \omega_-)$, which are indicated by blue dots in dispersion diagram of Fig. 3.2a, where the SPP unidirectionality is topologically protected and therefore immune to back-scattering. when excited by light of frequency ω_- , only the left-traveling mode is allowed at the interface as shown in Fig. 3.2c. In comparison, when tuning the light frequency to ω_+ , the SPP wave launched only travels toward the right (Fig. 3.2(d)). In both cases, the propagating SPP experiences no scattering at the sharp bending points placed along its paths, unlike ordinary SPPs. We note that SPP modes outside the bulk gaps can also be unidirectional within selected frequency ranges (Fig. 3.2a), though these out-of-gap unidirectional waves are not topologically protected and subject to scattering with the bulk modes.

The numerical results are based on a Finite Element Method simulation, using COMSOL Multiphysics software. The 2D simulations are performed in the Optics module, using the Electromagnetic Waves, Fre-

quency Domain (ewfd) solver. A scattering Boundary Condition is applied on the outer boundaries. The gyrotropic material is modeled by the anisotropic dielectric tensor. The SPPs are excited by a point source or illuminating a plane wave to a metal grating on the surface. A plane wave is illuminated by a source located on top of the metal grating with a distance larger than a half wavelength. The input power is 1W. A finer mesh is applied at the interface of the metal and gyrotropic media.

3.2 Magneto-Optics Properties of Indium Antimonide

In this section, we report the measured data (collected by Cen's group in WVU) of the THz reflectances of undoped InSb single crystals in a Voigt geometry with transverse magnetic fields up to 0.7 T and at various temperatures from 5 K to 300 K. We consider the effect of all charge carriers (holes and electrons) using the permittivity elements defined in (2.15-2.17). Based on the measured data, we extract the material parameters and use them in the following sections.

First, in Fig 3.3a,d,g we compare the dispersion diagrams of an ideal dissipation-less plasma system (solid line) and a realistic plasma medium with finite carrier mobility (dashed line) for isotropic ($B = 0$) and gyrotropic ($B \neq 0$) cases. When a nonzero magnetic field is applied, the single bulk optical band (Fig. 3.3a) splits into three bands (Fig. 3.3d, g). The lowest band, unique in the multi-carrier case, is produced by the field responses of the electron-hole hybrid [57]. The three bands are separated by two bandgaps: BG1 and BG2. As shown in Figure 3.3d and g, the positions and sizes of the bandgaps are field-dependent. In the large field limit ($B \rightarrow \infty$), BG_1 closes near the heavy hole cyclotron frequency $\omega_c^{(hh)}$, and the bottom edge of BG_2 asymptotically approaches the electron cyclotron frequency $\omega_c^{(e)}$.

In realistic materials with finite carriers mobilities, the nonzero carrier scattering rates lead to modified plasmon dispersions (dashed curves, Fig. 3.3a, d, g). True energy gaps that strictly forbid the bulk plasmon propagation no longer exist, but the optical densities of states inside the bandgaps are still particularly low.

3.2.1 Reflection from InSb Sample Interface

The presence of field-induced bulk optical bandgaps strongly modulates the reflectance of light incidences that follow the Voigt configuration (inset in Fig. 3.3b). Solving the wave equation while considering the continuity of tangential components of the electric and magnetic fields at the boundary, we obtain the reflection coefficient for a TM plane wave that incidents normally from a semi-infinite dielectric medium (with an isotropic permittivity ε_d) to a semi-infinite gyrotropic plasma as

$$r_{TM} = \frac{\sqrt{\varepsilon_{\text{eff}}} - \sqrt{\varepsilon_d}}{\sqrt{\varepsilon_{\text{eff}}} + \sqrt{\varepsilon_d}}. \quad (3.2)$$

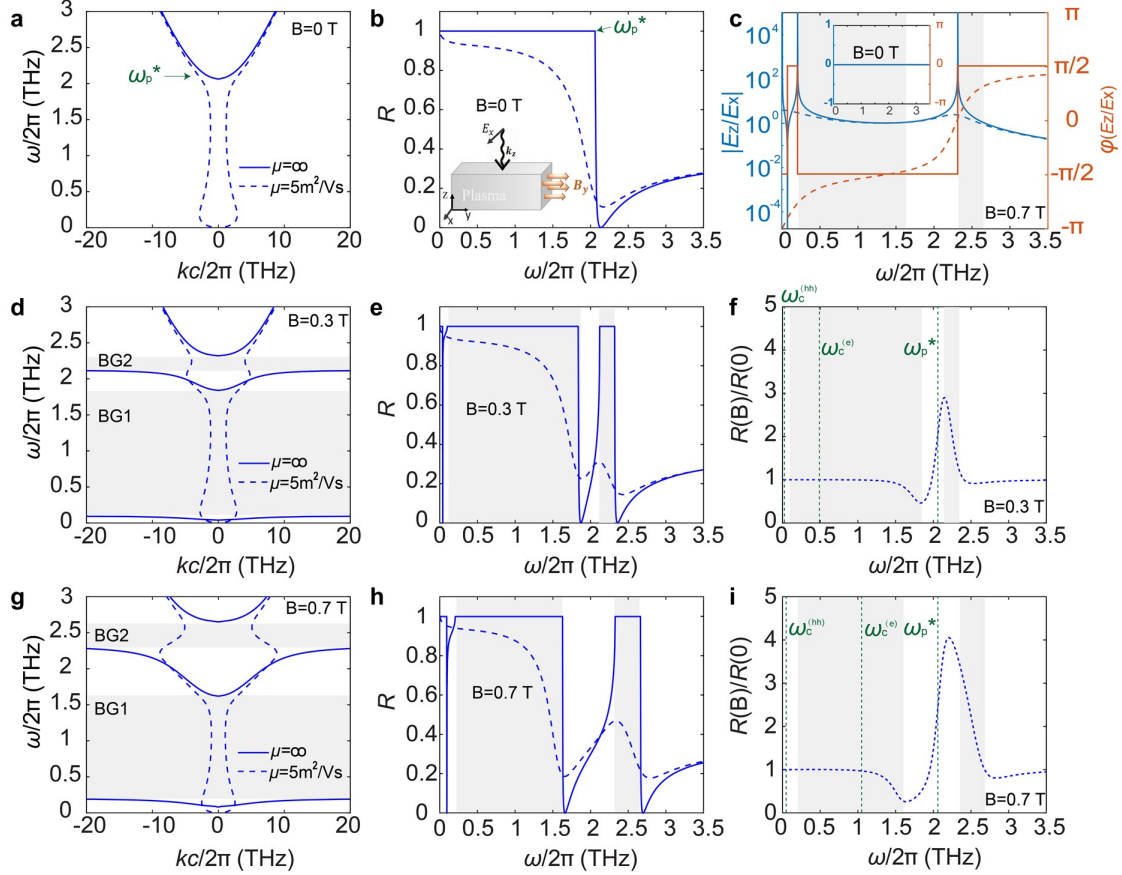


Figure 3.3: Magnetic field induced bulk plasmon band gap (a, d, g) The calculated dispersion diagrams of TM bulk modes in isotropic ($B = 0$) and gyrotropic ($B \neq 0$) plasma media. Room temperature carrier properties of an undoped InSb single crystal sample are used in this calculation: $n_e = 1.5 \times 10^{22} m^{-3}$, $m_e^* = 0.019m_0$, $n_{hh} = 1.49 \times 10^{22} m^{-3}$, $m_{hh}^* = 0.43m_0$, $n_{lh} = 1.38 \times 10^{20} m^{-3}$, $m_{lh}^* = 0.019m_0$, $\varepsilon_\infty = 15.7$. Blue solid curves correspond to the ideal dissipation-less cases with infinite mobility and the dashed curves correspond to practical cases with finite carrier mobilities of $\mu_e = \mu_{lh} = 5m^2/Vs$ and $\mu_{hh} = 0.01m^2/Vs$. (b, e, h) The calculated Voigt-configuration reflectance at an air/plasma interface. Inset in (b) shows the modeling and experiment geometry. (c) The polarization of TM mode at $B = 0.7T$ and $B = 0T$ (inset). (f, i) The field-induced reflectance change calculated by dividing the nonzero-field reflectance by the zero-field value. In all plots, the two field-induced bandgaps are highlighted in grey. Reprinted with permission from [4].

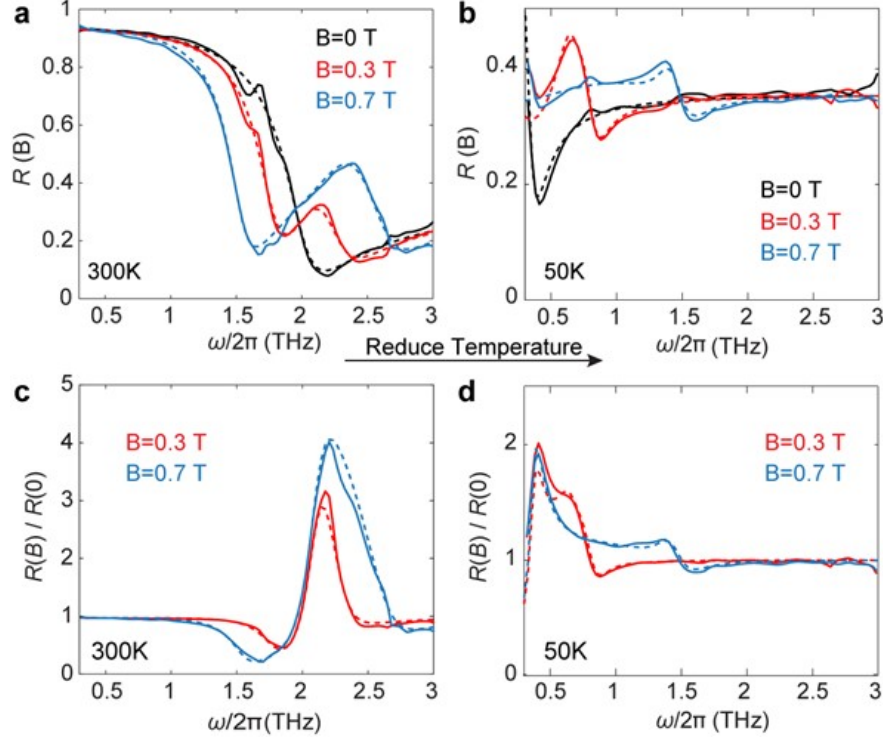


Figure 3.4: Measured field-dependent THz reflectances of undoped InSb (a, b) Reflectance spectra of InSb at 300K and 50K measured under different in-plane magnetic fields. (c, d) Corresponding field-induced reflectance changes comparing data obtained with and without a magnetic field. Dashed curves in (a-d) show the fitting results based on reflectance equation, r_{TM} . Reprinted with permission from [4], and produced by Cen's group.

The detail of derivation is in Subsection (2.7.1). Figure 3.3b, e and h plot the reflectance ($R = |r_{TM}|^2$) spectra for an air/plasma interface ($\epsilon_d = 1$) under different field strengths. Near-unity reflectances are found inside BG_1 and BG_2 , whereas the reflectances in each TM bands are significantly suppressed. As shown, while the reflectance spectra of a lossy system deviate from the ideal lossless cases, the magneto-optic modulations near the plasmon bandgap are very significant. Figure 3.3f and 3.3i highlight the field effects by calculating the ratio between the nonzero-field reflectance, $R(B)$, and the zero-field reflectance, $R(0)$. The field-induced reflectance modulation is particularly strong in the middle band and BG_2 . As already discussed, the bandwidth of such frequency window increases with the external field. The polarization of TM modes is determined by $E_z/E_x = -i\epsilon_g/\epsilon_t$. Fig. 3.3c shows the polarization of the biased TM bands. Undoped InSb with a low impurity density is a quasi-intrinsic semiconductor where $n_e \approx n_{hh} + n_{lh}$. In addition, the effective masses of the three carrier species follow the relation of $m_e^* \approx m_{lh}^* \gg m_{hh}^*$. Under these conditions, at zero field ($B = 0$), TM modes are linearly polarized as shown in inset plot of Fig. 3.3c.

To study the field-controlled reflectance changes in experiments, we perform terahertz time-domain spectroscopy (THz-TDS) measurements in Voigt configuration on nominally undoped (001) InSb single crystals (MTI Corp.) at different temperatures and fields. Figure 3.4a and b show the variable-field reflectance

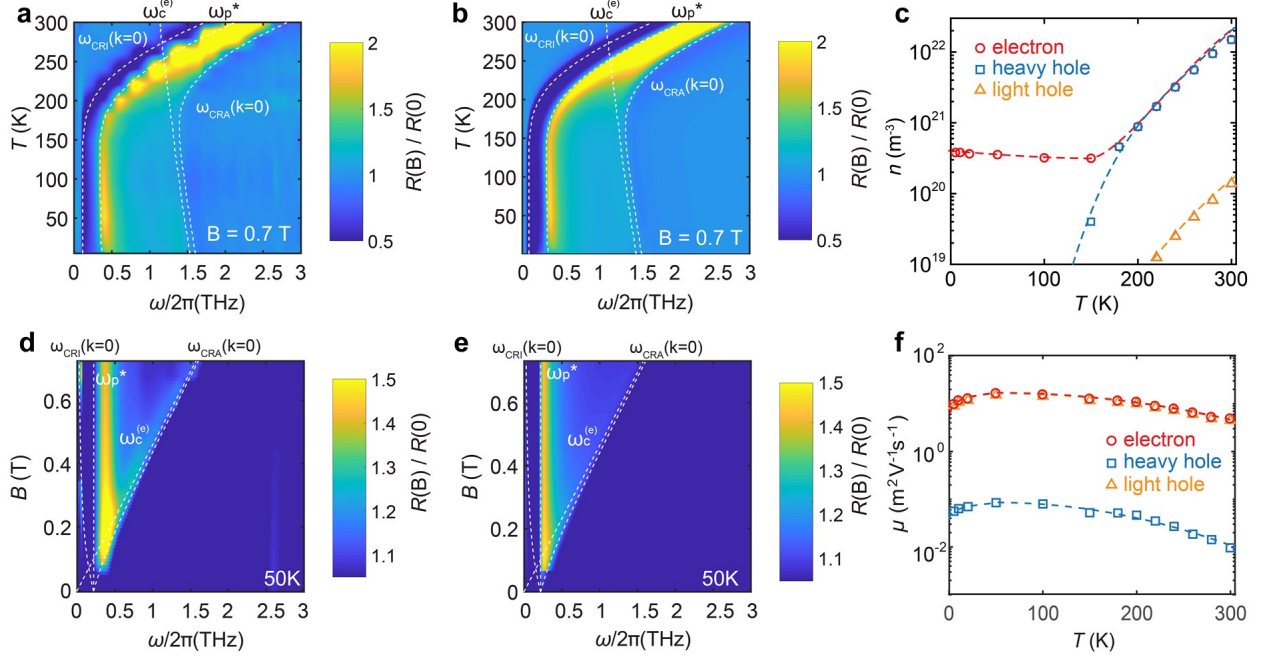


Figure 3.5: Temperature-frequency (a, b) and magnetic field-frequency (d, e) diagrams of the THz reflectance from an InSb sample. Dashed lines trace the changes in the critical frequencies. (a, d) show the experimental data, and (b, e) show the simulated results. (c, f) The carrier densities(c), mobility(f) of electron, heavy hole, light hole at various temperatures. Reprinted with permission from [4], and produced by Cen's group.

spectra obtained at 300 K and 50 K. Here, the absolute reflectance $R(B)$ is measured using an Au plate as the reference, which has near constant THz reflectances below 3 THz. Due to the positioning error associated with the sample exchange and the atmospheric light absorptions [68] that varies as the lab humidity fluctuates, minor spurious signals in $R(B)$ are inevitable. In comparison, the self referenced field-induced reflectance change spectra $R(B)/R(0)$ tends to be more robust (Fig. 3.4c, d). At 300 K, a single reflectance enhancement peak near 2.2 THz is detected (Fig. 3.4c). As shown by the theoretical calculation (Fig. 3.3f, i), the position of this peak is field-independent and determined by ω_p^* . At 50 K, this peak moves to 0.45 THz, indicating a much lower plasma frequency caused by the weakened thermal activation of carriers. Since ω_p^* is very low at 50 K, BG_2 becomes well separated from ω_p^* even for small magnetic fields. As a result, a second peak emerges in $R(B)/R(0)$, which has a field-dependent center frequency that traces the position of BG_2 ($\sim \omega_c^{(e)}$) (Fig. 3.4d). For both temperatures, the observed data can be well fitted by the theoretical model as described by equation (3.2) (dashed line curves, Fig. 3.4a-d).

To better visualize the dependence of the light reflection on temperature and field, we plot the experimental data obtained at $5K \leq T \leq 300K$ and in forms of $0T \leq B \leq 0.7T$ temperature-frequency and field-frequency diagrams (Fig. 3.5a, d). For comparison, theoretical calculation results are shown in Fig. 3.5b and e. On these diagrams, the changes in critical frequencies, including $\omega_c^{(e)}$, ω_p^* and the lower edges of middle and lower frequency bands, $\omega_{CRI}(k=0)$ and $\omega_{CRA}(k=0)$, respectively, are traced by dashed lines.

Clearly, the field-induced reflectance modulations mainly occur within the frequency range between $\omega_{CRI}(k=0)$ and $\omega_{CRA}(k=0)$. Such frequency window is wider at low temperatures when ω_p^* is much smaller than $\omega_c^{(e)}$. The width reaches 1.2 THz at 50 K for a field of 0.7 T. The reflectance is enhanced by the magnetic field for frequencies above ω_p^* , and suppressed for frequencies below ω_p^* . As the temperature drops from 300K to 150 K, since ω_p^* is reduced by more than 80%, the polarity of field-induced reflectance change alters for a wide range of light frequencies. In comparison, $\omega_c^{(e)}$ only depends on the temperature weakly due to the small reduction in effective mass [123]. At a fixed temperature, $R(B)/R(0)$ is largest when ω_p^* and $\omega_c^{(e)}$ are in resonance.

3.2.2 Temperature-Dependent InSb Carrier Parameters

Based on the THz reflectance data, temperature-dependent carrier parameters in the undoped InSb sample are extracted and shown in Fig. 3.5c and f. Above 150 K, the conduction in InSb is dominated by thermally activated intrinsic carriers. Consequently, the change in electron and hole densities follows the Arrhenius law ($n \sim \exp(-E_a/2k_B T)$), where the activation energy $E_a \sim 0.29$ eV represent the electronic bandgap size. Below 150 K, as the population of the thermally excited intrinsic carriers diminishes, extrinsic carriers doped from ionized impurities prevail, leading to the nearly constant $10^{20} m^{-3}$ level low-temperature electron densities. The changes in electron and holes mobilities also fall into two temperature regimes (Fig. 3.5f). At higher temperatures ($T > 50K$), electron-phonon interaction is the dominant venue of carrier scattering in InSb [78]. As the phonon density decreases with the reducing temperature, carrier mobilities rise. This trend is however reversed for temperatures below 50 K. Such behavior is due to the scattering between carriers and the charged impurity dopants, which dominates over the carrier-phonon scattering process at low temperatures and is stronger when the thermal energy is low.

By rotating the sample in-plane, carrier properties along different directions in the (001) plane can be characterized and compared. While the THz magneto-reflectance is largely isotropic at room temperature, clear anisotropy is observed at low temperatures. As shown in Fig. 3.6, the low temperature carrier mobility is highest along the [110] crystal axis, and lowest along the axis (Fig. 3.6b). The trend of the electron density is opposite to the mobility, which minimizes along the [110] axis and maximizes along the axis (Fig. 3.6a). Such uniaxial anisotropy, distinct from the Hamiltonian calculated based on the Zincblende cubic lattice structure [124], is likely caused by the anisotropic energy profile associated with the impurity dopants. Consistent with this attribution, similar anisotropy was not observed in experiments where the effects related to the impurity doping are weak, such as when high-purity samples are used [125] or when intrinsic thermal carriers dominate [66].

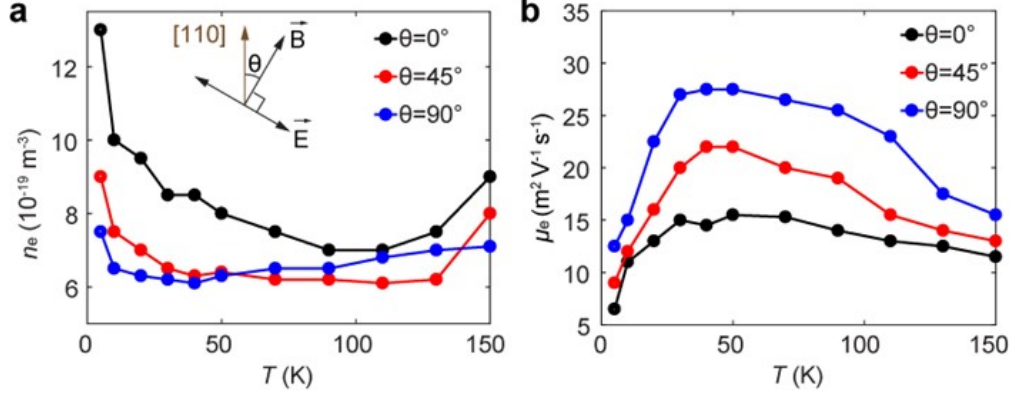


Figure 3.6: Anisotropy of carrier properties in InSb. (a, b) Temperature-dependent electron density (a) and mobility (b) measured at different in-plane sample rotations. As shown by the inset of (a), marks the angle between the external magnetic field and the $[110]$ lattice axis. Reprinted with permission from [4], and produced by Cen's group.

3.3 SPP Properties for Realistic InSb Model

In this section, the propagation properties of topological SPPs are examined by considering a realistic InSb model. We consider that for SPP applications we require, or it is at least very desirable, that i. $L_{\text{SPP}}/\lambda_{\text{SPP}} \gg 1$, where SPP propagation length is $L_{\text{SPP}} = 1/(2\text{Im}(k_{\text{SPP}}))$ and SPP wavelength is $\lambda_{\text{SPP}} = 2\pi/\text{Re}(k_{\text{SPP}})$, ii. SPPs that are nonreciprocal, so that they are backscattering-immune, and iii. SPPs exist in the bulk bandgaps, so that they will not diffract into the bulk upon encountering a discontinuity. To meet these criteria, the requirements on the material properties are very stringent.

The SPP dispersion diagram and propagation length of the SPP excited at the interface of a gold/InSb interface at three different temperatures are shown in Fig. 3.7. The gray regions indicate the bandgaps and propagation length is proportional to the size of circles. At lower temperatures the propagation length is larger due to the higher mobility, although the bandgaps become very narrow.

Figure 3.8a shows the bulk and SPP dispersion for InSb at 230°K with carrier parameters which are $n_e = 3 \times 10^{21} \text{ m}^{-3}$, $\mu = 9 \text{ m}^2/\text{Vs}$, $m^* = 0.015m_0$, $\varepsilon_\infty = 15.68$, extracted from measurement, and $B = 0.7\text{T}$, $\varepsilon_m = -800 + i550$. Loss leads to modified bulk plasmon dispersions, in which case there no longer exists a true bandgap (comparing the solid black lines in Fig. 3.8a with the dotted black lines, which indicate the dissipation-less case from Fig. 3.1a). However, there are still distinguishable regions of dispersion. Below the dashed horizontal line the SPP is nonreciprocal (NR), and sometimes unidirectional.

The field profile of the SPPs at two dispersion points P1 and P3 (Fig. 3.8a) are shown in Fig. 3.8b, obtained from COMSOL simulation. In a dissipative system, nonreciprocal (unidirectional) SPPs are still immune to back-scattering upon encountering a discontinuity. Figure 3.8c shows the propagation length of SPPs supported by InSb at three different temperatures. At high temperature the mobility is low ($\mu = 5.2$

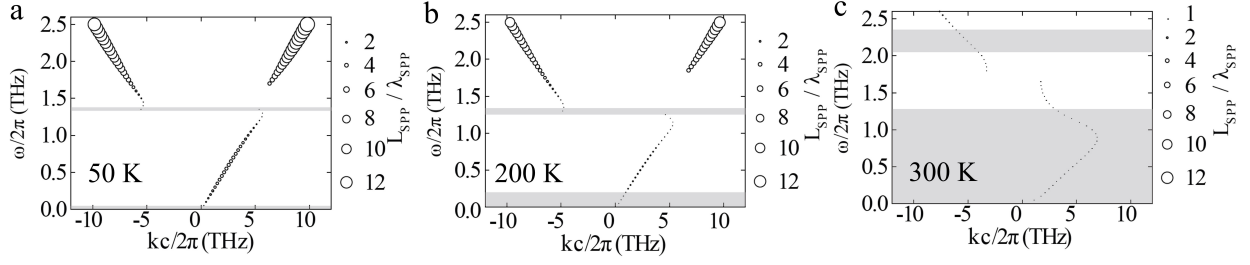


Figure 3.7: (a,b,c) The SPP dispersion diagrams and SPP propagation length (indicated by the size of the circles) at different temperatures by considering realistic InSb model. The carrier density and mobility at each temperature are extracted from the measurement as $n_e = 3.5 \times 10^{20} \text{ m}^{-3}$, $\mu = 18 \text{ m}^2/\text{Vs}$ at 50°K , $n_e = 8.5 \times 10^{20} \text{ m}^{-3}$, $\mu = 11.5 \text{ m}^2/\text{Vs}$ at 200°K , and $n_e = 1 \times 10^{22} \text{ m}^{-3}$, $\mu = 5.2 \text{ m}^2/\text{Vs}$ at 300°K . Shaded gray regions indicate the bandgaps. Reproduced with permission from [2], and produced by Cen's group.

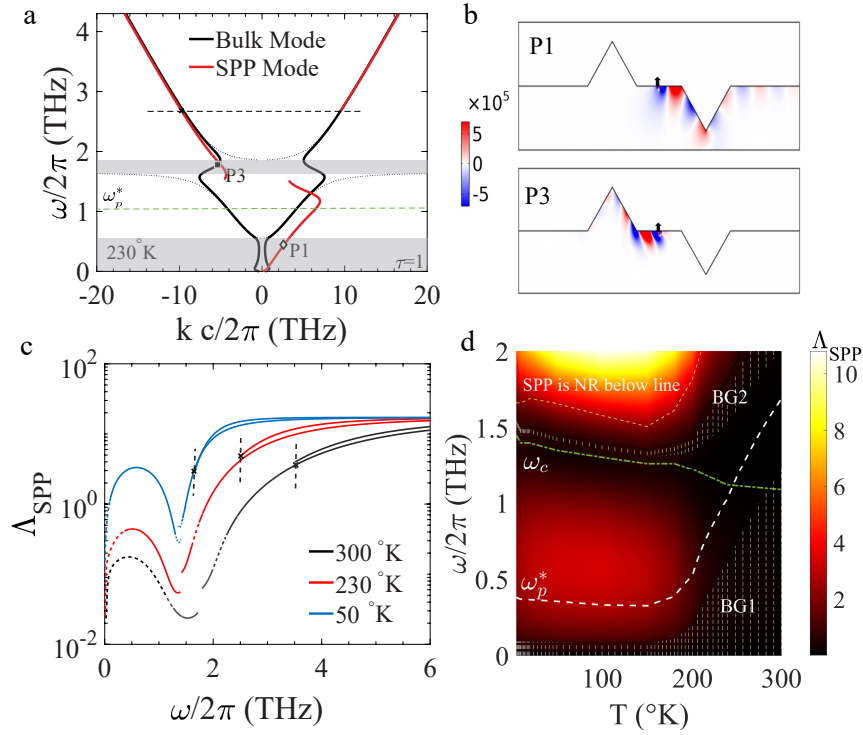


Figure 3.8: Bulk modes and nonreciprocal InSb-metal interface SPPs for a realistic InSb model with finite dissipation, (a-b) bulk and SPP dispersion diagrams using InSb material parameters at $T = 230^\circ\text{K}$. Solid lines correspond to finite dissipation and dotted lines correspond to the infinite mobility cases. (b) The electric field distribution of the unidirectional SPP, at two resonance frequencies P1 and P3, excited by a point source located at the interface for the finite-mobility case. (c) SPP propagation length (L_{SPP}) in a dissipative system at three different temperature, where $\Lambda_{SPP} = L_{SPP}/\lambda_{SPP}$. (d) Density plot of normalized SPP propagation length, Λ_{SPP} , versus frequency and temperature. Shaded regions indicate the bandgaps. Reprinted with permission from [2].

Table 3.1: SPP propagation length and bandgap width in frequency at various temperatures. BG_1 (which starts at 0 THz; the provided value is for the top of the bandgap) and BG_2 are the lower and upper bandgaps, respectively. BTWN-BGs indicates at the midpoint between the two bandgaps (in the bulk passband), $\epsilon_m = -800 + i550$ [9], $B = 0.7T$, and $\Lambda_{SPP} = L_{SPP}/\lambda_{SPP}$.

| Temperature ($^{\circ}K$) | 300 | 250 | 200 | 150 | 100 | 50 |
|-----------------------------|---------------|---------------|---------------|---------------|---------------|---------------|
| BG_1 (THz) | 1.23 | 0.72 | 0.19 | 0.08 | 0.08 | 0.08 |
| BG_2 (THz) | 2.01- 2.32 | 1.60- 1.84 | 1.33- 1.41 | 1.30- 1.34 | 1.35- 1.38 | 1.39- 1.43 |
| Λ in- BG_1 | 0.17 | 0.30 | 0.76 | 0.91 | 1.03 | 1.00 |
| Λ BTWN-BGs | 0.03 | 0.25 | 1.20 | 2.90 | 3.30 | 3.30 |
| Λ in- BG_2 | 0.46 | 0.48 | 0.50 | 0.75 | 0.66 | 0.61 |

m^2/Vs), so that the propagation length of the one-way SPP (at frequencies below the dashed line, where SPPs are nonreciprocal) is a small fraction of the SPP wavelength (Fig. 3.8c, black curve). By reducing the temperature, the bandgap range decreases but the mobility increases, resulting in longer propagation lengths as shown in Fig. 3.8c, blue curve. In each case, only to the left of the dashed vertical lines the SPP is nonreciprocal. Moreover, only along the dashed sections is the SPP within the bandgaps.

In Table 3.1 the values for the bandgap frequency range and the propagation length of the nonreciprocal SPPs at different frequencies, in and between the two bandgaps, and at various temperatures, are listed for $B = 0.7T$. As shown, there is a trade-off between the propagation length and the size of the bandgap – as temperature is lowered, the bandgap can become quite narrow and impractical. Therefore, temperature needs to be carefully chosen, low enough to yield sufficient SPP propagation lengths yet not too low so that the bandgap is wide-enough to work within. Furthermore, unless magnetic bias is adjusted appropriately, the SPP will not exist within the bandgap.

Given that one may consider operation within the bandgap as most desirable, for this bias, only for the lowest temperature is $L_{SPP}/\lambda_{SPP} \approx 1$, although longer propagation lengths are found between the two bandgaps. Similar to Table 3.1, Fig. 3.8d shows a density plot of SPP propagation length $\Lambda_{SPP} = L_{SPP}/\lambda_{SPP}$ versus frequency and temperature. The temperature–bandgap width tradeoff is prominent, as are the relatively short values of non-reciprocal SPP propagation length except between the bandgaps.

Table 3.2 provides a comparison of SPP properties between undoped, N-doped, and P-doped samples at $T = 77^{\circ}K$. For the undoped case, material parameters values were taken from measurements, whereas for the doped cases we used parameter values from the manufacturer website. The P-doped case has very low mobility and poor SPP properties, and won't be discussed further. The undoped case discussed above provides good SPP propagation below 2 THz and $T \lesssim 200^{\circ}K$. Because of the large carrier density in the N-doped case, the plasma frequency, and, hence, the upper bandgap, occurs at higher frequency than for the undoped case, around 10THz for $B = 0.7T$. However, for this strength bias, ω_c/ω_p is small, and poor SPP propagation is obtained. In order to obtain comparable SPP performance for the N-doped material,

Table 3.2: Comparison of plasmon propagation properties in the undoped, N-doped and P-doped crystals at $T = 77^\circ\text{K}$, considering $m^* = 0.015m_0$, $\epsilon_\infty = 15.7$ and $\epsilon_m = -800 + i550$. $\Lambda = L_{\text{SPP}}/\lambda_{\text{SPP}}$. Dashes indicate no SPP exists. BG₁ starts at 0 THz; the provide value is for the top of the bandgap.

| $T = 77^\circ\text{K}$ | undoped | N-doped | | P-doped |
|-------------------------------------|---------------|---------------|---------------|------------|
| $n_e \times 10^{21}(\text{m}^{-3})$ | 0.32 | 350 | | 35 |
| $\mu(\text{m}^2/\text{Vs})$ | 17 | 4.5 | | 0.2 |
| $\omega_p^*/2\pi(\text{THz})$ | 0.33 | 10.9 | 10.9 | 3.4 |
| B (T) | 0.7 | 0.7 | 15 | 0.7 |
| ω_c/ω_p^* | 3.9 | 0.12 | 2.5 | 0.37 |
| Γ/ω_p | 0.08 | 0.01 | 0.01 | 0.7 |
| BG ₁ (THz) | 0.08 | 10.3 | 3.70 | 2.9 |
| BG ₂ (THz) | 1.35- 1.38 | 11.0- 11.6 | 30.0- 31.7 | 3.7 4.2 |
| Λ in-BG1 | 1.0 | 0.02 | 1.6 | 0.2 |
| Λ BTWN-BGs | 3.3 | - | 3.3 | - |
| Λ in-BG2 | 0.65 | 0.5 | 1.1 | - |

one would need $B = 15\text{T}$, which is difficult to obtain, at which point the higher bandgap occurs near 30 THz (here we assume the mobility is the same as the low-THz values).

In summary, one may conclude that for working at low THz ($\lesssim 2\text{THz}$) and moderate bias strength ($\lesssim 1\text{T}$) the undoped material is the only viable option. Room temperature operation is not feasible. For the N-doped material, aside from $B = 15\text{T}$, below $\lesssim 5\text{T}$, there is no SPP between the two bandgaps, but for biases levels such as $B = 5, 7.5, 12\text{T}$ the maximum $L_{\text{SPP}}/\lambda_{\text{SPP}}$ is 0.4, 1.1 and 2.3, respectively. If an n-doped InSb crystal with a lower level of doping is used, a weaker magnetic bias would be required (still, several T) to obtain SPPs with reasonable propagation lengths. However, the bias and bandgap frequency range are still very much higher than for the undoped case.

It is worth noting that properties of the metal layer also impact performance. For example, using parameters of the undoped sample in Table 3.2, if the metal permittivity were $\epsilon'_m = (-2.3 + i8.6) \times 10^5$ obtained using a standard Drude model, the maximum propagation length of the SPP between two bandgaps is $7.4\lambda_{\text{SPP}}$, more than twice the value reported in Table 3.2. Metal deposition quality, surface roughness, etc., will also play an important role which are not the subject of this work. However, for some applications such as switches and nonlinear devices, a very long SPP propagation length is not required.

3.4 Experimentally Detection of Tunable Unidirectional SPP

To realize the gyrotropic/isotropic heterostructure in experiment, Au films are deposited on the surfaces of undoped InSb single crystals. Here, magnetized InSb serves as the gyrotropic conducting medium. Its high electron mobility and small effective mass allows the generation of strong magneto-optical effects with weak magnetic fields [57, 59, 60, 126–128]. Grating structures are fabricated in the Au layer to provide the

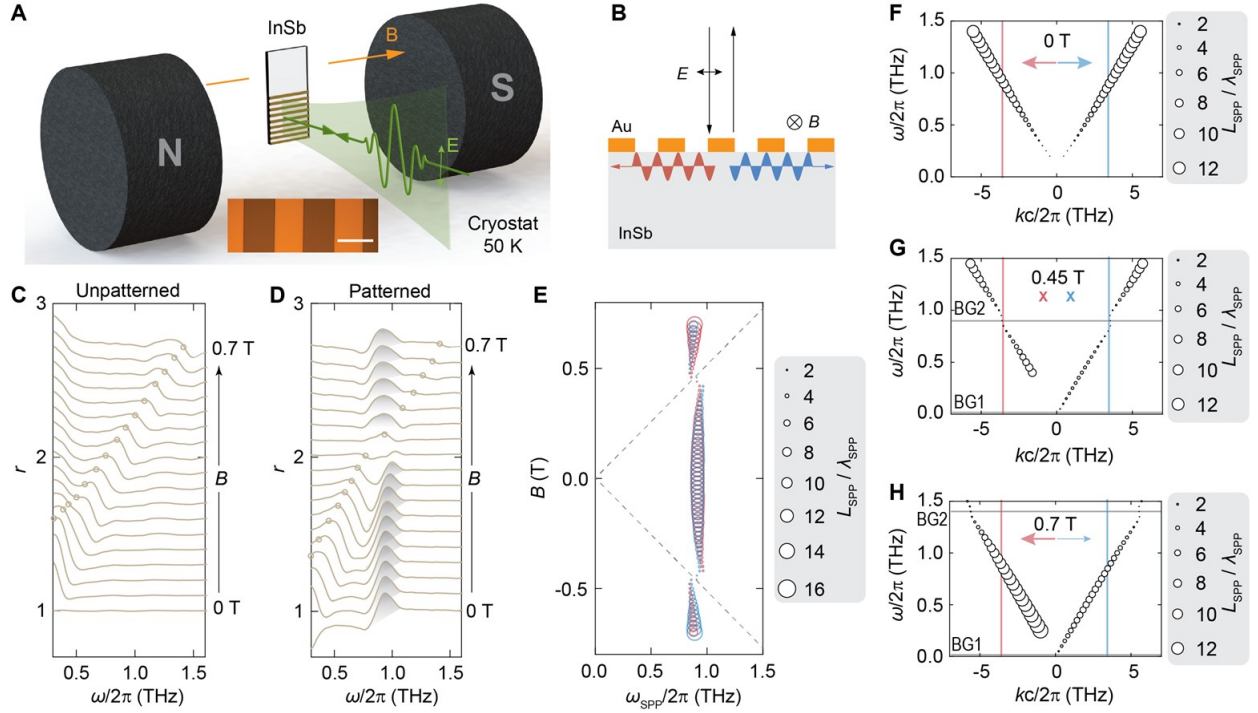


Figure 3.9: Surface magnetoplasmons generated at InSb/Au interface by normal incident light (A) Schematic of the measurement configuration. Inset shows the optical image of the Au grating (scale bar represents 50 μm). (B) Side view of the measurement geometry. (C, D) Field-dependent reflectance spectra obtained on the unpatterned half of the sample (C) and the patterned half (D) at 50 K. The cyclotron frequencies are marked by small circles, and the SPP peaks are highlighted in grey. (E) Calculated SPP resonance frequencies for different fields. Left-traveling SPPs are plotted using red bubbles and right-traveling SPPs are plotted with blue bubbles. The bubble size represents the SPP propagation lengths normalized by the wavelengths ($L_{\text{SPP}}/\lambda_{\text{SPP}}$). (F-H) SPP dispersions for three different magnetic fields. The red and blue lines show the grating resonance conditions for the left-traveling (red) and right-traveling (blue) SPPs under normal incidence. In G and H, the two field-induced bulk gaps are marked by grey shaded areas. Reprinted with permission from [3], and produced based on collected data by Cen's group following our designs and simulations.

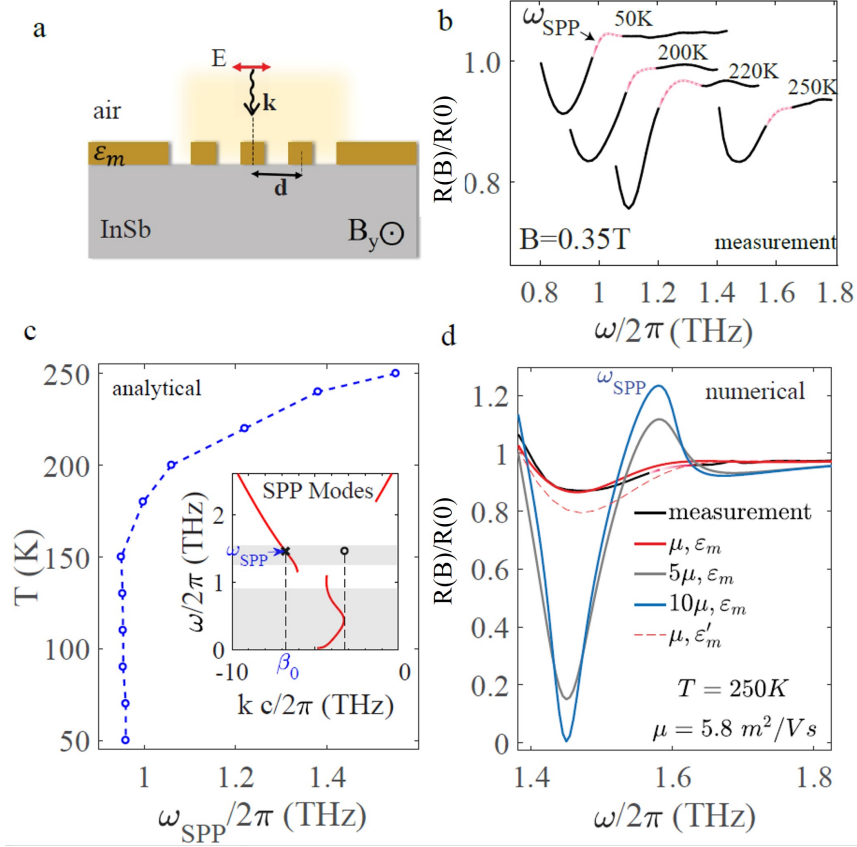


Figure 3.10: The far-field measurement of the unidirectional SPP at various temperatures. (a) The schematic geometry of the structure under test. (b) The reflection spectrum of the pattern InSb sample, measured at various temperatures. $R(B)$ and $R(0)$ are the reflectance of the biased/unbiased pattern sample, respectively. The red peaks are observed unidirectional SPP resonances. (c) The analytically estimated SPP resonance frequencies at different temperatures, obtained using the SPP dispersion diagram and the effective momentum $\beta_0 = 2\pi/d$ due to the symmetric grating as illustrated in the insert plot. (d) The reflection spectrum of the pattern InSb, results from a COMSOL simulation. Reprinted with permission from [2].

momentum matching and allow the excitation of SPPs from free-space light (Fig. 3.9A). In experiment, the magnetic field is kept parallel to the grating grooves and the incident polarization is perpendicular to the grooves. The SPPs launched need to satisfy the momentum conservation rule

$$k_{SPP} = \frac{\omega}{c} \sin(\theta) \pm \frac{2\pi}{d}, \quad (3.3)$$

where d is the grating constant and θ is the incident angle. Equation (3.3) traces out two parallel straight lines in the (k, ω) plane. The intersections of these two lines with the SPP dispersion curve determine the SPP modes that can be excited as depicted in Figs. 3.9F-H. Signatures of the SPPs are detected in a reflection geometry using the THz time-domain spectroscopy (THz-TDS) method. Figures 3.9C and 3.9D compare the 50 K THz reflectance ($r = E_{\text{reflection}}/E_{\text{incidence}}$) measured with a normal incidence ($\theta = 0$) on the two different halves of the same sample: one with a bare surface (Fig. 3.9C) and the other with an

Au grating structure on top (Fig. 3.9D). In this InSb sample, the electron mobility maximizes at 50K is $\mu = 22 \text{ m}^2/\text{Vs}$, where the carrier density $n = 1 \times 10^{22} \text{ m}^{-3}$ and the carrier scattering rate $\Gamma = e/\mu m^* = 5.7 \times 10^{11} \text{ s}^{-1}$ ($m^* = 0.014m_0$ is the effective electron mass) are relatively low, corresponding to an effective plasma frequency of $\omega_p^* = \omega_p/\sqrt{\epsilon_\infty} \approx 0.2 \text{ THz}$. On the unpatterned region, free-space light cannot directly couple to the SPPs, and the most noticeable feature observed is the field-induced reflectance modulations near $\omega_c = eB/m^*$ which blue-shift as the magnetic field increases (Fig. 3.9C). In comparison, the reflectance peaks associated with SPPs, as well as their anticrossing with the cyclotron resonances, are clearly visible in the data acquired on the region covered by Au grating (Fig. 3.9D).

At zero field, since SPP dispersion equation (3.1) and (3.3) are both symmetric in the k-space, a pair of SPP modes are simultaneously generated, which travel in opposite directions but have the same frequency and propagation length (Fig. 3.9F). This pair of SPPs are represented by a single peak in the reflectance spectrum (Fig. 3.9D). Applying a nonzero field, the SPP branches below ω_c are no longer k-symmetric (Figs. 3.9G and 3.9H). When $B = 0.45\text{T}$, ω_c overlaps with the SPP frequency and causes the SPP propagation in both directions to be significantly damped (Fig. 3.9G). When magnetic bias intensity further increases to 0.7T, a pair of SPP modes are again excited with approximately the same frequency, though the left-traveling wave has a substantially longer propagation length compared to the right-traveling one (Fig. 3.9H). Figure 3.9E plots the SPP resonance frequencies calculated for different field values, which are highly consistent with the experimental observations. In general, at 50 K, left-traveling and right-traveling SPPs excited by the normal incidence light are degenerate in energy. They are either generated in pairs or both suppressed when varying the magnetic field.

Figure 3.10b shows the ratio of $R(B)/R(0)$, where $R(B)$ and $R(0)$ are the measured reflectance of the biased/unbiased pattern sample, respectively, at various temperatures and fixed magnetic bias intensity. We found that this self-reference reflectance ratio is more robust comparing to $R(B)$, because in which the spurious signals due to for example positioning samples and environment humidity variation (which affects the light absorption) are eliminated. The schematic of the structure under test is shown in Fig. 3.10a, where the SPP is excited using a symmetric metal grating under normally incident plane wave. The period of grating is $d = 84\mu\text{m}$ the metal thickness is $t = 0.5\mu\text{m}$. In Fig. 3.10b, the red peaks indicate the SPP resonances of the biased sample. By applying $B=0.35\text{T}$, the SPP resonance frequencies are within or above the upper bandgap, depending on frequency. The period of the grating is $d = 84\mu\text{m}$ with the filling factor $1/2$, providing the effective momentum $\beta_0 = 2\pi/d$ for the system under a normally incident plane wave. Using the SPP dispersion diagram the SPP resonance frequency can be obtained at different temperatures as shown in Fig. 3.10c. The measured resonance frequencies are consistent with the values theoretically estimated. Figure 3.10d shows the reflection spectrum of the pattern InSb obtained using a COMSOL simulation. The InSb crystal is characterized by $n_e = 4.5 \times 10^{21} \text{ m}^{-3}$, $m^* = 0.0175m_0$, $\epsilon_\infty = 15.68$ and

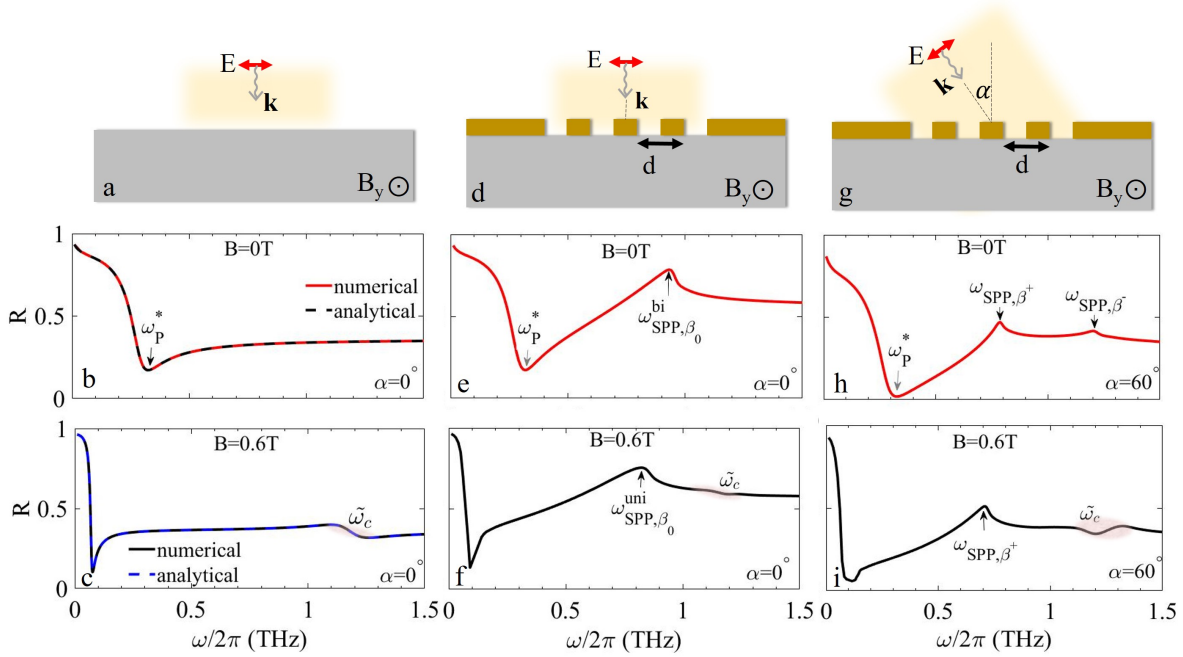


Figure 3.11: (a) a half-space plasma medium characterized by $n_e = 0.25 \times 10^{21} \text{ m}^{-3}$, $\mu = 22 \text{ m}^2/\text{Vs}$, $m^* = 0.015m_0$ and $\epsilon_\infty = 15.68$, under a normally incident plane wave. Reflectance spectrum of (b) an unbiased plasma and (c) a biased plasma ($B = 0.6\text{T}$) of bare sample. (d) A plasma medium covered by a metal sheet with a grating ($d = 84\mu\text{m}$ is the period of grating), where (e) and (f) show the reflectance spectrums for $B = 0$ and $B = 0.6\text{T}$, respectively. (g) A patterned plasma medium under an oblique plane wave with incident angle $\alpha = 60^\circ$. (h) Reflectance spectrum of g when (h) $B = 0$ and (i) $B = 0.6\text{T}$.

different mobility values. $\epsilon_m = -800 + i550$, $\epsilon'_m = (-2.3 + i8.6) \times 10^5$ and $B = 0.35\text{T}$. As an example, for $T = 250^\circ\text{K}$ and considering a realistic value of mobility ($\mu = 5.8\text{m}^2/\text{Vs}$) as shown the numerical result is well-matched with the measurement result. The reflectance corresponding to larger mobility has also been shown in Fig. 3.10d. If the mobility were higher, the SPP resonance becomes stronger; the red resonance peaks in Fig. 3.10b become larger.

Finally, in Fig. 3.10d simulation results for reflectance are shown for a metal grating having permittivity $\epsilon'_m = (-2.3 + i8.6) \times 10^5$, the standard Drude model (red-dashed curve). It can be seen that the THz-measured value [9] used in this work, $\epsilon_m = -800 + i550$, provides better agreement with measurement than the higher-permittivity model, leading to confidence in this lower value. We note that the two different metal permittivity values do not significantly change the resonance frequencies shown in Fig. 3.10c.

3.4.1 Verification of SPP Unidirectional Behavior by a Tilted Sample

So far, we excited and detected SPPs at the interface of biased InSb and metal by applying a metal grating under normally incident plane wave. In the following, we explain how to determine the unidirectional nature

of SPPs by comparing the reflectance spectrum of a bare sample under normally incident plane wave (Fig. 3.11a), a patterned sample with a grating under normally incident plane wave (Fig. 3.11d), and a patterned sample under an oblique incident plane wave (Fig. 3.11g).

Figures 3.11b and 3.11c show the reflectance of the unbiased and biased bare sample, respectively. The transparency of the plasma increases inside the plasmon band gap. $\omega_p^* = \omega_p / \sqrt{\epsilon_\infty}$ is the reduced plasma frequency, and $\tilde{\omega}_c$ denotes where the material response is magnetic field dependent. Figures 3.11e and 3.11f are the reflectance of unbiased and biased patterned sample under normally incident wave, respectively. SPPs with the effective momentum $\beta_0 = 2\pi/d$, where $d = 84\mu\text{m}$ is the period of grating, are excited. A new peak in R appears compared to the bare sample reflection spectrum, which corresponds to the SPP resonance. In the unbiased case, SPPs are bidirectional. The right- and left-going SPPs have the same resonance frequencies ($f = 0.94\text{THz}$). In the biased case, the peak denotes the unidirectional SPP resonance (with the resonance frequency $f = 0.83\text{THz}$).

When a normally incident wave is used, the SPP resonance peaks in R only indicate the existence of the surface wave, not their propagation direction. The unidirectional nature of the excited SPP can be ascertained by applying an oblique incident wave (Fig. 3.11g). In this case, the symmetric grating provides two different effective momentum for the right- and left- going SPPs (β^\pm obtained from Eq. (3.3)). For unbiased plasma, it is equivalent to two different SPP resonance frequencies $f^+ = 0.78\text{THz}$ and $f^- = 1.2\text{THz}$, such that two peaks appear in R (Fig. 3.11h), because the unbiased plasma allows SPP propagation in both directions. However, in the biased case, there is only one SPP resonance peak $f^+ = 0.71\text{THz}$ (see Fig. 3.11i); ideally, there is no resonance for the left-going SPP due to topological effect. Therefore, when an oblique incident wave is applied, based on the number of SPP resonance peaks in the reflectance spectrum we can determine whether SPPs are unidirectional or not. In the following, we experimentally examine the unidirectional nature of SPP using the above technique. However, because of some limits in our experimental set-up, instead of using an oblique incident wave, we equivalently used a tilted sample illuminated by a normal incident wave. As shown in Fig. 3.12A, mounting the sample next to a silver mirror and forming a normal angle between the two surfaces, a THz beam focused on the sample-mirror boundary hits the two surfaces consecutively with an angle and gets retro-reflected in the end. One complication associated with this setup is that the reflectance measured is a combined result of $\pm 45^\circ$ incidences: θ for the beam portion that hits the sample first is $+45^\circ$, whereas the other portion that gets reflected by the mirror first hits the sample surface with a -45° angle. The sample reflectances corresponding to the two incident angles are linked by symmetry. For simplicity, we first focus on the case of $+45^\circ$, and the other case of -45° can be directly inferred by the relation of $r(-\theta, B) = r(\theta, -B)$.

For $+45^\circ$, Eq. (3.3) results in two slanted lines in the (k, ω) plane that are no longer k -symmetric (solid lines, Figs. 3.12E–3.12G). Such asymmetry lifts the energy degeneracy between the SPPs excited in opposite

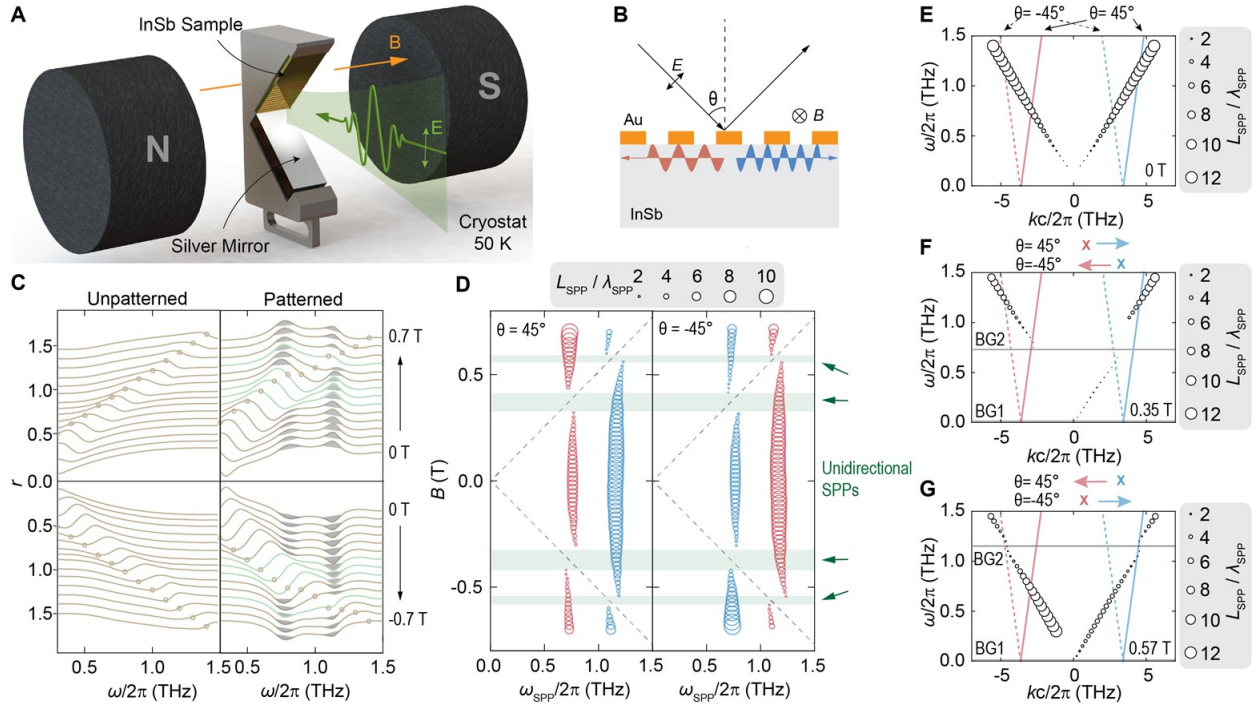


Figure 3.12: Unidirectional SPPs generated by light with a nonzero incidence angle. (A) Schematic of the measurement configuration. (B) Side view of the measurement geometry. (C) Field-dependent reflectance spectra measured on unpatterned and patterned sample halves at 50 K. Curves corresponding to unidirectional SPP excitations are highlighted in green. (D) SPP resonance frequencies calculated for the two incidence angles of $\pm 45^\circ$. The field ranges corresponding to unidirectional SPPs are marked in green. (E)–(G) SPP dispersions for three field values. Reprinted with permission from [3], and produced based on collected data by Cen’s group following our designs and simulations.

directions and thus allows them to be distinguished experimentally as shown by the two separate SPP peaks in Fig. 3.12C. As the external field varies, the cyclotron resonance intercepts with the left- and right-traveling SPP modes one at a time (Figs. 3.12C and 3.12D), allowing them to be manipulated individually. This effect produces multiple magnetic field windows in which the SPP launched is unidirectional (Fig. 3.12D, green shaded regions). Near $B = 0.35T$, the left-traveling mode is suppressed by the field, and only the right-traveling SPP is allowed at the interface (Fig. 3.12F). The situation is reversed near $B = 0.57T$, where only the left-traveling SPP is allowed (Fig. 3.12G). Comparing the SPP dispersions shown in Figs. 3.9G, 3.9H and Fig. 3.12G to the ideal lossless case shown in Fig. 3.2a, a big difference is that the SPP modes between the two bulk gaps are no longer unidirectional for magnetic fields larger than 0.4 T. Since the SPPs outside the bulk gaps are not topologically protected, their directionality is sensitive to the changes in symmetry-unrelated sample parameters. When the carrier density of InSb is low (e.g., at 50 K), the SPP dispersion between the bulk gaps is strongly affected by the surface quality of the Au film. In this work, a literature-reported Au film permittivity of $\varepsilon_m = -800 + i500$ obtained from SPP-based measurements [9,129] is found to be most consistent with our experimental observations. If the bulk permittivity value $\varepsilon_m^{Drude} = -2.3 \times 10^5 + i8.6 \times 10^5$ [130] can be realized at the surface of the Au films, the SPP dispersion at the interface will become much more similar to the ideal case as shown in Fig. 3.13.

Figures 3.14A, E, and I compare the normal-incidence reflectances measured at 50 K, 180 K ($n_e = 4.5 \times 10^{21} \text{m}^{-3}, \omega_p^* = 0.4 \text{THz}, \mu = 11 \text{m}^2/\text{Vs}$), and 250K ($n_e = 4.5 \times 10^{20} \text{m}^{-3}, \omega_p^* = 1.1 \text{THz}, \mu = 6 \text{m}^2/\text{Vs}$). Here, instead of extracting the absolute reflectance $R(B)$, which requires a reference sample to be repeatedly positioned to precisely match the different sample positions at varied temperatures, the reflectance data is processed in a self-referenced manner. That is, the raw reflectance signal detected at a nonzero field is divided by its zero-field value, $r(B)/r(0)$, which captures the field-induced reflectance change without the need for separate reference measurements. On bare InSb (Figs. 3.14A, E, and I, top), the most outstanding features of $r(B)/r(0)$ are a peak near ω_p^* and a plateau that broadens as B increases. The right edge of the plateau traces the bottom of the upper bulk band, which approximates ω_c when $\omega_p^* \ll \omega_c$. With the Au grating, the broadening of the plateau appears to be intercepted at the zero-field SPP frequency (Figs. 3.14A, E, and I, bottom), and the peak near the plateau edge indicates the SPP frequency under the influence of the nonzero field. The single SPP peak detected at $\theta = 0^\circ$ splits into two when θ changes to $\pm 45^\circ$ (Figs. 3.14B, F, and J)). At 50 K, the higher frequency peak represents the forward-propagating (as compared to the in-plane direction of the incidence light) modes generated by the $\pm 45^\circ$ incidences $\omega_{SPP}^{(f)}(\pm 45^\circ)$, and the lower frequency peak represents the counterpropagating modes $\omega_{SPP}^{(c)}(\pm 45^\circ)$ (Fig. 3.14C). At 180K and 250K, the two peaks come from the forward-traveling mode generated by the $+45^\circ$ incidence $\omega_{SPP}^{(f)}(+45^\circ)$ and the countertraveling mode generated by the -45° incidence $[\omega_{SPP}^{(f)}(-45^\circ)]$, both modes can only propagate toward the right (Figs. 3.14G and K). As shown in Figs. 3.14D, H, and L, the ω_p^* makes the bulk gaps

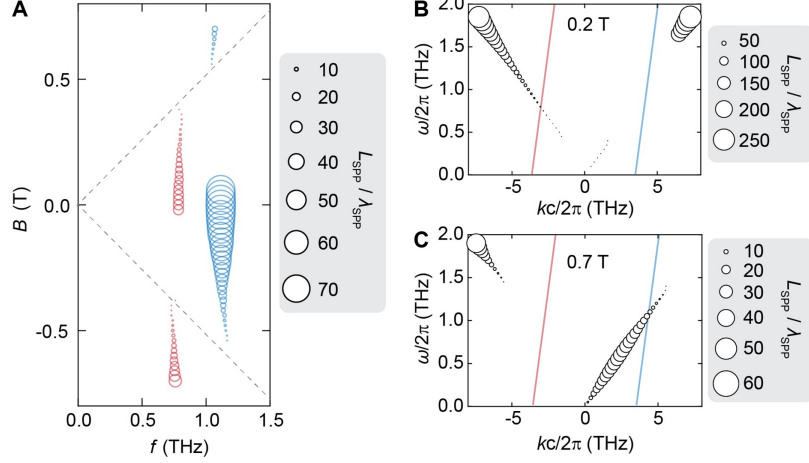
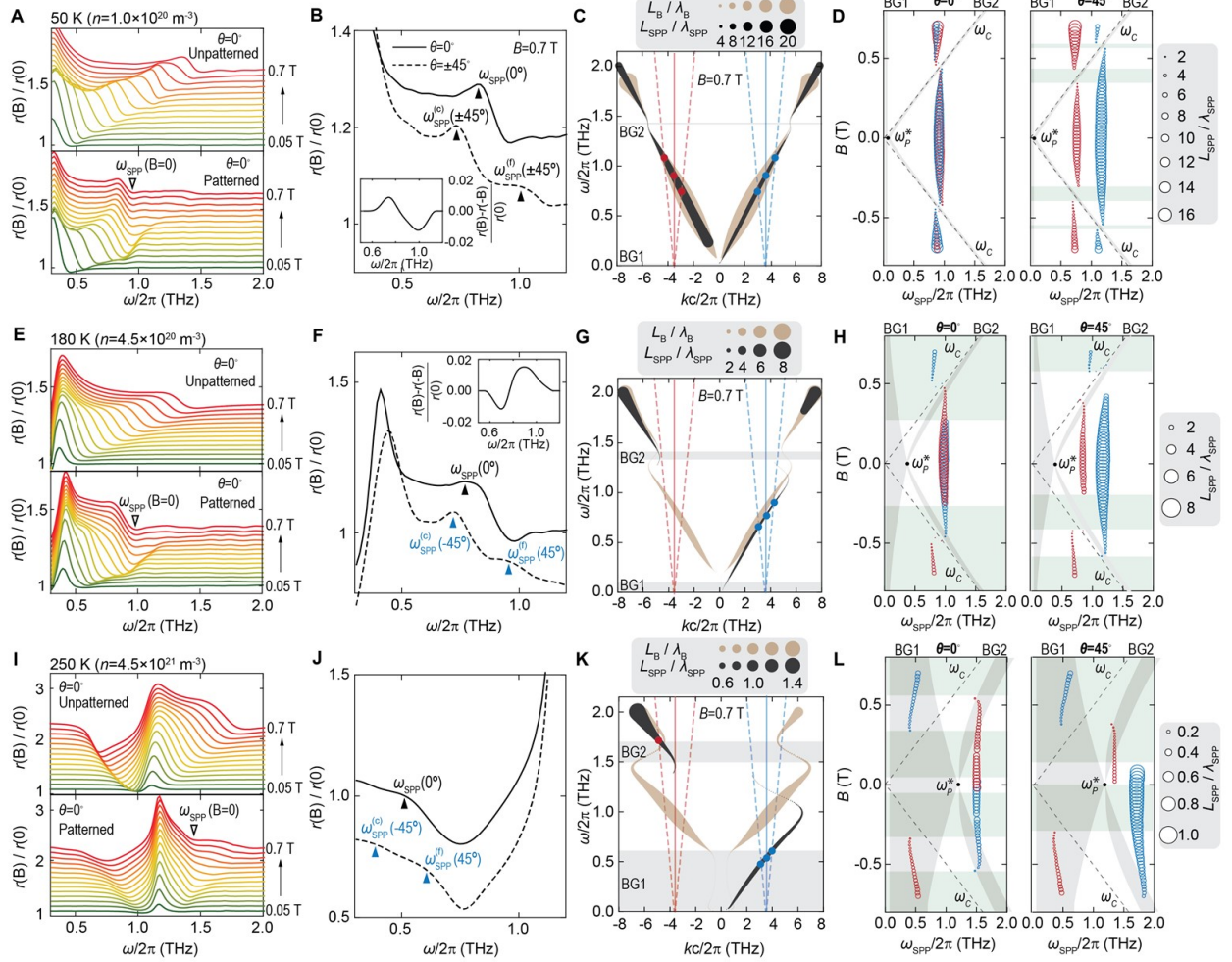


Figure 3.13: Calculated InSb/Au interfacial SPP properties at 50 K when using the Drude model-based Au permittivity value $\epsilon_m^{Drude} = -2.3 \times 10^5 + i8.6 \times 10^5$. (A) Field dependent SPP resonances for a 45 degree light incidence. (B, C) SPP dispersions for $B = 0.2$ T and $B = 0.7$ T, respectively. Reprinted with permission from supplement of [3], and produced by Cen's group.

(gray shaded areas) and the unidirectional magnetic field windows (green shaded areas) both more sizable at higher temperatures. As a result, it is much easier to generate topologically protected unidirectional SPPs at 250 K (modes in regions where the two shaded areas overlap). Nonetheless, due to the reduced electron mobility, the propagation lengths of these modes are short.

An important feature of the SPPs at the gyrotropic/isotropic interface is that they are nonreciprocal. Since the operation of $B \rightarrow -B$ mirrors the k -asymmetric SPP dispersion curve with respect to $k = 0$, for any single θ value, flipping the field orientation will lead to the excitation of different SPP modes. The $\theta = \pm 45^\circ$ dual incident angle setup weakens such effect significantly, but due to the nonperfect beam shape in the experiment and the weak imbalance between the two incidence angles, the nonreciprocal SPP excitations can still be detected. The insets of Figs. 3.14B and F plot the differences between the data measured at ± 0.7 T. The absolute value of the difference signal maximizes near the two SPP resonances, but the sign of the signal changes in between, indicating a spectral weight shift between the two modes as the field orientation flips. Notably, the sign of the difference signal also flips when raising the temperature from 50K to 180K. This observation is consistent with the different SPP asymmetry found at the two temperatures (Figs. 3.14C and G). At 50K, the $k < 0$ SPP branch below BG2 is stronger than the $k > 0$ branch in the sense that it has much longer propagation lengths. At 180 K, the $k > 0$ branch becomes the stronger one since the $k < 0$ branch is no longer present.



3.5 Summary

In this chapter, we studied the propagation properties of unidirectional SPPs in the Voigt configuration by considering ideal and realistic conditions. We evaluated the magneto-optical properties of InSb samples at various temperatures and magnetic field intensities and extracted the carrier parameters using measured reflectance data from the interface. We found that for very low temperatures, InSb is not a suitable platform for topological SPPs due to an extremely narrow bandgap, whereas for higher temperatures (say, above 250 K), the propagation length is not long enough due to low mobility. At temperatures between 150 K and 220 K, moderate bandgap width and $L_{SPP}/\lambda_{SPP} > 1$ are obtainable using undoped InSb. We have successfully excited and detected unidirectional SPPs at the interface of isotropic metal and gyrotropic interface. We determined that their properties are tunable by temperature and magnetic field intensity.

Chapter 4

Narrow-Beam Unidirectional SPP in Magnetized Semiconductor

In this chapter, we study the properties of unidirectional SPPs at the interfaces of a gyrotropic plasma slab and a dielectric below the plasma frequency. We mainly focus on unidirectional SPPs within a newly-discovered frequency region, wherein SPPs form two narrow beams. These beams are important for directional flow of energy on the surface of a plasmonic system. The angle of beams is dynamically controllable by magnetic field intensity.

We have identified a bulk bandgap common to all propagation directions of the plasma bulk modes, within which the SPPs exist. As discussed in Chapter 2, the upper bandgap for the perpendicular case and lower bandgap for the parallel case determine the common bandgap of all bulk modes. Here, we consider the SPP modes that cross these two common bandgaps and discuss their dispersion features at different frequency regimes in the common bandgaps. We present a Green function model for a finite thickness gyrotropic layer. Then, by applying the Sommerfeld integral model for infinite thickness, the field profile of the SPP waves propagating at the interface of the half-space magnetized plasma configuration is studied. Next, SPPs excited on the surfaces of the magnetized plasma slab with finite thickness are investigated to find the optimum thickness. Additionally, we investigate the back-scattering immune properties of a surface wave forming two narrow beams. Power flow, group velocity, and Poynting vector of the unidirectional SPPs are discussed. Also, a quasi static analysis is presented. From the results of this project, paper [5] has been published in the journal IEEE Transaction on Antennas and Propagation.

The geometry of interest in this chapter is depicted in Fig. 4.1, showing a finite-thickness gyrotropic slab of thickness h , immersed in a simple medium characterized by ε_r . The gyrotropic medium is assumed to be a plasma biased by a static external magnetic field $\mathbf{B}_0 = \hat{\mathbf{y}}B_0$. the magnetized plasma is characterized by the dielectric tensor $\bar{\varepsilon}_r = \varepsilon_t (\bar{\mathbf{I}} - \hat{\mathbf{y}}\hat{\mathbf{y}}) + i\varepsilon_g (\hat{\mathbf{y}} \times \bar{\mathbf{I}}) + \varepsilon_a \hat{\mathbf{y}}\hat{\mathbf{y}}$, where the permittivity elements are defined in (2.12-2.14). This permittivity model is representative of a common gas plasma and is a simplified model of solid state plasma like InSb [122]. It is also a local model. Since the effect of non-locality is evident only for very large wavenumbers, and the backward waves vanish when considering realistic levels of loss [82], non-locality is ignored here. Throughout this chapter, unless otherwise noted, we use the following values for the magnetized plasma: $\omega_p = 2\pi(20 \text{ THz})$, $\Gamma = 0.015\omega_p$ and $\omega_c/\omega_p = 0.4$. The cyclotron frequency is associated with $B_0 = 6.3 \text{ T}$ using the effective mass $m^* = 0.022m_e$, where m_e is the electron mass [122]. The wavenumber associated with a bulk mode propagating within the slab is denoted \mathbf{k}_b , and is represented in a local coordinate system where α_b denotes the angle that \mathbf{k}_b makes with respect to the y-axis. In the following, ρ refers to the radial distance in the $x - y$ plane.

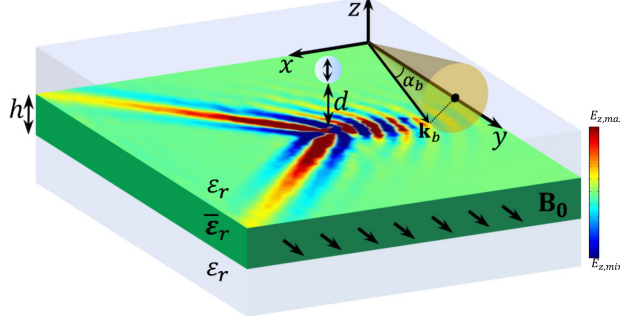


Figure 4.1: Slab of gyrotropic material with finite thickness h . The slab is biased with a static magnetic field along the y -axis. A vertical dipole is suspended a distance d above the slab and is responsible for exciting the displayed field pattern near the top surface of the slab. Reprinted with permission from [5].

4.1 Green Function for a Finite-thickness Plasma

In Ref. [86] a Green's function has been presented for a simple material-gyrotropic plasma interface. In this section, we expand that analysis to consider a finite-thickness gyrotropic layer. Using this model we obtained the electric field profile of unidirectional SPPs at the interfaces of a magnetized plasma slab. We present a closed-form expression (as a Sommerfeld integral) for the Green function in the simple dielectric regions above and below the slab. Importantly, we also provide the Green function coefficient in quotient form for each case, which leads to the identification of the SPP dispersion equation (setting the denominator to zero).

The procedure to derive the Green function follows that in [86, 131]. The incident field excited by an electric dipole source, with dipole moment $\mathbf{p} = \hat{\mathbf{x}}p_x + \hat{\mathbf{y}}p_y + \hat{\mathbf{z}}p_z$, suspended a distance d above the first interface, is given by $\mathbf{E}^p(\mathbf{r}) = (\nabla\nabla + \bar{\mathbf{I}}k_0^2\epsilon_r) \cdot \pi^p(\mathbf{r})$, where $\pi^p(\mathbf{r})$ denotes the principal Hertzian potential due to the dipole source, which we write in terms of the principal Green function, $\pi^p(\mathbf{r}) = g^p(\mathbf{r}, \mathbf{r}_0)\mathbf{p}/\epsilon_0\epsilon_r$, where $g^p(\mathbf{r}, \mathbf{r}_0) = e^{ik_0\sqrt{\epsilon_r}|\mathbf{r}-\mathbf{r}_0|}/4\pi|\mathbf{r}-\mathbf{r}_0|$ such that ϵ_r is the relative permittivity of the top and bottom media (see Fig. 4.1) and \mathbf{r}_0 denotes the source point location. Following [86], the reflected, and transmitted electric fields for a biased-plasma slab of finite thickness are written as Sommerfeld integrals

$$\mathbf{E}^r(\mathbf{r}) = \int d^2\mathbf{k}_s e^{i\mathbf{k}_s \cdot (\mathbf{r}-\mathbf{r}_0)} \frac{e^{-\gamma_0(d+z)}}{8\pi^2\epsilon_0\epsilon_r\gamma_0} \bar{\mathbf{C}}^r \cdot \mathbf{p}, \quad (4.1)$$

$$\mathbf{E}^t(\mathbf{r}) = \int d^2\mathbf{k}_s e^{i\mathbf{k}_s \cdot (\mathbf{r}-\mathbf{r}_0)} \frac{e^{-\gamma_0(d-z)}}{8\pi^2\epsilon_0\epsilon_r\gamma_0} \bar{\mathbf{C}}^t \cdot \mathbf{p}, \quad (4.2)$$

where $\bar{\mathbf{C}}^r$ and $\bar{\mathbf{C}}^t$ are tensors defined as

$$\bar{\mathbf{C}}^r = \left(\bar{\mathbf{I}}_s - \frac{\hat{\mathbf{z}}\mathbf{k}_s}{i\gamma_0} \right) \cdot \bar{\mathbf{R}} \cdot (k_0^2\epsilon_r\bar{\mathbf{I}}_s - \mathbf{k}_s\mathbf{k}_s + i\gamma_0\mathbf{k}_s\hat{\mathbf{z}}), \quad (4.3)$$

$$\bar{\mathbf{C}}^t = \left(\bar{\mathbf{I}}_s + \frac{\hat{\mathbf{z}}\mathbf{k}_s}{i\gamma_0} \right) \cdot \bar{\mathbf{T}} \cdot (k_0^2\epsilon_r\bar{\mathbf{I}}_s - \mathbf{k}_s\mathbf{k}_s + i\gamma_0\mathbf{k}_s\hat{\mathbf{z}}), \quad (4.4)$$

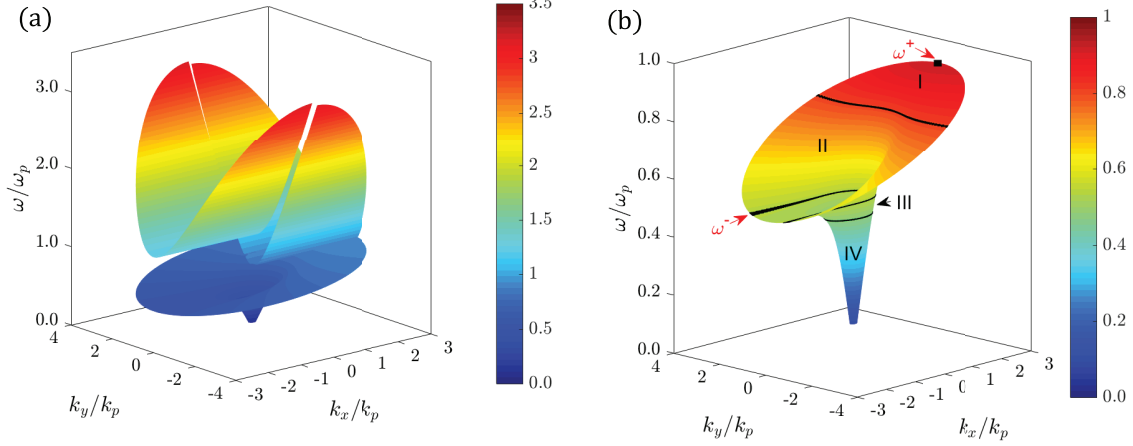


Figure 4.2: SPP dispersion surface for a biased-plasma-vacuum interface, obtained by solving for the roots of (2.86). (a) Perspective view of the upper and lower bands. (b) Close-up of the lower band, where the solid black lines are the equi-frequency contours for a few representative frequencies and ω^\pm outline the region of SPP resonance. The designations I-IV refer to Fig. 4.4. The common bulk-bandgap is in Regions II and III. Reprinted with permission from [5].

such that $\bar{\mathbf{I}}_s = \hat{\mathbf{x}}\hat{\mathbf{x}} + \hat{\mathbf{y}}\hat{\mathbf{y}}$ and $\gamma_0 = \sqrt{k_x^2 + k_y^2 - k_0^2 \epsilon_r}$. $\bar{\mathbf{R}}$ and $\bar{\mathbf{T}}$ matrices are the reflection and transmission tensors, respectively, for the biased-plasma slab, which have been derived and defined in Ref. [5]-Appendix. Taking into account that the scattered magnetic field is $\mathbf{H}(\mathbf{k}_s, z) = \mathbf{k}_0 \times \mathbf{E}(\mathbf{k}_s, z)/\omega\mu_0$, the Poynting vector can be obtained using $\langle \mathbf{S} \rangle = \text{Re}(\mathbf{E} \times \mathbf{H}^*)/2$.

In all of the numerical examples to follow, we consider the z component of the scattered electric field due to a z directed dipole moment, $\mathbf{p} = \hat{\mathbf{z}}p_z$, placed at a height d above a symmetric slab of thickness h for which $\epsilon_r = 1$ and $\mathbf{r}_0 = (0, 0, d)$. In this case, the z component of the scattered field simplifies to

$$E_z^r(\mathbf{r}) = \int d^2\mathbf{k}_s e^{i\mathbf{k}_s \cdot \mathbf{r}} \frac{e^{-\gamma_0(d+z)}}{8\pi^2 \epsilon_0 \gamma_0} C_{zz}^r p_z, \quad (4.5)$$

$$E_z^t(\mathbf{r}) = \int d^2\mathbf{k}_s e^{i\mathbf{k}_s \cdot \mathbf{r}} \frac{e^{-\gamma_0(d-z)}}{8\pi^2 \epsilon_0 \gamma_0} C_{zz}^t p_z. \quad (4.6)$$

4.2 SPP Propagation Properties Below the Plasma Frequency

A surface mode propagating in the x - y plane generally possesses two wavevector components, k_x and k_y . Therefore, a three-dimensional surface is needed to completely describe the SPP dispersion. The SPP dispersion equation, Eq. (2.86) was derived in Chapter 2, Section (2.6). We search the roots of the SPP dispersion equation by varying k_x and k_y when the top region is air ($\epsilon_r = 1$).

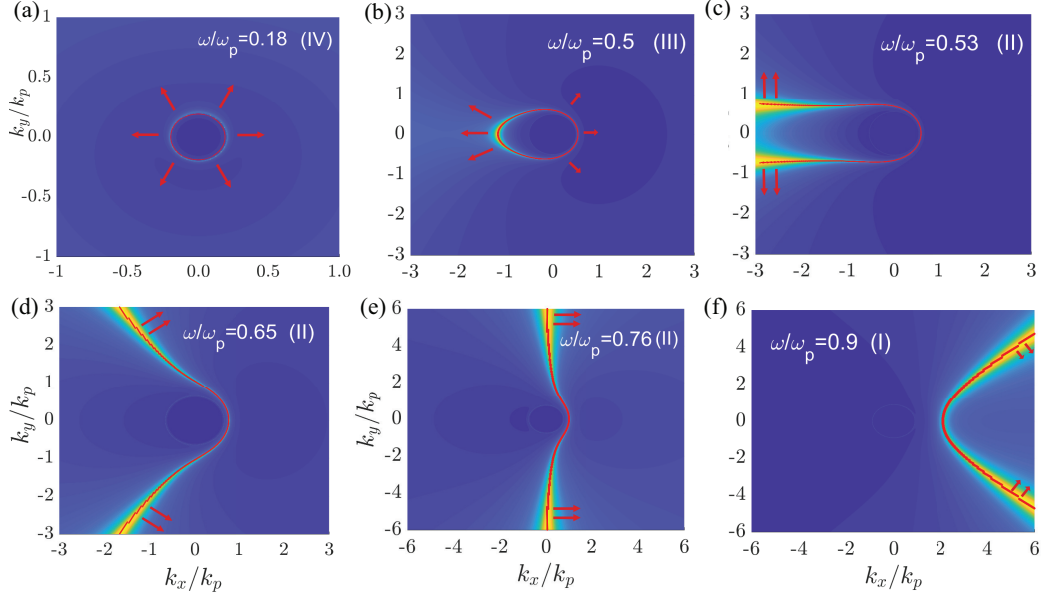


Figure 4.3: Density plot of the scattered field integrand in Eq. (4.5), and equi-frequency contours (solid red), which correspond to the intersection of the surface dispersion shown in Fig. 4.2b and an ω -constant plane, for a half-space biased-plasma medium at different frequencies. The notation I-IV refers to the regions shown in Fig. 4.4. Red arrows indicate the group velocity vectors. Reprinted with permission from [5].

As shown in Fig. 4.2, the SPP modes form two frequency bands. The upper band passes through the upper bulk bandgap, and the lower band passes through the lower bulk bandgap. In the case of a magnetized plasma-opaque material (such as metal as the upper region), the upper band of SPP modes are topological, unidirectional, and back-scattering immune SPPs which have been well studied in [36, 38, 39]. For the case that the magnetized plasma is covered by a transparent medium as considered here, the upper band represents fast surface waves (leaky waves); only the real part of the frequency is shown in Fig. 4.2(a). These surface waves leak rapidly into the transparent medium. However, the lower band is the main interest here, and dispersion in this lower band leads to beam-like SPPs, which have only recently been considered [80, 86, 87]. The SPP dispersion surface of lower band looks like an asymmetric hyperbolic funnel, which represent the nonreciprocal propagation behavior. In this chapter, we investigate the propagation properties of SPPs in the lower band in detail.

Figure 4.3 shows several equi-frequency contours (EFC) of the dispersion surface at different frequencies (red lines). The colorful background in Fig. 4.3 are density plots of the scattered field integrand in relation (4.5), in which $h \rightarrow \infty$ (single interface configuration).

The phase and group velocities of an SPP are calculated as $\mathbf{v}_p = \hat{\mathbf{k}}_s \omega / |\mathbf{k}_s|$ and

$$\mathbf{v}_g = \nabla_{\mathbf{k}_s} \omega(\mathbf{k}_s) = \hat{\mathbf{x}} \frac{\partial \omega}{\partial k_x} + \hat{\mathbf{y}} \frac{\partial \omega}{\partial k_y}, \quad (4.7)$$

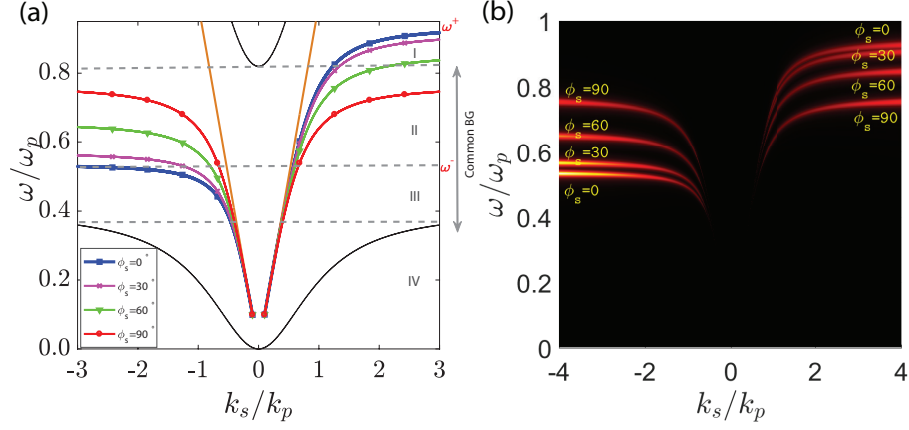


Figure 4.4: (a) Two dimensional dispersion of the SPP for different propagation angles, ϕ_s , with respect to the positive (negative) x-axis for right (left) branches of the dispersion. The bulk dispersion (solid black lines) for $\alpha_b = 0^\circ$ indicate the lower bulk bandgap common to all propagation angles. The solid orange lines show the dispersion of light in vacuum, e.g., $\omega/\omega_p = \pm k_s/k_p$. (b) Density plot of the scattered field integrand in Eq. (4.5) in the $\omega - k_s$ plane. The bright parts correspond to the flat parts of the 2D dispersion curves in part (a), representing the dominant contribution to the narrow beams. Reprinted with permission from [5].

respectively. In the lossless case, the group velocity represents the directional flow of electromagnetic energy. It is orthogonal to the equi-frequency contours. The group velocity vectors are shown in Fig. 4.3 by red arrows. According to Fig. 4.3a, the EFCs at low frequencies are nearly circular, and the group velocity vectors show that energy flows isotropically. Hence, the resulting field pattern is essentially omni-directional. As frequency increases, the EFC contour is elliptic-like (Fig. 4.3b) and the energy begins to flow asymmetrically. At the opening of the hyperbolic dispersion funnel, starting from $\omega = 0.53\omega_p$ frequency, the EFC becomes hyperbolic-like with the arms of the curve widening as frequency increases (Fig. 4.3c-e), and then flipping direction (Fig. 4.3f). The hyperbolic-like EFC of the lower SPP band indicates narrow SPP beams formation. Because in this case the group velocity vectors dominantly show that the energy intensely flows on the surface in two specific directions. It is where the narrow beams are formed (e.g., Fig. 4.3, Panels c-f). However, we found that the group velocity of these beams is a small fraction of the speed of wave in vacuum (less than $0.05c$, where c is the speed of light), representing very slow surface waves. The near-flat dispersion in Fig. 4.4, also reveals this fact as discussed later.

Several two dimensional traces of the SPP dispersion surface shown in Fig. 4.2b at different propagation angles are shown in Fig. 4.4a. In this 2D line graph, each branch of the SPP dispersion converges to $\omega_{\mathbf{k}_s} = \frac{1}{2}\omega_c \cos \phi_s + \frac{1}{2}\sqrt{2\omega_p^2 + \omega_c^2 (1 + \sin^2 \phi_s)}$, in the limit $k_s = |\mathbf{k}_s| \rightarrow \infty$, as derived later using the quasi-static approximation for the plasma half-space. The maximum and minimum quasi-static resonance, $\omega^\pm = \omega_k(\phi_s = 0, \phi_s = 180^\circ)$, indicated in Figs. 4.2b and 4.4a, correspond to an SPP mode which propagates perpendicular to the bias. In Fig. 4.4a, the bulk dispersion for $\alpha_b = 0^\circ$ is shown by black lines to demonstrate the common bulk-bandgap that the SPPs in the lower-SPP-band cross.

This 2D dispersion diagram is divided into four frequency regions: in Regions I and IV, there is no common bulk bandgap, whereas in Regions II and III, there exists a common bulk bandgap. In Region II, where the EFC is hyperbolic-like (see Fig. 4.3c-f), we estimate directional propagation such that the SPP field pattern form two narrow beams which are symmetric with respect to the x -axis, and since $\omega(-\mathbf{k}_s) \neq \omega(\mathbf{k}_s)$, unidirectional behavior is also possible, making this frequency regime of central interest. Although in Region III there still exists a common bulk bandgap, narrow beams do not form in the SPP field pattern due to the fact that the EFC is ellipsoidal (see Fig. 4.3b). In Region IV, the dispersion diagram is almost symmetric and it is where the EFC is nearly circular (Fig. 4.3a), indicating that the SPP field pattern is approximately omni-directional.

Similar to Fig. 4.3, the density plot of the scattered electric field integrand in Eq. (4.5) is shown in Fig. 4.4b for different SPP angles. The brightest parts correspond to the flat parts of the dispersion curve in Fig. 4.4a. This means that for a given frequency in region (II), the flat part coincident with the $\omega = \text{constant}$ line has the most contribution in forming the narrow beams discussed, and gives insight into the group velocity of beam.

4.3 SPP Field Profile at the Interface of a Half-space Gyrotropic Medium

Considering a half-space gyrotropic medium, a vertical dipole source at $(\rho, z) = (0, 0)$ excites SPPs at the interface. To obtain the electric field distribution of SPP waves due to the vertical dipole source, we apply Sommerfeld integral (4.5) for $h \rightarrow \infty$, derived in Section (4.1) as well as finite element modeling using COMSOL. The scattered fields near the interface for several frequencies that lie in the four regions shown in Fig. 4.4 and for radial distance $\rho = 0.7\lambda$, height $z = 0.016\lambda_p$, and $0 < \varphi < 2\pi$, calculated using the Sommerfeld integral, is shown as the polar patterns in Fig. 4.5b,d,f. The electric field distribution at the x - y plane obtained in COMSOL are also shown in Fig. 4.5a,c,e, and agree with the Green function analysis. As shown in Fig. 4.5a,b, the expected behavior of surface wave propagation for operating frequencies that lie in Region IV of the dispersion (see Figs. 4.2 and 4.4), is nearly omnidirectional. In Region III, propagation is bi-directional, with the SPP intensity concentrated to one half plane, as shown in Fig. 4.5c,d. As frequencies change from lying in Region IV to Regions II and I of Fig. 4.4, the SPP increasingly tends toward being unidirectional. Interestingly, for frequencies that satisfy the SPP resonant condition, $\omega^- < \omega < \omega^+$ (Regions I and II), Fig. 4.5e,f, show that narrow-beam directional propagation is obtained, consistent with the previous discussion of equi-frequency contours. As shown in the polar pattern of Fig. 4.5f, at $\omega = \omega^- = 0.53\omega_p$, the field pattern forms two narrow beams which approach each other as the operating frequency increases. Eventually, the two beams join to form a single beam at $\omega = 0.76\omega_p$, corresponding to the saturation

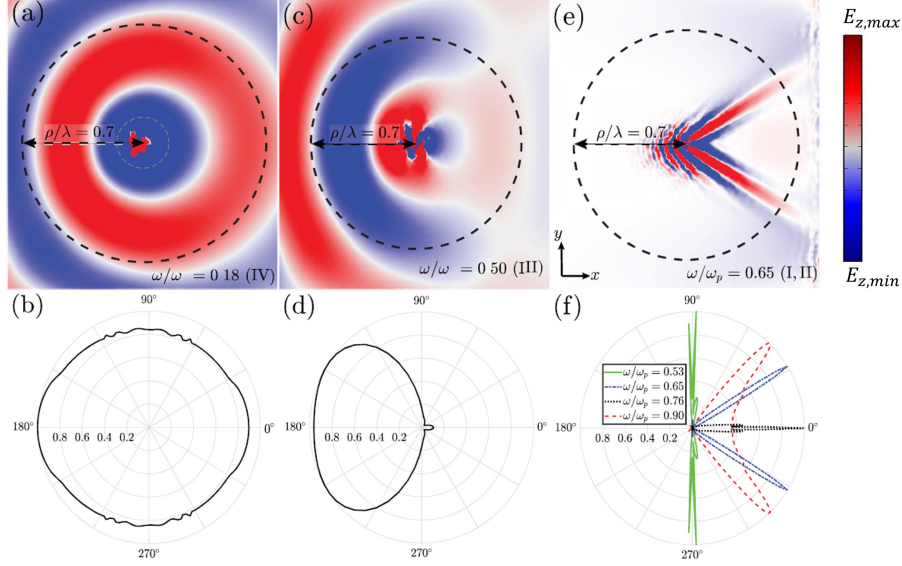


Figure 4.5: Top panels: polar patterns of the scattered electric field, $|E_z^r|$, obtained from the Green function for a magnetized plasma-vacuum interface, $(\rho, z, \varphi) = (0.7\lambda, 0.016\lambda_p, 0 < \varphi < 2\pi)$, and $\Gamma = 0.015\omega_p$. The panel dimensions are $2\lambda \times 2\lambda$. Bottom panels: the electric field distribution in the x-y plane generated using COMSOL. The dashed circle of radius $\rho = 0.7\lambda$ indicates the spatial contour over which the Green function results in the bottom panels are shown. Panel (f) shows results for several values of frequency, whereas the corresponding panel (e) is for one of the frequencies in Panel (f). λ is free space wavelength and $\lambda_p = 2\pi c/\omega_p$. Reprinted with permission from [5].

frequency of the $\phi_s = 90^\circ$ branch in Fig. 4.4, and then split to form two beams for $0.76\omega_p < \omega < \omega^+$. Therefore, the angle of the beams with respect to the x -axis is adjustable with frequency as well as the magnetic bias. Furthermore, if the direction of the magnetic bias is flipped, the beams propagate in the opposite direction.

In what follows, we particularly consider SPPs properties in the resonance frequency range, $\omega^- < \omega < \omega^+$ where there are two narrow beams in the field pattern. We chose $\omega = 0.65\omega_p$, a frequency within the resonance frequency range as an example to discuss the results. At this specific frequency, there are two beams with angles $\varphi_{beam1,2} = \pm 32^\circ$ with respect to the x -axis.

We should note that in the general lossy case, the group velocity is ill-defined as an energy-transport velocity, and one should examine the Poynting vector and energy transport velocity. In this work, we incorporate realistic material loss, but the results do not qualitatively change in the lossless case, in which case the meaning of the group velocity is very clear: it is S_{avg}/W_{stored} , where S_{avg} is the vertically-averaged Poynting vector associated with the mode and W_{stored} is the vertically-averaged stored energy density. Here, we consider the group velocity as the energy transport velocity merely in the sense of the beam angle, although for quantitative values of the magnitude of the energy velocity, one should examine the Poynting vector, as discussed next.

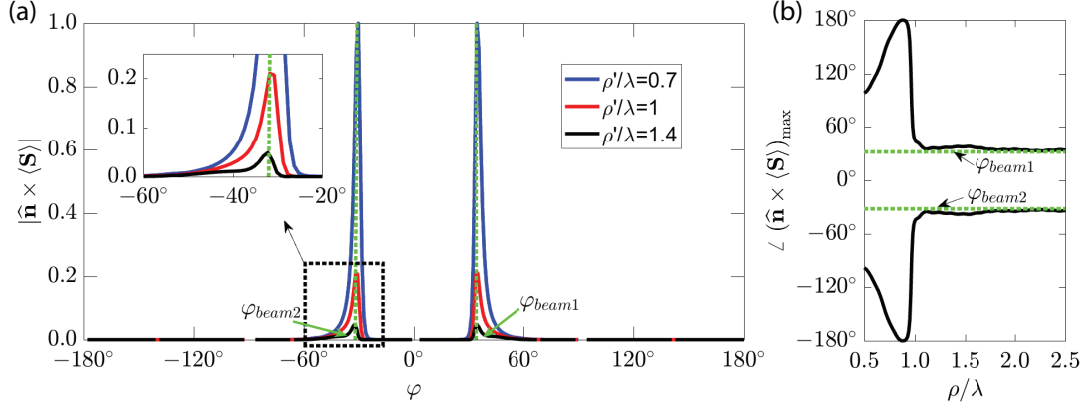


Figure 4.6: Poynting vector: (a) absolute value of tangential Poynting vector for observation points on circles with different radii, $(\rho, z, \varphi) = (\rho', 0.016\lambda_p, -\pi < \varphi < \pi)$ (b) direction of maximum Poynting vector for observation points along the two main narrow beams, $(\rho, z, \varphi) = (\rho, 0.016\lambda_p, \varphi_{beam1,2} = \pm 32^\circ)$. \hat{n} is the unit normal vector to the interface. The dashed lines show the beam angles, and it is seen that the Poynting vector becomes aligned with the beam angle, as expected, for observation points not too close to the source. The operating and collision frequency are $\omega = 0.65\omega_p$ and $\Gamma = 0.015\omega_p$, respectively. Reprinted with permission from [5].

The tangential Poynting vector indicates the power carried by the surface waves. The magnitude of the tangential Poynting vector at $\omega = 0.65\omega_p$ for a set of observation points on different circular contours in space having different radii is shown in Fig. 4.6a. For each radial distance there are two peak values which occur exactly at the position of the narrow beams, $\varphi_{beam1,2}$. Then, to find the direction of the maximum radiation power, the angle of the Poynting vector for points located along the beams is extracted (see Fig. 4.6b). As shown, the Poynting vector angle converges to the beam angles for large radial distance, i.e. in the far-field of the source. The Poynting vector and group velocity are in the same direction, pointing along the beam angle.

The SPPs within the resonant range are robust to the presence of discontinuities. To have an indication

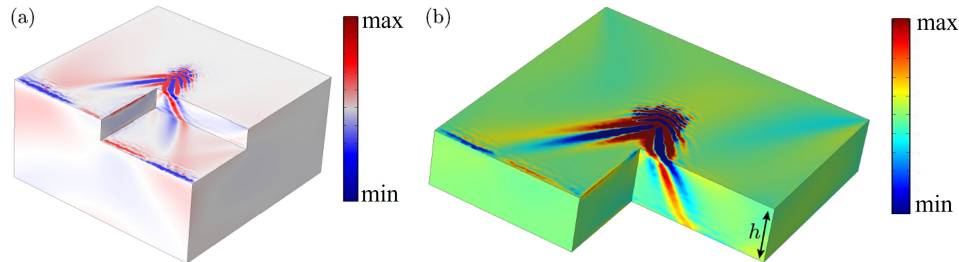


Figure 4.7: a. Electric field distribution (E_z) computed using COMSOL at the interface of a half-space gyrotropic plasma in the presence of a hole discontinuity. b. The same as (a), but at the interface of a finite thickness slab ($h = 0.12\lambda_p$) in the presence of a discontinuity; the SPP, excited on the top interface by a point dipole, propagates around the open surface to the bottom side of the plasma. $\Gamma = 0.04\omega_p$. Reprinted with permission from [5].

of the inherent robustness of these SPPs, a discontinuity in the form of a hole/block is constructed in an attempt to impede the SPP. A unidirectional SPP that crosses a band gap in reciprocal space is immune to the effects of back-scattering and diffraction. To illustrate this, Fig. 4.7a shows the electric field due to a electric point source near the vacuum-plasma interface of a plasma half-space. The SPP passes through the discontinuity without reflection or diffraction.

4.3.1 SPP Field Profile on the Surfaces of a Magnetized Plasma Slab

For a finite thickness slab, we consider the excitation of SPPs at the first interface ($z = 0$) and the bottom interface ($z = -h$) due to a vertical dipole source positioned at the first interface ($d = 0$). Similar to single-interface configuration, the SPPs propagating on the surfaces of the plasma slab are robust to discontinuities. As shown in Fig. 4.7b, upon encountering the end of the plasma, SPPs pass onto the bottom surface without reflection or diffraction. In Figs. 4.5 and 4.7, to obtain convergence in COMSOL the material loss had to be increased, and values $0.015\omega_p < \Gamma \leq 0.06\omega_p$ were used, although it is important to note that the value of loss does not affect the beam direction.

Figure 4.8(a-e) shows how the beams at the upper interface evolve with slab thickness for a set observation point $(\rho, z, \varphi) = (0.5\lambda, 0.03\lambda, 0 < \varphi < 2\pi)$ and thickness values that fall within the range $0 < h < 0.3\lambda_p$. The frequency of operation is set within the bulk bandgap of the plasma, $\omega = 0.65\omega_p$, and the collision frequency is set to $\Gamma = 0.015\omega_p$. The values of thickness considered in Fig. 4.8(a-d) are (a) $h = 0.3\lambda_p$, (b) $h = 0.1\lambda_p$, (c) $h = 0.07\lambda_p$, and (d) $h = 0.045\lambda_p$. Each pattern is normalized with respect to the beam maximum obtained for a thick slab, $|E_z^r|_{\max} = 5 \times 10^{14}$ V/m, in the limit $h \rightarrow \infty$, assuming the magnitude of the electric current dipole is $J_0 = 1$ A·m, where $J_0 = -j\omega p_z$ and p_z is the electric dipole moment. In Fig. 4.8e it is shown that the beam maximum grows logistically with thickness and asymptotically approaches the thick slab ($h \rightarrow \infty$) result as thickness increases. Using this curve, we can obtain the optimal thickness within which the surface wave energy does not couple from the upper interface to the lower interface.

When the slab becomes thin enough, it is also possible that a source on the upper interface excites SPPs on the bottom interface. The two bottom-surface SPP beams are in the opposite direction of the SPP beams on the top interface. Figure 4.9a,b shows the squared amplitude of the electric field at the bottom interface ($z = -h$) and top interface ($z = 0$), obtained using the FEM method in COMSOL, while Fig. 4.9c,d shows the squared amplitude of the transmitted and reflected field obtained by evaluating (4.6) and (4.5) respectively, for a small distance below and above the slab. For a thin slab, there are two forward beams on the top interface and two backward beams on the bottom interface.

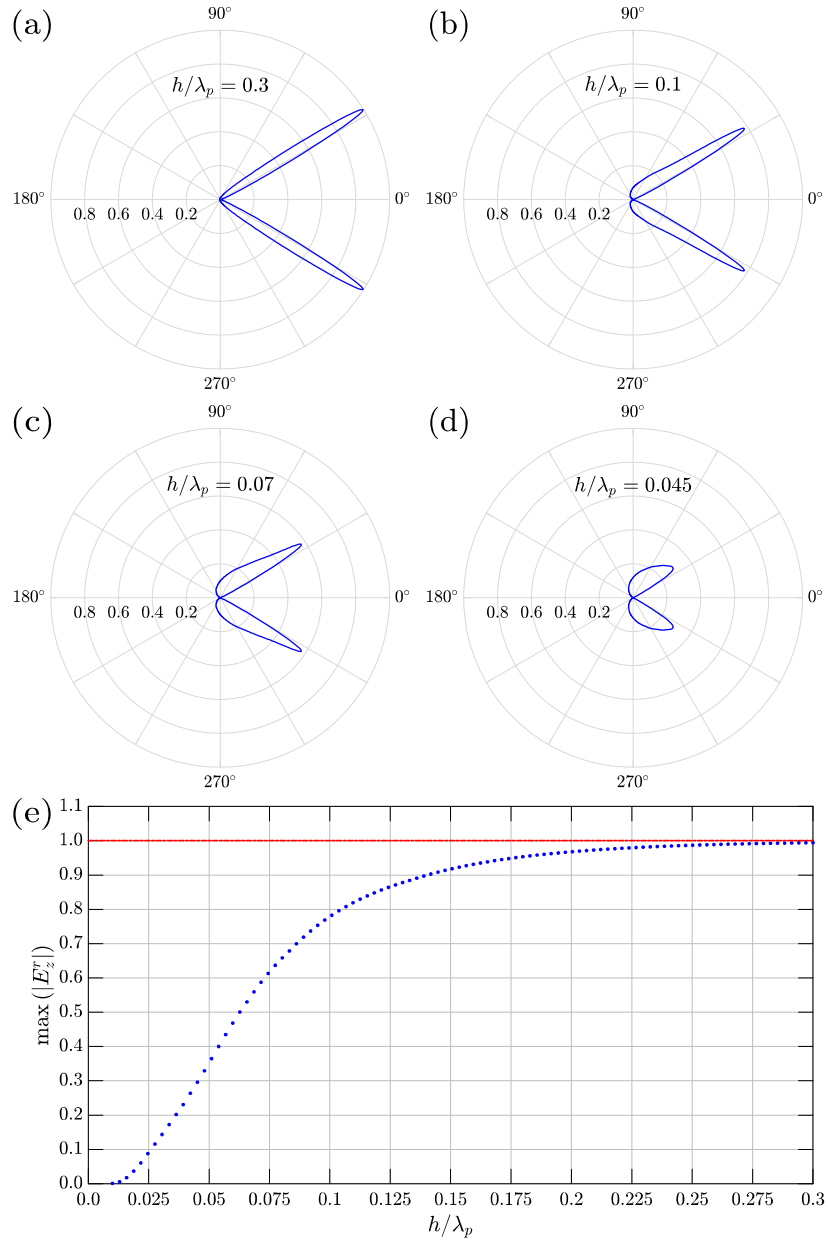


Figure 4.8: SPP beam pattern excited by a vertical dipole source at the first interface of a finite thickness biased-plasma slab, obtained by evaluating integral (4.5) for set observation point $(\rho, z, \varphi) = (0.5\lambda, 0.03\lambda, 0 < \varphi < 2\pi)$ where λ denotes the free space wavelength. The frequency of operation is set within the bulk bandgap of the plasma $\omega = 0.65\omega_p$ and the collision frequency is set to $\Gamma = 0.015\omega_p$. Four values of thickness are considered such that (a) $h = 0.3\lambda_p$, (b) $h = 0.1\lambda_p$, (c) $h = 0.07\lambda_p$, and (d) $h = 0.045\lambda_p$. Panel (e) shows how the beam grows logarithmically as thickness increases. Reprinted with permission from [5], generated by coauthor A. Holmes.

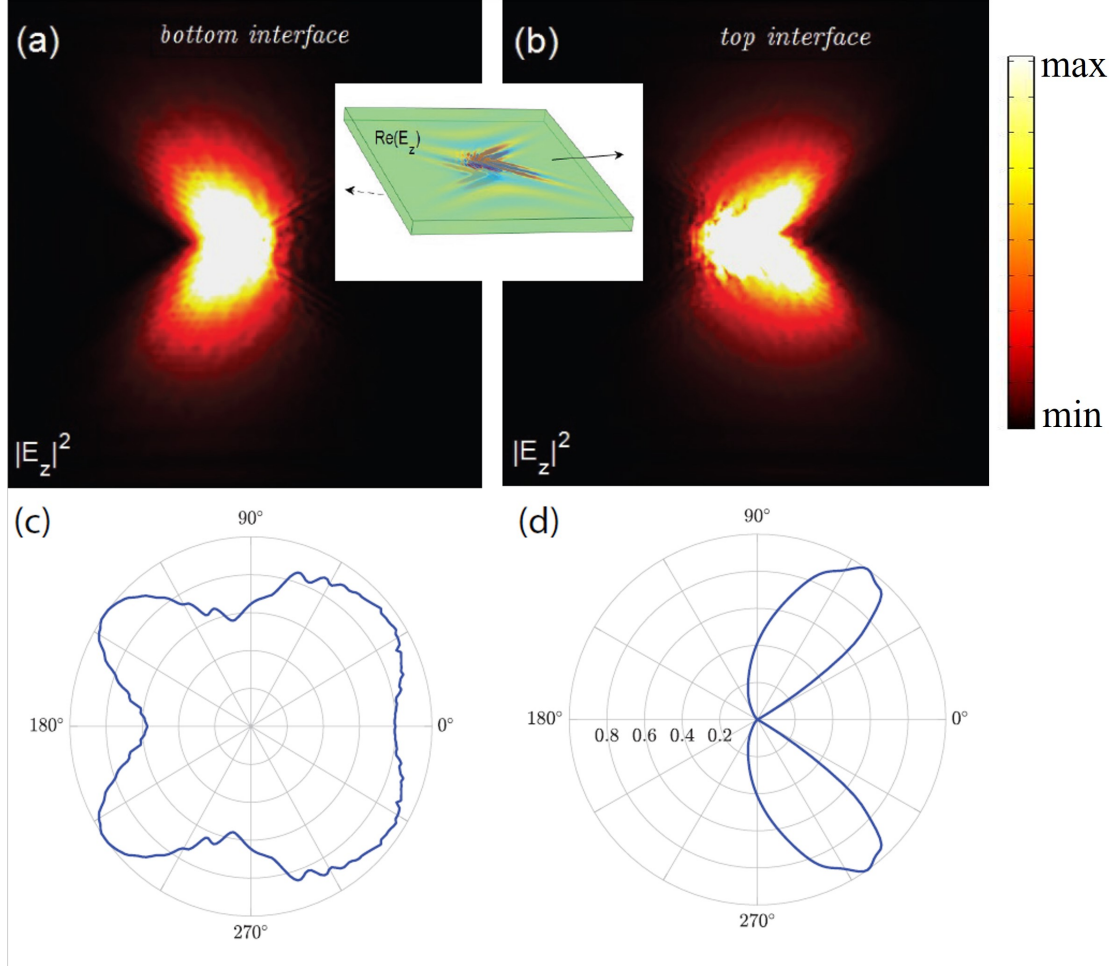


Figure 4.9: Squared amplitude of the scattered electric field profile (z component) excited by a vertical dipole source located at the first interface ($d = 0$) of a thin finite thickness biased-plasma slab of thickness $h = 0.04\lambda_p$. The squared amplitudes of the scattered electric field below and above the slab are obtained in (a)-(b) using the FEM in COMSOL ($\Gamma = 0.05\omega_p$) and in (c)-(d) by evaluating the Sommerfeld integrals in (4.5)-(4.6). In (c) the observation point is chosen to be $z = -h - 0.1\lambda$, $\rho = 0.9\lambda$ and $0 < \varphi < 2\pi$, and in (d) the observation point is chosen to be $z = 0.03\lambda$, $\rho = 0.5\lambda$, and $0 < \varphi < 2\pi$, and $\Gamma = 0.015\omega_p$. The operating frequency is $\omega = 0.65\omega_p$. Reprinted with permission from [5], (c-d) plots generated by coauthor A. Holmes.

4.4 Quasi-Static Approximation

Further insight into the SPPs excited on the surfaces of the magnetized-plasma slab can be gained by a quasi static approximation, where the electric field is written in terms of the electro-static potential, ϕ_k , such that $E_k \approx -\nabla\phi_k$, assuming the associated magnetic field is negligible. Solving Gauss' law in both isotropic and gyrotropic media, and applying boundary conditions for the tangential components of the electric field at each interface, the electric potential for a slab shown in Fig. 4.1 is obtained as $\phi_k = CF(z)e^{i\mathbf{k}_s \cdot \mathbf{r}}$ where C is an amplitude constant and

$$F = \begin{cases} e^{-k_s z} & z > 0 \\ \cosh \tilde{k}_s z + i\alpha \sinh \tilde{k}_s z & -h < z < 0, \\ \left(\cosh \tilde{k}_s h - i\alpha \sinh \tilde{k}_s h \right) e^{k_s(z+h)} & z < -h \end{cases} \quad (4.8)$$

such that $k_s = \sqrt{k_x^2 + k_y^2}$, $\tilde{k}_s = \sqrt{k_x^2 + \varepsilon_a k_y^2 / \varepsilon_t}$, and α is a complicated function of material parameters and wavenumbers (omitted since it is not needed in the following). Enforcing continuity of the normal components of electric displacement at the two interfaces leads to the quasi-static SPP dispersion relation

$$\varepsilon_g^2 k_x^2 - \varepsilon_t^2 \tilde{k}_s^2 - \varepsilon_r^2 k_s^2 = 2\varepsilon_r \varepsilon_t k_s \tilde{k}_s \coth \tilde{k}_s h. \quad (4.9)$$

The quasi-static approximation is valid only for SPPs with short wavelength ($k_s \rightarrow \infty$). In the limit $h \rightarrow \infty$, the dispersion relation reduces to that derived for a single interface [86],

$$\varepsilon_r k_s + k_x \varepsilon_g + \tilde{k}_s \varepsilon_t = 0. \quad (4.10)$$

By substituting the dispersive permittivity elements (2.13-2.14), $k_x = k_s \cos \phi_s$ and $k_y = k_s \sin \phi_s$ into Eq. (4.10), where k_s and ϕ_s are the SPP wave number and the propagation angle with respect to x-axis, the solutions $\omega_{\mathbf{k}}$ can be found as [86]

$$\omega_{\mathbf{k}_s} = \frac{1}{2} \omega_c \cos \phi_s + \frac{1}{2} \sqrt{2\omega_p^2 + \omega_c^2 (1 + \sin^2 \phi_s)}, \quad (4.11)$$

They represent the SPP modes with short wavelength which are only dependent on the SPPs directions, ϕ_s .

Here, the quasi-static approach for magnetized plasma slab is used to find the evidence of the existence of backward beams at the bottom interface of the plasma slab from the dispersion diagram. Figure 4.10 shows the solutions to the quasi-static relation (4.9) for magnetized plasma slab with thickness of $h = 0.25\lambda_p$ and for several values of cyclotron frequency, representing the SPP resonance in the quasi-static limit. For a given ω value, there are four values of ϕ_s , two of which correspond to the forward beams on the top

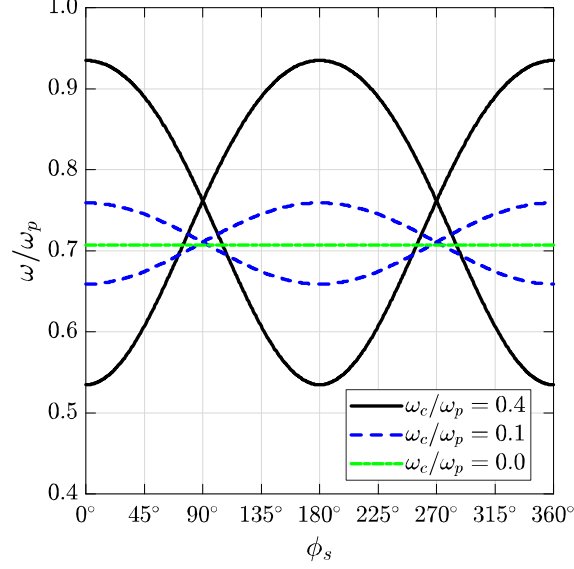


Figure 4.10: Solutions to the quasi-static SPP dispersion relation (4.9) for a finite thickness slab of thickness $h = 0.25\lambda_p$ and wavenumber $k_s = 10k_p \gg 1/h$. The cyclotron frequency ranges from 0 to $0.4\omega_p$. Reprinted with permission from [5].

interface and the other two correspond to the backward beams on the bottom interface. This suggests that four beams may be present in the scattered field profile for operating frequencies that fall within the SPP resonant range $\omega^- < \omega < \omega^+$. For example, consider an operating frequency of $\omega = 0.65\omega_p$ and cyclotron frequency $\omega_c = 0.4\omega_p$, from the quasi static dispersion, we find that the in-plane wavevector, and hence, phase velocity, of the SPP (approximately) makes an angle $\phi_s \in \{58^\circ, 122^\circ, 238^\circ, 302^\circ\}$ with respect to the x-axis. The group velocity (i.e. the direction of energy flow as indicated by the direction of the beams for the lossless case) of the SPP is perpendicular to the phase velocity and therefore, makes an angle $\phi_s \pm 90^\circ \in \{148^\circ, 32^\circ, 328^\circ, 212^\circ\}$ with respect to the x-axis. The scattered field profile shows four beams with the expected angles with respect to the x-axis. Two forward beams are present on the top interfaces at angles $\{32^\circ, 328^\circ\}$ and two backward beams on the bottom interfaces at angles $\{148^\circ, 212^\circ\}$. That is, the quasi-static analysis provides four symmetric beams, two of which will be excited on a given interface (top or bottom).

Furthermore, In the presence of a magnetic bias, the SPP resonance depends on the direction of the SPP modes, however, it is independent of the slab thickness for large values of k_s . As the magnetic bias tends toward zero ($\omega_c \rightarrow 0$), the SPP resonance becomes a flat curve, which means the SPP resonance is direction independent, $\lim_{\omega_c \rightarrow 0} \omega_{SPP} = \omega_p/\sqrt{2}$. As magnetic bias increases, the SPP resonant range also increases.

4.5 Summary

In this chapter, we have investigated the behavior of surface plasmon polaritons propagating at the interface between air and gyrotropic plasma for both single-interface and finite-thickness biased-plasma slab configurations. The operating frequency is chosen to lie within the lower common band gap, wherein omni-directional, bidirectional, and narrow directional SPP beam patterns are observed. Operating in the bandgap gives the SPP interesting properties that protect it from backscatter and diffraction in the presence of a discontinuity. For a frequency window within the bandgap, the SPPs form two narrow beams. The direction of the SPP beams are adjustable with operation frequency and also the bias magnetic field. The Green function and quasi-static approximation to the dispersion have also been obtained for a finite-thickness slab. We evaluated the effect of thickness on properties of narrow beam SPPs. We obtained the optimized thickness to limit propagation on the top surface.

Chapter 5

Chern Numbers in Magnetized Semiconductors

Topological plasma systems are characterized by integer Chern invariants. In a continuous photonic system characterized by a local Drude model, the material response is ill-behaved at large wavenumbers, leading to noninteger Chern invariants. So this local model does not lead to topological specifications for the magnetized continua. This problem has been solved previously by introducing an ad hoc material model including a spatial cutoff material response. Using this model, the non integer Chern numbers problem is solved, but in cost of interpolating the material response and introducing a new mode that may not be physically relevant. Here, we suggest to solve the problem by applying the physical nonlocal model of hydrodynamic model.

In this chapter, we derive the Berry phase for a nonlocal plasma system. Then, we recalculate the Chern numbers for a local Drude and nonlocal spatial cutoff model. Then, we take into account the effect of nonlocality using the hydrodynamic model and determine the associated Chern numbers. The difference of these three models are discussed. Eventually, we conclude that hydrodynamic model forms a complete, self-consistent physical model, that clarifies the topological wave physics of continuous media. Article [6] has been published from the outcomes of this project.

5.1 Chern Number Relations for a Nonlocal System

For a spatially dispersive material, consider an eigenfunction $f_n = \begin{pmatrix} \mathbf{E} & \mathbf{H} \end{pmatrix}^T$ with eigenvalues ω_n . The envelope of TM mode ($H_x = H_y = E_z = 0$) and TE mode ($E_x = E_y = H_z = 0$) are $f_{nk}^{\text{TM}} = \begin{pmatrix} -\bar{\epsilon}^{-1} \cdot (\mathbf{k} \times \hat{\mathbf{z}}) / \omega_n \epsilon_0 & \mathbf{1}_{3 \times 1} \cdot \hat{\mathbf{z}} \end{pmatrix}^T$ and $f_{nk}^{\text{TE}} = \begin{pmatrix} \mathbf{1}_{3 \times 1} \cdot \hat{\mathbf{z}} & \mathbf{k} \times \hat{\mathbf{z}} / \mu_0 \omega_n \end{pmatrix}^T$, respectively. $\mathbf{1}_{3 \times 1}$ is a 3×1 tensor with elements equal to one. The Berry potential is the phase difference between the eigenfunctions at k and $k + dk$. It is written in terms of the envelope of electromagnetic field as

$$\mathbf{A}_{nk} = \frac{\text{Re}\{i f_{nk}^* \cdot \frac{1}{2} \frac{\partial}{\partial \omega_n} (\omega_n M) \partial_{\mathbf{k}} f_{nk}\}}{f_{nk}^* \cdot \frac{1}{2} \frac{\partial}{\partial \omega_n} (\omega_n M) f_{nk}} \quad (5.1)$$

where M is the material matrix ($M_{11} = \epsilon_0 \bar{\epsilon}$, $M_{22} = \mu_0 \mathbf{I}_{3 \times 3}$, $M_{12} = M_{21} = 0$, where $\mathbf{I}_{3 \times 3}$ is a 3×3 identity matrix). This Berry potential relation was first derived for periodic photonic crystal structures [26, 27]. However, it can be used for spatially dispersive continuous materials as proved in Ref. [30]. Using the Berry potential vector, the Berry curvature is determined by $F_{\mathbf{k}} = \partial A_x / \partial k_y - \partial A_y / \partial k_x$. The Chern numbers are calculated by the surface integration of the Berry curvature over the entire momentum space of the wave vector. In analogy to electromagnetic, Berry phase, Berry curvature and Chern number act like magnetic potential vector, magnetic field, and magnetic flux, respectively. In topological materials, the Chern numbers are integer invariants and sum to zero. To obtain integer Chern invariants for continua media, the momentum space must be a close surface with no boundaries. To realize this condition, the $k_x - k_y$ plane, which is

the momentum space of the continuous materials, is mapped into the Riemann sphere, as suggested in [30]. Using Stock's theorem and the fact that the wave functions are not defined at the origin and infinity, the surface integral in the Chern number relation is written as two line integrals around the boundary of the surface near the south and north poles. Then,

$$C_n = \frac{1}{2\pi} \int_{k=\infty} \mathbf{A}_{n,\mathbf{k}} \cdot d\mathbf{l} - \frac{1}{2\pi} \int_{k=0^+} \mathbf{A}_{n,\mathbf{k}} \cdot d\mathbf{l}. \quad (5.2)$$

Since the system is φ independent due to the symmetry about the z -axis, we have $\mathbf{A}_{n,\mathbf{k}} \cdot d\mathbf{l} = \mathbf{A}_{n,\varphi} k d\varphi$. The Chern number attributed to the n^{th} eigenmode is calculated by $C_n = \lim_{k \rightarrow \infty} (A_{n,\varphi=0}k) - \lim_{k \rightarrow 0^+} (A_{n,\varphi=0}k)$. In the following, we simplify the Berry phase relation (5.1) for a nonlocal model by calculating each term individually. Starting with

$$\bar{\varepsilon}^{-1} = \begin{bmatrix} \alpha_t & \alpha_g & 0 \\ -\alpha_g & \alpha_t & 0 \\ 0 & 0 & \alpha_a \end{bmatrix}, \quad (5.3)$$

the matrix elements are obtained as

$$\alpha_t = \frac{\varepsilon_t}{\varepsilon_t^2 - \varepsilon_g^2}, \quad \alpha_g = -i \frac{\varepsilon_g}{\varepsilon_t^2 - \varepsilon_g^2}, \quad \alpha_a = \frac{1}{\varepsilon_a}, \quad (5.4)$$

By expanding $\bar{\varepsilon}^{-1} \cdot \mathbf{k} \times \hat{\mathbf{z}}/\omega\varepsilon_0$, the TM eigenmode envelope is

$$f_{nk}^{TM} = \begin{pmatrix} f_{11} & f_{21} & 0 & 0 & 0 & 1 \end{pmatrix}^T, \quad (5.5)$$

where

$$f_{11} = \frac{-1}{\omega\varepsilon_0}(\alpha_t k_y - \alpha_g k_x), \quad f_{21} = \frac{-1}{\omega\varepsilon_0}(-\alpha_g k_y - \alpha_t k_x). \quad (5.6)$$

To obtain the relations for a nonlocal material model, we assume that α_t and α_g are k -dependent, then using the partial differential relation of $\partial_{\mathbf{k}} = \frac{\partial}{\partial k_x} \hat{\mathbf{x}} + \frac{\partial}{\partial k_y} \hat{\mathbf{y}}$ we have

$$\partial_k f_{nk} = \begin{pmatrix} F_{11} & F_{21} & 0 & 0 & 0 & 0 \end{pmatrix}^T, \quad (5.7)$$

where

$$F_{11} = \partial_{\mathbf{k}} f_{11} = \frac{-1}{\omega\varepsilon_0} \left[\left(\frac{\varpi_t \delta}{k} k_x k_y - \frac{\varpi_g \delta}{k} k_x^2 - \alpha_g \right) \hat{\mathbf{x}} + \left(\alpha_t + \frac{\varpi_t \delta}{k} k_y^2 - \frac{\varpi_g \delta}{k} k_x k_y \right) \hat{\mathbf{y}} \right] \quad (5.8)$$

$$F_{21} = \partial_{\mathbf{k}} f_{21} = \frac{-1}{\omega\varepsilon_0} \left[\left(-\frac{\varpi_g \delta}{k} k_x k_y - \frac{\varpi_t \delta}{k} k_x^2 - \alpha_t \right) \hat{\mathbf{x}} + \left(-\alpha_g - \frac{\varpi_g \delta}{k} k_y^2 - \frac{\varpi_t \delta}{k} k_x k_y \right) \hat{\mathbf{y}} \right], \quad (5.9)$$

in which we used the partial derivative terms

$$\frac{\partial \alpha_{t,g}}{\partial k_x} = \frac{\partial \alpha_{t,g}}{\partial \chi} \frac{\partial \chi}{\partial k} \frac{\partial k}{\partial k_x} = \varpi_{t,g} \delta_k \frac{k_x}{k} \quad (5.10)$$

$$\frac{\partial \alpha_{t,g}}{\partial k_y} = \frac{\partial \alpha_{t,g}}{\partial \chi} \frac{\partial \chi}{\partial k} \frac{\partial k}{\partial k_y} = \varpi_{t,g} \delta_k \frac{k_y}{k}, \quad (5.11)$$

where $k = \sqrt{k_x^2 + k_y^2}$. We simplify the next term of the Berry potential relation as

$$\frac{\partial}{\partial \omega}(\omega M(k, \omega)) = \begin{pmatrix} (\beta_{ij})_{3 \times 3} & \mathbf{0}_{3 \times 3} \\ \mathbf{0}_{3 \times 3} & \mu_0 \mathbf{I}_{3 \times 3} \end{pmatrix}. \quad (5.12)$$

where $\beta_{11} = \beta_{22} = \beta_t$, $\beta_{12} = -\beta_{21} = \beta_g$, and $\beta_{t,g} = \frac{\partial}{\partial \omega}(\omega \varepsilon_0 \varepsilon_{t,g})$. Using $\alpha_t^* = \alpha_t$ and $\alpha_g^* = -\alpha_g$, the denominator of relation (5.1) is simplified as

$$\begin{aligned} D &= f_{nk}^* \cdot \frac{1}{2} \frac{\partial}{\partial \omega}(\omega M) f_{nk} \\ &= \frac{k^2}{2(\omega \varepsilon_0)^2} \left[(|\alpha_t|^2 + |\alpha_g|^2) \beta_t - 2\alpha_t \alpha_g \beta_g \right] + \mu_0/2 \end{aligned} \quad (5.13)$$

and the numerator is given as

$$N = i f_{nk}^* \cdot \frac{1}{2} \frac{\partial}{\partial \omega}(\omega M) \partial_{\mathbf{k}} f_{nk} = N_x \hat{\mathbf{x}} + N_y \hat{\mathbf{y}} \quad (5.14)$$

where

$$\begin{aligned} N_x &= \frac{i}{2(\omega \varepsilon_0)^2} \left[\beta_t (\alpha_t k_y - \alpha_g k_x)^* \left(\frac{\varpi_t \delta}{k} k_x k_y - \frac{\varpi_g \delta}{k} k_x^2 - \alpha_g \right) \right. \\ &\quad + \beta_g (\alpha_t k_y - \alpha_g k_x)^* \left(-\frac{\varpi_g \delta}{k} k_x k_y - \frac{\varpi_t \delta}{k} k_x^2 - \alpha_t \right) \\ &\quad - \beta_g (-\alpha_g k_y - \alpha_t k_x)^* \left(\frac{\varpi_t \delta}{k} k_x k_y - \frac{\varpi_g \delta}{k} k_x^2 - \alpha_g \right) \\ &\quad \left. + \beta_t (-\alpha_g k_y - \alpha_t k_x)^* \left(-\frac{\varpi_g \delta}{k} k_x k_y - \frac{\varpi_t \delta}{k} k_x^2 - \alpha_t \right) \right] \end{aligned} \quad (5.15)$$

and

$$\begin{aligned}
N_y = & \frac{i}{2(\omega\varepsilon_0)^2} \left[\beta_t(\alpha_t k_y - \alpha_g k_x)^* \left(\alpha_t + \frac{\varpi_t \delta}{k} k_y^2 - \frac{\varpi_g \delta}{k} k_x k_y \right) \right. \\
& + \beta_g(\alpha_t k_y - \alpha_g k_x)^* \left(-\alpha_g - \frac{\varpi_g \delta}{k} k_y^2 - \frac{\varpi_t \delta}{k} k_x k_y \right) \\
& - \beta_g(-\alpha_g k_y - \alpha_t k_x)^* \left(\alpha_t + \frac{\varpi_t \delta}{k} k_y^2 - \frac{\varpi_g \delta}{k} k_x k_y \right) \\
& \left. + \beta_t(-\alpha_g k_y - \alpha_t k_x)^* \left(-\alpha_g - \frac{\varpi_g \delta}{k} k_y^2 - \frac{\varpi_t \delta}{k} k_x k_y \right) \right]. \tag{5.16}
\end{aligned}$$

So the Berry phase is written as

$$\mathbf{A}_{nk}^{TM} = \frac{\text{Re}\{N_x \hat{\mathbf{x}} + N_y \hat{\mathbf{y}}\}}{D}. \tag{5.17}$$

Then, using $\hat{\phi} = -\sin(\varphi)\hat{\mathbf{x}} + \cos(\varphi)\hat{\mathbf{y}}$ we have

$$A_{n\varphi}^{TM} = \mathbf{A}_{nk}^{TM} \cdot \hat{\phi} = \frac{\text{Re}\{-N_x \sin(\varphi) + N_y \cos(\varphi)\}}{D}. \tag{5.18}$$

At $\varphi = 0$, $k_y = 0$ and $k = k_x$. Then,

$$A_n^{TM}(\varphi = 0) = \frac{\text{Re}\{N_y(\varphi = 0)\}}{D}. \tag{5.19}$$

Finally,

$$A_n^{TM}(\varphi = 0)k = \frac{\text{Re}\left\{\frac{ik^2}{2(\omega\varepsilon_0)^2} \left\{(|\alpha_t|^2 + |\alpha_g|^2)\beta_g + 2\alpha_t\alpha_g\beta_t\right\}\right\}}{\frac{k^2}{2(\omega\varepsilon_0)^2} \left((|\alpha_t|^2 + |\alpha_g|^2)\beta_t - 2\alpha_t\alpha_g\beta_g\right) + \mu_0/2}. \tag{5.20}$$

This relation can be used for any nonlocal model by defining relevant $\alpha_{t,g}$ and $\beta_{t,g}$ quantities. In what follows, we define $\alpha_{t,g}$ and $\beta_{t,g}$ for different material models and calculate the associated Chern numbers. In the following we drop the superscript TM from A_n^{TM} , so from here A_n is the Berry potential related to the TM eigenmodes.

5.2 Chern Numbers of a Local Drude Model

For a local Drude model with the permittivity elements defined in (2.12-2.14), assuming $\Gamma = 0$ and $\varepsilon_\infty = 1$, we set the nonlocal factor equal to 1, $\chi = 1$, in the relations derived in the last section. Then we obtain

$$\alpha_t = \frac{\varepsilon_t}{\varepsilon_t^2 - \varepsilon_g^2}, \quad \alpha_g = -i \frac{\varepsilon_g}{\varepsilon_t^2 - \varepsilon_g^2} \tag{5.21}$$

$$\beta_t = \varepsilon_0 \left(1 + \frac{\omega_p^2(\omega^2 + \omega_c^2)}{(\omega^2 - \omega_c^2)^2}\right), \quad \beta_g = i\varepsilon_0 \frac{2\omega\omega_c\omega_p^2}{(\omega^2 - \omega_c^2)^2}. \tag{5.22}$$

To calculate the Chern numbers we need to obtain $\lim(A_{n,\phi=0}k)$ at large and small wavenumbers ($k \rightarrow \infty$ and $k \rightarrow 0^+$) for each frequency band. We determine the eigenvalues related to the upper and lower limit of each TM band, i.e., the poles and zeros of the dispersion equation. Substitution of the permittivity elements of the local model into the dispersion equation $k_{\text{TM}}^2 = k_0^2 (\varepsilon_t^2 - \varepsilon_g^2) / \varepsilon_t$ gives

$$k^2 = \left(\frac{1}{c^2}\right) \frac{\omega^2(\omega^2 - \omega_c^2) - 2\omega^2\omega_p^2 + \omega_p^4}{(\omega^2 - \omega_c^2 - \omega_p^2)}. \quad (5.23)$$

$\omega_{n1} \rightarrow \infty$ and $\omega_{n2} = \sqrt{\omega_c^2 + \omega_p^2}$ are the poles of the above equation, corresponding to the limits of the high and low frequency bands at $k \rightarrow \infty$, respectively. Figure 2.2a shows the TM dispersion bands of the local Drude model (black lines). The zeros of the dispersion equation are

$$\omega_{n3,4}^2 = \frac{1}{2} (\omega_c^2 + 2\omega_p^2) \left(1 \pm \sqrt{1 - \left(\frac{2\omega_p^2}{\omega_c^2 + 2\omega_p^2}\right)^2} \right), \quad (5.24)$$

which correspond to the limits of the high and low frequency bands at $k \rightarrow 0$. When $k \rightarrow \infty$ and $\omega = \omega_{n1} \rightarrow \infty$, then $\varepsilon_g = 0$, $\varepsilon_t = 1$, and subsequently $\alpha_t = 1$, $\alpha_g = \beta_g = 0$. So,

$$\lim_{k \rightarrow \infty, \omega = \omega_{n1} \rightarrow \infty} (A_{n,\phi=0}k) = \frac{\text{Re}\left\{\frac{ik^2}{2(\omega\varepsilon_0)^2} \left[\left(|\alpha_t|^2 + |\alpha_g|^2\right) \beta_g + 2\alpha_t\alpha_g\beta_t \right] \right\}}{\frac{k^2}{2(\omega\varepsilon_0)^2} \left[\left(|\alpha_t|^2 + |\alpha_g|^2\right) \beta_t - 2\alpha_t\alpha_g\beta_g \right] + \mu_0/2} \Bigg|_{\alpha_g=\beta_g=0} = 0. \quad (5.25)$$

When $k \rightarrow \infty$ and $\omega_n = \omega_{n2} = \sqrt{\omega_c^2 + \omega_p^2}$, then $\varepsilon_t = 0$ and $\alpha_t = 0$. We have

$$\lim_{k \rightarrow \infty, \omega \rightarrow \omega_{n2}} (A_{n,\phi=0}k) = \frac{\text{Re}\{i\beta_g\}}{\beta_t} \Bigg|_{\omega_{n2}=\sqrt{\omega_c^2+\omega_p^2}} = -\frac{\text{sgn}(\omega_c)}{\sqrt{1 + \left(\frac{\omega_p}{\omega_c}\right)^2}}. \quad (5.26)$$

The zeros of the dispersion equation are the poles of α_t and α_g , i.e., $\alpha_t \rightarrow \infty$ and $\alpha_g \rightarrow \infty$ at $k \rightarrow 0$ and $\alpha_g/\alpha_t = -i\varepsilon_g/\varepsilon_t = \mp i$. Then,

$$\lim_{k \rightarrow 0, \omega = \omega_{n3}, \omega_{n4}} (A_{n,\phi=0}k) = \lim_{\alpha_t \rightarrow \infty} \frac{\text{Re}\{(2i\beta_g \pm 2\beta_t)\}}{2\beta_t \pm i2\beta_g} = \pm 1. \quad (5.27)$$

Finally, the Chern numbers associated to the high and low frequency bands are, respectively

$$C_1 = \lim_{k \rightarrow \infty} (A_{n,\phi=0}k) - \lim_{k \rightarrow 0^+} (A_{n,\phi=0}k) = 0 - (-1) = 1 \quad (5.28)$$

$$C_2 = \lim_{k \rightarrow \infty} (A_{n,\phi=0}k) - \lim_{k \rightarrow 0^+} (A_{n,\phi=0}k) = -\frac{\text{sgn}(\omega_c)}{\sqrt{1 + \left(\frac{\omega_p}{\omega_c}\right)^2}} - 1. \quad (5.29)$$

In Fig. 2.2a, the Chern numbers associated to each frequency band in the local Drude model are shown. The second band is not characterized by an integer number, because this band is not well-behaved at large momentum and it converges to $\omega_\infty = \sqrt{\omega_c^2 + \omega_p^2}$ at the $k \rightarrow \infty$ limit. This problem can be solved by considering a nonlocal material model as discussed in the following.

5.3 Chern Numbers of the Nonlocal Hydrodynamic Model

Consider a nonlocal hydrodynamic material model with the permittivity elements defined in (2.28), in which the nonlocal factor is $\chi = 1/(1 - k^2/k_m^2)$, where $k_m = \omega/\beta$. We obtain

$$\alpha_t = \frac{\varepsilon_{t, \text{nl}}(k, \omega)}{\varepsilon_{t, \text{nl}}^2(k, \omega) - \varepsilon_{g, \text{nl}}^2(k, \omega)} \quad (5.30)$$

$$\alpha_g = -i \frac{\varepsilon_{g, \text{nl}}(k, \omega)}{\varepsilon_{t, \text{nl}}^2(k, \omega) - \varepsilon_{g, \text{nl}}^2(k, \omega)} \quad (5.31)$$

$$\beta_g = \varepsilon_0 (\omega^2 + 2\beta^2 \chi) \frac{\chi^2 2\omega_c \omega_p^2}{\omega (\omega^2 - \chi^2 \omega_c^2)^2} \quad (5.32)$$

$$\beta_t = \varepsilon_0 \left(1 + 2 \left(\frac{\beta}{\omega} \right)^2 \frac{\omega_p^2 \chi^2}{\omega^2 - \chi^2 \omega_c^2} - \Theta \right), \quad (5.33)$$

where

$$\Theta = \frac{2\chi^4 \frac{-2\beta^2}{\omega^2} \omega_c^2 \omega_p^2 - \chi^3 \omega_p^2 \omega_c^2 - \omega^2 \omega_p^2 \chi}{(\omega^2 - \chi^2 \omega_c^2)^2}. \quad (5.34)$$

In the limit of $k \rightarrow 0$, the nonlocal factor is $\chi \rightarrow 1$. Similar to the local Drude model, the zeros of the HD dispersion equation of $k_{TM}^2 = \varepsilon_{\text{eff}}(k, \omega) k_0^2$ are the poles of α_t and α_g , i.e. at which $\alpha_t \rightarrow \infty$ and $\alpha_g \rightarrow \infty$. Then, since $\alpha_g/\alpha_t = -i\varepsilon_g/\varepsilon_t = \mp i$, we have $\lim_{k \rightarrow 0} A_{n, \phi=0} k = \pm 1$. As shown in Fig. 2.2a (red dashed lines), both frequency bands of the HD model go to infinity ($\omega_\infty \rightarrow \infty$) when $k \rightarrow \infty$. In this limit, $\varepsilon_g = 0$, $\varepsilon_t = 1$ and subsequently $\alpha_t = 1, \alpha_g = \beta_g = 0$. Therefore, $\lim_{k \rightarrow \infty, \omega_n \rightarrow \infty} A_{n, \phi=0} k = 0$. Finally, the high and low frequency bands of the nonlocal hydrodynamic model are respectively assigned by the Chern numbers of

$$C_1 = \lim_{k \rightarrow \infty} (A_{n, \phi=0} k) - \lim_{k \rightarrow 0^+} (A_{n, \phi=0} k) = 0 - (-1) = 1 \quad (5.35)$$

$$C_2 = \lim_{k \rightarrow \infty} (A_{n, \phi=0} k) - \lim_{k \rightarrow 0^+} (A_{n, \phi=0} k) = 0 - 1 = -1. \quad (5.36)$$

The Chern numbers are integer invariants and sum of them is zero. By reversing the magnetic bias, the sign of the Chern numbers becomes opposite. For trivial modes, the Chern number is equal to zero. In the hydrodynamic model, as shown in Fig. 2.2a the eigenfunctions are well-behave at large momentum such that

the north pole is mapped to the momentum at $k \rightarrow \infty$ and the Riemann surface becomes a closed surface. The dispersion bands of the nonlocal hydrodynamic model are tagged by the relevant Chern numbers in Fig. 2.2.

5.4 Chern Numbers of the Nonlocal Spatial Cutoff Model

Here, we consider a non-local spatial cutoff material model with the permittivity elements defined in (2.30-2.32), assuming $\varepsilon_\infty = 1$ and $\Gamma = 0$. For this case we define

$$\alpha_t = \frac{\varepsilon_t(k, \omega)}{\varepsilon_t^2(k, \omega) - \varepsilon_g^2(k, \omega)}, \quad \alpha_g = -i \frac{\varepsilon_g(k, \omega)}{\varepsilon_t^2(k, \omega) - \varepsilon_g^2(k, \omega)}, \quad (5.37)$$

$$\beta_t = \varepsilon_0 \left(1 + \kappa \frac{\omega_p^2(\omega^2 + \omega_c^2)}{(\omega^2 - \omega_c^2)^2} \right), \quad \beta_g = i\kappa\varepsilon_0 \frac{2\omega\omega_c\omega_p^2}{(\omega^2 - \omega_c^2)^2}, \quad (5.38)$$

replacing χ with κ in relations (5.10-5.11), where $\kappa = 1/(1 + k^2/k_{\text{max}}^2)$ is a nonlocal factor and k_m is a cutoff wavenumber manually added to the material model. For this model, when $k \rightarrow \infty$, then $\kappa \rightarrow 0$. The poles of the dispersion equation are $\omega_{n1} \rightarrow \infty$ and

$$\omega_{n2} = \lim_{\kappa \rightarrow 0} \sqrt{\omega_c^2 + \kappa\omega_p^2} = |\omega_c|,$$

which means that the second frequency band is not flat and steadily converges to $|\omega_c|$, and as a result, the associated Chern number changes. To calculate this value, we have

$$\lim_{k \rightarrow \infty, \omega = \omega_{n2}} (A_{n, \phi=0} k) = \frac{\text{Re}\{i\beta_g\}}{\beta_t} \bigg|_{\substack{\omega_{n2}=|\omega_c| \\ \kappa \rightarrow 0}} \quad (5.39)$$

$$= \frac{-\kappa 2\omega\omega_c\omega_p^2}{(\omega^2 - \omega_c^2)^2 + \kappa\omega_p^2(\omega^2 + \omega_c^2)} \bigg|_{\substack{\omega_{n2}=|\omega_c| \\ \kappa \rightarrow 0}} = -\text{sgn}(\omega_c). \quad (5.40)$$

At $k \rightarrow 0$ limit, since $\kappa \rightarrow 1$ we obtain the same value as the local model for $\lim_{k \rightarrow 0, \omega = \omega_{n4}} (A_{n, \phi=0} k) = 1$. Hence, the second band is assigned by an integer number as $C_2 = -\text{sgn}(\omega_c) - 1 = -2$. The high frequency band is still assigned by integer value of 1, similar to the local Drude model. Therefore, by considering this spatial cutoff model we obtain integer Chern invariants for each frequency band. But there is still a problem; the sum of Chern numbers is not zero ($\sum C_n = +1 - 2 = -1 \neq 0$). To solve this issue, it has been suggested to consider an interpolated material response as $\bar{\varepsilon}_{r, \tau}(\omega) = \varepsilon_\infty + \tau [\bar{\varepsilon}_r(\omega) - \varepsilon_\infty] + (1 - \tau) [\bar{\varepsilon}_{\text{Drude}} - \varepsilon_\infty]$ [30]. The permittivity elements are given in (2.34-2.36). The interpolated material model represents a continuous transition between an isotropic plasma ($\tau \rightarrow 0^+$) with the plasma frequency of ω_m and a gyrotropic plasma ($\tau \rightarrow 1^-$) with the plasma frequency of ω_p . By this assumption, a new frequency band appears at very low

frequencies as shown by the black dashed line in Fig. 5.1a. To calculate the Chern number associated to this frequency band we determine

$$\beta_t^\tau = \varepsilon_0 \left[1 + \tau \kappa \omega_p^2 \frac{\omega^2 + \omega_c^2}{(\omega^2 - \omega_c^2)^2} + (1 - \tau) \frac{\omega_m^2}{\omega^2} \right] \quad (5.41)$$

$$\beta_g^\tau = \tau \beta_g = i \varepsilon_0 \kappa \tau \frac{2 \omega \omega_c \omega_p^2}{(\omega^2 - \omega_c^2)^2}. \quad (5.42)$$

The low frequency band is asymptotic to $\omega^2 \simeq (1 - \tau) \omega_m^2 = \delta \ll 1$ at $k \rightarrow \infty$ ($\kappa \rightarrow 0$), then $\varepsilon_t(k, \omega) = 0$, $\alpha_t = 0$. Thus,

$$\lim_{k \rightarrow \infty, \kappa \rightarrow 0, \omega^2 = \delta} A_n(\phi = 0)k = \frac{i \beta_g}{\beta_t} \Big|_{\omega^2 = (1 - \tau) \omega_m^2, \kappa \rightarrow 0} = 0. \quad (5.43)$$

At $k \rightarrow 0$ limit, $\kappa \rightarrow 1$, and $\lim_{k \rightarrow 0, \omega = 0} (A_{n, \phi=0}k) = -1$ as before. Therefore,

$$C_3 = \lim_{k \rightarrow \infty, \omega = \delta \ll 1} (A_{n, \phi=0}k) - \lim_{k \rightarrow 0, \omega = 0} (A_{n, \phi=0}k) = 0 - (-1) = 1. \quad (5.44)$$

Therefore, by considering this interpolated model, the sum of Chern numbers becomes zero. Figure 5.1a shows the band dispersion diagram and associated Chern numbers of the nonlocal spatial cutoff model. In summary, for the spatial cutoff model one solves the problem of non-integer Chern numbers, but must introduce an interpolated response to obtain Chern numbers that sum to zero (also introducing a new mode that may not be physically relevant). However, we found that by a slight modification in the nonlocal factor can also avoid the need for an interpolated response. If the nonlocal factor in the spatial cutoff model is modified to $\kappa = 1/(1 - k^2/k_{\max}^2)$, the low frequency band of the spatial cutoff model resembles the corresponding band in the hydrodynamic model (a more physically realistic nonlocal model) as shown in Fig. 5.1b for the limit $|k| \leq k_{\max}^-$, assuming k_{\max} is a large number (we call this model the Modified Spatial Cutoff model, MSC). Consequently, the associated Chern value changes from -2 to -1 . Therefore, the sum of Chern numbers becomes zero without considering the interpolated material response ($\tau = 1$). In addition, by this sign change, the bands Chern numbers are equal to those in the HD model.

5.5 Summary

In this chapter, we reviewed the Chern number calculation in local Drude model and spatial cutoff models. We followed the method to calculate the Chern numbers in the hydrodynamic Drude model. We determined integer Chern invariants which validates the topological behavior of plasma continua by considering the effect of pressure in the material model. Comparing to the spatial cutoff model, we obtain the Chern index of -1 for the low frequency band of the HD model. That is because the general behavior of the low frequency band of the hydrodynamic model is different than the corresponding band in the spatial cutoff model. Therefore,

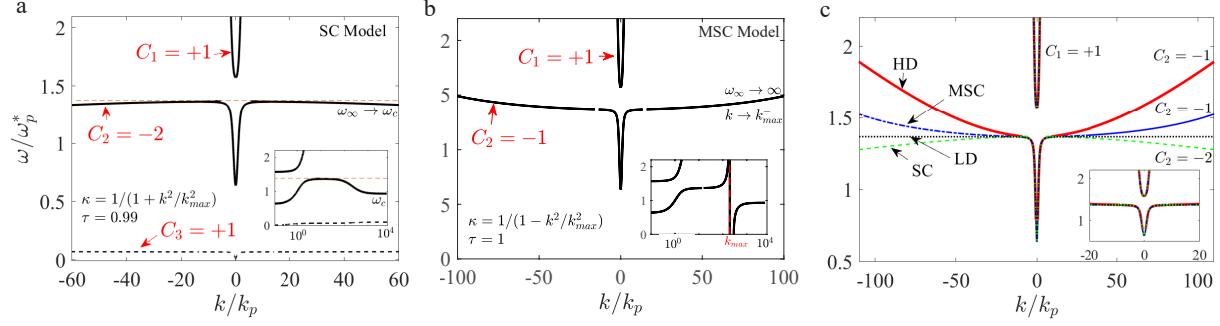


Figure 5.1: Dispersion bands and associated Chern numbers of (a) spatial cutoff (SC) model with nonlocal factor of $\kappa = 1/(1 + k^2/k_{\max}^2)$, (b) modified spatial cutoff (MSC) model with nonlocal factor $\kappa = 1/(1 - k^2/k_{\max}^2)$, where $k_{\max} = 200k_p$. (c) a dispersion plot including dispersion diagram of four material models; SC, MSC, hydrodynamic (HD) and local Drude (LD) models. The magnetized plasma region is characterized by $n_e = 3.6 \times 10^{21}(\text{m}^{-3})$, $\varepsilon_\infty = 15.68$, $m^* = 0.0175m_0$, $B_0 = 0.6\text{T}$, $\mu = \infty$, given $\omega_p^* = 2\pi(1.03\text{THz})$, $\omega_c/\omega_p = 0.23$ and $\gamma = 0$. Reprinted with permission from [6].

the sum of Chern numbers becomes zero without the need to consider the interpolated material response ($\tau = 1$). Therefore, the hydrodynamic model resolved the non integer Chern invariants in the local Drude model, also nonphysical response at large wavenumbers, and the need to interpolate the interfaced materials permittivity functions in the spatial cutoff model. It provides a physically well-grounded theory.

There is a summary of the above discussion in Table 5.1, including a comparison of different material models and Chern numbers. Also, Figure 5.1c illustrates the band diagram and associated Chern index of all four models discussed above; local Drude, spatial cutoff, modified spatial cutoff and hydrodynamic models.

Table 5.1: Comparison of material dielectric tensor and Chern numbers of the LD, SC, MSC and HD models

| Material Model | | Local Drude [30] | Spatial Cutoff [30] | Modified Spatial Cutoff | Hydrodynamic |
|--|----------------------------|---|---|--|--|
| Dielectric tensor | | $\tilde{\varepsilon} = \varepsilon_t(\mathbf{I} - \hat{\mathbf{z}}\hat{\mathbf{z}}) + i\varepsilon_g(\hat{\mathbf{z}} \times \mathbf{I}) + \varepsilon_a\hat{\mathbf{z}}\hat{\mathbf{z}}$ | | | |
| permittivity elements | $\varepsilon_a(k, \omega)$ | $1 - \frac{\omega_p^2}{\omega^2}$ | $1 - \kappa \frac{\omega_p^2}{\omega^2}$ | $1 - \chi \frac{\omega_p^2}{\omega^2}$ | |
| | $\varepsilon_t(k, \omega)$ | $1 - \frac{\omega_p^2}{\omega^2 - \omega_c^2}$ | $1 - \kappa \frac{\omega_p^2}{\omega^2 - \omega_c^2}$ | $1 - \chi \frac{\omega_p^2}{\omega^2 - \chi^2 \omega_c^2}$ | |
| | $\varepsilon_g(k, \omega)$ | $\frac{\omega_c \omega_p^2}{\omega(\omega_c^2 - \omega^2)}$ | $\kappa \frac{\omega_c \omega_p^2}{\omega(\omega_c^2 - \omega^2)}$ | $\frac{-1}{\omega} \frac{\chi^2 \omega_c \omega_p^2}{\omega^2 - \chi^2 \omega_c^2}$ | |
| nonlocality factor | | - | $\kappa = \frac{1}{1 + k^2/k_{\max}^2}$ | $\kappa = \frac{1}{1 - k^2/k_{\max}^2}$ | $\chi = \frac{1}{1 - k^2/k_m^2}, (k_m = \frac{\omega}{\beta})$ |
| Chern numbers | | $C_1 = +1$ $C_2 = -1 - \text{sgn}(\omega_c)/\sqrt{1 + (\omega_p/\omega_c)^2}$ | $C_1 = +1$ $C_2 = -2$ | $C_1 = +1$ $C_2 = -1$ | $C_1 = +1$ $C_2 = -1$ |
| Features | | non integer Chern number, $C_2 \notin \mathbb{Z}$ non zero sum, $\sum_i C_i \neq 0$ number of bands: $n_i = 2$ | integer Chern number, $C_i \in \mathbb{Z}$ non zero sum, $\sum_i C_i \neq 0$ $n_i = 2$ | integer Chern number, $C_i \in \mathbb{Z}$ zero sum, $\sum_i C_i = 0$ $n_i = 2$ | integer Chern number, $C_i \in \mathbb{Z}$ zero sum, $\sum_i C_i = 0$ $n_i = 2$ |
| Note: For SC model by considering the interpolate material response, the numbers of bands increases to $n_i = 3$ with Chern numbers $\{+1, -2, +1\}$ and zero sum $\sum_i C_i = 0$, but this method has difficulties of interpolating the interfaced materials. | | | | | |

Chapter 6

Unidirectional Curved SPP in a Radially Magnetized System

In the literature unidirectional SPPs have been studied in the plasma systems that are biased by axial magnetic field, in which cases the SPPs have linear trajectories for propagation. We found that if we bias a plasma region by a radial magnetic field, the SPPs travel on a circular path rather than a linear path, which allows to effectively guide SPPs on the curvatures. Applying radial bias is a new way for excitation of curved SPPs in a plasma system. Some potential applications for curved SPPs are applying them for angular momentum generation, particle manipulation, and in design of tweezers. In plasmonic circuitry, the curved SPPs can be used in design of the optimal plasmonic junctions with minimum radiation loss, which leads to efficient power transmission.

In this chapter, we derive dielectric tensor and bulk and SPP dispersion equation for a radially magnetized plasma system. We describe the curved topological SPPs properties and the required conditions for their excitation. Then, we explain our Green's function (GF) model, applicable to the curved SPPs. We present numerical results based on the finite element method using COMSOL to illustrate the circular propagation of the SPPs and validate the GF model. We discuss the effect of different parameters such as loss and permittivity of top layer on propagation features. Lastly, we propose to use the curved SPPs in design of nonreciprocal circular bend junctions. Paper [7] extracted from this project has been accepted by the IEEE Transaction on Antennas and propagation journal.

6.1 Bulk and SPP Modes in a Radially Magnetized Plasma System

Consider a plasma medium consisting of n_e free electrons with the effective mass of m^* per volume, which is magnetized by a static magnetic field bias $\mathbf{B}_c = B_0 \hat{\mathbf{b}}_c$ where B_0 is the magnetic field strength and $\hat{\mathbf{b}}_c$ is a unit vector along the direction of the magnetic field. As derived in Chapter 2, in a general manner, the material is characterized by a dielectric tensor

$$\bar{\epsilon} = \epsilon_t(\bar{\mathbf{I}} - \hat{\mathbf{b}}_c \hat{\mathbf{b}}_c) + i\epsilon_g(\hat{\mathbf{b}}_c \times \bar{\mathbf{I}}) + \epsilon_a \hat{\mathbf{b}}_c \hat{\mathbf{b}}_c \quad (6.1)$$

where the permittivity elements are defined in (2.12-2.14) using a Drude model.

In this chapter, we apply a uniform radial bias, $\mathbf{B}_c = B_0 \hat{\rho}$ to magnetize the plasma region. Figure 6.1a illustrates the geometry scheme of the system under study. It includes a plasma slab under radial bias, covered by an isotropic material. The radial bias can be practically implemented using concave permanent magnets. We consider a ferromagnetic metallic cylinder in the middle of the plasma disk, whose interaction with the surrounding permanent magnets provides a uniform radial bias through the plasma region. Later on, we assume the radius of metal piece (r_m) is very small comparing to the disk radius ($r_m \rightarrow 0$). We also assume

that the plasma thickness is large, then the system is two half-spaces of gyrotropic/isotropic media. The plasma region is model by (6.1), where $\hat{\mathbf{b}}_c = \hat{\rho}$ and $\bar{\mathbf{I}}$ is a dyadic tensor in polar coordinates with $(\hat{\rho}, \hat{\phi}, \hat{\mathbf{z}})$ unit basis. Next, we study the properties of the bulk modes propagating inside the radially magnetized plasma region. Then, we look for the SPPs excited at the interface of the isotropic/radially magnetized plasma media. A plane wave propagating in the gyrotropic medium with the wave vector $\mathbf{k} = k_\rho \hat{\rho}' + k_z \hat{\mathbf{z}}$ satisfies the wave equation $\mathbf{k} \times (\mathbf{k} \times \mathbf{E}) + k_0^2 \bar{\varepsilon}_r \cdot \mathbf{E} = \mathbf{0}$. The non-zero solution of \mathbf{E} exists only if $|k_0^2 \bar{\varepsilon}_r - k^2 \bar{\mathbf{I}} + \mathbf{k}\mathbf{k}| = 0$. This determinant is the dispersion equation of the bulk modes propagating with an arbitrary direction in a gyrotropic medium. Consider an orthogonal coordinate system, having a unit vector along the magnetic bias as $\{\hat{\mathbf{k}}_t, \hat{\rho}, \hat{\mathbf{k}}_t \times \hat{\rho}\}$. The wave vector in this coordinate is rewritten as $\mathbf{k} = \mathbf{k}_t + q_\rho \hat{\rho}$ with $\mathbf{k}_t = q_\phi \hat{\phi} + k_z \hat{\mathbf{z}}$, where $q_\rho = k_\rho \cos(\phi_{\mathbf{k}} - \phi_{\mathbf{b}})$ and $q_\phi = k_\rho \sin(\phi_{\mathbf{k}} - \phi_{\mathbf{b}})$; $\phi_{\mathbf{k}}$ and $\phi_{\mathbf{b}}$ are the angle of the wave and bias vectors with respect to the x -axis, respectively. By plugging $\bar{\varepsilon}$ and \mathbf{k} into the above determinant, we derive

$$k_t^2 = \frac{1}{2\varepsilon_t} \left[-\kappa \pm \sqrt{\kappa^2 - 4\varepsilon_t \nu} \right], \quad (6.2)$$

where $\kappa = q_\rho^2(\varepsilon_t + \varepsilon_a) + k_0^2(\varepsilon_g^2 - \varepsilon_t(\varepsilon_t + \varepsilon_a))$, $\nu = \varepsilon_a(q_\rho^2 - k_0^2\varepsilon_t)^2 - \varepsilon_a\varepsilon_g^2k_0^4$, and $k_t^2 = q_\phi^2 + k_z^2$. We look for the bulk modes propagating perpendicular to the bias. Thus, we set $q_\rho = 0$ in (6.2) and determine two equations as $k_1^2 = \varepsilon_{\text{eff}}k_0^2$ and $k_2^2 = \varepsilon_a k_0^2$ where $\varepsilon_{\text{eff}} = (\varepsilon_t^2 - \varepsilon_g^2)/\varepsilon_t$, k_0 is the free space wavenumber, and $k_j^2 = q_\phi^2 + k_{zj}^2$, $j \in \{1, 2\}$. These equations characterize the nontrivial TM^ρ modes with E_ϕ, E_z, H_ρ (no electric field component along the bias vector) and trivial TE^ρ modes with H_ϕ, H_z, E_ρ (no magnetic field component along the bias), respectively. The nontrivial modes are dependent on the magnetic bias, unlike the trivial modes. Note that in a cylindrical rod pure TE and pure TM modes exist only when the field configurations are symmetric and independent of ϕ . Here, nontrivial TM and trivial TE modes have phase variation of $\exp(im\phi)$. Therefore, they cannot be pure TE and TM modes; they are hybrid modes. A wave with $q_\rho = 0$ is a traveling wave on a cylindrical shell, which can be decomposed into nontrivial TM and trivial TE modes in a radially magnetized system. It has a vortex-like behavior and its phase varies as $\exp(im\phi)$. An electromagnetic vortex is a differentiated plane wave which can be generated by three homogeneous plane wave interference [132, 133].

Next, by enforcing continuity of the tangential components of the electric and magnetic fields of these particular bulk modes at the interface, we derive the SPP dispersion equation as

$$\frac{\sqrt{k_s^2 - k_0^2\varepsilon_r}}{\varepsilon_r} + \frac{\sqrt{k_s^2 - k_0^2\varepsilon_{\text{eff}}}}{\varepsilon_{\text{eff}}} = \frac{\varepsilon_g k_s}{\varepsilon_t \varepsilon_{\text{eff}}}, \quad (6.3)$$

where $k_s = q_\phi$ is the propagation constant of the surface wave and ε_r is the effective permittivity of the isotropic region. This dispersion relation is the same as for axial bias in the Voigt configuration. Figure 6.1b shows the dispersion diagrams of the nontrivial TM, trivial TE bulk modes, and the SPP modes. The shaded

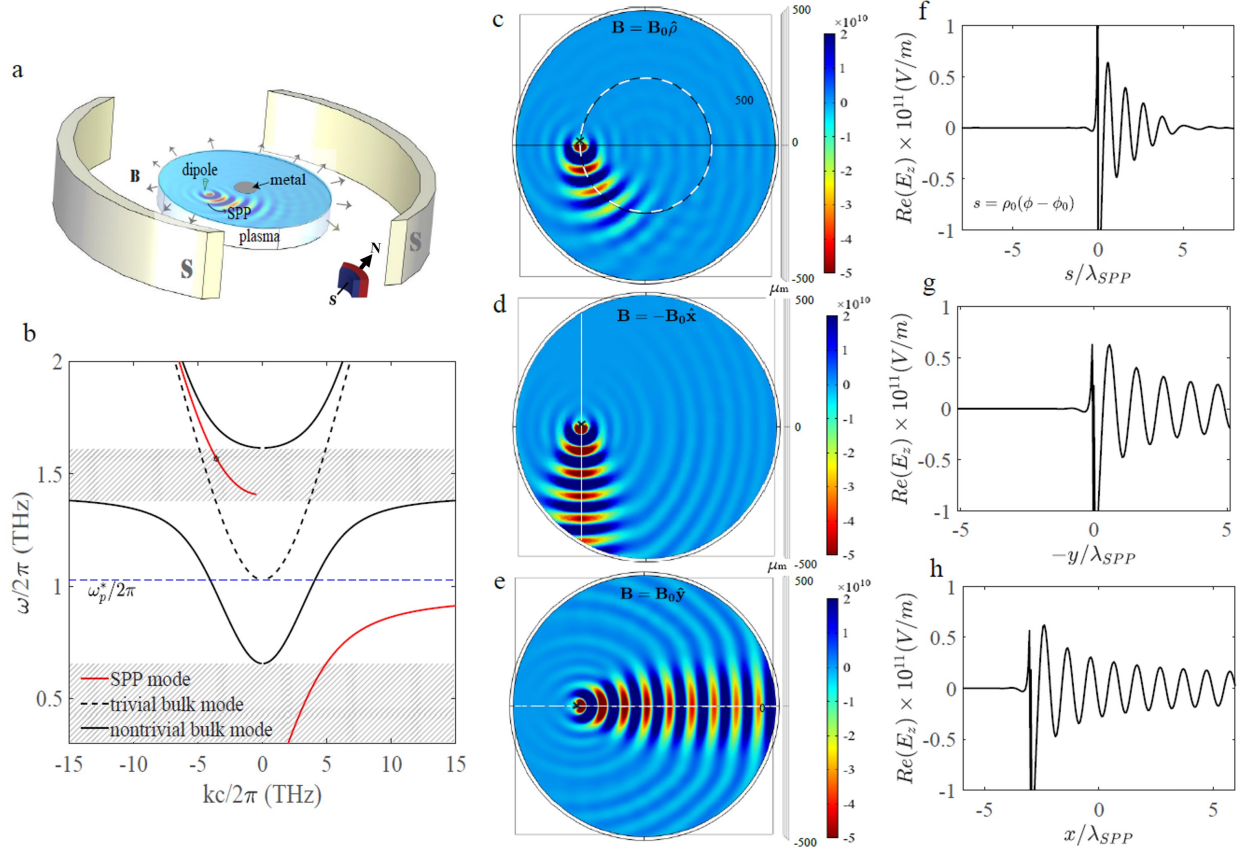


Figure 6.1: Unidirectional curved SPP vs. linear propagating SPP. (a) Geometry sketch (b) Bulk and SPP dispersion diagrams. The gray regions denote the band gaps. The electric field profile (E_z) of the SPP propagating at the interface of an isotropic medium and a plasma region magnetized by (c) a static radial bias $\mathbf{B} = B_0 \hat{\rho}$ that is centered on the origin, (d) an axial bias $\mathbf{B} = -B_0 \hat{x}$, and (e) an axial bias $\mathbf{B} = B_0 \hat{y}$. The SPPs are excited by a point source with the input power of 1W, located at $(\rho_0, \phi_0, z) = (R_a/2, \pi, 0)$, where $R_a = 500\mu\text{m}$ is the radius of the plasma region. (f,g,h) The electric field oscillation, respectively along the circular, vertical and horizontal trajectories shown by white dashed lines in (c,d,e). λ_{SPP} is the SPP wavelength. In (f), s is the arc length defined as $s = \rho_0 \cos(\phi - \phi_0)$ where ϕ is the angle of the observation point with respect to the x-axis and ρ_0 is the radius of the dashed circle. The magnetized plasma is characterized by Eq. (2.11) where $n_e = 3.6 \times 10^{21} \text{m}^{-3}$, $m^* = 0.0175m_0$, $\varepsilon_\infty = 15.68$, $B_0 = 0.6\text{T}$, given $\omega_p^* = \omega_p/\sqrt{\varepsilon_\infty} = 2\pi(1.03\text{THz})$, $\omega_c/\omega_p^* = 0.93$ and $\Gamma = 0.00015\omega_p$. The resonance frequency $f = 1.567\text{THz}$ is within the upper band gap. Reprinted with permission from [7].

gray regions indicate bandgaps between the nontrivial bulk bands. Like usual topological plasma systems when an axial bias is applied, the SPPs crossing the nontrivial bandgaps are potentially topological. Their frequency response is asymmetric.

Then, we have simulated the system under study using COMSOL Multiphysics. The magnetized plasma is characterized by (6.1) where $n_e = 3.6 \times 10^{21} \text{m}^{-3}$, $m^* = 0.0175m_0$, $\varepsilon_\infty = 15.68$, $B_0 = 0.6 \text{T}$, given $\omega_p^* = \omega_p/\sqrt{\varepsilon_\infty} = 2\pi(1.03 \text{THz})$, $\omega_c/\omega_p^* = 0.93$ and $\Gamma = 0.00015\omega_p$, related to an undoped InSb crystal at moderate temperatures. The top region is metal with dielectric constant of $\varepsilon_r = -10^4$. The SPPs are excited by a point source located at the interface of the gyrotropic/isotropic media, operating at a frequency within the upper nontrivial bandgap. The electric field profile at the interface is shown in Fig. 6.1c. It shows the SPPs propagating counter clock-wise (CCW) on a circular path about the origin. There is no propagation in the opposite direction due to the unidirectional nature of the wave. So, the excited SPPs have a circular trajectory rather than a linear trajectory as a result of applying the radial bias.

For comparison, we obtain the field profile of the SPPs when the axial biases $\hat{\mathbf{b}}_c = -\hat{\mathbf{x}}$ and $\hat{\mathbf{b}}_c = \hat{\mathbf{y}}$ are applied (the usual cases). The results are shown in Figs. 6.1d and 6.1e. Here, the unidirectional SPPs have linear propagation. They are characterized by the same dispersion equation as Eq. 6.3, but with surface momentum $k_s = -q_y$ and $k_s = q_x$, respectively. Comparing Fig. 6.1c with Fig. 6.1d and Fig. 6.1e, the deviation of the SPPs from a straight line to a circular path is evident. In all cases, the SPPs tend to propagate perpendicular to the static bias. For that reason, in the radial bias system the surface plasmons gain orbital angular momentum and form curved SPPs.

The line graphs in Fig. 6.1f,g,h indicate the electric field oscillation along the circular, vertical and horizontal straight line traces shown by white dashed lines in the field profile plots. According to the period of the oscillation, the SPP wavelength for radial and axial bias cases are almost equal ($\lambda_{SPP} \simeq 84 \mu\text{m}$). The obtained wavelength is consistent with the estimated value obtained from the dispersion diagram ($\lambda_{SPP} = 2\pi/\text{Re}(k_s)$). The SPPs have similar propagation properties, however, the decay rate of the curved SPP is much higher. We find that the curved SPPs are leaky modes, while the linear SPPs in the axially biased systems are confined propagating modes. The difference in results is due to the hybrid nature of the nontrivial and trivial bulk modes in the radially biased system. In fact, the curved SPPs excited at a resonance frequency within the upper nontrivial bandgap can be coupled to the trivial TE cylindrical bulk modes. This does not occur in an axially biased system, because in that case the trivial TE and nontrivial TM modes are orthogonal modes, and hence, the TE modes do not contribute to the excitation of the TM SPP. Consequently, the TM SPPs are confined modes at frequencies within the nontrivial bandgaps and their energy does not couple to the trivial TE mode.

6.2 Dyadic Green's Function for a Radially Magnetized Plasma

Here, we analytically obtain the electric field of the curved SPPs in a radially magnetized system based on a green's function analysis. They are excited by a point source at the interface of two half-space media where the $z < 0$ region is filled by a radially magnetized plasma and the $z > 0$ region is an isotropic material. The radial bias is centered on the origin and the dipole with dipole moment of $\mathbf{p} = \gamma \hat{\mathbf{z}}$ is located inside the isotropic region at $\mathbf{r}_0 = (\rho_0, \phi_0, d)$.

The primary electric and magnetic fields are $\mathbf{E}^p(\mathbf{r}) = (\varepsilon_r k_0^2 \mathbf{I} + \nabla \nabla) \cdot \pi^p$ and $\mathbf{H}^p(\mathbf{r}) = i\omega \varepsilon_0 \varepsilon_r \nabla \times \pi^p$, where the Hertzian potential π^p is given by $\pi^p(\mathbf{r}) = g^p(\mathbf{r}, \mathbf{r}_0) \mathbf{p} / \varepsilon_r \varepsilon_0$. The primary Green's function is

$$g^p(\mathbf{r}, \mathbf{r}_0) = \frac{e^{-i\sqrt{\varepsilon_r k_0^2} |\mathbf{r} - \mathbf{r}_0|}}{4\pi |\mathbf{r} - \mathbf{r}_0|} = \frac{1}{(2\pi)^2} \int_0^\infty \int_0^{2\pi} \frac{e^{-\gamma_0 |z-d|}}{2\gamma_0} e^{i\mathbf{q} \cdot (\mathbf{r} - \mathbf{r}_0)} q d\phi_{\mathbf{q}} dq \quad (6.4)$$

where $\mathbf{q} \cdot \mathbf{r} = q\rho \cos(\phi_{\mathbf{q}} - \phi_{\mathbf{r}})$ and $\mathbf{q} \cdot \mathbf{r}_0 = q\rho_0 \cos(\phi_{\mathbf{q}} - \phi_0)$ with $\{\phi_{\mathbf{q}}, \phi_{\mathbf{r}}, \phi_0\}$ denoting the angles \mathbf{q} , \mathbf{r} , and \mathbf{r}_0 make with the Cartesian unit vector $\hat{\mathbf{x}}$. The exponential factor is $\gamma_0 = \sqrt{q^2 - \varepsilon_r k_0^2}$, where ε_r is the dielectric constant of the isotropic region ($z > 0$). Using the Fourier transform pairs and nabla relations in a polar coordinate, we have

$$\mathbf{E}^p(\mathbf{r}) = \frac{\gamma g^p(\mathbf{r}, \mathbf{r}_0)}{\varepsilon_r \varepsilon_0} \left[\nabla_t \partial_z + \left(\frac{\partial^2}{\partial z^2} + \varepsilon_r k_0^2 \right) \hat{\mathbf{z}} \right] \quad (6.5)$$

$$\mathbf{E}^p(z, \mathbf{q}) = \mathbf{E}_{||}^p + E_z^p \hat{\mathbf{z}} = \frac{\gamma g^p(z, \mathbf{q})}{\varepsilon_r \varepsilon_0} \left[i\mathbf{q} \partial_z + \left(\frac{\partial^2}{\partial z^2} + \varepsilon_r k_0^2 \right) \hat{\mathbf{z}} \right] \quad (6.6)$$

where $g^p(z, \mathbf{q}) = e^{-i\mathbf{q} \cdot \mathbf{r}_0} e^{-\gamma_0 |z-d|} / 2\gamma_0$. The total field in the isotropic region is a superposition of the primary and scattered field, $\mathbf{E}^{(1)}(\mathbf{r}) = \mathbf{E}^p(\mathbf{r}) + \mathbf{E}^s(\mathbf{r})$. Let $\bar{\mathbf{R}}$ be a reflection tensor such that the tangential components of the scattered field at the interface are related to the tangential primary field as

$$\mathbf{E}_{||}^s(z, \mathbf{q}) = \mathbf{E}_{||}^s(\mathbf{q}) e^{-\gamma_0 z} = \bar{\mathbf{R}}(\mathbf{q}) \cdot \mathbf{E}_{||}^p(0, \mathbf{q}) e^{-\gamma_0 z}. \quad (6.7)$$

Substitution of (6.6) gives

$$\mathbf{E}_{||}^s(z, \mathbf{q}) = \bar{\mathbf{R}}(\mathbf{q}) \cdot i\mathbf{q} \frac{\gamma}{2\varepsilon_r \varepsilon_0} e^{-\gamma_0(z+d)} e^{-i\mathbf{q} \cdot \mathbf{r}_0}. \quad (6.8)$$

According to the Gauss's law for the scattered field $\nabla \cdot \mathbf{E}^s = 0$, the z component of the scattered field is $E_z^s(\mathbf{r}) = -\int \nabla_t \cdot \mathbf{E}_{||}^s(\mathbf{r}) dz$. Using (6.8) we have,

$$E_z^s(z, \mathbf{q}) = -i\mathbf{q} \cdot \mathbf{E}_{||}^s(\mathbf{q}) \int e^{-\gamma_0 z} dz = \frac{-\gamma}{2\varepsilon_r \varepsilon_0 \gamma_0} \mathbf{q} \cdot \bar{\mathbf{R}}(\mathbf{q}) \cdot \mathbf{q} e^{-\gamma_0(z+d)} e^{-i\mathbf{q} \cdot \mathbf{r}_0}. \quad (6.9)$$

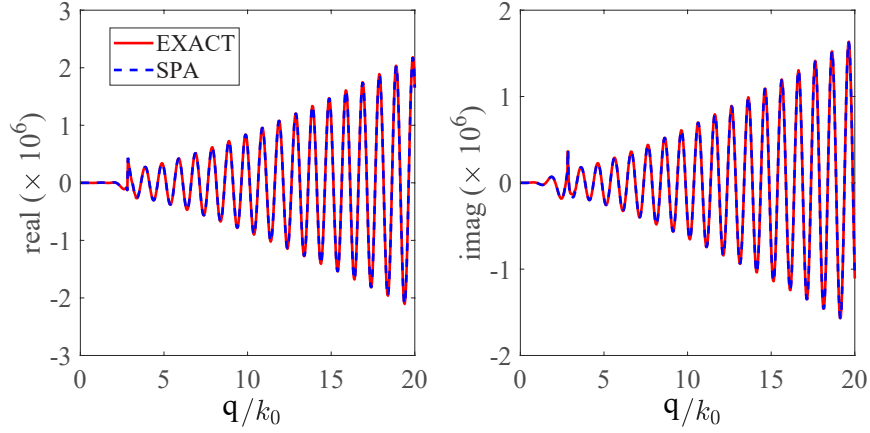


Figure 6.2: Saddle point approximation vs. exact solution (the integrand of (6.12) and (6.11), respectively, over q variation) for $f = 1.567\text{THz}$ at $(\rho = 250\mu\text{m}, \phi = 5\pi/4, z = 0.003\lambda_p)$. $n_e = 3.6 \times 10^{21}\text{m}^{-3}$, $m^* = 0.0175m_0$, $\varepsilon_\infty = 15.68$, $B_0 = 0.6\text{T}$, and $\varepsilon_r = 8$. Reprinted with permission from [7].

Finally, by taking the spatial Fourier transform we have

$$\mathbf{E}_{||}^s(\mathbf{r}) = \frac{1}{(2\pi)^2} \int_0^\infty \int_0^{2\pi} \bar{\mathbf{R}}(\mathbf{q}) \cdot i\mathbf{q} \frac{\gamma e^{-\gamma_0(z+d)}}{2\varepsilon_r\varepsilon_0} e^{i\mathbf{q}\cdot(\mathbf{r}-\mathbf{r}_0)} q d\phi_{\mathbf{q}} dq \quad (6.10)$$

and

$$E_z^s(\mathbf{r}) = \frac{1}{(2\pi)^2} \int_0^\infty \int_0^{2\pi} C^r(\mathbf{q}) \frac{-\gamma}{\varepsilon_r\varepsilon_0} \frac{e^{-\gamma_0(z+d)}}{2\gamma_0} e^{i\mathbf{q}\cdot(\mathbf{r}-\mathbf{r}_0)} q d\phi_{\mathbf{q}} dq \quad (6.11)$$

where $C^r(\mathbf{q}) = \mathbf{q} \cdot \bar{\mathbf{R}}(\mathbf{q}) \cdot \mathbf{q}$. Using these 2D Sommerfeld integrals, the field computation is very time consuming and it does not converge well. To solve this problem, we use a saddle point approximation and simplify (6.11) to a 1D integral as

$$E_z^s(\mathbf{r}) = \int_0^\infty I(q) \frac{-\gamma e^{-\gamma_0(z+d)}}{2\varepsilon_r\varepsilon_0\gamma_0} q dq \quad (6.12)$$

where

$$I(q) = \frac{1}{(2\pi)^2} \sqrt{\frac{\pi}{2q|g(\phi_{\mathbf{s}})|}} \left[C^r(q, \phi_{\mathbf{s}}) e^{iqg(\phi_{\mathbf{s}})} e^{i\pi\varsigma/4} + C^r(q, \phi_{\mathbf{s}} - \pi) e^{-iqg(\phi_{\mathbf{s}})} e^{-i\pi\varsigma/4} \right] \quad (6.13)$$

with $g(\phi_{\mathbf{s}}) = \rho \cos(\phi_{\mathbf{s}} - \phi_{\mathbf{r}}) - \rho_0 \cos(\phi_{\mathbf{s}} - \phi_0)$, ς is the sign of $g''(\phi_{\mathbf{s}})$, and the saddle point is

$$\phi_{\mathbf{s}} = \tan^{-1} \left(\frac{\rho_0 \sin(\phi_0) - \rho \sin(\phi_{\mathbf{r}})}{\rho_0 \cos(\phi_0) - \rho \cos(\phi_{\mathbf{r}})} \right) \quad (6.14)$$

where $\phi_{\mathbf{s}} \in (0, \pi)$. Figure 6.2 shows that the approximated relation is matched with the exact solution.

6.2.1 Reflection Tensor in a Radially Biased System

A plane wave in a gyrotropic medium satisfies the wave equation $\mathbf{k} \times (\mathbf{k} \times \mathbf{E}) + k_0^2 \bar{\varepsilon}_r \cdot \mathbf{E} = \mathbf{0}$. Consider a coordinate system, having a unit vector along the magnetic bias $\{\hat{\mathbf{k}}_t, \hat{\rho}, \hat{\mathbf{k}}_t \times \hat{\rho}\}$, where $\mathbf{k} = \mathbf{k}_t + q_\rho \hat{\rho}$ with $\mathbf{k}_t = q_\varphi \hat{\phi} + k_z \hat{\mathbf{z}}$. We define $q_\rho \equiv k_\rho \cos(\phi_{\mathbf{k}} - \phi_b)$ and $q_\varphi \equiv k_\rho \sin(\phi_{\mathbf{k}} - \phi_b)$ where $q_\rho, q_\varphi \in [-\infty, \infty]$. Note that the permittivity tensor is given in $(\hat{\rho}, \hat{\phi}, \hat{\mathbf{z}})$ polar basis which is related to $(\tilde{\rho}, \tilde{\phi}, \hat{\mathbf{z}})$ basis by projection relations of $\tilde{\rho} \cdot \hat{\rho} = \cos(\phi_{\mathbf{k}} - \phi_b)$ and $\tilde{\rho} \cdot \hat{\phi} = \sin(\phi_{\mathbf{k}} - \phi_b)$. Also, the permittivity elements are not spatially dependent. In the wave equation, the non-zero solution of \mathbf{E} exists only if $|k_0^2 \bar{\varepsilon}_r - k^2 \bar{\mathbf{I}} + \mathbf{k}\mathbf{k}| = 0$. The determinant is a general relation for dispersion equation of the bulk modes propagating in a gyrotropic medium in any arbitrary direction. By plugging $\bar{\varepsilon}_r$ tensor and \mathbf{k} into the dispersion relation, we obtain two solutions for k_z as

$$k_{zj} = \sqrt{-q_\varphi^2 + \frac{1}{2\varepsilon_t} \left[-\kappa \pm \sqrt{\kappa^2 - 4\varepsilon_t \nu} \right]} \quad (6.15)$$

for $j \in \{1, 2\}$ where

$$\kappa = q_\rho^2 (\varepsilon_t + \varepsilon_a) + k_0^2 (\varepsilon_g^2 - \varepsilon_t (\varepsilon_t + \varepsilon_a)) \quad (6.16)$$

$$\nu = \varepsilon_a (q_\rho^2 - k_0^2 \varepsilon_t)^2 - \varepsilon_a \varepsilon_g^2 k_0^4. \quad (6.17)$$

Hence, the field in the gyrotropic region ($z < 0$) can be written as a superposition of two waves with the wave vectors $\mathbf{k}_j = \mathbf{k}_{tj} + q_\rho \hat{\rho}$ where $\mathbf{k}_{tj} = q_\varphi \hat{\phi} + k_{zj} \hat{\mathbf{z}}$. The electric field vector in the selected coordinate is written as $\mathbf{E}_j = \mathbf{E}_{0j} e^{i\mathbf{k}_j \cdot \mathbf{r}} = [\alpha_1 \hat{\mathbf{k}}_{tj} + \alpha_2 \hat{\rho} + \alpha_3 (\hat{\mathbf{k}}_{tj} \times \hat{\rho})] e^{i\mathbf{k}_j \cdot \mathbf{r}}$. By plugging \mathbf{E} , \mathbf{k} and $\bar{\varepsilon}_r$ into the wave equation, the unknown coefficients α_i are obtained. Then we have

$$\mathbf{E}_0 \sim \mathbf{k}_{tj} + q_\rho \theta_j \hat{\rho} + \Delta_j (\mathbf{k}_{tj} \times \hat{\rho}) \quad (6.18)$$

where

$$\Delta_j \equiv \frac{i\varepsilon_g k_0^2}{\varepsilon_t k_0^2 - k_j^2}, \quad \theta_j \equiv \frac{-k_{tj}^2}{\varepsilon_a k_0^2 - k_{tj}^2} \quad (6.19)$$

and the magnetic field is $\mathbf{H} = (\mathbf{k} \times \mathbf{E}) / \omega \mu_0$. In the isotropic region, the field can be expanded as $\mathbf{E} = [B_1 (\mathbf{k}_d \times \hat{\mathbf{z}}) + B_2 \mathbf{k}_d \times (\mathbf{k}_d \times \hat{\mathbf{z}})] e^{i\mathbf{k}_d \cdot \mathbf{r}}$ where $\mathbf{k}_d = q_\rho \hat{\rho} + q_\varphi \hat{\phi} + k_{zd} \hat{\mathbf{z}}$ and $k_d = k_0^2 \varepsilon_r$, taking into consideration the equality of the tangential momentum at the interface. Finally, we decompose the field vectors in both regions to their components in a regular polar coordinate system. Let $\bar{\mathbf{Y}}_g$ and $\bar{\mathbf{Y}}_0$ be the admittance tensors in the gyrotropic and the isotropic regions, respectively. The tangential electric and magnetic field components are related as

$$\begin{pmatrix} -\eta_0 H_\varphi \\ \eta_0 H_\rho \end{pmatrix}_{(2)} = \bar{\mathbf{Y}}_g \cdot \begin{pmatrix} E_\rho \\ E_\varphi \end{pmatrix}_{(2)} = \bar{\mathbf{Y}}_g \cdot \mathbf{E}_{||}^{(2)} \quad (6.20)$$

and

$$\begin{pmatrix} -\eta_0 H_\varphi \\ \eta_0 H_\rho \end{pmatrix}_{(1)} = \pm \bar{\mathbf{Y}}_0 \cdot \begin{pmatrix} E_\rho \\ E_\varphi \end{pmatrix}_{(1)} = \pm \bar{\mathbf{Y}}_0 \cdot \mathbf{E}_{||}^{(1)} \quad (6.21)$$

with the \pm sign indicates upward and downward propagating waves respectively and

$$\bar{\mathbf{Y}}_0 = \frac{1}{ik_0 \gamma_{zd}} \begin{pmatrix} -\gamma_{zd}^2 + q_\rho^2 & q_\rho q_\varphi \\ q_\rho q_\varphi & -\gamma_{zd}^2 + q_\varphi^2 \end{pmatrix} \quad (6.22)$$

$$\bar{\mathbf{Y}}_g = \frac{-1}{k_0 F} \begin{bmatrix} \Lambda_{11} & \Lambda_{12} \\ \Lambda_{21} & \Lambda_{22} \end{bmatrix} \quad (6.23)$$

have units of admittance where

$$F = q_\rho \theta_1 (q_\varphi - i\Delta_2 \gamma_{z2}) - q_\rho \theta_2 (q_\varphi - i\Delta_1 \gamma_{z1}) \quad (6.24)$$

$$\Lambda_{11} = q_\rho \Phi_1 (q_\varphi - i\Delta_2 \gamma_{z2}) - q_\rho \Phi_2 (q_\varphi - i\Delta_1 \gamma_{z1}) \quad (6.25)$$

$$\Lambda_{12} = -\theta_2 \Phi_1 q_\rho^2 + \theta_1 \Phi_2 q_\rho^2 \quad (6.26)$$

$$\Lambda_{21} = \Delta_1 k_{t1}^2 (q_\varphi - i\Delta_2 \gamma_{z2}) - \Delta_2 k_{t2}^2 (q_\varphi - i\Delta_1 \gamma_{z1}) \quad (6.27)$$

$$\Lambda_{22} = -\theta_2 \Delta_1 k_{t1}^2 q_\rho + \theta_1 \Delta_2 k_{t2}^2 q_\rho \quad (6.28)$$

with $\Phi_j = \Delta_j q_\varphi - i(\theta_j - 1)\gamma_{zj}$, $\gamma_{zd} = -ik_{zd}$, and $\gamma_{zj} = ik_{zj}$. In the isotropic region, $\mathbf{E}_{||}^{(1)} = \mathbf{E}_{||}^p + \mathbf{E}_{||}^s$ and $\mathbf{E}_{||}^s = \bar{\mathbf{R}}(\mathbf{q}) \cdot \mathbf{E}_{||}^p$. By imposing the continuity of tangential fields at $z = 0$, the reflection tensor is $\bar{\mathbf{R}} = (\bar{\mathbf{Y}}_0 + \bar{\mathbf{Y}}_g)^{-1} \cdot (\bar{\mathbf{Y}}_0 - \bar{\mathbf{Y}}_g)$.

6.3 Electric Field Profile of Curved SPPs and Their Propagation Properties

In this section, we calculate the scattered electric field using integral relation (6.12) derived from the above Green's function analysis. We obtained the field density profile shown in Fig. 6.3a by computing the electric field of the observation points on a plane above the interface with local position $(\rho, \phi_r, z = 0.003\lambda_p)$, where $\lambda_p = 2\pi/\omega_p$. The top region is a dielectric with $\varepsilon_r = 8$. The plot shows one-way SPPs with CCW propagation on a circular path. For comparison, we generated Fig. 6.3b based on a numerical computation using COMSOL, which is consistent with the GF result. The following carrier parameters is used to characterize the magnetized; $n_e = 3.6 \times 10^{21} \text{m}^{-3}$, $m^* = 0.0175m_0$, $\varepsilon_\infty = 15.68$, $B_0 = 0.6 \text{T}$ and $\Gamma = 0.00015\omega_p$. Next, the data are extracted from the circular traces shown by white dashed lines and shown in the line graph in Fig. 6.3c. As shown, the results arising from the GF model are very close to the COMSOL results, which

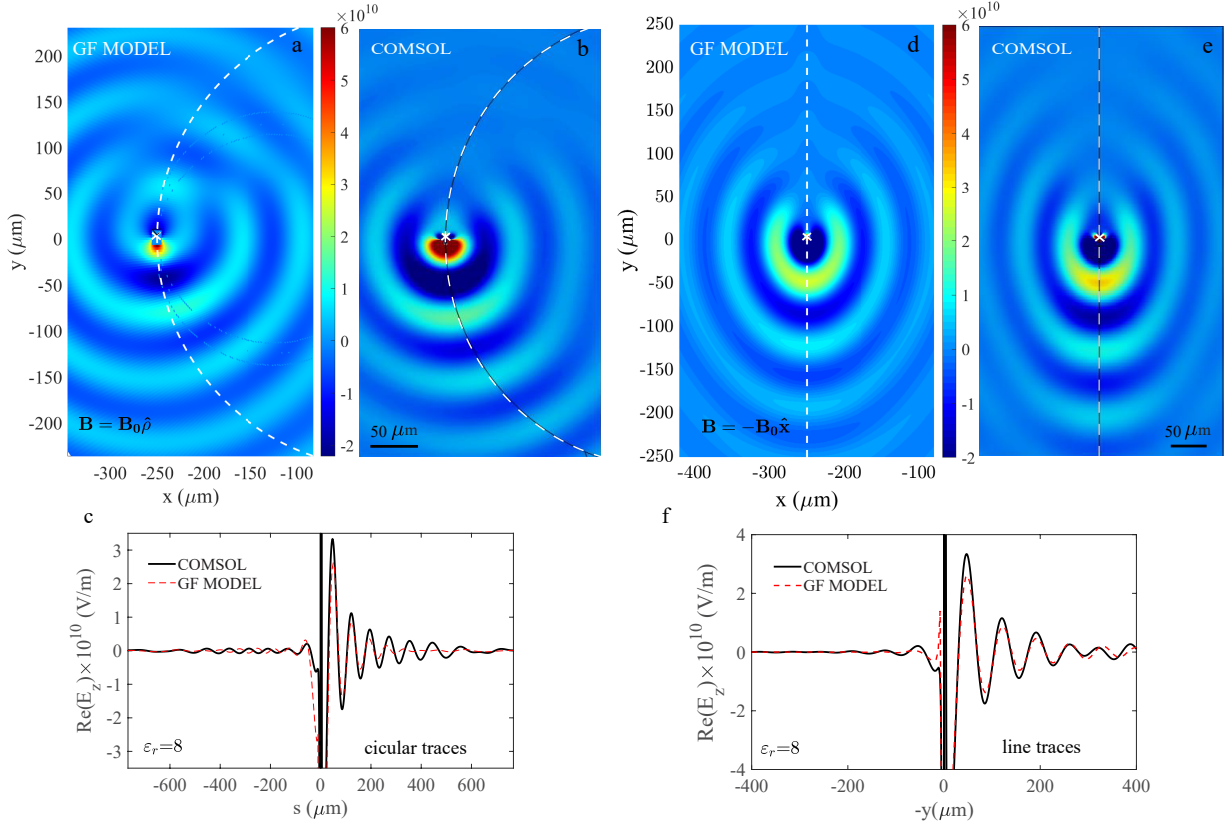


Figure 6.3: Electric field distribution (E_z) of the curved SPPs excited at the interface of dielectric/ radially magnetized plasma ($\mathbf{B} = B_0 \hat{\rho}$) media using (a) Green's function model (6.12) and (b) a full-wave COMSOL simulation. The radial bias is centered on the origin and the dipole with input power 1W is located at $(250\mu\text{m}, \pi, 0)$. The observation points are on a plane with distance $z = 0.003\lambda_p$ above the interface ($\lambda_p = 2\pi/\omega_p$). (c) The electric field oscillation along the circular trajectories (white dashed semicircles). The electric field profile of the linear propagating SPPs excited at the interface of the dielectric/axially biased plasma ($\mathbf{B} = -B_0 \hat{x}$) using (d) GF model (e) COMSOL simulation. (f) The extracted data from dashed line trajectories. The resonance frequency is $f = 1.567$ THz. Reprinted with permission from [7].

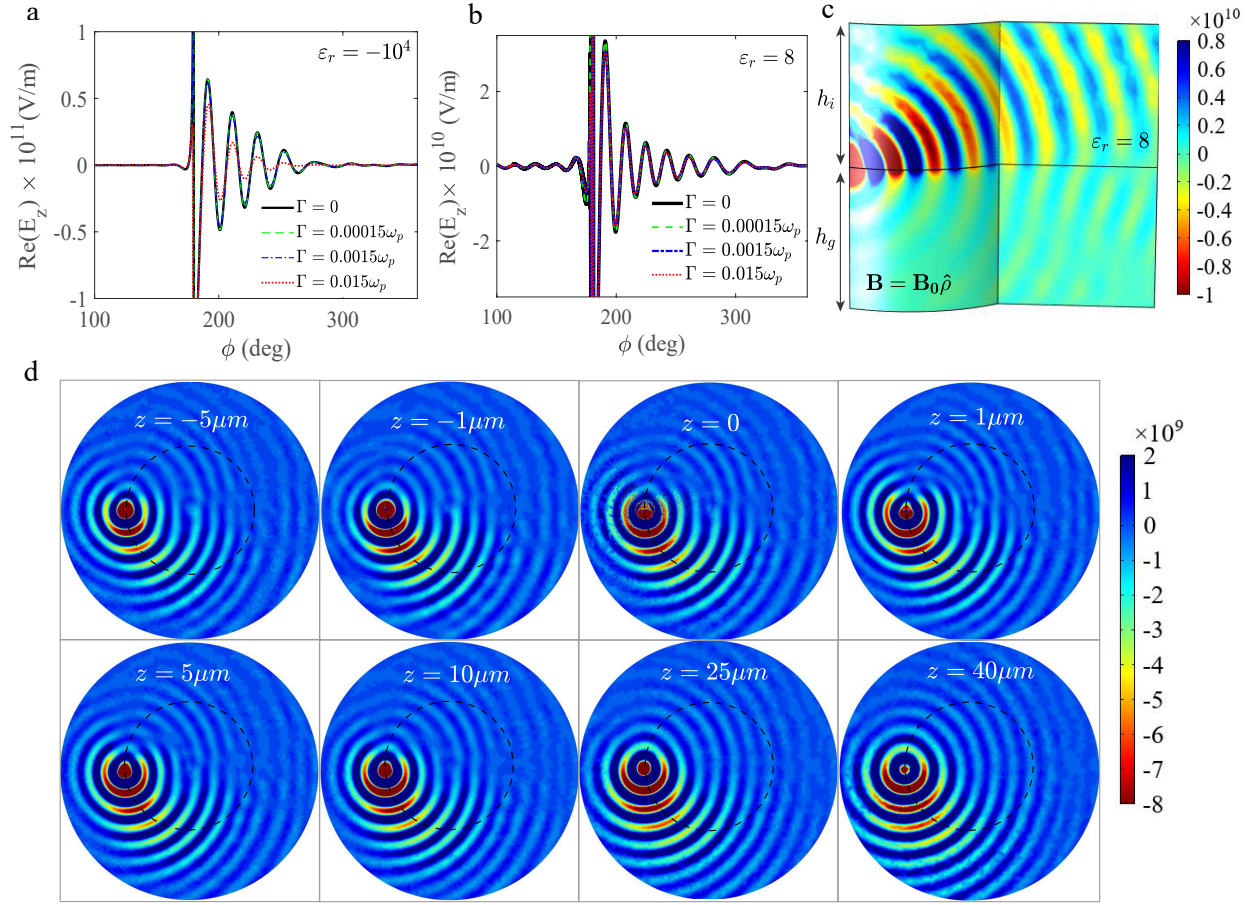


Figure 6.4: (a,b) Unidirectional curved SPPs by considering different amounts of dissipation (metal or dielectric on top) (c) A vertical cross-section view of the two-layer magnetized system ($h_i = h_g = 200\mu\text{m}$). Energy leakage occurs in the dielectric region after several wavelengths of curved SPP propagation (d) Electric field density of the curved SPPs on the surfaces parallel to the interface located at different distances (z) from the interface $z = 0$ ($\epsilon_r = 8$). $n_e = 3.6 \times 10^{21}\text{m}^{-3}$, $m^* = 0.0175m_0$, $\epsilon_\infty = 15.68$, $B_0 = 0.6\text{T}$, $f = 1.567\text{THz}$. Reprinted with permission from [7].

validates the accuracy of our GF model for radially biased system.

We also develop the GF model presented in [86, 131] for an axial bias along the $-x$ direction. For this case, the SPPs are propagating along a straight line. Figure 6.3d and 6.3e demonstrate the electric field density and Fig. 6.3g shows the SPP oscillation along the dashed line trajectories using axial GF model and COMSOL simulation.

Figure 6.4a,b shows the unidirectional curved SPP oscillation along the circular path in the radially magnetized system by considering different amounts of dissipation when the top region is metal or dielectric. As shown, by reducing the loss, the magnitude increases and the curved SPPs propagate longer, as expected. However, even in a loss-less system the SPPs do not rotate on a full circle. They stop their orbital propagation

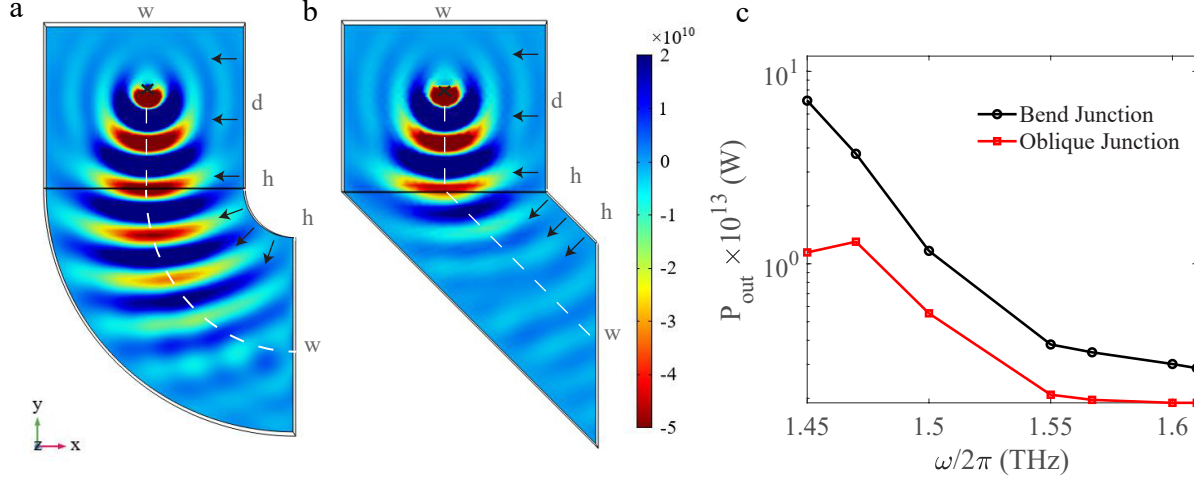


Figure 6.5: Electric field profile of the SPP propagating at the interface of metal/magnetized plasma, passing through (a) a 90° circular bend junction under radial bias vs. (b) an oblique junction under $5\pi/4$ axial bias. (c) Output power vs. frequency. $n_e = 3.6 \times 10^{21} \text{m}^{-3}$, $m^* = 0.0175m_0$, $\varepsilon_\infty = 15.68$, $B_0 = 0.6 \text{T}$, $\Gamma = 0.00015\omega_p$, $\varepsilon_r = -10^4$, $f = 1.567 \text{THz}$, $w = 4h = 360 \mu\text{m}$, $d = 300 \mu\text{m}$. Reprinted with permission from [7].

on the surface after several SPP wavelengths of propagation and they radiate to the plasma or dielectric region. The leakage to the dielectric is illustrated in Fig. 6.4c, showing a vertical cross section of the system (including the dielectric and the radially magnetized plasma); a cut cylinder that is intersected by a plane. The curved SPP is leaky for this operating frequency, as discussed in Section 6.1. In addition, for the case of dielectric on top, the mode lies within the light cone of the dielectric region. Figure 6.4d shows the electric field profile on surfaces parallel to the interface, located at different heights below and above the interface. In the plasma region and close to the surface, the SPPs spiral on a circle centered at the origin. In the dielectric region, they remain on this path at distances close to the interface. Moving farther vertically from the interface, SPPs spiral out of the circle. We also observed that SPPs are more confined to the surface when the top layer is a metal.

6.4 An Application for Curved SPPs

Waveguide bends connecting two straight waveguides are important components in plasmonic integrated circuits. Using unidirectional curved SPPs, a bent waveguide with minimal bending loss can be designed. We propose that a 90-degree circular bend magnetized by a radial bias can be used as a nonreciprocal plasmonic junction. As shown in Fig. 6.5a, the excited unidirectional SPPs steer from a straight line to a circular path through the 90 degree bend, resulting in reduction of the radiation loss due to the curvature of the waveguide junction. Black arrows indicate the magnetic bias vectors applied in each segment. It forms an optical nonreciprocal plasmonic junction, which allows power transmission only in one direction.

To provide a comparison to the axial-bias case, in Fig. 6.5b, two straight waveguides are connected by an oblique junction magnetized by an axial bias with angle of $5\pi/4$ radian. When unidirectional SPPs reach the input port of the oblique junction, they change direction and align themselves along a line perpendicular to the bias. That is because the unidirectional SPPs inherently tend to propagate perpendicular to the magnetic bias at frequencies within the nontrivial bandgap.

The surface power that flows through these two junctions are computed at the output ports for different operating frequencies within the upper bandgap and shown in Fig. 6.5c. The power is transmitted through the radially magnetized circular bend more than two times higher than the power transmitted through the oblique junction. In addition, the power transmission is significantly higher than an unbiased circular junction. In the circular bend with radial bias, the energy routing only occurs in one direction. By reversing the magnetic field direction, the energy is routed in the opposite direction.

6.5 Summary

To sum up, in this chapter we obtained unidirectional curved SPPs by applying an in-plane radial magnetic bias in topological continua. In a magnetized system, the unidirectional SPP trajectories are steerable by the magnetic bias direction. We derived a Green's function model for a radially magnetized system. The properties of the unidirectional curved SPPs were compared to the linear SPPs. Using unidirectional curved SPPs, a nonreciprocal bent waveguide with minimum bending loss was proposed for plasmonic integrated circuits.

Chapter 7

Nonreciprocal Effects in CrI₃/graphene Heterostructure vs. Magnetized graphene Monolayer

In this chapter we examine the unidirectional SPPs in two-dimensional plasmonic platforms. First, we discuss the topological behaviors of a graphene monolayer magnetized by external magnets. Then, we consider a ferromagnetic monolayer underneath graphene and examine the nonreciprocal response of this multi-layer structure due to the exchange field. We evaluate whether this 2D magnet can be alternatively used instead of external bulky magnets to create strong non-reciprocity or not. Elimination of the external magnets in this way leads to invention of magnet-less nonreciprocal devices for planar applications.

This chapter is organized as follow. First we discuss and compare the optical conductivity of isolated graphene monolayer and CrI₃/graphene multi-layer. Then, we obtain dispersion diagram of surface modes propagating on infinite sheet of graphene biased by an external magnetic field as well as those propagating on CrI₃ heterostructure. Next, we derive an approximation dispersion relation for the edge modes excited the the edge of a semi-infinite sheet. We look for the nonreciprocal edge modes in both structures under study. Finally, we compute the Faraday rotation. In this regard, we have published article [8] in the journal Physical Review B.

7.1 Optical Conductivity of Graphene and CrI₃/Graphene

Consider a graphene sheet located on the x-y plane and biased by the electrostatic electric and magnetic fields $\mathbf{E}_0 = E_0 \hat{\mathbf{z}}$ and $\mathbf{B}_0 = B_0 \hat{\mathbf{z}}$. Graphene is characterized by the conductivity tensor

$$\bar{\sigma}(\omega, \mu_c, \tau, T, B_0) = \begin{bmatrix} \sigma_{xx} & \sigma_{xy} \\ \sigma_{yx} & \sigma_{yy} \end{bmatrix} = \begin{bmatrix} \sigma_d & \sigma_o \\ -\sigma_o & \sigma_d \end{bmatrix}, \quad (7.1)$$

where $\sigma_{xx} = \sigma_{yy} = \sigma_d$ and $\sigma_{xy} = -\sigma_{yx} = \sigma_o$. Using the Kuba formalism, the diagonal and off-diagonal conductivity terms are defined as [134–136]

$$\begin{aligned} \sigma_d = & \frac{e^2 v_f^2 |eB_0| (\omega - i2\Gamma)\hbar}{-i\pi} \sum_{n=0}^{\infty} \\ & \left\{ \frac{f_d(M_n) - f_d(M_{n+1}) + f_d(-M_{n+1}) - f_d(-M_n)}{(M_{n+1} - M_n)^2 - (\omega - i2\Gamma)^2 \hbar^2} \left(1 - \frac{\Delta^2}{M_n M_{n+1}}\right) \frac{1}{M_{n+1} - M_n} \right. \\ & \left. + \frac{f_d(-M_n) - f_d(M_{n+1}) + f_d(-M_{n+1}) - f_d(M_n)}{(M_{n+1} + M_n)^2 - (\omega - i2\Gamma)^2 \hbar^2} \left(1 + \frac{\Delta^2}{M_n M_{n+1}}\right) \frac{1}{M_{n+1} + M_n} \right\}, \end{aligned} \quad (7.2)$$

and

$$\begin{aligned} \sigma_o = & -\frac{e^2 v_f^2 e B_0}{\pi} \sum_{n=0}^{\infty} \{ [f_d(M_n) - f_d(M_{n+1}) - f_d(-M_{n+1}) + f_d(-M_n)] \times \\ & [(1 - \frac{\Delta^2}{M_n M_{n+1}}) \frac{1}{(M_{n+1} - M_n)^2 - (\omega - i2\Gamma)^2 \hbar^2} \\ & + (1 + \frac{\Delta^2}{M_n M_{n+1}}) \frac{1}{(M_{n+1} + M_n)^2 - (\omega - i2\Gamma)^2 \hbar^2}] \}, \end{aligned} \quad (7.3)$$

where

$$M_n = \sqrt{\Delta^2 + 2n v_f^2 |e B_0| \hbar}, \quad (7.4)$$

and f_d is the Fermi-Dirac distribution function

$$f_d(\epsilon) = \frac{1}{e^{(\epsilon - \mu_c)/k_B T} + 1}, \quad (7.5)$$

where $-e$ is the electron charge, Δ is the energy gap, ϵ denotes energy, \hbar is the reduced Planck's constant, k_B is the Boltzmann's constant, ω is radial frequency, T is temperature, τ is scattering time which is associated to the collision frequency as $\Gamma = 1/2\tau$. μ_c is chemical potential which is proportional to the carrier density and can be controlled by the electric bias and doping. In the absence of the magnetic bias, graphene is an isotropic material. By applying the magnetic field bias, it turns to a gyrotropic material. When the magnetic field intensity is low ($B_0 \rightarrow 0$), the energy gap is negligible ($\Delta \approx 0$). In this condition, the diagonal conductivity term can be expanded in the integral form as

$$\sigma_d = \frac{ie^2(\omega - i2\Gamma)}{\pi \hbar^2} \left[\frac{1}{(\omega - i2\Gamma)^2} \int_0^\infty \epsilon \left(\frac{\partial f_d(\epsilon)}{\partial \epsilon} - \frac{\partial f_d(-\epsilon)}{\partial \epsilon} \right) d\epsilon - \int_0^\infty \frac{f_d(-\epsilon) - f_d(\epsilon)}{(\omega - i2\Gamma)^2 - 4(\epsilon/\hbar)^2} d\epsilon \right], \quad (7.6)$$

where the first term represents the intra-band contributions, and the second term represents the inter-band contributions ($\sigma_d = \sigma_{d,\text{intra}} + \sigma_{d,\text{inter}}$). The intra-band term can be written as a close form as

$$\sigma_{d,\text{intra}} = -i \frac{e^2 k_B T}{\pi \hbar^2 (\omega - i2\Gamma)} \left(\frac{\mu_c}{k_B T} + 2 \ln(e^{-\mu_c/k_B T} + 1) \right), \quad (7.7)$$

and in the limit $k_B T \ll \mu_c, \hbar \omega$, the inter-band term is approximately given by

$$\sigma_{d,\text{inter}} \simeq \frac{-ie^2}{4\pi \hbar} \ln \left(\frac{2\mu_c - (\omega - i2\Gamma)\hbar}{2\mu_c + (\omega - i2\Gamma)\hbar} \right). \quad (7.8)$$

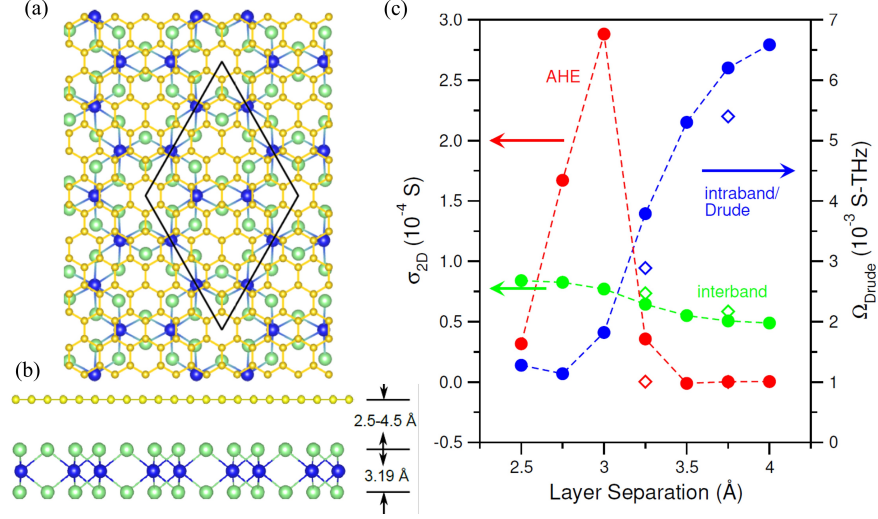


Figure 7.1: (a) Top and (b) side views of the $(\sqrt{3} \times \sqrt{3})$ CrI₃-(5×5) graphene structure (C: yellow; Cr: blue; I: green), with the commensurate supercell given in black. (c) Calculated 2D contributions to the optical properties: Drude intraband contribution, Ω_{Drude} (blue); anomalous Hall, σ_{xy}^{2D} (red); and interband, σ_{xx}^{2D} (green). The empty diamonds at 3.25 and 3.75 Å correspond to the twisted (2×2) CrI₃-($\sqrt{31} \times \sqrt{31}$) graphene calculations. Reprinted with permission from [8], and generated by Prof. Weinert.

For low magnetic field intensity, the off-diagonal Hall conductivity term is given by

$$\sigma_o = -\frac{e^2 v_f^2 e B_0}{\pi \hbar^2} \left[\frac{1}{(\omega - i2\Gamma)^2} \int_0^\infty \left(\frac{\partial f_d(\epsilon)}{\partial \epsilon} + \frac{\partial f_d(-\epsilon)}{\partial \epsilon} \right) d\epsilon + \int_0^\infty \frac{\left(\frac{\partial f_d(\epsilon)}{\partial \epsilon} + \frac{\partial f_d(-\epsilon)}{\partial \epsilon} \right)}{(\omega - i2\Gamma)^2 - 4(\epsilon/\hbar)^2} d\epsilon \right]. \quad (7.9)$$

Similarly, the first term represents the intra-band Hall contribution which is simplified to a close form as

$$\sigma_{o,\text{intra}} = -\frac{e^2 v_f^2 e B_0}{\pi \hbar^2 (\omega - i2\Gamma)^2} \left[1 - \frac{2}{e^{-\mu_c/k_B T} + 1} \right] \quad (7.10)$$

CrI₃ is a monolayer ferromagnetic insulator providing the magnetic moment of $3\mu_B$. The electronic band structure and magneto-optical response of this monolayer has been studied in Ref. [137]. In Ref. [116], it is derived that graphene and CrI₃ ferromagnetic monolayer form a van der Waals (vdW) heterostructure based on the first-principle calculations. CrI₃ induces a strong magnetic exchange field in the graphene layer, leading to the realization of quantum Hall effects. At equilibrium distance, since the Dirac points of graphene is not located in the bandgap of CrI₃, the Chern insulator states are not exist. However, it can be solved by applying pressure perpendicular to the plane to reduce the distance between the monolayers and tune the Dirac point in the CrI₃ bandgap. In Ref. [8], Prof. Weinert has studied the electronic band structure of CrI₃/graphene due to the effect of exchange field, and computed the optical conductivity of this multi-layer using density functional theory.

The top and side view of vdW heterostructures of CrI₃/graphene is shown in Fig. 7.1a and b, respectively,

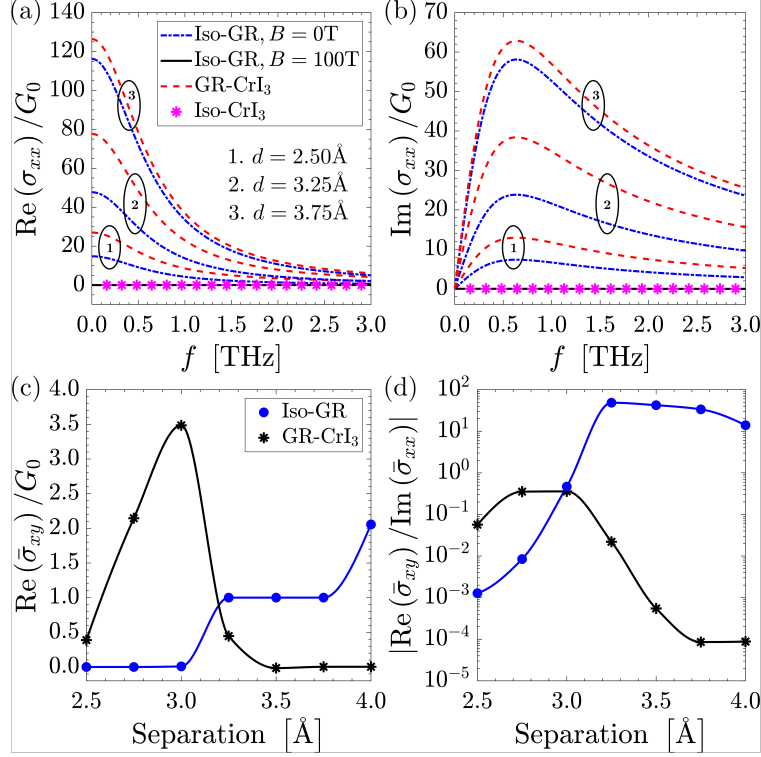


Figure 7.2: (a, b): Two-dimensional conductivity of graphene in the presence of the CrI_3 exchange field for separations $d \in \{2.5\text{\AA}, 3.25\text{\AA}, 3.75\text{\AA}\}$, and the conductivity of isolated graphene (Iso-GR) computed by considering an external field of 100T, the chemical potential $\mu = -0.3$ eV, $\Gamma = 2 \times 10^{12} \text{ s}^{-1}$ and $T = 40$ K. (c) Off-diagonal element vs. CrI_3 -graphene separation compared with the isolated-graphene external bias case. (d) The off-diagonal element normalized by the frequency average of the diagonal element. $G_0 = 2e^2/h$. Reprinted with permission from [8], and generated by coauthor A. Holmes using the optical conductivity data computed by Prof. Weinert.

which is composed of 5×5 graphene on a free-standing $\sqrt{3} \times \sqrt{3}$ CrI_3 monolayer with a small lattice mismatch of $\sim 1\%$. The separation distance between two layers varies in range of 2.5-4.5 \AA . The 2D optical conductivity for graphene- CrI_3 and isolated graphene were calculated within the independent particle approximation [138] and shown in Fig. 7.1c. For graphene, with its linearly dispersing bands, the real part of the interband contribution of $\sigma_{2D}^{xx}(\omega)$ goes to $e^2/4\hbar$ for low frequencies; the calculated conductivity correctly obeys this limit, suggesting that the computational parameters (particularly k -point sampling) are adequate for the present purposes. The intraband Drude-like contribution to the 2D conductivity tensor, $\sigma_{2D}^{\text{Drude}}$, is given in terms of the plasma frequency tensor ω_p^2

$$(\omega_p^2)_{\alpha\beta} \sim \sum_{nk} f_{nk} \frac{\partial^2 \epsilon_{nk}}{\partial k_\alpha \partial k_\beta} \quad (7.11)$$

by

$$\sigma_{2D}^{\text{Drude}} = \frac{L}{4\pi} \frac{(\hbar\omega_p)^2}{(\hbar\omega)^2 + (\hbar\gamma)^2} (\gamma + i\omega) \quad (7.12)$$

$$\equiv \Omega_{\text{Drude}} \frac{\gamma_\nu + i\nu}{\nu^2 + \gamma_\nu^2}, \quad (7.13)$$

where $\omega = 2\pi\nu$ and $\gamma_\nu = 2\pi\gamma$. As expected, Ω_{Drude} increases as the Fermi level crosses into the CrI₃ conduction band. For reasonable values of $\hbar\gamma$, the intraband dominates the interband contribution to σ_{xx} .

Because of the exchange field due to the CrI₃, there is a small contribution to σ_{xy} , but the largest contribution (within the present approximations) comes from the anomalous Hall effect (AHE),

$$\sigma_{xy}^{\text{AHE}} \sim \text{Im} \sum_{nm} (f_n - f_m) \langle u_m | \frac{d}{dk_x} u_n \rangle \langle u_m | \frac{d}{dk_y} u_n \rangle^* . \quad (7.14)$$

This term grows, and is large, as the graphene Dirac point and Fermi level approach the bottom of the CrI₃ conduction band, and then a sudden collapse as the Fermi level crosses into the CrI₃. Thus, for the equilibrium spacing, this contribution is again small. If the large value of σ_{xy} is due to the proximity of the Fermi level near the bottom of the CrI₃ conduction band – and the existence of mini-bands in the graphene majority bands – it is possible that a GW or hybrid functional calculation that increases the gap might show a large AHE contribution at the equilibrium separation.

The optical conductivity elements of CrI₃/graphene are shown in Fig. 7.2, based on the data computed by Prof. Weinert in [8]. For comparison, the plot also shows the conductivity computed (i) assuming isolated graphene in an external bias of 100 T and $\mu = -0.3\text{eV}$ [135], the effective equilibrium exchange field and potential as described above; (ii) isolated graphene $B = 0$ T using μ^\pm for separations $d \in \{2.5\text{\AA}, 3.25\text{\AA}, 3.75\text{\AA}\}$; and (iii) the calculated CrI₃ conductivity [137], which is negligible at the considered frequencies. Figures 7.2a and b show the diagonal elements vs. frequency, and Fig. 7.2c shows the off-diagonal element vs. CrI₃-graphene separation (which are nondispersive in our calculation). For the external bias case, Fig. 7.2c, the effective fields (“below the Dirac point” values) corresponding to different separation are assumed. In Fig. 7.2c,d, we show the mean conductivity for 0 to 5 THz. As an example, for the CrI₃-graphene data (for a separation of 3.75 Å), this mean is 33 G_0 , and for isolated biased graphene ($B_0 = 100$ T), 0.03488 G_0 . The diagonal elements of the conductivity are dominated by the Drude intraband contribution at the considered frequencies ($\sigma_{xx}^{2D-\text{Drude}} = i\Omega/(\omega + 2i\Gamma)$), and resemble very closely the conductivity for isolated graphene with no magnetic bias, but with the exchange-field induced spin-dependent values of chemical potential μ^\pm . Because of transfer of the Drude weight to the Landau levels in the case of an external bias, the exchange field diagonal conductivity is several orders of magnitude larger than the equivalent external field conductivity, i.e., for the external bias case, the formation of Landau levels depresses the diagonal conductivity away from

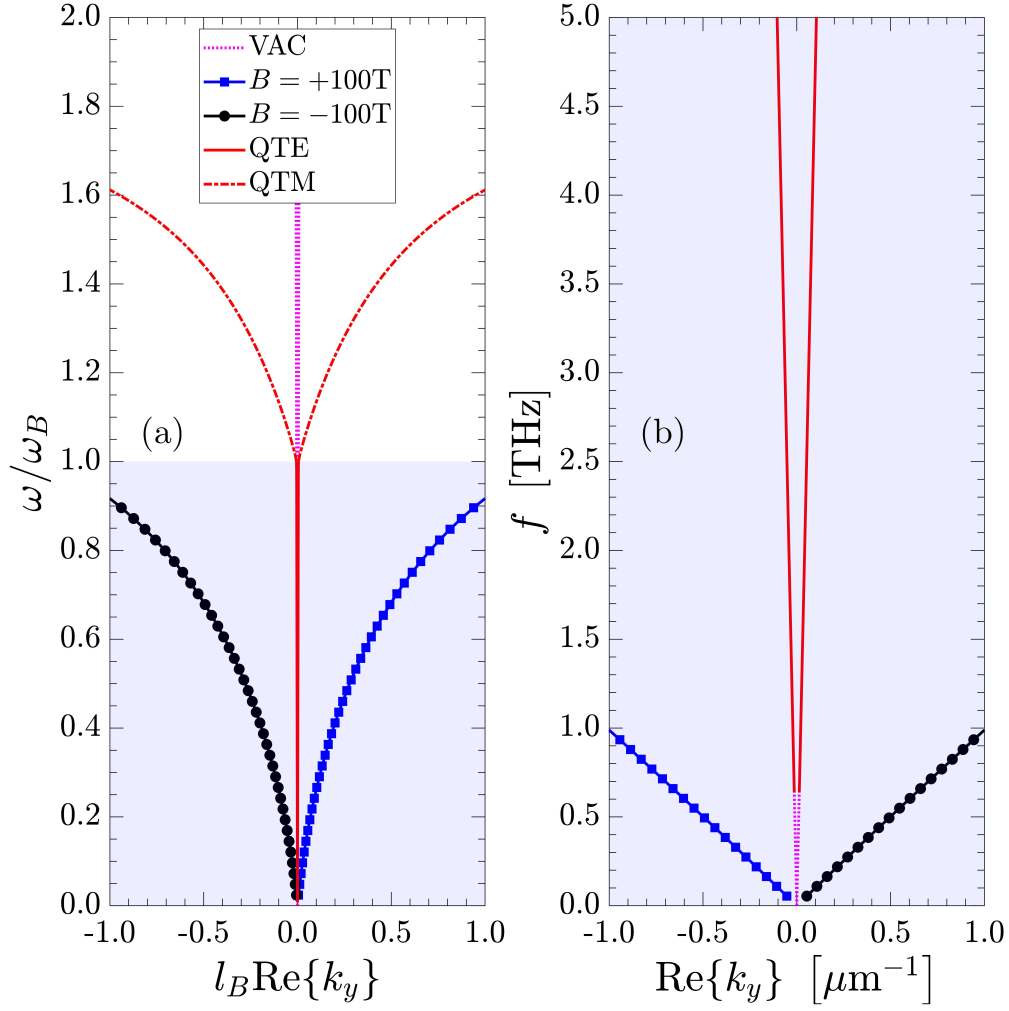


Figure 7.3: Dispersion bands of bulk quasi TM (dashed red) and bulk quasi TE modes (solid red) for graphene in an external bias. The blue dots show the TM edge modes for external bias $B = 100\text{T}$ and black dots are the edge modes when the bias is reversed ($B = -100\text{T}$). The shaded region indicates the bulk band gap. $\omega_B = 526.2 \times 10^{12}$ is the frequency of the first Landau level, $\mu = -0.3$ eV, $T = 40$ K, $\Gamma = 2 \times 10^{12} \text{ s}^{-1}$, $B = 100$ T, and $l_B = \sqrt{\hbar/eB} = 2.6$ nm is the magnetic length. VAC indicates vacuum dispersion. Panel b is a better illustration of the optical response at low frequency range by applying denormalized scales in the axes. Reprinted with permission from [8], and generated by coauthor A. Holmes.

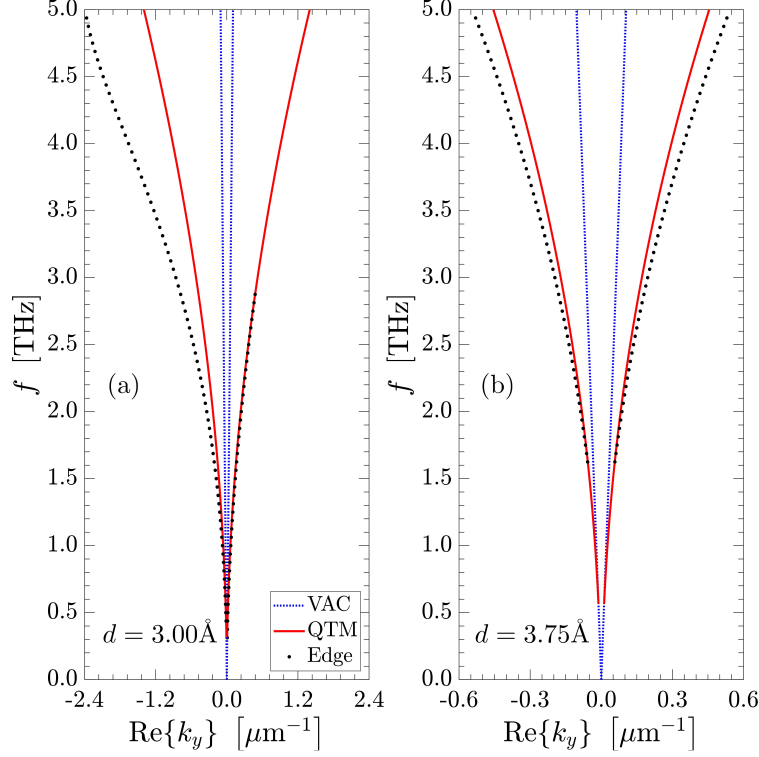


Figure 7.4: Bulk (solid red) and edge (dots) TM-like dispersion of graphene modes in an exchange field for two CrI₃-graphene separations. VAC indicates vacuum dispersion. Reprinted with permission from [8], and generated by coauthor A. Holmes.

the Landau level, while forcing the off-diagonal elements to be nonzero due to cyclotron motion of the charge carriers. This results in relatively large ratios of the off-diagonal to diagonal elements for the external bias, in contrast to the exchange bias case where the diagonal elements are relatively unaffected and hence the ratios are smaller.

For some separations, the corresponding chemical potential is quite different for the two spins, as is the effective bias field. Therefore, for the external bias computation, we adjust the spins accordingly and sum over the two spins. For the off-diagonal elements, the exchange field values are similar in magnitude to the external bias case having the same effective field. Figure 7.2d shows the off-diagonal values of the conductivity normalized by the frequency average of the diagonal element since this ratio is an indication of the non-reciprocity of the material. Notably, the non-reciprocity of the exchange field case is much weaker than for the external field bias.

From Fig. 7.2, the CrI₃ conductivity is much smaller in magnitude than that of graphene. Since these effectively combine in parallel from an electromagnetic standpoint, we can ignore the presence of the CrI₃ in the electromagnetic calculations. This was confirmed by computing the dispersion of the CrI₃-graphene system including both conductivities, as in [139].

7.2 Surface Bulk Modes in the Infinite Sheets of Graphene and CrI3/Graphene

Consider a two-dimensional (2D) material surface with anisotropic surface conductivity. The infinite sheet is coated by an isotropic material characterized by μ_0 and ε . In Ref. [140], a dyadic Green's function model has been presented for a general 2D anisotropic surface and the field was obtained in terms of Sommerfeld integral. The surface modes propagating on the surface with the wavevector $\mathbf{k} = k_x \hat{\mathbf{x}} + k_y \hat{\mathbf{y}}$ satisfy a dispersion equation of the form

$$D(k_x, k_y) = k_x k_y (\sigma_{yx} + \sigma_{xy}) + (k_y^2 - k_1^2) \sigma_{yy} = 0 \\ + (k_x^2 - k_1^2) \sigma_{xx} - 2ip\varepsilon\omega \left(1 + \frac{1}{4}\eta^2 (\sigma_{xx}\sigma_{yy} - \sigma_{xy}\sigma_{yx}) \right), \quad (7.15)$$

where $p = \sqrt{k^2 - k_1^2}$, $k = |\mathbf{k}|$ is the in-plane wave number, and $k_1 = \omega\sqrt{\mu_0\varepsilon}$ is the dielectric wavevector. The square root in p leads to a two-sheeted Riemann surface in the q -plane, and associated branch cuts. The standard hyperbolic branch cuts [141] separate the proper (where $\text{Re}(p) > 0$, such that the radiation condition as $|z| \rightarrow \infty$ is satisfied) and improper sheets. By substituting $\sigma_{xx} = \sigma_{yy} = \sigma_d$ and $\sigma_{xy} = -\sigma_{yx} = \sigma_o$, Eq. (7.15) reduces to

$$D(k) = (p^2 - k_1^2) s_d - ipk_1 (1 + s_d^2 + s_o^2), \quad (7.16)$$

where $s_d = \eta\sigma_d/2$, $s_o = \eta\sigma_o/2$, and $\eta = \sqrt{\mu_0/\varepsilon}$, and $D(k) = 0$ can be solved to yield

$$k^\pm = k_1 \left[\frac{1}{2s_d^2} \left(-is^2 \pm \sqrt{4s_d^2 - s^4} \right)^2 + 1 \right]^{1/2}, \quad (7.17)$$

where $s^2 = s_d^2 + s_o^2 + 1$. For an isotropic 2D sheet, $s_o = 0$, then Eq. (7.17) becomes

$$k^+ = k^{TM} = k_1 \sqrt{1 - \frac{1}{s_d^2}}, \quad k^- = k^{TE} = k_1 \sqrt{1 - s_d^2}, \quad (7.18)$$

for the transverse-magnetic (TM) and transverse-electric (TE) cases, respectively, where transverse is defined with respect to the radial coordinate. For isolated and unbiased graphene characterized by isotropic complex surface conductivity, $\sigma = \sigma' + i\sigma''$, a proper TE surface wave exists if and only if $\sigma'' < 0$, and a proper TM surface wave exists for $\sigma'' > 0$. If $\mu \neq 0$, pure TM and TE modes do not exist in the presence of a magnetic bias, although usually the modes retain similar characteristics (quasi-TM/TE). Using these relations, we can obtain the surface bulk modes in an infinite graphene sheet biased by an external static magnetic field or CrI3/Graphene under the exchange field by applying the corresponding conductivity elements.

The dispersion diagram of surface bulk modes for graphene in an external magnetic bias field are shown in Fig. 7.3 (dot and solid red lines). Due to the normalization, the dispersion diagrams are essentially independent of B for $|B| \gtrsim 1$ T. For the external bias case, the Landau levels are given by

$$M_n = \sqrt{2nv_F^2 |eB| \hbar} \approx 36.3 \text{ meV } \sqrt{n |B|}, \quad (7.19)$$

where $v_F \simeq 10^6$ m/s is the graphene electron Fermi velocity.

Figure 7.4 (red lines) shows the bulk dispersion for a graphene half-space due to the exchange fields corresponding to separations of 3.0 Å, Fig. 7.4(a), and 3.75 Å, Fig. 7.4(b).

For the exchange field (Fig. 7.4), the bulk SPPs are not gapped, whereas for the external bias case (Fig. 7.3) the bulk SPPs are strongly gapped. This is a result of the behavior of $\text{Im}(\sigma)$: Since TM and quasi-TM modes require $\text{Im}(\sigma) > 0$ for a proper surface wave, gaps appear for $\text{Im}(\sigma) < 0$, which does not occur for the exchange case in the far-infrared, where the conductivity dispersion is Drude-like. In the external bias case, the formation of Landau levels causes this sign change at lower frequencies, resulting in the TM gap shown in Fig. 7.3.

7.3 Unidirectional Edge Modes in the Semi-Infinite Sheets of Graphene and CrI3/Graphene

Consider a laterally-infinite anisotropic sheet located at $z = 0$, with an edge at $y = 0$. The localized edge modes propagating on the edge can be found using a quasi-static approximation. Following the methods in Refs. [142–144], we derive the following approximated relation for the edge modes

$$|k_y| = \bar{\varepsilon} \frac{1 + \sqrt{2}}{\eta_{xx} \pm \chi_{xy}}. \quad (7.20)$$

where $\bar{\varepsilon} \equiv (\varepsilon_1 + \varepsilon_2)/2$, and $\eta_{xx} \equiv \sigma_{xx}/i\omega$ and $\chi_{xy} \equiv \sigma_{xy}/\omega$. The detail of computation is in Ref. [8]-Appendix II.

The dispersion diagram of edge modes in semi-infinite graphene sheet under an out of plane external magnetic bias is shown in Fig. 7.3 (black and blue lines). The edge modes dispersion is asymmetric. The edge modes cross the surface bulk bandgap and they are unidirectional. They flip directions upon reversing the bias field (black curve turns to the blue curve).

Figure 7.4 (black dot-lines) shows the edge dispersions for a graphene half-space due to the exchange fields corresponding to separations of 3.0 Å and 3.75 Å. For 3 Å separation, the right-going edge mode exists until approximately 3 THz, above which the edge mode leaks into the bulk SPP (mathematically, it crosses

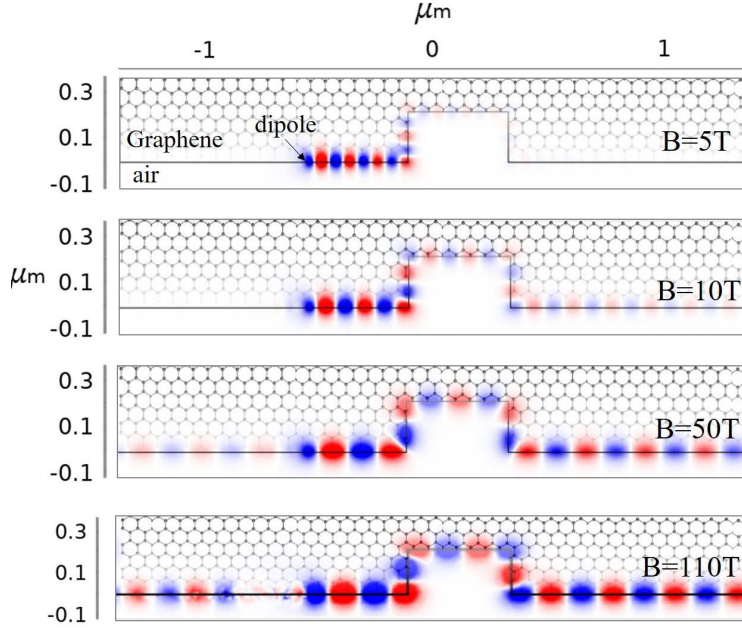


Figure 7.5: Edge SPP launched by a dipole source near the graphene edge for several values of external magnetic bias. $f = 13.87$ THz, $\mu=0.05$ eV, $T=40$ K, $\Gamma = 2 \times 10^{12}$ s $^{-1}$. Reprinted with permission from [8].

onto an improper Riemann sheet through a branch point associated with the bulk mode wave number); the leaky mode (not shown) then approximately follows the bulk dispersion, with slightly lower wave number. In this case, the edge mode is strongly nonreciprocal (unidirectional). However, for the equilibrium separation of 3.75 \AA separation, the edge mode is essentially reciprocal.

Figure 7.5 shows the edge SPP on externally-biased graphene due to a dipole source in the vicinity of the edge, computed using COMSOL. The size of the discontinuity is on the order of λ_{SPP} (e.g., the length of the discontinuity contour in the second panel is $5\lambda_{\text{SPP}}$). It is clear that as the magnetic bias increases, the SPP propagates further, while its wavelength increases. The edge SPP is clearly robust, and propagates around the discontinuity with no reflection or diffraction. The edge modes are unidirectional and propagating only in one direction. Their propagation properties are consistent with dispersion diagram in Fig. 7.3.

Figure 7.6 shows the edge SPP on the exchange-field biased graphene due to a dipole source in the vicinity of the graphene-vacuum edge, computed using COMSOL. In correspondence with the dispersion shown in Fig. 7.4, for the equilibrium separation of 3.75 \AA the SPP is essentially reciprocal and propagating in both directions, as it is at 2.5 THz for separation 3 \AA . However, for 3 \AA and 4 THz, the SPP is unidirectional. However, because $L_{\text{SPP}}/\lambda_{\text{SPP}}$ is short, the SPP does not propagate well.

Figure 7.7a, and b show edge SPP propagation length and guided wavelength on the graphene layer as a function of CrI₃-graphene separation. The SPP propagation length $1/2\text{Im}(k_y)$ generally increases with separation, and decreases with increasing frequency. The SPP wavelength is quite long, $L_{\text{SPP}}/\lambda_{\text{SPP}} \ll 1$,

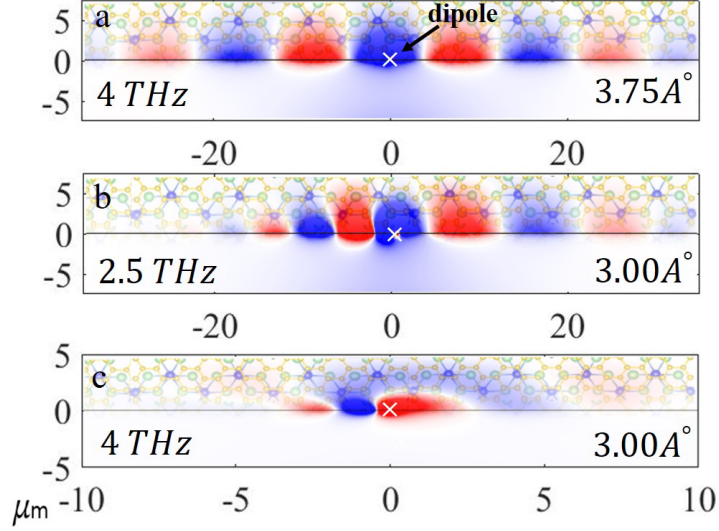


Figure 7.6: Edge SPP launched by a dipole source near the graphene-vacuum edge for the exchange field magnetic bias corresponding to two CrI₃-graphene separations. Reprinted with permission from [8].

and so the SPP seems not to be very useful.

7.4 Faraday Rotation in Graphene Monolayer vs. in Graphene/CrI3

The corresponding edge SPP propagation length and wavelength on the graphene layer in an external field as a function of the external bias are shown in Fig. 7.7 c, and d. As the magnetic bias increases, the SPP propagation length increases, and $L_{\text{SPP}}/\lambda_{\text{SPP}} > 1$; for large magnetic bias, $L_{\text{SPP}}/\lambda_{\text{SPP}} \approx 6-8$. For $\mu = -0.3$ eV, the results are the same as shown in Fig. 7.7 for $B > 80$ T, since for larger chemical potentials the SPP is not well-formed and is not quasi-TM below a critical bias. In the $B = 0$ case, states are not filled and the SPP is not formed for $\hbar\omega \gg \mu$. In the external magnetic bias case, the value of B plays a role, with larger B moving the first Lambda Level (LL) to higher frequencies, increasing the band gap.

When an external static magnetic field is applied perpendicular to a 2D material like graphene, the Dirac cone band structure splits and forms the well-known Landau levels. Due to the magneto-optical interaction, the optical conductivity tensor has non-zero off-diagonal elements and diagonal components also alters. As a result, when a light with linear polarization is illuminated to the magnetized surface, the transmitted or reflected light will gain an extra field component perpendicular to the original polarization direction. Then, the polarization direction of the transmitted (reflected) light is rotated compare to the incident light. This rotation is called Faraday (Kerr) rotation. This phenomenon is generally observed in metals, ferromagnets, and highly doped semiconductors. Faraday (Kerr) rotation indicates the nonreciprocal response

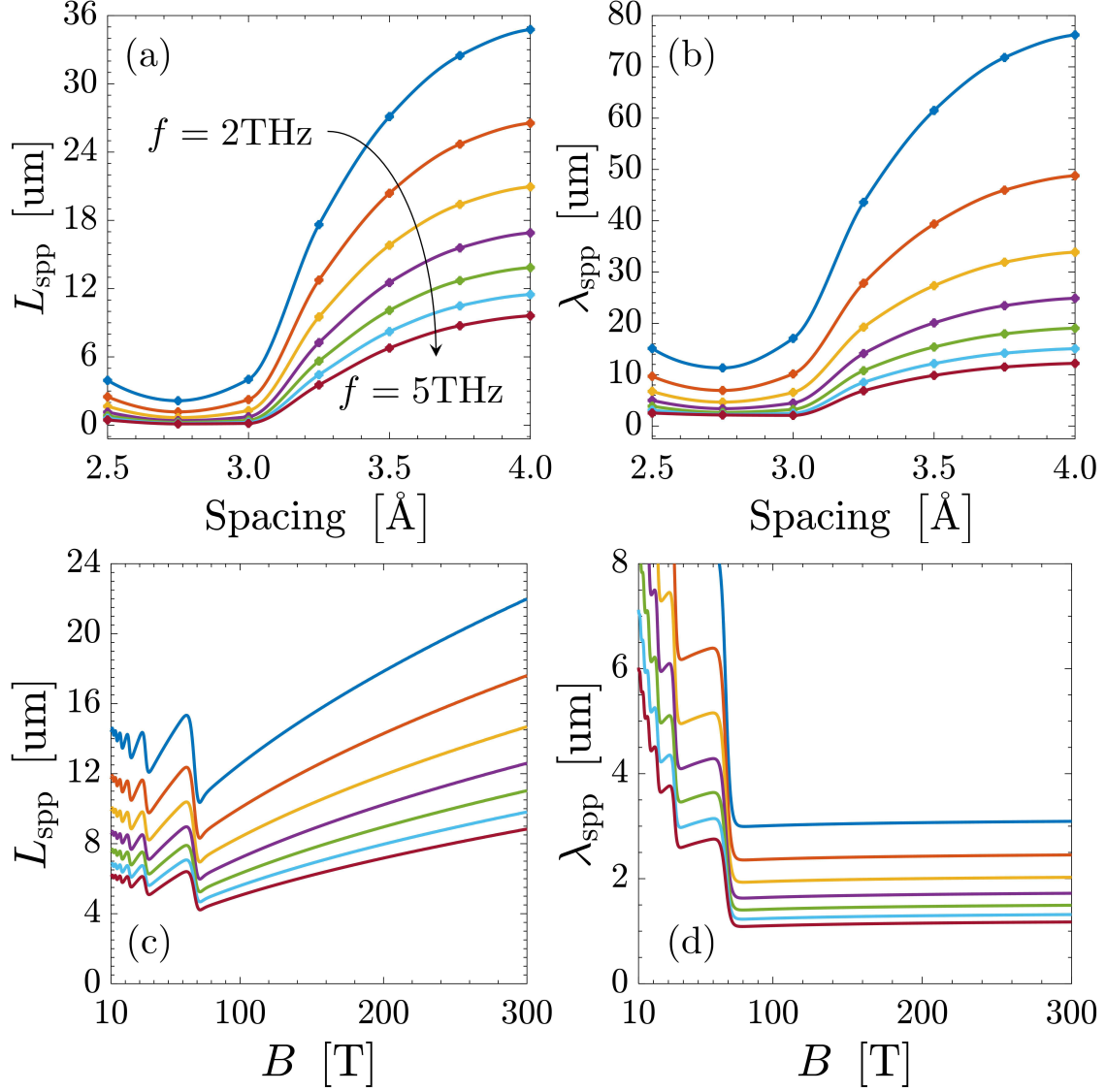


Figure 7.7: (a) Edge SPP propagation length (left branch of Fig. 7.4) and (b) SPP wavelength on graphene in an exchange field as CrI₃-graphene separation varies. (c) Edge SPP propagation length and (d) SPP wavelength on graphene in an external bias for different frequencies. $\mu=0.05$ eV, $T=40$ K, $\Gamma = 2 \times 10^{12} \text{ s}^{-1}$. For (c)-(d), the first LL occurs at $8.8\sqrt{|B|}$, well beyond the considered frequencies. For comparison for the separations 2.5 Å, 3 Å, 3.5 Å, 4 Å, the effective bias fields are 750 T, 600 T, 450 T, and 90 T, respectively. Reprinted with permission from [8], and generated by coauthor A. Holmes.

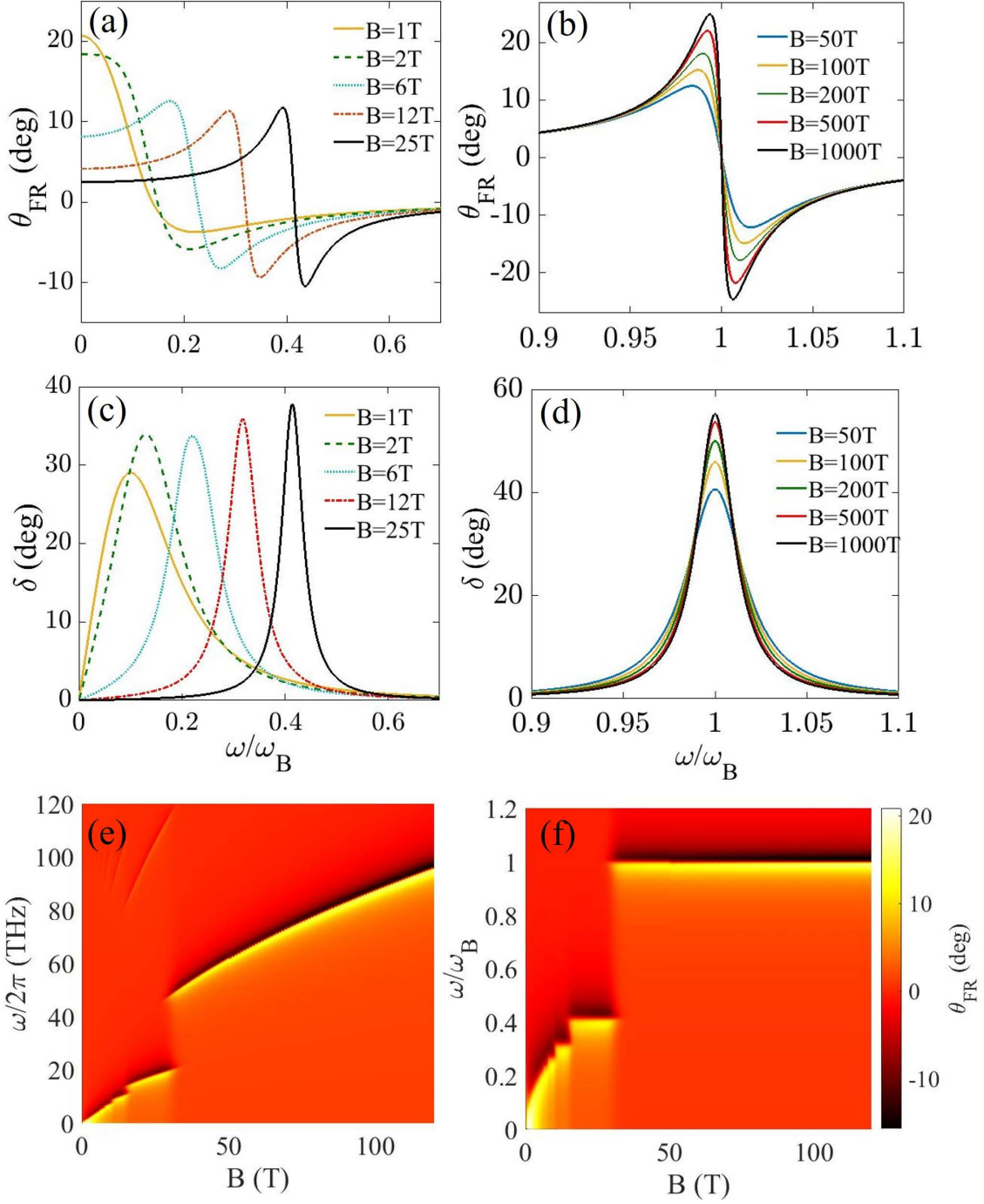


Figure 7.8: (a,b) Faraday rotation and (c,d) ellipticity of graphene as a function of frequency for different external bias values, and (e, f) density plots of Faraday rotation. ω_B is the frequency of the first Landau level for each bias. $\mu=0.2$ eV, $T=40$ K, and $\Gamma=2$ THz. Reprinted with permission from [8].

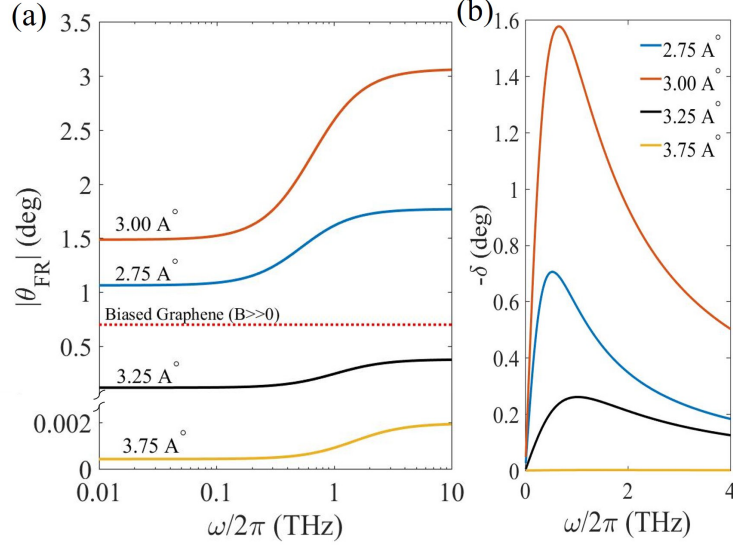


Figure 7.9: (a) Faraday rotation and (b) ellipticity of the CrI₃-graphene heterostructure as a function of frequency for different separations. The dotted curve shows FR for externally-biased graphene using the effective field strengths corresponding to different layer separations. Reprinted with permission from [8].

of the material. In a graphene sheet, generally applying a larger chemical potential μ_c , scattering time τ , and magnetic field B lead to larger Faraday (Kerr) rotations. For magnetic field intensity less than 10 T, the cyclotron frequency of graphene is low. So, a moderate Faraday rotation is achievable at low THz frequencies, which limits the application. For example, for 7T magnetic field only 6 degree Faraday rotation has been reported below 10 THz. Some techniques have been proposed to solve this issue. For instance, by using pattern graphene or metal metasurface, and metal grating on top of graphene sheet, the interaction of light-magneto plasmons increases at frequencies far away from the cyclotron frequency, which leads to Faraday rotation enhancement. However, these structures decrease the transmittance (reflectance) which is not ideal. There is always a trade-off between the material transmission and Faraday rotation. Excitation of magneto-plasmon appears as a dip in the transmittance response, but as a peak in the Faraday rotation spectrum. One can increase the Faraday rotation by applying extremely large magnetic field, which also results in a higher transmission compared to the artificially designed structures (e.g. metasurfaces). Here, we determine Faraday rotation from graphene monolayer biased by an extremely large magnetic field.

Faraday rotation (FR) on magnetically-biased graphene has been studied in [145, 146], among other works. The Faraday rotation is computed as [147]

$$\theta_{\text{FR}} = \frac{1}{2} \arg \left(\frac{t_{pp} - it_{ps}}{t_{pp} + it_{ps}} \right), \quad (7.21)$$

and the ellipticity as

$$\delta = \frac{|t_{pp} - it_{ps}|^2 - |t_{pp} + it_{ps}|^2}{|t_{pp} - it_{ps}|^2 + |t_{pp} + it_{ps}|^2}, \quad (7.22)$$

where $t_{pp} = E_p^t/E_p^i$, $t_{ps} = E_s^t/E_p^i$; $p = x, y$, $s = x, y$, $s \neq p$; and the superscripts indicate incident (i) or transmitted (t) fields. For graphene in a homogeneous medium, the transmission coefficients are

$$t_{xx} = \frac{4/\eta + 2\sigma_{xx}}{4\sigma_{xx} + \eta(\sigma_{xx}^2 + \sigma_{xy}^2) + 4/\eta}, \quad (7.23)$$

$$t_{xy} = \frac{2\sigma_{xy}}{4\sigma_{xx} + \eta(\sigma_{xx}^2 + \sigma_{xy}^2) + 4/\eta}, \quad (7.24)$$

where $\eta = \sqrt{\mu/\varepsilon}$.

For externally-biased graphene, Fig. 7.8, large Faraday rotations can be obtained. As B increases, the FR resonance first blue-shifts (Fig. 7.8a), and eventually stabilizes in frequency (Fig. 7.8b) at the first LL, but the peak FR continues to increase with increasing B . Ellipticity behaves in a similar manner as FR.

As discussed above, since the conductivity of the CrI_3 is much smaller than the conductivity of graphene at the considered frequencies, we can neglect the Faraday rotation contribution of the CrI_3 , and only consider the FR of graphene under the influence of the exchange field.

Faraday rotations for the exchange field case are shown in Fig. 7.9 for various CrI_3 -graphene separations. For closer-than-equilibrium separations, modest Faraday rotations are observed, but for the equilibrium separation, Faraday rotation is negligible since σ_{xy}/σ_{xx} is small.

7.5 Summary

In this chapter, we evaluated the nonreciprocal response of graphene/ CrI_3 in comparison to the isolated graphene magnetized by external magnetic field. The optical conductivity of a monolayer chromium triiodide (CrI_3)-graphene van der Waals (vdW) heterostructure is extracted using density-functional theory by considering the effect of exchange field. The exchange field provides an effective magnetic field of hundreds of Tesla. These enormous fields serve as the magnetic bias for the graphene layer. Graphene conductivity and SPP properties for the exchange field were considered, and compared with the external bias case. Since no Landau levels occur for the exchange field, the resulting non-reciprocity is found to be considerably weaker than for an equivalent external field bias (where strongly nonreciprocal electromagnetic edge modes that are tightly-confined, robust, and unidirectional are shown to exist). Faraday rotation due to the exchange field was also shown to be modest compared to the external bias case.

Conclusion

To sum up the outcomes of this research, we have studied topological SPPs in magnetized semiconductors as well as 2D plasmonic platforms. This study paves the path toward real-world applications of these unique waves. The results can be used for development of nonreciprocal plasmonic components for high-frequency on-chip integrated circuits.

We have modeled and characterized the THz reflectance of undoped InSb crystals for a wide range of temperature and field intensity. The carrier parameters of both holes and electrons have been extracted. The contribution of holes and electrons to the field-induced modulation and band structure has been examined. We showed that the magneto-reflectance spectrum can be modified by relatively changing the plasma frequency and cyclotron frequencies. The SPPs propagation behaviors at the interface of metal/InSb have been studied. The SPP propagation length and bandgap width were determined at different temperatures. From practical viewpoint, we found it difficult to observe unidirectional SPPs at low temperature due to narrow bandgaps. To widen the bandgap, higher carrier density or correspondingly larger plasma frequency are required, which can be realized by increasing temperature or using doped samples. However, at higher temperature, the SPP propagation length is not desirable due to low mobility of undoped InSb. We found that at moderate temperatures, undoped InSb is a suitable plasmonic platform because moderate bandgap and long propagation length can be achieved. We have successfully observed nonreciprocal SPPs at the interface between Au film and magnetized InSb crystal. Using tilted samples we showed that at resonance frequencies within the bandgap, SPPs are unidirectional. We adjusted the nonreciprocal window and optimized propagation length by tuning the carrier parameters of InSb. This optimization leads to the long-lasting unidirectional SPPs that exist at the gyrotropic metal-isotropic metal interface. These results provide a unique venue for exploring nonreciprocal plasmonic functionality.

Then, we have investigated the propagation of SPPs in a newly-discovered frequency range below the plasma frequency in a system where the plasma medium interfaces with a dielectric layer. In this frequency window, SPPs form two narrow beams which is desirable for directional and optimum energy routing on the surface. We also observed two other types of propagation outside this window below the plasma frequency; omni-directional, bidirectional. We showed that the propagation angle of narrow beams is tunable by frequency and magnetic field intensity. We evaluated the resilience of narrow beams to defects and discontinuities. We presented Green's function and quasi-static models for a plasma slab and examined the effect of thickness.

By considering a hydrodynamic model, we have studied the effect of nonlocality on bulk band structure and associated Chern numbers in the plasmonic Voigt system. We compared the results with the local Drude model and spatial cutoff model. We emphasized the advantage of applying hydrodynamic model including physical material response at large wavenumbers, and obtaining integer Chern numbers without the need for an interpolated material response.

Next, we showed that in a magnetized plasma system, the unidirectional SPP trajectories are steerable by magnetic bias direction. In a Voigt system, when in-plane axial bias is applied, the SPPs have a linear trajectory perpendicular to the magnetic vector. In a radially biased system, unidirectional SPPs are propagating on a circular path. We derived a Green's function model for a half-space plasma medium biased by radial magnetic field. Using curved SPPs, we proposed a circular plasmonic junction with minimal bending loss and nonreciprocal effects, which can be used in plasmonic integrated circuits.

Finally, we have examined the nonreciprocal response arising from the exchange field in CrI₃-graphene heterostructure. Comparing to an isolated graphene monolayer biased by external magnetic field, we found that the nonreciprocal response in the CrI₃-graphene vdW heterostructure is considerably weaker. That is due to the absence of Lambda-Levels in the material optical band structure. We have detected weak nonreciprocal edge modes at non-equilibrium separation distance between monolayers. We have also determined modest Faraday rotation. In conclusion, the effective out-of-plane magnetic field due to the exchange field does not generate equal nonreciprocal response as the magnetic field produced by external magnets.

Our research presents a comprehensive study on propagation features of unidirectional SPPs in different plasmonic layered media. Our work paves the path toward the real-world applications of topological SPPs using continuous crystals. From the wave propagating aspects, the unidirectional SPPs are important for efficient energy routing on the surface, or in design of nonreciprocal components such as circulators and isolators. In which devices the wave propagate only in one direction, not in the opposite direction. They are typically used for protection of sensitive sources from the undesired reflected power. We believe that the results presented in this dissertation will be of interest to a broad research community working in plasmonics, nanophotonics, and nonreciprocal optics.

Bibliography

- [1] Junxi Zhang, Lide Zhang, and Wei Xu. Surface plasmon polaritons: physics and applications. *Journal of Physics D: Applied Physics*, 45(11):113001, 2012.
- [2] Samaneh Pakniyat, Yi Liang, Yinxiao Xiang, Cheng Cen, Jun Chen, and George W Hanson. Indium antimonide—constraints on practicality as a magneto-optical platform for topological surface plasmon polaritons. *Journal of Applied Physics*, 128(18):183101, 2020.
- [3] Yi Liang, Samaneh Pakniyat, Yinxiao Xiang, Jun Chen, Fan Shi, George W Hanson, and Cheng Cen. Tunable unidirectional surface plasmon polaritons at the interface between gyrotropic and isotropic conductors. *Optica*, 8(7):952–959, 2021.
- [4] Yi Liang, Samaneh Pakniyat, Yinxiao Xiang, Fan Shi, George W Hanson, and Cheng Cen. Temperature-dependent transverse-field magneto-plasmons properties in insb. *Optical Materials*, 112:110831, 2021.
- [5] Samaneh Pakniyat, Alexander M Holmes, George W Hanson, S Ali Hassani Gangaraj, Mauro Antezza, Mário G Silveirinha, Shahrokh Jam, and Francesco Monticone. Non-reciprocal, robust surface plasmon polaritons on gyrotropic interfaces. *IEEE Transactions on Antennas and Propagation*, 68(5):3718–3729, 2020.
- [6] Samaneh Pakniyat, S Ali Hassani Gangaraj, and George W Hanson. Chern invariants of topological continua: A self-consistent nonlocal hydrodynamic model. *Physical Review B*, 105(3):035310, 2022.
- [7] A. M. Holmes S. Pakniyat and G. W. Hanson. Unidirectional curved surface plasmon polariton in a radially magnetized system,. *IEEE Transactions on Antennas and Propagation*, doi: 10.1109/TAP.2022.3191129, 2022.
- [8] Alexander M Holmes, Samaneh Pakniyat, S Ali Hassani Gangaraj, Francesco Monticone, Michael Weinert, and George W Hanson. Exchange splitting and exchange-induced nonreciprocal photonic be-

- havior of graphene in cr i 3-graphene van der waals heterostructures. *Physical Review B*, 102(7):075435, 2020.
- [9] Shashank Pandey, Barun Gupta, Ashish Chanana, and Ajay Nahata. Non-drude like behaviour of metals in the terahertz spectral range. *Advances in Physics: X*, 1(2):176–193, 2016.
 - [10] Jiao Lin, JP Balthasar Mueller, Qian Wang, Guanghui Yuan, Nicholas Antoniou, Xiao-Cong Yuan, and Federico Capasso. Polarization-controlled tunable directional coupling of surface plasmon polaritons. *Science*, 340(6130):331–334, 2013.
 - [11] Fei Ding and Sergey I Bozhevolnyi. A review of unidirectional surface plasmon polariton metacouplers. *IEEE Journal of Selected Topics in Quantum Electronics*, 25(3):1–11, 2019.
 - [12] Jianjun Chen, Zhi Li, Xiang Zhang, Jinghua Xiao, and Qihuang Gong. Submicron bidirectional all-optical plasmonic switches. *Scientific reports*, 3(1):1–6, 2013.
 - [13] Wenjie Yao, Shang Liu, Huimin Liao, Zhi Li, Chengwei Sun, Jianjun Chen, and Qihuang Gong. Efficient directional excitation of surface plasmons by a single-element nanoantenna. *Nano letters*, 15(5):3115–3121, 2015.
 - [14] Fernando López-Tejiera, Sergio G Rodrigo, Luis Martin-Moreno, Francisco J García-Vidal, Eloïse Devaux, Thomas W Ebbesen, Joachim R Krenn, IP Radko, Sergey I Bozhevolnyi, María U González, et al. Efficient unidirectional nanoslit couplers for surface plasmons. *Nature Physics*, 3(5):324–328, 2007.
 - [15] Yongmin Liu, Stefano Palomba, Yongshik Park, Thomas Zentgraf, Xiaobo Yin, and Xiang Zhang. Compact magnetic antennas for directional excitation of surface plasmons. *Nano letters*, 12(9):4853–4858, 2012.
 - [16] Francisco J Rodríguez-Fortuño, Giuseppe Marino, Pavel Ginzburg, Daniel O’Connor, Alejandro Martínez, Gregory A Wurtz, and Anatoly V Zayats. Near-field interference for the unidirectional excitation of electromagnetic guided modes. *Science*, 340(6130):328–330, 2013.
 - [17] Sen Wang, Chunying Zhao, and Xing Li. Dynamical manipulation of surface plasmon polaritons. *Applied Sciences*, 9(16):3297, 2019.
 - [18] Viktor S Asadchy, Mohammad Sajjad Mirmoosa, Ana Díaz-Rubio, Shanhui Fan, and Sergei A Tretyakov. Tutorial on electromagnetic nonreciprocity and its origins. *Proceedings of the IEEE*, 108(10):1684–1727, 2020.

- [19] Xiao-Gang Wen. Topological orders in rigid states. *International Journal of Modern Physics B*, 4(02):239–271, 1990.
- [20] MP Do Carmo. Differential geometry of curves and surfaces (englewood cliff, nj, 1976).
- [21] David J Thouless, Mahito Kohmoto, M Peter Nightingale, and Marcel den Nijs. Quantized hall conductance in a two-dimensional periodic potential. *Physical review letters*, 49(6):405, 1982.
- [22] Barry Simon. Holonomy, the quantum adiabatic theorem, and berry’s phase. *Physical Review Letters*, 51(24):2167, 1983.
- [23] Yasuhiro Hatsugai. Chern number and edge states in the integer quantum hall effect. *Physical review letters*, 71(22):3697, 1993.
- [24] Chong Wang, Andrew C Potter, and T Senthil. Classification of interacting electronic topological insulators in three dimensions. *Science*, 343(6171):629–631, 2014.
- [25] M Zahid Hasan and Charles L Kane. Colloquium: topological insulators. *Reviews of modern physics*, 82(4):3045, 2010.
- [26] FDM Haldane and S Raghu. Possible realization of directional optical waveguides in photonic crystals with broken time-reversal symmetry. *Physical review letters*, 100(1):013904, 2008.
- [27] Srinivas Raghu and Frederick Duncan Michael Haldane. Analogs of quantum-hall-effect edge states in photonic crystals. *Physical Review A*, 78(3):033834, 2008.
- [28] Ling Lu, John D Joannopoulos, and Marin Soljačić. Topological photonics. *Nature photonics*, 8(11):821–829, 2014.
- [29] Tomoki Ozawa, Hannah M Price, Alberto Amo, Nathan Goldman, Mohammad Hafezi, Ling Lu, Mikael C Rechtsman, David Schuster, Jonathan Simon, Oded Zilberberg, et al. Topological photonics. *Reviews of Modern Physics*, 91(1):015006, 2019.
- [30] Mário G Silveirinha. Chern invariants for continuous media. *Physical Review B*, 92(12):125153, 2015.
- [31] Farzad Zangeneh-Nejad, Andrea Alù, and Romain Fleury. Topological wave insulators: a review. *Comptes Rendus. Physique*, 21(4-5):467–499, 2020.
- [32] MS Kushwaha and P Halevi. Magnetoplasmons in thin films in the voigt configuration. *Physical Review B*, 36(11):5960, 1987.
- [33] JJ Brion, RF Wallis, A Hartstein, and E Burstein. Theory of surface magnetoplasmons in semiconductors. *Physical Review Letters*, 28(22):1455, 1972.

- [34] Alexander G Schuchinsky and Xiyu Yan. Migration and collision of magnetoplasmon modes in magnetised planar semiconductor-dielectric layered structures. In *Metamaterials and Plasmonics: Fundamentals, Modelling, Applications*, pages 255–266. Springer, 2009.
- [35] Manvir S Kushwaha. Plasmons and magnetoplasmons in semiconductor heterostructures. *Surface Science Reports*, 41(1-8):1–416, 2001.
- [36] Arthur R Davoyan and Nader Engheta. Theory of wave propagation in magnetized near-zero-epsilon metamaterials: evidence for one-way photonic states and magnetically switched transparency and opacity. *Physical review letters*, 111(25):257401, 2013.
- [37] S Ali Hassani Gangaraj, Mário G Silveirinha, and George W Hanson. Berry phase, berry connection, and chern number for a continuum bianisotropic material from a classical electromagnetics perspective. *IEEE journal on multiscale and multiphysics computational techniques*, 2:3–17, 2017.
- [38] S Ali Hassani Gangaraj, Andrei Nemilentsau, and George W Hanson. The effects of three-dimensional defects on one-way surface plasmon propagation for photonic topological insulators comprised of continuum media. *Scientific reports*, 6(1):1–10, 2016.
- [39] S Ali Hassani Gangaraj, George W Hanson, and Mauro Antezza. Erratum: Robust entanglement with three-dimensional nonreciprocal photonic topological insulators [phys. rev. a 95, 063807 (2017)]. *Physical Review A*, 97(6):069902, 2018.
- [40] Seyyed Ali Hassani Gangaraj and George W Hanson. Topologically protected unidirectional surface states in biased ferrites: duality and application to directional couplers. *IEEE Antennas and Wireless Propagation Letters*, 16:449–452, 2016.
- [41] Biao Yang, Mark Lawrence, Wenlong Gao, Qinghua Guo, and Shuang Zhang. One-way helical electromagnetic wave propagation supported by magnetized plasma. *Scientific reports*, 6(1):1–6, 2016.
- [42] Wenlong Gao, Biao Yang, Mark Lawrence, Fengzhou Fang, Benjamin Béri, and Shuang Zhang. Photonic weyl degeneracies in magnetized plasma. *Nature communications*, 7(1):1–8, 2016.
- [43] NP Armitage, EJ Mele, and Ashvin Vishwanath. Weyl and dirac semimetals in three-dimensional solids. *Reviews of Modern Physics*, 90(1):015001, 2018.
- [44] Kunal Shastri and Francesco Monticone. Dissipation-induced topological transitions in continuous weyl materials. *Physical Review Research*, 2(3):033065, 2020.

- [45] Kostya S Novoselov, Andre K Geim, Sergei V Morozov, De-eng Jiang, Yanshui Zhang, Sergey V Dubonos, Irina V Grigorieva, and Alexandr A Firsov. Electric field effect in atomically thin carbon films. *science*, 306(5696):666–669, 2004.
- [46] S Das Sarma, Shaffique Adam, EH Hwang, and Enrico Rossi. Electronic transport in two-dimensional graphene. *Reviews of modern physics*, 83(2):407, 2011.
- [47] Dafei Jin, Ling Lu, Zhong Wang, Chen Fang, John D Joannopoulos, Marin Soljačić, Liang Fu, and Nicholas X Fang. Topological magnetoplasmon. *Nature communications*, 7(1):1–10, 2016.
- [48] Michael V Berry. The quantum phase, five years after. *Geometric phases in physics*, pages 7–28, 1989.
- [49] Alexander Pines. Berry’s phasel. *Annu. Rev. Phys. Chem.*, 601:46, 1990.
- [50] S Ali Hassani Gangaraj, Boyuan Jin, Christos Argyropoulos, and Francesco Monticone. Broadband field enhancement and giant nonlinear effects in terminated unidirectional plasmonic waveguides. *Physical Review Applied*, 14(5):054061, 2020.
- [51] Edwin Moncada-Villa, Victor Fernández-Hurtado, Francisco J Garcia-Vidal, Antonio García-Martín, and Juan Carlos Cuevas. Magnetic field control of near-field radiative heat transfer and the realization of highly tunable hyperbolic thermal emitters. *Physical Review B*, 92(12):125418, 2015.
- [52] Fei Fan, Shi-Tong Xu, Xiang-Hui Wang, and Sheng-Jiang Chang. Terahertz polarization converter and one-way transmission based on double-layer magneto-plasmonics of magnetized insb. *Optics express*, 24(23):26431–26443, 2016.
- [53] Kosmas L Tsakmakidis, Linfang Shen, Sebastian A Schulz, Xiaodong Zheng, John Upham, Xiaohua Deng, Hatice Altug, Alexander F Vakakis, and Robert W Boyd. Breaking lorentz reciprocity to overcome the time-bandwidth limit in physics and engineering. *Science*, 356(6344):1260–1264, 2017.
- [54] Edwin Moncada-Villa, Antonio I Fernández-Domínguez, and Juan C Cuevas. Magnetic-field controlled anomalous refraction in doped semiconductors. *JOSA B*, 36(4):935–941, 2019.
- [55] Hao Hu, Liangliang Liu, Xiao Hu, Dongjue Liu, and Dongliang Gao. Routing emission with a multi-channel nonreciprocal waveguide. *Photonics Research*, 7(6):642–646, 2019.
- [56] Weixuan Zhang and Xiangdong Zhang. Backscattering-immune computing of spatial differentiation by nonreciprocal plasmonics. *Physical Review Applied*, 11(5):054033, 2019.
- [57] ED Palik and JK Furdyna. Infrared and microwave magnetoplasma effects in semiconductors. *Reports on Progress in Physics*, 33(3):1193, 1970.

- [58] Bo Han Cheng, Hong Wen Chen, Kai Jiun Chang, Yung-Chiang Lan, and Din Ping Tsai. Magnetically controlled planar hyperbolic metamaterials for subwavelength resolution. *Scientific reports*, 5(1):1–9, 2015.
- [59] Bin Hu, Ying Zhang, and Qi Jie Wang. Surface magneto plasmons and their applications in the infrared frequencies. *Nanophotonics*, 4(4):383–396, 2015.
- [60] Jan Chochol, Kamil Postava, Michael Čada, Mathias Vanwolleghem, Lukáš Halagačka, Jean-François Lampin, and Jaromír Pištora. Magneto-optical properties of insb for terahertz applications. *AIP Advances*, 6(11):115021, 2016.
- [61] Pawan Kumar, Manish Kumar, and VK Tripathi. Linear mode conversion of terahertz radiation into terahertz surface magnetoplasmons on a rippled surface of magnetized n-insb. *Optics Letters*, 41(7):1408–1411, 2016.
- [62] Fei Fan, Sai Chen, and Sheng-Jiang Chang. A review of magneto-optical microstructure devices at terahertz frequencies. *IEEE Journal of Selected Topics in Quantum Electronics*, 23(4):1–11, 2016.
- [63] Shuai Lin, Khagendra Bhattarai, Jiangfeng Zhou, and Diyar Talbayev. Giant thz surface plasmon polariton induced by high-index dielectric metasurface. *Scientific Reports*, 7(1):1–8, 2017.
- [64] Shukai Yu, Kate H Heffernan, and Diyar Talbayev. Beyond the effective mass approximation: A predictive theory of the nonlinear optical response of conduction electrons. *Physical Review B*, 95(12):125201, 2017.
- [65] D Yavorskiy, K Karpierz, M Grynberg, W Knap, and J Lusakowski. Indium antimonide detector for spectral characterization of terahertz sources. *Journal of Applied Physics*, 123(6):064502, 2018.
- [66] Sarah Houver, Lucas Huber, Matteo Savoini, Elsa Abreu, and Steven L Johnson. 2d thz spectroscopic investigation of ballistic conduction-band electron dynamics in insb. *Optics express*, 27(8):10854–10865, 2019.
- [67] Dongyang Wang, Biao Yang, Wenlong Gao, Hongwei Jia, Quanlong Yang, Xieyu Chen, Minggui Wei, Changxu Liu, Miguel Navarro-Cía, Jianguang Han, et al. Photonic weyl points due to broken time-reversal symmetry in magnetized semiconductor. *Nature Physics*, 15(11):1150–1155, 2019.
- [68] Tengfei Li, Fei Fan, Yunyun Ji, Zhiyu Tan, Qianyi Mu, and Shengjiang Chang. Terahertz tunable filter and modulator based on magneto plasmon in transverse magnetized insb. *Optics Letters*, 45(1):1–4, 2020.

- [69] Zhi-Yu Tan, Fei Fan, and Sheng-Jiang Chang. Active broadband manipulation of terahertz photonic spin based on gyrotropic pancharatnam-berry metasurface. *IEEE Journal of Selected Topics in Quantum Electronics*, 26(6):1–8, 2020.
- [70] SM Hanham, AI Fernández-Domínguez, Jing Hua Teng, SS Ang, KP Lim, Soon Fatt Yoon, CY Ngo, N Klein, JB Pendry, and Stefan A Maier. Broadband terahertz plasmonic response of touching insb disks. *Advanced Materials*, 24(35):OP226–OP230, 2012.
- [71] Bin Hu, Qi Jie Wang, and Ying Zhang. Slowing down terahertz waves with tunable group velocities in a broad frequency range by surface magneto plasmons. *Optics Express*, 20(9):10071–10076, 2012.
- [72] Bin Hu, Qi Jie Wang, and Ying Zhang. Broadly tunable one-way terahertz plasmonic waveguide based on nonreciprocal surface magneto plasmons. *Optics letters*, 37(11):1895–1897, 2012.
- [73] Shuai Lin, Sinhara Silva, Jiangfeng Zhou, and Diyar Talbayev. A one-way mirror: High-performance terahertz optical isolator based on magnetoplasmonics. *Advanced Optical Materials*, 6(19):1800572, 2018.
- [74] Qianyi Mu, Fei Fan, Sai Chen, Shitong Xu, Chuanzhong Xiong, Xin Zhang, Xianghui Wang, and Shengjiang Chang. Tunable magneto-optical polarization device for terahertz waves based on insb and its plasmonic structure. *Photonics Research*, 7(3):325–331, 2019.
- [75] M Oszwaldowski and M Zimpel. Temperature dependence of intrinsic carrier concentration and density of states effective mass of heavy holes in insb. *Journal of Physics and Chemistry of Solids*, 49(10):1179–1185, 1988.
- [76] SC Howells and LA Schlie. Transient terahertz reflection spectroscopy of undoped insb from 0.1 to 1.1 thz. *Applied Physics Letters*, 69(4):550–552, 1996.
- [77] X Wang, AA Belyanin, SA Crooker, DM Mittleman, and Jun Kono. Interference-induced terahertz transparency in a semiconductor magneto-plasma. *Nature Physics*, 6(2):126–130, 2010.
- [78] K Alfaramawi, MA Alzamil, et al. Temperature-dependent scattering processes of n-type indium antimonide. *Optoelectron Adv Mater*, 3:569–573, 2009.
- [79] S Ali Hassani Gangaraj and Francesco Monticone. Topologically-protected one-way leaky waves in nonreciprocal plasmonic structures. *Journal of Physics: Condensed Matter*, 30(10):104002, 2018.
- [80] S Ali Hassani Gangaraj, George W Hanson, Mário G Silveirinha, Kunal Shastri, Mauro Antezza, and Francesco Monticone. Unidirectional and diffractionless surface plasmon polaritons on three-dimensional nonreciprocal plasmonic platforms. *Physical Review B*, 99(24):245414, 2019.

- [81] SR Seshadri. Excitation of surface waves on a perfectly conducting screen covered with anisotropic plasma. *IRE Transactions on Microwave Theory and Techniques*, 10(6):573–578, 1962.
- [82] S Ali Hassani Gangaraj and Francesco Monticone. Do truly unidirectional surface plasmon-polaritons exist? *Optica*, 6(9):1158–1165, 2019.
- [83] Mário G Silveirinha. Bulk-edge correspondence for topological photonic continua. *Physical Review B*, 94(20):205105, 2016.
- [84] Todd Van Mechelen and Zubin Jacob. Unidirectional maxwellian spin waves. *Nanophotonics*, 8(8):1399–1416, 2019.
- [85] Mário G Silveirinha. Quantized angular momentum in topological optical systems. *Nature communications*, 10(1):1–8, 2019.
- [86] Mário G Silveirinha, S Ali Hassani Gangaraj, George W Hanson, and Mauro Antezza. Fluctuation-induced forces on an atom near a photonic topological material. *Physical Review A*, 97(2):022509, 2018.
- [87] S Ali Hassani Gangaraj, George W Hanson, Mauro Antezza, and Mário G Silveirinha. Spontaneous lateral atomic recoil force close to a photonic topological material. *Physical Review B*, 97(20):201108, 2018.
- [88] Yarden Mazor and Ben Z Steinberg. Metaweaves: sector-way nonreciprocal metasurfaces. *Physical Review Letters*, 112(15):153901, 2014.
- [89] Alex Leviyev, Binyamin Stein, A Christofi, T Galfsky, H Krishnamoorthy, Igor L Kuskovsky, V Menon, and AB Khanikaev. Nonreciprocity and one-way topological transitions in hyperbolic metamaterials. *APL Photonics*, 2(7):076103, 2017.
- [90] Siddharth Buddhiraju, Yu Shi, Alex Song, Casey Wojcik, Momchil Minkov, Ian AD Williamson, Avik Dutt, and Shanhui Fan. Absence of unidirectionally propagating surface plasmon-polaritons at nonreciprocal metal-dielectric interfaces. *Nature communications*, 11(1):1–6, 2020.
- [91] Francesco Monticone. A truly one-way lane for surface plasmon polaritons. *Nature Photonics*, 14(8):461–465, 2020.
- [92] Mário G Silveirinha. Proof of the bulk-edge correspondence through a link between topological photonics and fluctuation-electrodynamics. *Physical Review X*, 9(1):011037, 2019.
- [93] Clément Tauber, Pierre Delplace, and Antoine Venaille. Anomalous bulk-edge correspondence in continuous media. *Physical Review Research*, 2(1):013147, 2020.

- [94] S Ali Hassani Gangaraj and Francesco Monticone. Physical violations of the bulk-edge correspondence in topological electromagnetics. *Physical review letters*, 124(15):153901, 2020.
- [95] Peng Zhang, Sheng Wang, Yongmin Liu, Xiaobo Yin, Changgui Lu, Zhigang Chen, and Xiang Zhang. Plasmonic airy beams with dynamically controlled trajectories. *Optics letters*, 36(16):3191–3193, 2011.
- [96] Felix Bleckmann, Alexander Minovich, Jakob Frohnhaus, Dragomir N Neshev, and Stefan Linden. Manipulation of airy surface plasmon beams. *Optics letters*, 38(9):1443–1445, 2013.
- [97] Kai Xiao, Shibiao Wei, Changjun Min, Guanghui Yuan, SW Zhu, T Lei, and X-C Yuan. Dynamic cosine-gauss plasmonic beam through phase control. *Optics express*, 22(11):13541–13546, 2014.
- [98] Jiao Lin, Jean Dellinger, Patrice Genevet, Benoit Cluzel, Frederique de Fornel, and Federico Capasso. Cosine-gauss plasmon beam: a localized long-range nondiffracting surface wave. *Physical Review Letters*, 109(9):093904, 2012.
- [99] Igor V Minin, Oleg V Minin, Dmitry S Ponomarev, and Igor A Glinskiy. Photonic hook plasmons: a new curved surface wave. *Annalen der Physik*, 530(12):1800359, 2018.
- [100] Igor V Minin, Oleg V Minin, Igor A Glinskiy, Rustam A Khabibullin, Radu Malureanu, A Lavrinenko, DI Yakubovsky, VS Volkov, and DS Ponomarev. Experimental verification of a plasmonic hook in a dielectric janus particle. *Applied Physics Letters*, 118(13):131107, 2021.
- [101] XiaoFei Zang, YiMing Zhu, ChenXi Mao, WeiWei Xu, HongZhen Ding, JingYa Xie, QingQing Cheng, Lin Chen, Yan Peng, Qing Hu, et al. Manipulating terahertz plasmonic vortex based on geometric and dynamic phase. *Advanced Optical Materials*, 7(3):1801328, 2019.
- [102] Hwi Kim, Junghyun Park, Seong-Woo Cho, Seung-Yeol Lee, Minsu Kang, and Byoungcho Lee. Synthesis and dynamic switching of surface plasmon vortices with plasmonic vortex lens. *Nano letters*, 10(2):529–536, 2010.
- [103] Yuquan Zhang, Changjun Min, Xiujie Dou, Xianyou Wang, Hendrik Paul Urbach, Michael G Somekh, and Xiaocong Yuan. Plasmonic tweezers: for nanoscale optical trapping and beyond. *Light: Science & Applications*, 10(1):1–41, 2021.
- [104] Yurui Fang and Mengtao Sun. Nanoplasmonic waveguides: towards applications in integrated nanophotonic circuits. *Light: Science & Applications*, 4(6):e294–e294, 2015.
- [105] Michael A McGuire, Hemant Dixit, Valentino R Cooper, and Brian C Sales. Coupling of crystal structure and magnetism in the layered, ferromagnetic insulator CrI_3 . *Chemistry of Materials*, 27(2):612–620, 2015.

- [106] Bevin Huang, Genevieve Clark, Efrén Navarro-Moratalla, Dahlia R Klein, Ran Cheng, Kyle L Seyler, Ding Zhong, Emma Schmidgall, Michael A McGuire, David H Cobden, et al. Layer-dependent ferromagnetism in a van der waals crystal down to the monolayer limit. *Nature*, 546(7657):270–273, 2017.
- [107] Junyi Liu, Qiang Sun, Yoshiyuki Kawazoe, and Puru Jena. Exfoliating biocompatible ferromagnetic cr-trihalide monolayers. *Physical Chemistry Chemical Physics*, 18(13):8777–8784, 2016.
- [108] Wei-Bing Zhang, Qian Qu, Peng Zhu, and Chi-Hang Lam. Robust intrinsic ferromagnetism and half semiconductivity in stable two-dimensional single-layer chromium trihalides. *Journal of Materials Chemistry C*, 3(48):12457–12468, 2015.
- [109] Bevin Huang, Genevieve Clark, Dahlia R Klein, David MacNeill, Efrén Navarro-Moratalla, Kyle L Seyler, Nathan Wilson, Michael A McGuire, David H Cobden, Di Xiao, et al. Electrical control of 2d magnetism in bilayer cri3. *Nature nanotechnology*, 13(7):544–548, 2018.
- [110] Shengwei Jiang, Lizhong Li, Zefang Wang, Kin Fai Mak, and Jie Shan. Controlling magnetism in 2d cri3 by electrostatic doping. *Nature nanotechnology*, 13(7):549–553, 2018.
- [111] Dante J O’Hara, Tiancong Zhu, Amanda H Trout, Adam S Ahmed, Yunqiu Kelly Luo, Choong Hee Lee, Mark R Brenner, Siddharth Rajan, Jay A Gupta, David W McComb, et al. Room temperature intrinsic ferromagnetism in epitaxial manganese selenide films in the monolayer limit. *Nano letters*, 18(5):3125–3131, 2018.
- [112] Min Kan, Subash Adhikari, and Qiang Sun. Ferromagnetism in mnx_2 ($x = \text{s, se}$) monolayers. *Physical Chemistry Chemical Physics*, 16(10):4990–4994, 2014.
- [113] Xingxing Li and Jinlong Yang. Crxt_3 ($x = \text{si, ge}$) nanosheets: two dimensional intrinsic ferromagnetic semiconductors. *Journal of Materials Chemistry C*, 2(34):7071–7076, 2014.
- [114] Cheng Gong, Lin Li, Zhenglu Li, Huiwen Ji, Alex Stern, Yang Xia, Ting Cao, Wei Bao, Chenzhe Wang, Yuan Wang, et al. Discovery of intrinsic ferromagnetism in two-dimensional van der waals crystals. *Nature*, 546(7657):265–269, 2017.
- [115] Klaus Zollner, Paulo E Faria Junior, and Jaroslav Fabian. Proximity exchange effects in mose 2 and wse 2 heterostructures with cri 3: Twist angle, layer, and gate dependence. *Physical Review B*, 100(8):085128, 2019.
- [116] Jiayong Zhang, Bao Zhao, Tong Zhou, Yang Xue, Chunlan Ma, and Zhongqin Yang. Strong magnetization and chern insulators in compressed graphene/cr3 van der waals heterostructures. *Physical Review B*, 97(8):085401, 2018.

- [117] Zhenhua Qiao, Shengyuan A Yang, Wanxiang Feng, Wang-Kong Tse, Jun Ding, Yugui Yao, Jian Wang, and Qian Niu. Quantum anomalous hall effect in graphene from rashba and exchange effects. *Physical Review B*, 82(16):161414, 2010.
- [118] Søren Raza, Sergey I Bozhevolnyi, Martijn Wubs, and N Asger Mortensen. Nonlocal optical response in metallic nanostructures. *Journal of Physics: Condensed Matter*, 27(18):183204, 2015.
- [119] P Halevi. Hydrodynamic model for the degenerate free-electron gas: generalization to arbitrary frequencies. *Physical Review B*, 51(12):7497, 1995.
- [120] Cristian Ciraci, John B Pendry, and David R Smith. Hydrodynamic model for plasmonics: a macroscopic approach to a microscopic problem. *ChemPhysChem*, 14(6):1109–1116, 2013.
- [121] Hollis C Chen. *Theory of electromagnetic waves: a coordinate-free approach*. McGraw-Hill, 1983.
- [122] ED Palik, R Kaplan, RW Gammon, H Kaplan, RF Wallis, and JJ Quinn. Coupled surface magnetoplasmon-optic-phonon polariton modes on insb. *Physical Review B*, 13(6):2497, 1976.
- [123] Giorgio Carelli, N Ioli, A Messina, A Moretti, S Schepis, and Franco Strumia. Temperature dependence of insb reflectivity in the far infrared: determination of the electron effective mass. *International journal of infrared and millimeter waves*, 19(9):1191–1199, 1998.
- [124] MH Weiler, RL Aggarwal, and Benjamin Lax. Warping-and inversion-asymmetry-induced cyclotron-harmonic transitions in insb. *Physical Review B*, 17(8):3269, 1978.
- [125] PS Alekseev and AP Alekseeva. Magnetocrystalline anisotropy of the gaas-type semiconductors in a strong magnetic field. *Physical Review B*, 82(12):125201, 2010.
- [126] U Merkt. Surface cyclotron resonance on insb in voigt configuration. *Physical Review B*, 32(10):6699, 1985.
- [127] Jan Chochol, Kamil Postava, Michael Čada, and Jaromír Pištora. Experimental demonstration of magnetoplasmon polariton at insb (inas)/dielectric interface for terahertz sensor application. *Scientific reports*, 7(1):1–8, 2017.
- [128] A Hartstein and E Burstein. Observation of magnetoplasma type surface polaritons on n-insb. *Solid State Communications*, 14(11):1223–1227, 1974.
- [129] Shashank Pandey, Shuchang Liu, Barun Gupta, and Ajay Nahata. Self-referenced measurements of the dielectric properties of metals using terahertz time-domain spectroscopy via the excitation of surface plasmon-polaritons. *Photonics Research*, 1(4):148–153, 2013.

- [130] Mark A Ordal, LL Long, RJ Bell, SE Bell, RR Bell, RW Alexander, and CA Ward. Optical properties of the metals al, co, cu, au, fe, pb, ni, pd, pt, ag, ti, and w in the infrared and far infrared. *Applied optics*, 22(7):1099–1119, 1983.
- [131] Mário G Silveirinha. Optical instabilities and spontaneous light emission by polarizable moving matter. *Physical Review X*, 4(3):031013, 2014.
- [132] Jan Masajada and Bogusława Dubik. Optical vortex generation by three plane wave interference. *Optics Communications*, 198(1-3):21–27, 2001.
- [133] JH Hannay and JF Nye. A differentiated plane wave as an electromagnetic vortex. *Journal of Optics*, 17(4):045603, 2015.
- [134] M Dressel and G Grüner. Electrodynamics of solids cambridge university press. *Cambridge, UK*, 2002.
- [135] VP Gusynin, SG Sharapov, and JP Carbotte. Magneto-optical conductivity in graphene. *Journal of Physics: Condensed Matter*, 19(2):026222, 2006.
- [136] George W Hanson. Dyadic green’s functions and guided surface waves for a surface conductivity model of graphene. *Journal of Applied Physics*, 103(6):064302, 2008.
- [137] Meng Wu, Zhenglu Li, Ting Cao, and Steven G Louie. Physical origin of giant excitonic and magneto-optical responses in two-dimensional ferromagnetic insulators. *Nature communications*, 10(1):1–8, 2019.
- [138] M Gajdoš, K Hummer, G Kresse, J Furthmüller, and FJPRB Bechstedt. Linear optical properties in the projector-augmented wave methodology. *Physical Review B*, 73(4):045112, 2006.
- [139] George W Hanson. Quasi-transverse electromagnetic modes supported by a graphene parallel-plate waveguide. *Journal of Applied Physics*, 104(8):084314, 2008.
- [140] George W Hanson. Dyadic green’s functions for an anisotropic, non-local model of biased graphene. *IEEE Transactions on antennas and propagation*, 56(3):747–757, 2008.
- [141] Akira Ishimaru. *Electromagnetic wave propagation, radiation, and scattering: from fundamentals to applications*. John Wiley & Sons, 2017.
- [142] Weihua Wang, Peter Apell, and Jari Kinaret. Edge plasmons in graphene nanostructures. *Physical Review B*, 84(8):085423, 2011.
- [143] DB Mast, AJ Dahm, and AL Fetter. Observation of bulk and edge magnetoplasmons in a two-dimensional electron fluid. *Physical review letters*, 54(15):1706, 1985.

- [144] Alexander L Fetter. Edge magnetoplasmons in a bounded two-dimensional electron fluid. *Physical Review B*, 32(12):7676, 1985.
- [145] I Fialkovsky and DV Vassilevich. Faraday rotation in graphene. *The European Physical Journal B*, 85(11):1–10, 2012.
- [146] Iris Crassee, Julien Levallois, Andrew L Walter, Markus Ostler, Aaron Bostwick, Eli Rotenberg, Thomas Seyller, Dirk Van Der Marel, and Alexey B Kuzmenko. Giant faraday rotation in single- and multilayer graphene. *Nature Physics*, 7(1):48–51, 2011.
- [147] Aires Ferreira, J Viana-Gomes, Yu V Bludov, V Pereira, NMR Peres, and AH Castro Neto. Faraday effect in graphene enclosed in an optical cavity and the equation of motion method for the study of magneto-optical transport in solids. *Physical Review B*, 84(23):235410, 2011.

Curriculum Vitae

EDUCATION

- **Ph.D. Candidate in Electrical Engineering** 2020 — present
University of Wisconsin Milwaukee, Milwaukee, USA
Doctoral dissertation: Nonreciprocal Electromagnetics of Layered Media,
Advisor: Prof. George W Hanson, GPA: 4 out of 4.
- **Visiting Research Scholar** 2018 — 2020
University of Wisconsin Milwaukee, Milwaukee, USA
Advisor: Prof. George W Hanson.
- **Ph.D. Degree in Electrical Engineering- Major: Communication-Fields** 2014 — 2021
Shiraz University of Technology, Department of Electronic Engineering, Shiraz, Iran,
Doctoral dissertation: Design and implementation of Plasmonic Structures using Transformation Optics.
Advisor: Prof. Shahrokh Jam, GPA: 19 out of 20.
- **Master's Degree in Electrical Engineering- Major: Communication-Fields** 2011 — 2014
Shiraz University, Department of Communications and Electronics, Shiraz, Iran,
Thesis: Simulation and analysis of beam-wave interaction in TWT by 3D large signal model,
Advisor: Prof. Habibollah Abiri, GPA: 17.83 out of 20.
- **Bachelor's Degree in Electrical Engineering- Major: Communication** 2006 — 2010
Shiraz University, Department of Communications and Electronics, Shiraz, Iran.

Academic Work Experience

- Research Assistant, University of Wisconsin Milwaukee, Milwaukee, USA. (2020 — present)
- Visiting Research Scholar, University of Wisconsin Milwaukee, Milwaukee, USA (2018 — 2020)
- Teaching Assistance at Shiraz University of Technology, Shiraz, Fars, Iran. (2014 — 2015)
 - Instructor of Microwaves Engineering, Antenna Engineering, Numerical Techniques in Electromagnetics courses
- Adjoint professor at Azad University, Neyriz Branch, Neyriz, Fars, Iran. (2011 — 2013)
 - Instructor of Electromagnetics, Electric Circuits, Logical Circuits and Microwave Engineering, Fields and Waves Electromagnetics, etc.
- Teaching Assistance at Shiraz University, Shiraz, Fars, Iran. (2010 — 2010)
 - Instructor of Electronic Circuits lab.

Executive Work Experience

Expert in communication and traffic control systems, (2015 — 2018)

Employee in Provincial Department of Road Maintenance and Transportation of Fars, Iran.

Publications

- 7 Peer- reviewed Journal Papers published in Optica, Optics Express, IEEE Transactions on Antennas and Propagation, Phys. Rev. B, Journal of Applied Physics, Optical Materials international journals and 1 paper has been published in an Iranian domestic journal.
- 10 Conference Papers presented in international conferences, including:
 - IEEE International Symposium on Antenna and Propagation, USNC-URSI Radio Science Meeting, in Denver, USA, July 2022 conference, - 3rd URSI AT-AP-RASC, Gran Canarias, Spain, May-June 2022 conference, - 2021 International Conference on Electromagnetics in Advanced Applications (ICEAA), Honolulu, Hawaii, USA, August 9-13, 2021, - URSI Commission B International Symposium on Electromagnetic Theory 2019, San Diego, California, USA, 2019,
 - 2020 IEEE International Symposium on Antennas and Propagation and North America Radio Science Meeting, Montreal, Canada, 2020.

- 4 Conference Papers presented in Iranian domestic conferences.
- A manuscripts is under review by IEEE Transactions on Antennas and Propagation journal.
- Google Scholar Profile: <https://scholar.google.com/citations?user=Ju-JIm4AAAAJ>

Award and Grants

- Chancellor's Graduate Student Award for Spring 2022, Fall 2021, Spring 2021, Fall 2020, Spring 2020 semesters, University of Wisconsin-Milwaukee
- Research Visiting Scholarship awarded by Ministry of Science, Research and Technology of Iran, 2017
- National Science Foundation, Grant number EFMA-1741673, Role: PhD student/Research Assistant

Volunteer Activities

- Reviewing 9 papers in Peer-Reviewed journals including:
Applied Physics Letter, Transactions on Microwave Theory and Techniques Journal, IEEE Antennas and Wireless Propagation Letters, Advanced Electromagnetics Journal. Serving as a chair of 8 sessions in international conferences.
- Training workshops for electromagnetic simulation software

Research Interests

Electromagnetics, Plasmonics, Photonics, Nanoelectronics, Quantum Optics.

Computer Skills

MATLAB, COMSOL Multiphysics, CST, HFSS, SPICE, Scientific workplace, Adobe Illustrator, Latex, Microsoft Word.

Publications from this thesis

Peer-Reviewed Journal Papers

1. **Samaneh Pakniyat**, Alexander M Holmes, George W Hanson, S Ali Hassani Gangaraj, Mauro Antezza, Mario G Silveirinha, Shahrokh Jam, and Francesco Monticone. "Non-reciprocal, robust surface

plasmon polaritons on gyrotropic interfaces,” **IEEE Transactions on Antennas and Propagation**, 68(5):3718-3729, 2020.

2. **Samaneh Pakniyat**, Yi Liang, Yinxiao Xiang, Cheng Cen, Jun Chen, and George W Hanson, ”Indium antimonide—constraints on practicality as a magneto-optical platform for topological surface plasmon polaritons,” **Journal of Applied Physics**, 128(18):183101, 2020.

3. Alexander M Holmes, **Samaneh Pakniyat**, S Ali Hassani Gangaraj, Francesco Monticone, Michael Weinert, and George W Hanson, ”Exchange splitting and exchange-induced nonreciprocal photonic behavior of graphene in CrI₃-graphene van der waals heterostructures,” **Physical Review B**, 102(7):075435, 2020.

4. Yi Liang, **Samaneh Pakniyat**, Yinxiao Xiang, Jun Chen, Fan Shi, George W Hanson, and Cheng Cen, ”Tunable unidirectional surface plasmon polaritons at the interface between gyrotropic and isotropic conductors,” **Optica**, 8(7):952959, 2021.

5. Yi Liang, **Samaneh Pakniyat**, Yinxiao Xiang, Fan Shi, George W Hanson, and Cheng Cen, ”Temperature-dependent transverse-field magneto-plasmons properties in insb,” **Optical Materials**, 112:110831, 2021.

6. **Samaneh Pakniyat**, S Ali Hassani Gangaraj, and George W Hanson, ”Chern invariants of topological continua: A self-consistent nonlocal hydrodynamic model,” **Physical Review B**, 105(3):035310, 2022.

7. **Samaneh Pakniyat**, Alex Holmes, and George W Hanson, ”Unidirectional Curved Surface Plasmon Polariton in a Radially Magnetized System,” in *IEEE Transactions on Antennas and Propagation*, 2022, doi: 10.1109/TAP.2022.3191129.

Conference Papers

1. S. Pakniyat, S. Ali Hassani Gangaraj, and G. W. Hanson, Chern Numbers in Magnetized Plasma System Characterized by a Nonlocal Hydrodynamic Model, IEEE International Symposium on Antenna and Propagation, USNC-URSI Radio Science Meeting, in Denver, USA, July 2022 .
2. S. Pakniyat, A.M. Holmes, and G. W. Hanson, Surface Plasmon Polariton Properties in Topological Continua under Radial Bias Using a Coordinate Free Dyadic Green's Function, ICEAA-IEEE APWC-USNC URSI RSM 2021, Honolulu, Hawaii, USA, August 9-13, 2021.
3. Y. Liang, S. Pakniyat, Y. Xiang, J. Chen, F. Shi, G. W. Hanson, C. Cen, Tunable unidirectional surface plasmon-polaritons at the interface between gyrotropic and isotropic conductors, ICEAA-IEEE APWC-USNC URSI RSM 2021, Honolulu, Hawaii, USA, August 9-13, 2021.
5. S. Pakniyat, Y. Liang, Y. Xiang, J. Chen, G. W. Hanson, C. Cen, Experimental Realization of Topological Surface Plasmon Polaritons in Magnetized InSb Crystal, 2020 IEEE International Symposium on Antennas and Propagation and North America Radio Science Meeting, Montreal, Canada, July 5-10, 2020.
5. S. Pakniyat, AM. Holmes, GW. Hanson, S. Jam, Quasi-Topological Surface Plasmon Polaritons on Gyrotropic Interfaces, URSI Commission B International Symposium on Electromagnetic Theory, San Diego, California, USA, May 27-31, 2019.